Myosin Dynamics During Asymmetric Stem Cell Division

Inauguraldissertation

zur Erlangung der Würde eines Doktors der Philosophie

vorgelegt der Philosophisch-Naturwissenschaftlichen Fakultät

der Universität Basel

von

Anna Tsankova

aus Bulgarien und Deutschland

Basel, 2018

Genehmigt von der Philosophisch-Naturwissenschaftlichen Fakultät

auf Antrag von

Prof. Clemens Cabernard und Prof. Markus Affolter

Basel, den 20.09.2016

Prof. Dr. Jörg Schibler

Table of contents

List of Figures

Abstract

Cell and tissue morphogenesis depend on the correct regulation of non-muscle Myosin 2 (NM2) but how this motor protein is spatiotemporally controlled is not fully understood. Using live cell imaging and a genetically encoded Myosin activity sensor, we found that in asymmetrically dividing *Drosophila* stem cells, called neuroblasts, Myosin's biased activity depends both on cell cycle and polarity cues. During early prophase of asymmetric cell division (ACD) Myosin is recruited to the cortex prior to nuclear envelope breakdown (NEB) through the Drosophila Rho Kinase (Drok). Later, the polarity protein Partner of Inscuteable (Pins) enriches Drok at the apical cortex, where Drok phosphorylates and activates Myosin. During late metaphase Pins recruits another kinase, Protein Kinase N (PKN) specifically to the apical neuroblast cortex, which is required for the correct temporal relocalization of activated Myosin. Our results strongly suggest that the sequential activity of PKN and Drok is essential for the correct spatiotemporal regulation of apical Myosin activation and subsequent relocalization.

Furthermore, we used green-to-red photoconversion of Myosin in wild type neuroblasts to address the question about the underlying mechanism of Myosin distribution. In the current work we show that the apical and basal Myosin molecules accumulate at the cleavage furrow through two distinct spatiotemporally regulated cortical flows – a basally directed Myosin flow starting after anaphase onset followed by an opposing apical-to-basal cortical flow. Furthermore, live imaging of neuroblasts expressing constitutively active forms of Myosin showed that misregulated Myosin activity targeted to the apical or the basal cortex without being relocalized, leads to cortical deformations, ectopic furrowing and cleavage furrow mispositioning. I propose that the spatiotemporal regulation of biased Myosin activity, relocalization and thus of both cortical flows are key determinants ensuring correct cortical expansion, cleavage furrow positioning and establishment of physical asymmetry of the dividing *Drosophila* neuroblasts.

Introduction

I. Cytokinesis

Cytokinesis is the process, which physically separates one mother cell into two daughter cells. It is initiated at early anaphase, when the metaphase microtubules reorganize and form a dense structure at the equatorial plane of the cell, called central spindle. Subsequently, the central spindle sends signals to the cortex and plays a key role in defining the position of the future cleavage furrow. This is followed by the assembly of the actomyosin ring and the subsequent constriction at the division site. The constriction of the cleavage furrow separates the cytoplasm into two domains, but the daughter cells remain connected through an intracellular bridge containing a region of high microtubule density, called midbody. During late telophase the final abscission takes place and allows the physical separation of the new cells (Figure 1). This process underlies very tight temporal and molecular control, ensuring the correct chromosome and organelle segregation. Cytokinesis failure can lead to the formation of tetraploid cells and in some instances also tumors. The molecular mechanisms regulating cytokinesis differ between different model organisms. Here I will predominantly refer to animal cytokinesis.

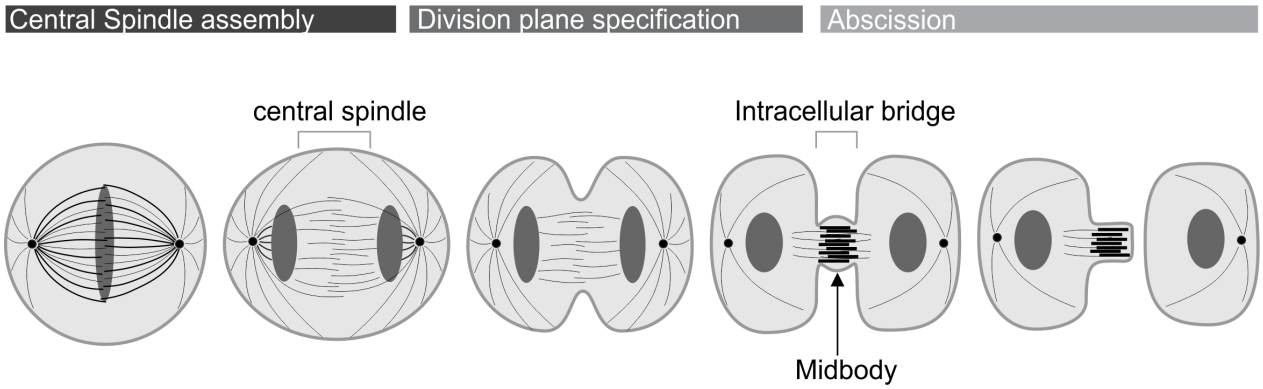

Figure 1: Steps of animal cell cytokinesis (adapted from[1]). Cytokinesis is initiated during anaphase through the assembly of the central spindle, which sends signals to the equatorial cortex and defines the division plane. During early telophase the cortex undergoes constriction and the cleavage furrow ingresses towards the inside of the cytoplasm, separating it into two domains. The intracellular bridge keeps the daughter cells connected until the final abscission is executed.

1. Central spindle assembly

The central spindle is a dense bundle of antiparallel microtubules of which the plus-ends overlap and are stabilized at the equatorial region of the cell (Figure 2). This structure has been shown in different model systems to play a key role during the first steps of cytokinesis. The central spindle sends signals to the cell cortex and establishes the position of the division plane between the two spindle poles.

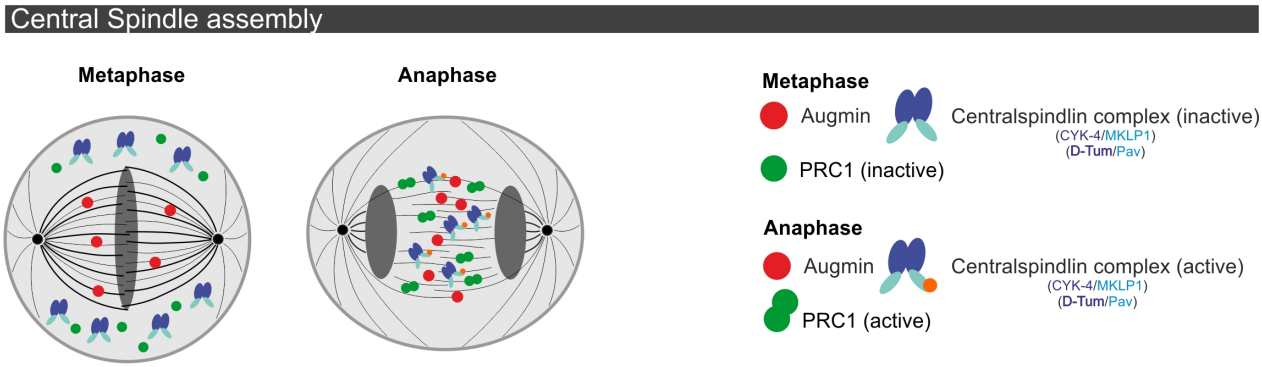

Figure 2: Central spindle assembly (adapted from[1]). During metaphase the centralspindlin and the PRC1 complexes are inactive and localized in the cytoplasm, whereas Augmin is already associated with the microtubules. During anaphase the centralspindlin and the PRC1 complexes are activated and accumulate at the central spindle region.

The microtubules of the central spindle are partially derived from the metaphase spindle and are also *de novo* assembled through non-centrosomal nucleation during anaphase, which is mediated by the Augmin complex[2,3]. There are different factors known to associate and contribute to the stabilization of the central spindle. The kinesin-4 (KIF4) and the Protein Required for Cytokinesis 1 (PRC1) bind antiparallel microtubules and ensure their stabilization[4]. KIF4 relocalizes towards the microtubule plus ends and inhibits their elongation once a specific length of the overlapping zone is reached[5]. Another important component of the central spindle is the heterotetrameric centralspindlin complex, which consists of two copies of the Kinesin MKLP1 (Pavarotti in flies) and the Rho-family GTPase Activating Protein (GAP), CYK-4 (Tumbleweed in flies)[6,7]. During early metaphase the centralspindlin complex is uniformly localized in the cytoplasm and appears only transiently at the mid-plane during late metaphase. At anaphase it relocalizes to the central spindle and is stabilized there. Interestingly, during anaphase the centralspindlin complex was also found at the cortical equatorial plane, corresponding to the future cleavage furrow[8]. In different systems it has been shown that the localization of MKLP1 and its microtubule binding properties are negatively regulated by CDK-1 phosphorylation[9]. Furthermore, phosphorylation of MKLP1 by Aurora B kinase during anaphase

together with dephosphorylation of the CDK1 phospho-site can promote the centralspindlin complex to bind and bundle central spindle microtubules[10]. Aurora B kinase, the Inner Centromere Protein (INCEP), Borealin and Survivin are the components of the Chromosomal Passenger Complex (CPC)[11]. CPC is the third key player in assembling the central spindle; it phosphorylates other factors like PRC1 or MKLP1 and bundles central spindle microtubules[12,13].

2. Division plane specification and actomyosin constriction

The specification of the division plane requires both signals from the astral microtubules and from the central spindle. These signals are redundant and their relative contribution might vary between different model systems. It has been proposed that two different populations of astral microtubules regulate the cortical contractility through a direct interaction with the different regions of the cortex[14]. On one hand, a pool of dynamic microtubules might inhibit contractility at the cell periphery, while another pool of stable microtubules directly induces contractility at the cell equator at the site of division (Figure 3)[15,16]. In addition, it was proposed that astral microtubules inhibit RhoA at the remaining cortical regions[15,17,18].

The role of the central spindle for specification of the division plane is better characterized. The central spindle activates the small GTPase RhoA locally at the equatorial site of the cortex and contributes in this way to the establishment of the cleavage furrow position[19,20]. Like most other GTPases, RhoA activity is regulated by Guanine-nucleotide Exchange Factors (GEFs) and GAPs. During cytokinesis in vertebrates the GEF ECT-2 (Pebble in flies) binds to the centralspindlin complex and is relocalized from the central spindle to the cortex during anaphase where it activates RhoA (Figure 3). The role of the GAPs is poorly understood. In addition to binding and recruiting ECT-2 to the central spindle, the Gap domain of CYK4 might regulate more directly the RhoA GTPase activity and promote a constant cycling of RhoA through GTP and GDP bound states[20-23]. Contradictive studies in *Xenopus* embryos and *C. elegans* have shown that the GAP domain of CYK4 might either promote inactivation of RhoA outside the contractile band, or activation of RhoA at the division site respectively[24-26]. Therefore, the role of the GAP domain for RhoA activity requires further investigation.

Once RhoA is activated at the equatorial cortex, it promotes the assembly and contraction of the actomyosin contractile ring. The contractile ring forms a broad band at the equatorial plane underneath the plasma membrane. It consists of Actin filaments, the non-muscle motor Myosin II, the crosslinkers Septins and the scaffold protein Anillin. Septins are

filamentous GTP binding proteins, which were shown to accumulate at the site of the division and contribute to membrane constriction. Septins are required in *D. melanogaster*, *C. elegans* and in mammalian systems for robust cytokinesis[27-29]. They are linked to Myosin and Actin filaments by Anillin, which is known to directly interact with Actin, activated Myosin-II and Septins[30,31].

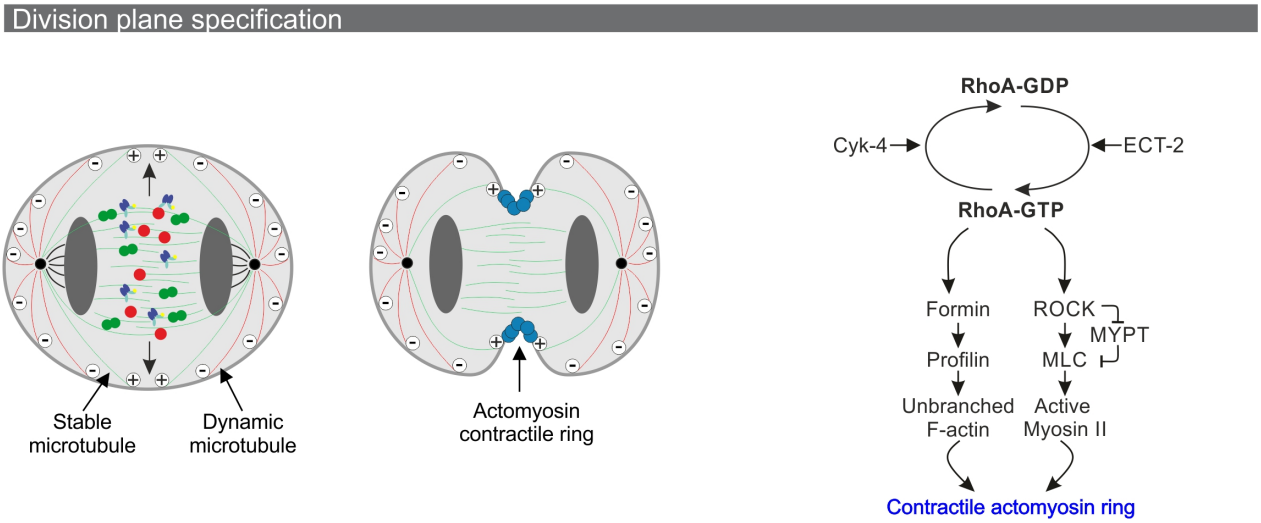

Figure 3: Division plane specification (on the left) and RhoA activation pathway (on the right) (adapted from[1]). Stable astral microtubules (shown in green) induce actomyosin contractility at the division site, whereas dynamic astral microtubules (shown in red) inhibit contractility at the cortex periphery. The signals from the central spindle are indicated with black arrows. During telophase the contractile ring (shown in blue) assembles at the division site. On the right the RhoA activation pathway is shown. ECT-2 and CYK-4 regulate the RhoA-GTP cycle and activated RhoA promotes polymerization of unbranched Actin filaments and activation of Myosin.

There is controversy about the architecture of the actomyosin contractile ring. Actin filaments might be ordered or randomly organized. Previously, it was assumed that the Actin filaments in the contractile ring are organized in a sarcomere manner, ordered along the division plane with opposite polarities and antiparallel to each other[32,33]. However, new studies have shown two additional structures of the actomyosin contractile ring, as a gel-like or random one-dimensional structure. The gel-like structure was observed for HeLa and for *D. discoideum* cells. In this case the neighboring Actin filaments are randomly organized towards the division plane and also have random parallel or antiparallel orientation towards each other[34,35]. In contrast, the random one-dimensional ring consists of Actin filaments, which are still parallel oriented towards the division plane but show random orientation towards each other. This type of actomyosin architecture was observed during late anaphase in the cytokinetic rings of fission yeast and also in motile fibroblasts[36,37].

How does RhoA induce the assembly of the actomyosin contractile ring? On one hand, RhoA-GTP activates the Formin Diaphanous (Dia) and Profilin, which induce polymerization of unbranched Actin filaments (Figure 3)[38-40]. On the other hand, RhoA-GTP recruits Myosin to the division site and activates it indirectly through the Myosin light chain kinase Rock and through inhibition of the Myosin phosphatase MYPT (The pathway of Myosin regulation is discussed in detail in Introduction; chapter II.2). Different mechanisms were shown to regulate the recruitment of Myosin at the cytokinetic ring in different model systems[41]. In *Dictyostelium* cells Myosin seems to flow along the cortex and reach the site of division and accumulate there[42]. Another mechanism was proposed for *Drosophila* S2 cells, where Myosin is generated *de novo* at the equatorial cortex and degraded from the cortical periphery[43].

After actomyosin has formed the broad band in the equatorial plane, it reduced its size down to 1-2 μm and allows the cytoplasmic separation of the two daughter cells by forming a tight ring at the site of the division. This phenomenon was shown in different model systems like sea urchin, *Drosophila* neuroblasts, HeLa cells and was very well documented for the early embryonic development of *C. elegans*[34,44]. It has been shown that the equatorial band folds towards the inside of the embryo and the contractile ring proteins enrich at the tip of the furrow. In this case the ring constriction rate was constant and proportional both to the initial size of the equatorial band and to the amount of Myosin II there[45,46]. This might be a regulatory mechanism to ensure the correct timing of the cell division independent of the cell size. Supporting these findings, constant constriction rates were also reported for hyphae in the filamentous fungus *N. Crassa,* Cos-7 cells and the fission yeast *S. pombe*[46-49]. Early models developed in the *C. elegans* embryo explained the constant constriction rates with a gradual disassembly of the Actin network. There the Actin network volume was measured using electron micrographs showing proportional disassembly during constriction without complete loss of its components[44]. More recent photobleaching experiments in *Drosophila* spermatocytes and *C. elegans* embryos confirmed these findings. In addition, an exchange between cortical and cytoplasmic pools of Myosin, Anillin and Septins was very slow after actomyosin constriction has been initiated[45].

This cleavage furrow constriction is triggered by the increased active tension at the cell equator, which is generated during this last step of cytokinesis. The canonical mechanism to generate the force for actomyosin cytokinetic constriction relies on the binding of the motor Myosin to the Actin filaments as it is established for muscles. In this case, the constriction

depends on the conformational changes, which Myosin undergoes after ATP hydrolysis. This leads to loosening the binding of the motor head domain of Myosin to Actin and allows antiparallel Actin filaments to slide together[50,51]. Although it is well established that Myosin plays an essential role for generating active tension at the cortex, it is still not completely clear what is the exact molecular mechanism of its action. In both cultured COS-7 cells and mice cardiac myocytes the cytokinesis failure caused by Myosin-II depletion could be rescued by a Moysin mutant, which was able to sustain tension but was not able to move along Actin filaments[47]. This suggests that Myosin might play a role as a cross-linker for Actin filaments rather than actively generating the force for furrow constriction.

An alternative mechanism was proposed, where active tension at the cytokinetic ring was generated independently of Myosin activity trough Actin polymerization and depolymerization. Proteins, which track the plus or minus ends of Actin filaments together with the filaments dynamic turnover might generate tension in the whole network and induce constriction during cytokinesis. These models were supported by a study in budding yeast, showing that Actin depolymerization coupled with filament cross-linking might be inducing the force during contractile ring constriction[49,52]. Taken together, these findings suggest that the mechanisms generating the constriction force might be differently regulated in different model systems.

3. Final abscission

The last step of cytokinesis is the final physical separation of both daughter cells. During the constriction of the actomyosin ring the dense array of the central spindle microtubules rearranges and forms a 1-2 μm thin intracellular bridge connecting both cells for several hours before the final abscission. The microtubules overlap in the middle of the intercellular bridge and form a structure called midbody, which retains its initial diameter of around 1.5 μm and later serves as the platform for the final abscission. The intercellular bridge further reduces its diameter up to 0.2 μm on both sides of the midbody, creating two additional ingression sites. The final abscission is induced sequentially on both sides of the midbody, where the compressed microtubules depolymerize, the plasma membrane is separated in the two daughter cells and the midbody is released. In order to fully understand this final step of cytokinesis, first the structure of the midbody should be discussed (Figure 4)[53].

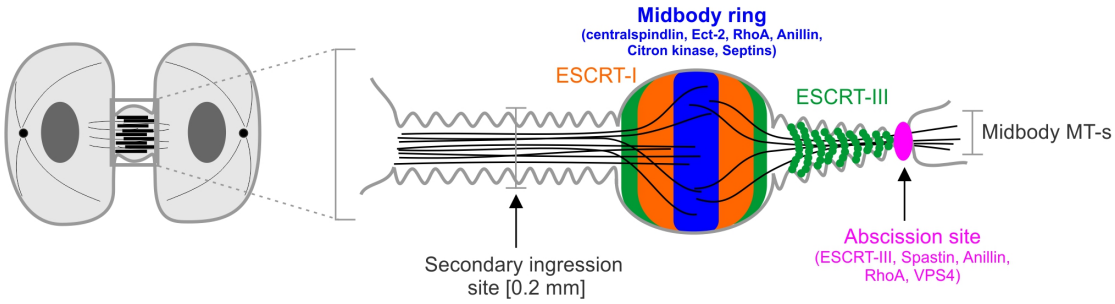

Figure 4: Structure of the intracellular bridge containing the midbody (adapted from[54]). The main midbody components are shown: the midbody ring (shown in blue), the midbody flank containing ESCRT-I (shown in orange), ESCRT-III (shown in green), the abscission site (shown in purple) and the midbody microtubules (MT-s; shown in grey).

The contractile ring forms the midbody ring at this late stage of cytokinesis. Since the midbody is derived from the central spindle it is not surprising that most of the spindle components also remain localized to the central microtubule-overlapping region of the midbody (also called midbody core) prior to abscission. The central midbody ring retains also Anillin, Septins, Citron kinase and RhoA[55,56]. Furthermore, centralspindlin and ECT-2 were also found in this region. The centralspindlin anchors to the plasma membrane by its CYK4 membrane-binding domain, leading to stabilization of the ingressed cleavage furrow[57-59]. Similarly to the centralspindlin complex, Anillin was shown to link the plasma membrane with the midbody ring, leading to midbody ring assembly, stabilization of the intracellular bridge and ensuring complete constriction. Studies in *Drosophila* S2 cells have shown that Anillin depletion leads to abnormally broad intracellular bridges and cytokinesis failure. The role of Anillin for linking plasma membrane and midbody ring, which ensures complete constriction and cytokinesis, depends on its binding to Septins[60,61]. Interestingly, the correct localization of both Anillin and RhoA at the midbody is dependent on Citron kinase[56]. Finally, the flanking regions around the midbody core, called the midbody flank, retain the central spindle proteins MKLP2 and AuroraB, as well as Anillin[62]. Another important component of the midbody flank is the Endosomal Sorting Complex Required for Transport-I (ESCRT-I). ESCRT-I was shown to localize to the intracellular bridge flanking the midbody ring from both sides and targets ESCRT-III to the cortical regions prior to abscission[63]. The abscission site is localized next to the midbody flank region. Proteins needed for the final abscission such as Spastin, ESCRT-III, the Vacoular Sorting Protein 4 (VPS4) and RhoA are found to enrich their localization there.

In recent years new studies have dramatically changed the understanding of the molecular mechanism underlying the final abscission and the physical separation of the two

daughter cells. Previously, final abscission was associated with vesicle trafficking along the microtubules towards the division site. Vesicles derived from recycling endosomes or from the Golgi pathway were assumed to insert separation membrane at the site of the intracellular bridge. Various vesicle trafficking proteins such as SNARE proteins, Rab proteins (including Rab35, Rab8 and Rab11) and exocyst proteins were shown to localize at the intracellular bridge. Disruption of membrane trafficking leads to cytokinesis failure at late stages in cytokinesis[64-66]. However, a recent study showed live imaging and electron microscopy data indicating that these vesicles disappear directly before abscission. This indicates that the vesicle trafficking might be regulating the assembly and stabilization of the intracellular bridge rather than the final abscission event. In the same study the authors showed the presence of 17 nm filaments, forming a helix structure around the intracellular bridge, which narrowed its length. Although, the molecular components of these filaments are not known yet, it was shown that ESCRT-III accumulates at the constriction zone and is required for the assembly of the 17 nm filaments and final constriction[67].

The role of ESCRT proteins in membrane scission was already well established for viral and endosomal vesicle budding and is conserved in cytokinesis of some archaea[63,68-70]. Furthermore, microtubule depolymerization is temporally associated with the membrane constriction at the abscission site. Microtubule depolymerization is triggered by the microtubule severing enzyme Spastin, which is recruited to the constriction zone by direct interaction with ESCRT-III[71-73]. The temporal regulation of the ESCRT-III recruitment to the midbody and therefore the abscission timing is regulated by Plk1 phosphorylation of the ESCRT binding protein Cep55. Phosphorylated Cep55 by Plk1 prevents it from targeting the central spindle and the midbody. After Plk1 degradation Cep55 relocalizes to the midbody and recruits the ESCRT-III complex to initiate abscission[70,74]. AuroraB prevents premature abscission by phosphorylating and inhibiting the regulatory region of the ESCRT-III component CHMP4C[75,76]. During the final stages of abscission the ESCRT-III disassembly factor VPS4 is recruited to the intracellular bridge and binds to ESCRT-III subunits there[77]. In this study it has been shown that the binding of VSP4 contributes not only to ESCRT disassembly, but also to the membrane neck narrowing prior to the final fission event. However, the role of VSP4 for ESCRT-III remodeling and the mechanism of the final membrane constriction inducing the membrane scission event remain elusive. Two models have been psoposed: On one hand, binding of VSP4 either triggers ESCRT-III self-assembly and membrane remodeling leading into a dome to the final scission, or on the other hand, VSP4

might trigger ESCRT-III disassembly and ESCRT polymers could constrict the membrane in a purse-string mechanism promoting scission[78,79].

II. Myosin

Myosins are a superfamily of motor proteins, most of which belong to the class 2, also known as conventional Myosins. Besides skeletal, cardiac, smooth muscle Myosins, also non-muscle Myosin 2 (NM2) belongs to this class. In the current work, I will concentrate on NM2 (henceforth called Myosin). NM2 is expressed in most differentiated cells in the human body and plays a major role in multiple processes such as morphogenesis, cell adhesion, migration and cell division. In contrast to many lower eukaryotes and also to *Drosophila*, where only one NM2 isoform is known, mammalian cells express three different NM2 isoforms, NM2A, NM2B and NM2C[80,81]. These isoforms were shown to have some specific but also some overlapping functions. This indicates that the diversity is needed to maintain the more complex functions in the mammalian organisms. On one hand, the different functions of the isoforms might be ensured by their differential expression in different tissues. Although, NM2A and NM2B are expressed almost ubiquitously, there are cases showing isoform specific expression[82]. In hematopoietic cells, for example, only NM2A was found[83]. Cardiac myocytes usually contain NM2B and NM2C, whereas the non-myocyte cells in the heart express NM2A[84]. Immunohistochemistry stainings in the developing mouse embryo showed that brain tissue was enriched for NM2B and NM2C. In the spleen, predominantly NM2A was detected[80]. Furthermore, differences in NM2A activity might also regulate the functional diversity. The ATPase activity of the different Myosin isoforms varies significantly and NM2A shows the highest ATP hydrolysis rate amongst all three isoforms[85]. Furthermore, different isoforms vary in how long they stay strongly bound to Actin per ATPase cycle (duty ratio). The duty ratio of NM2B is higher than the duty rate of NM2A and NM2C, indicating that NM2B probably regulates maintenance of tension on Actin filaments, using less energy and for longer periods of time[86,87]. The molecular mechanisms, which establish these kinetic differences, are not known yet. However, it is possible that activation through phosphorylation of specific isoforms and different binding partners might be the trigger.

1. Structure of non-muscle Myosin

Myosin is a hexameric protein complex, consisting of two Myosin Heavy Chains (MHCs), two Regulatory Light Chains (RLCs) and two Essential Light Chains (ELCs). The complex self-assembles into bipolar filaments. Each MHC includes three domains: a globular head domain, an α-helical rod domain and a short non-helical tail at the C-terminus (Figure 5).

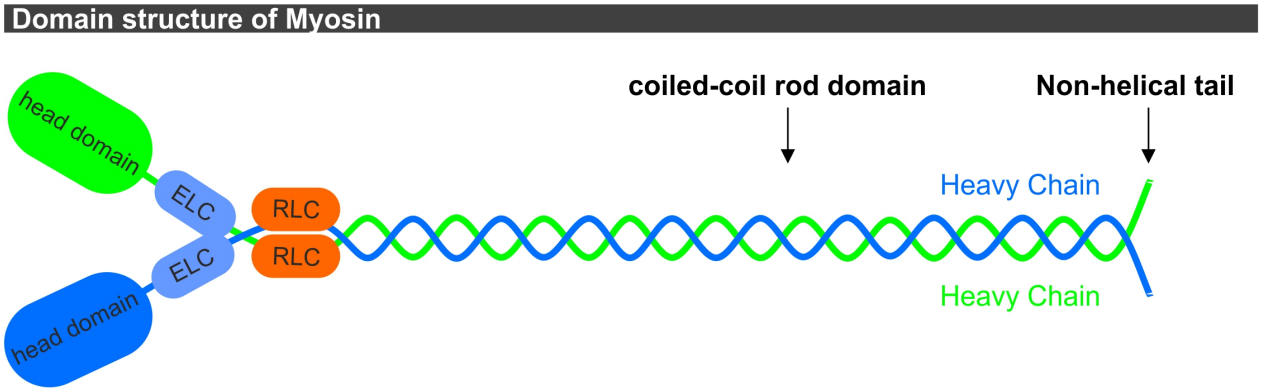

Figure 5: Non-muscle Myosin 2: domain structure (adapted from[88]). Each heavy chain is composed of one head domain, one coiled-coil rod domain and a short non-helical tail. The MHCs are shown either in green or dark blue. The Regulatory Light Chains (RLCs) are shown in orange and the Essential Light Chains (ELCs) are shown in blue.

The head domain is highly conserved, can bind Actin and has ATPase activity, which triggers the motor properties of the complex. The ELC connects the MHC with the RLC and in addition it ensures stability, flexibility and allows the rotation of the head domains during their mechanical movement upon ATP hydrolysis. The long coiled-coiled rod domain contains the α-helices of the two heavy chains, which are wrapped around each other and terminates in a non-helical tail. The rod domains induce the dimerization of two Myosin hexamers and their binding to Actin filaments in an antiparallel manner. The RLC contains conserved phospho-sites, known to play a key role in controlling Myosin's ATPase activity. In *Drosophila*, the RLC is encoded by the gene *spaghetti squash (sqh)* and the MHC by *zipper (zip)*[88,89].

2. Regulation of Myosin activity

The motor activity of Myosin is triggered by phosphorylation of two conserved sites within the RLC (Ser19 and Thr18), which leads to a transformation from a closed to an open conformation; in the open conformation, the motor head domains are in an ADP bound state and are able to bind two antiparallel Actin filaments[90]. Upon exchange of ADP with ATP the head domains release the binding to Actin filaments. Subsequently, hydrolysis of ATP enables rotation of the head domains, which triggers transformation of chemical energy into mechanical force

and induces the re-binding of the head domains to Actin filaments, pulling these together (lower panel Figure 6). Repeating this cycle is the main mechanism underlying the generation of cortical tension[89,91].

Since the ATPase activity of Myosin is regulated through cycles of phosphorylation and dephosphorylation, it is important to know the key players in this process. Multiple kinases and phosphatases were assumed to play a role in NM2's regulation by targeting various phosphorylation sites within both the MHC and the RLC. Phosphorylation within the RLC occurs at Ser1, Ser2, Thr9, Thr18 and Ser19[90,92].

The best-established model for Myosin activation includes phosphorylation at the two conserved sites Ser19 and Thr18 (corresponding to Ser21 and Thr20 in *Drosophila*), leading to a conformational change and increased ATPase activity. However, phosphorylation of these sites does not affect the affinity of Myosin to Actin[90,93]. Multiple kinases and phosphatases were already shown to phosphorylate Myosin at Ser19 and Thr18, such as the Myosin Light Chain Kinase (MLCK), Rho-associated Kinase (Rock), Leucine Zipper Interacting Protein Kinase (ZIPK), Citron kinase, the Serine/Threonine protein kinase MRCK (Myotonic Dystrophy kinase-related Cdc42-binding Kinase) and many others (upper panel Figure 6). These kinases show different cellular localization and different activation pathways, indicating that this might lead to regulation of different processes[94,96]. For example, Citron kinase and Rock are both activated through RhoA and are localized in the cytoplasm, where they activate Myosin and stabilize stress fibers and mature focal adhesions. MLCK is regulated by Ca^{2+}-calmodulin signaling and activates Myosin at the cell membrane[97,98]. MRCK is another kinase indicated in Myosin phosphorylation at the conserved site and is a known regulator of actomyosin contractility and cytoskeletal reorganization. MRCK is activated through binding to GTP-Cdc42. The activation loop of Myosin and its role in constricting Actin filaments are shown in Figure 6.

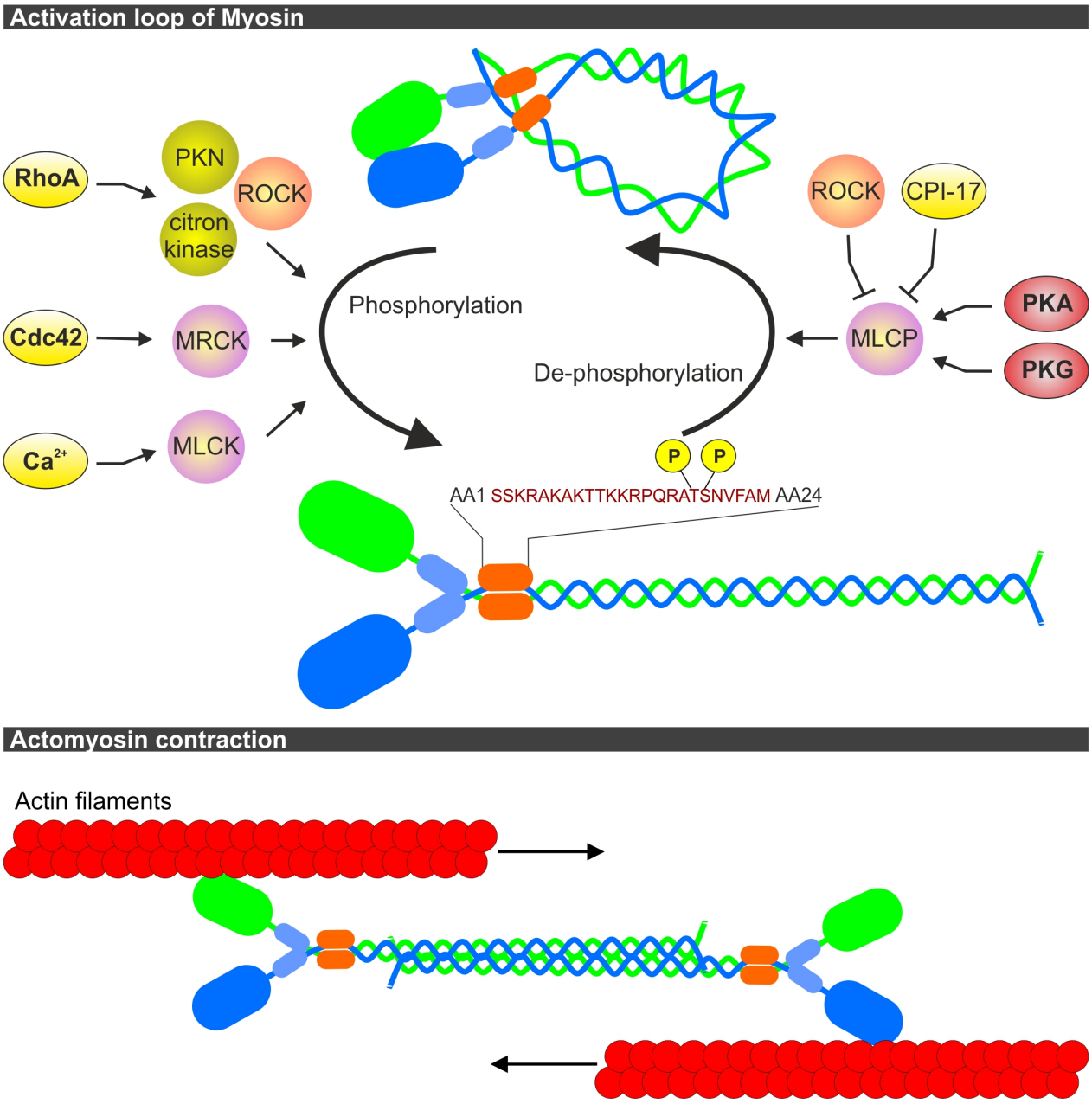

Figure 6: The activation mechanism of non-muscle Myosin 2 (adapted from[99]). Upper panel: Activation/Deactivation of Myosin is regulated through a phosphorylation/dephosphorylation loop at Ser19 and Thr18. Phosphorylation triggers a conformational change from a closed to an open state, which is able to bind Actin filaments. The kinases and phosphatases known to regulate Myosin's phosphorylation and dephosphorylation are also indicated with their upstream regulators. Lower panel: Myosin in an activated state bound to Actin filaments, which triggers ATP hydrolysis, allows rotation of the head domains and induces contraction of the Actin network.

In addition to this well described pathway of Myosin activation through phosphorylation of Ser19 and Thr18, there is some evidence that Ser1 and Ser2 and Thr9 of Myosin`s RLC are phosphorylated by Protein Kinase C (PKC), leading to inactivation of Myosin. Reduced Myosin ATPase activity upon PKC phosphorylation within the N-terminus of the RLC was reported already in 1984 by Nishikawa for smooth muscle Myosin 2[100]. Ikebe and colleagues used further biochemical experiments to identify the phosphorylation sites S1, S2 and Thr9 in 1990[92]. This

role of PKC was later confirmed for living cells, where studies have shown increased level of S1 and S2 phosphorylation in cells arrested in mitosis. Furthermore, it has been shown that downregulation of Myosin's activity through phosphorylation at S1 and S2 is important for the correct actomyosin reorganization during cell migration[101,102]. However, there are also controversy studies, which were not able to confirm these findings, using mutated RLC forms expressed in HeLa cells and primary human keratinocytes. Since all these studies were performed using different cell types, a cell specific phosphorylation mechanism could be an explanation for the different results[103].

RLC phosphorylation and thus Myosin activation is a tightly regulated reversible process, which is also regulated through dephosphorylation by phosphatases (upper panel Figure 6). For instance, Myosin Light Chain Phosphatase (MLCP), consisting of the catalytic subunit Protein Phosphatase 1 (PP1), the Myosin Binding Subunit (MBS) and M20, a third subunit of unknown function, is known to regulate Myosin activity. MLCP is a target of both PKA and PKG and phosphorylation leads to the activation of the phosphatase activity. On the other hand, Rock can directly phosphorylate MBS, which leads to inhibition of PP1 and thus to increased phosphorylation at Ser19[104]. However, there is another pathway through CPI-17, which regulates PP1 catalytic activity independently of the RhoA/Rock pathway and triggers indirectly an increased phosphorylation of Myosin's RLC. CPI-17 is activated through phosphorylation at Thr38 and is then able to bind and inhibit PP1. Thus, CPI-17 is another inhibitor of PP1. Different kinases, involving PKC, were suggested to play a role for CPI-17 activation in smooth muscles. Since smooth muscle Myosin is closely related to NM2 and their regulation pathways are very similar, it can be assumed that eventually CPI-17 could play a role in regulating phosphorylation and activation of NM2 too. This is supported by the expression pattern of CPI-17, which can be found not only in muscle tissues, but also in platelets, neurons and epithelia. However, the function and mechanism of action in these tissues is not completely clear[105].

Besides the phosphorylation within the RLC of Myosin, there is evidence that the C-terminus of MHC also undergoes phosphorylation at several sites through various kinases. These phosphorylation sites are located within the coiled-coiled and within the non-helical domain and regulate Myosin's filament disassembly in an isoform specific manner. PKC is known to phosphorylate S1916 of NM2-A, and S1937 of NM2-B[106,107]. Other kinases, known for their ability to phosphorylate the heavy chain of Myosin are the Casein kinase 2 (CK2) and the Transient Receptor Potential Melastatin 7 (TRPM7). TRPM7 can phosphorylate Thr1800, S1803 and S1808

within the coiled-coiled region of NM2-A. The role of these phospho-sites was analyzed using *in vitro* kinase assays, suggesting that phosphorylation decreases filament formation and alters the sub-cellular localization of NM2-A[108]. Phosphorylation through both PKC and CK2 was reported to decrease Myosin filament assembly specifically for NM2-B, which was not affected for NM2-A. However, the question about the molecular mechanism underlying the regulation of Myosin filament assembly and disassembly remains elusive.

Other than its role in filament assembly, phosphorylation of the MHC could be involved in regulating interaction partners and so further downstream cellular functions. The best studied example is the binding of the metastasis factor S100A4 (also called Mts1) specifically to NM2-A. S100A4 is associated with cellular mobility of cancer cells in metastatic tissues and the interaction with NM2 was also shown to both prevent Myosin filament assembly and induce filament disassembly. Experimental studies have proposed that the phosphorylation of S1943 within the non-helical region of NM2-A through CK2, but not phosphorylation of the aforementioned S1916 reduces the binding affinity of S100A4 to the C-terminus of the MHC[109]. Furthermore, recent biochemical protein structure analysis of the interaction complex could confirm the previous findings, indicating that only phosphorylation at S1943 but not at S1916 reduces the binding affinity of S100A4[110].

Another important interaction partner of Myosin, which binds within its heavy chain region, is Lethal giant larvae (Lgl). Lgl is a tumor suppressor protein, which forms a complex with the C-terminal region of MHC and controls cell proliferation. Lgl binds to the coiled-coil region of the MHC and negatively regulates Myosin filament formation. However, it has been shown that upon phosphorylation through PKC the interaction dissociates[111,112].

These data taken together show that indeed phosphorylation within MHC plays also an important role in Myosin regulation and further studies are needed in order to completely understand the molecular mechanism and the functions of these phosphorylation events. An interesting open question concerns the connection between Myosin RLC and MHC phosphorylation. In this regard, other model organisms with less isoform variability such as *Drosophila melanogaster* or *C. elegans* might lead the way.

3. Biological functions of NM2

Myosin's best studied role during cytokinesis through establishing contractile forces, triggering actomyosin constriction was discussed above (see chapter I.2 and II.2). Similarly, force

generation and actomyosin constriction trigger not only cleavage furrow ingression, but also regulate all other cell shape changes during cytokinesis such as cell rounding during metaphase (reviewed in[54,113]). However, NM2 regulates various other processes, which will be discussed below.

NM2 was shown to play a role in cell migration. Migrating cells such as fibroblasts are polarized cells and show a unique structure. At the front region, the leading edge, migrating cells have two Actin-based structures (the lamellipodium and the lamellum), which contain highly dynamic Actin filaments. The rearrangement of Actin filaments in this region triggers cell protrusion and cell migration. The posterior and the middle region of these cells are normally composed of highly bundled Actin, which prevent protrusion and induce adhesion disassembly[114]. The different actomyosin composition, defining the different regions of the cell, is not the only hallmark. The positioning of the nucleus, the microtubule-organizing center (MTOC) and the Golgi apparatus are further markers of cell polarization. During migration the MTOC and the Golgi reposition themselves towards the front of the nucleus at the side of the protrusion. Myosin is known to be essential for protrusion[115]. Previous studies have shown that a knock-down, chemical inhibition, or a knock-out of Myosin lead to compromised protrusion, absence of large Actin bundles and decreased rate of Actin retrograde flow in the lamellum[116,117]. However, the Actin filament structure of the lamellipodium does not seem to be affected. Thus, according to the proposed hypothesis NM2 could play a role in Actin retrograde flow in the lamellum, which is connected to the lamellipodium. On the other hand, Myosin could also regulate the polarity of the migrating cells by enriching at the tail region of the migrating cell, causing a local rearranging of Actin filaments. Such symmetry-braking events are needed to induce protrusion at the opposite site of the cell and trigger directional migration[118,119]. Furthermore, the motor activity of Myosin was shown to regulate the nucleus positioning. Inhibition of Myosin`s activity lead to mispositioning and an abnormal rotation of the nucleus. Myosin could regulate nucleus positioning, either by directly generating tension at the perinuclear Actin filaments, preventing rotation and leading the nucleus movement forward. Another possibility is that Myosin anchors the nucleus through a direct interaction with the nuclear transmembrane receptors, involved in nuclear redistribution during cell migration[120].

Myosin also plays a key role in regulating maturation of cell adhesions. Cells can establish cell-cell adhesions through interaction of their transmembrane E-Cadherins in the extracellular space. The corresponding component of the cell adhesion system, Catenin, binds intracellularly

to Actin and links Actin filaments to adhesion junctions. Myosin can regulate the dynamics of these junctions by binding to Actin, inducing tension at the Actin filaments. It was shown that Myosin's role to localize at the site of E-Cadherin junctions and to induce tension is dependent on RLC phosphorylation at S19 and Thr18[121,122]. By pulling on Actin filaments, Myosin is able to extend the interaction surface between the cells and enrich the junction density. Furthermore, Myosin was shown to play a role in maintaining the correct localization of the adhesion proteins and thus cell-cell contacts. Interestingly, Myosin depleted cells showed reduction of cell-cell adherent junctions, mislocalized E-Cadherin and β-Catenin during early mouse development[123]. Further studies indicate similar functions for Myosin in regulation of focal adhesions, which establish a connection between the cell and the extracellular matrix (ECM)[124].

Furthermore, actomyosin dynamics were very well studied in the context of tissue morphogenesis, especially during *Drosophila* early development. Fluctuations in Actin filaments are established through Myosin recruitment and can lead to different cell shape changes depending on the context. For example, during *Drosophila* gastrulation the cells of the future mesoderm undergo drastic cell shape changes, forming the ventral furrow and internalizing the mesoderm cells completely towards the inside of the embryo. These cell shape changes are triggered by recruitment of Myosin at the apical side, generating cycles of assembly and disassembly, which is needed to induce shrinking of the apical surface and thus bending the tissue. In order to make the shape changes irreversible, Myosin's activity pulses are followed by stages of persisting of medial Myosin. The activation of Myosin in the mesoderm is regulated through the canonical Rho-1/Rock pathway[125].

Another important mechanism during *Drosophila* gastrulation, regulated by Myosin activity is the germ band extension in the ectoderm, which requires cell intercalation. This process involves the shrinking of the vertical junction and extension of the newly formed horizontal junctions along the anterior-posterior axis. In this case, it was shown that Myosin pulses flow towards the vertical junctions, inducing their shrinking and stable planar pool of Myosin stabilizes the cell shape changes. This recent study identified a common G protein signaling pathway involved in regulation of Myosin's activity in both the mesoderm and the ectoderm. It was shown that $G\alpha_{12/13}$ regulates specifically the activation of the medial-apical Myosin, whereas Gβ13F and Gγ1 regulate both apical and junctional Myosin. These differences might be facilitated through specific downstream targets of $G\alpha_{12/13}$ and the Gβγ complex. The authors further showed that the signaling pathway is regulated through the common and

ubiquitously expressed G-protein coupled receptor (GPCR) Smog, which activates Myosin through the canonical Rho-1/Rock pathway in these two morphogenetic processes. Additionally, tissue-specific ligands such as Fog in the mesoderm might act in order to fine-tune Myosin's activity leading to a pulsatile regime, or to stable activation[125].

III. Protein Kinase N (PKN) as a putative Myosin regulator

PKN is a Serine/Threonine protein kinase of the PKC protein family. It was first isolated in 1994, however, little is known about the regulation and function of PKN. In humans there are three known isoforms to date – PKNα, PKNβ and PKNγ. PKNα and PKNγ are ubiquitously expressed in mouse, rat and human tissues[126,127]. Interestingly, PKNβ was not found in any healthy human tissues, but was expressed in various cancer cell lines[128]. Biochemical studies have shown that PKNα is enriched in rat neurons, localizing predominantly in the cytosolic fraction. Similarly, in different culture cells PKNα was also shown to localize in the cytoplasm under physiological conditions, whereas under stress conditions, PKN relocalized to the nucleus[129]. Furthermore, similar studies showed that under normal conditions PKNβ localizes to the nucleus and to the perinuclear material, but was not found in the cytoplasm[128]. To date there is only one homologue PKN isoform known in *Drosophila*.

1. Structure

The structure of the different PKN isoforms is conserved among them and also between different species. *Drosophila* and the human PKN isoforms show around 60% homology[130]. The N-terminal region of PKN contains three leucine zipper repeats of around 70 amino acids, called ACC domains. These domains are two antiparallel coiled-coil α-helices and act as binding surface for different interaction partners, such as the small GTPases RhoA and Rac1 (see below) and also the centrosome and Golgi localized PKN associated protein (CG-NAP)[131,132].

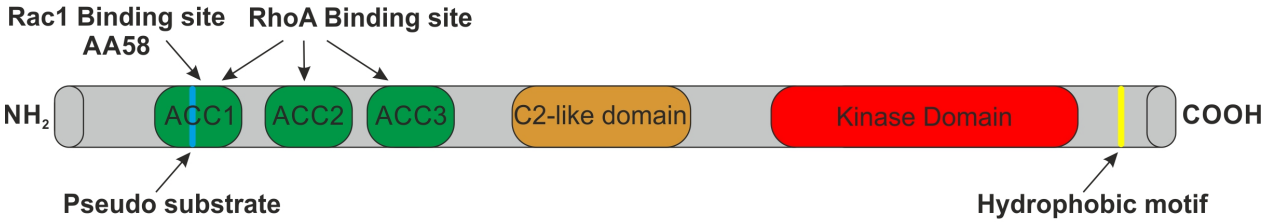

Figure 7: Domain structure of PKN (adapted from[133]). The three ACC domains are shown in green, with the indicated RhoA and Rac1 binding sites. The central C2-like domain is shown in orange and the C-terminal kinase domain is shown in red. The pseudo substrate motif is shown in blue.

The first structural evidence was shown for PKN as a complex with its binding partner RhoA[131]. RhoA binds within the first and the second, whereas Rac1 binds specifically the first ACC domain[131]. A highly conserved central region was detected in PKN, which was also found in PKC and it is assumed to be an inhibitory domain[134]. Although, the role of this region is not fully understood, there is evidence that phosphorylation within this region triggers further auto-phosphorylation events, leading to increased PKN kinase activity[134]. The C-terminus contains the PKC-like kinase domain, which shows a high sequence homology to the kinase domains of the PKC family members[135]. The structure of PKN is shown in Figure 7.

2. Regulation of PKN activity

The first studies showing PKN regulation revealed a number of unsaturated fatty acids (arachidonic acid and linoleic acid), phospholipids (phosphatidylinositol 4,5-biphosphat (PI4,5-P2) and phosphatidylinositol 3,4,5-triphosphat (PI3,4,5-P3)) and lysophospholipids (lysophosphatidic acid) as potential activators of PKN[135,136]. Later, in 1996 it was shown for the first time that PKN binds the small GTPase RhoA in a GTP-dependent manner, which leads to an increased kinase activity. *In vitro* experiments also confirmed these results by showing that isolated PKN was also stimulated by the addition of an active GTP bound form of RhoA[137,138]. Interestingly, mammalian PKNα binds with higher affinity to RhoA and only weakly to Rac1[139]. In contrast, it was shown that *Drosophila* PKN binds to Rac1, Rac2 and RhoA with the same affinity[130]. This indicates that PKN initially might have been a downstream target of both Rac and RhoA, separating into different isoforms during evolution to facilitate complex biological functions in the mammalian organisms through unique activation mechanisms. In summary, the data clearly shows that PKN is a downstream target of RhoA. Further studies showed also that PKN binds to the phosphoinositide-dependent protein kinase 1 (PDK1) and the interaction activates PKN[140,141]. A model for the activation of PKN was proposed based on the previously

shown data, according to which activated RhoA binds PKN and this leads to a conformational change of the complex. Subsequently, the conformational change allows PDK1 to bind and phosphorylate the PKN's activation loop sites within the kinase domain, leading to a catalytically active kinase complex (Thr774 for PKNα and Thr816 for PKNγ). The activation loop of PKN is shown in Figure 8.

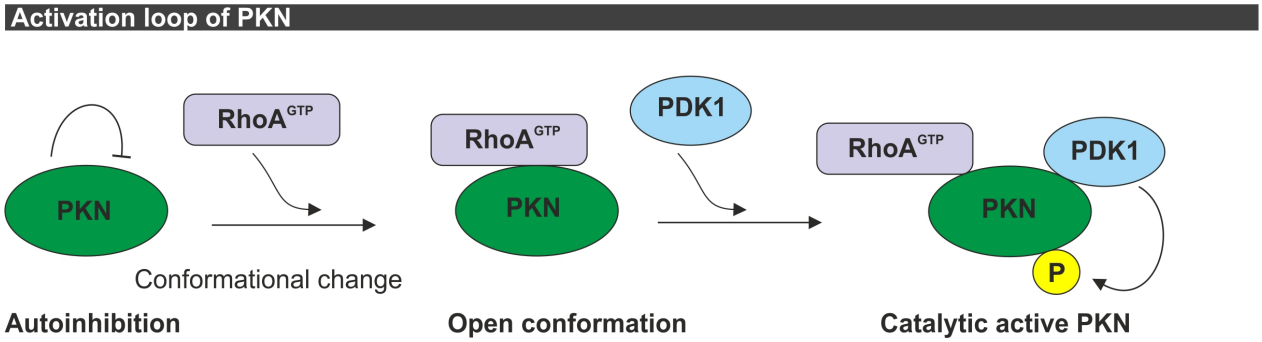

Figure 8: Activation loop of PKN. Upon binding of RhoA-GTP, PKN changes from an autoinhibitory to an activated state. Subsequently, PKN binds to and is been phosphorylated by PDK1, which finally activates the kinase.

Furthermore, it was reported that PKN binds also to MEK kinase 2 (MEKK2) leading to increased PKN activity. Since kinase inactive versions of MEKK2 bound to PKN did not decrease the activation level of PKN, it seems that the interaction of MEKK2 and PKN rather plays a scaffolding role, than activation via phosphorylation[142]. However, further studies are needed in order to fully understand the upstream regulation and activation mechanisms of PKN.

3. Biological functions

Firstly, PKN was shown to play a role in reorganization of Actin filaments and so to regulate cytoskeletal dynamics. Depletion of PKN's kinase activity in rat fibroblasts showed that these cells disrupt Actin stress fibers. Furthermore, expression of a kinase dead version of PKNα reverts the insulin-induced Actin stress fiber breakdown and membrane ruffling[140]. Furthermore, Calautti and colleagues showed in 2002 that PKN has a role in cell-cell adhesion in keratinocytes. In this system cell-cell adhesion is positively regulated by Fyn kinase triggered phosphorylation of β-Catenin and this is dependent on RhoA activity. In the study from 2002 the authors show that PKN is a direct link between RhoA activity and Fyn kinase to induce cell-cell adhesion in keratinocytes[143]. In this case, expressing a RhoA activated mutant, which was not able to bind PKN, prevents the positive effects on establishing cell-cell adhesion and does not induce phosphorylation of β-Catenin.

Another interesting role of PKN, shown in cultured NIH-3T3 cells, is PKN's activation and translocalization in vesicles as a response to hyperosmotic stress. This vesicle enrichment of PKN upon stress conditions is not dependent on its kinase activity, but induces an increased activation level of the kinase[144].

Furthermore, PKN was shown to be involved in apoptosis pathways. In two different cell types PKN is cleaved by Caspase-3 upon apoptosis induction by staurosporine. This generates a truncated, constitutively active form of PKN[145]. Later, it was shown that the caspase-cleaved PKN fragment is involved in apoptosis regulation. Under physiological conditions the Serine/Threonine kinase Akt phosphorylates the pro-apoptotic member of the Bcl-2 family, BAD, leading to inhibition of BAD and prevention of programmed cell death. Upon caspase-induced proteolytic cleavage of PKN, its C-terminus binds Akt and blocks the kinase activity of Akt and thus phosphorylation of BAD. This leads to induced programmed cell death[146]. Another study in *Xenopus* embryos showed that PKN might have a role in the regulation of cell cycle timing. Misaki and colleagues[147] injected embryos with an active form of PKN, leading to a significant delay of the cell cycle timing. *In vitro* studies showed that the delay in the mitotic timing is due to the PKN kinase activity, phosphorylating and inhibiting the phosphatase Cdc25C. Cdc25C is a key player involved in dephosphorylating the Thr15 and Thr14 residues of Cdc2, which is a conserved mechanism in different systems for activating both Cdc2 and Cyclin B Histone H1 kinase leading to mitotic entry[147]. Interestingly, in 2007 another study in HeLa cells also showed an additional role of PKN during mitosis[148]. In this case it was found that PKN plays a role in the mitotic exit and specifically during the final abscission. The study also indicates that PKN might induce mitotic entry via direct phosphorylation and thus activation of the phosphatase Cdc25B. Taken together, these data show that in different model systems, PKN might regulate the cell cycle via different mechanisms.

Interestingly, PKN seems to play a role in neurodegeneration. Under hyperphosphorylation the microtubule-binding protein (MAP) Tau is the major component of the so-called neurofibrillary tangles (NFTs), which besides the Amyloid beta (Aβ) plaques are the second hallmark of the Alzheimer's disease (AD). Interesting findings from Kawamata in 1998 showed that PKN co-localizes with the NFTs in brain tissues from Alzheimer's patients and is associated with abnormally modified Tau in the AD affected neurons[149]. Furthermore, a second study also showed biochemical assays, indicating that PKN can phosphorylate Tau *in vivo* and *in vitro*[150]. PKN-phosphorylated Tau in neuroblastoma cells lost its ability to associate with Tubulin,

compromising microtubule assembly. Upon dissociation from the microtubules, Tau is able to build the insoluble NFT aggregates during AD. Thus PKN might be involved in AD pathology through regulation of the interaction between Tau and Tubulin.

Not much is known about the biological functions of PKN in *Drosophila*. The *Drosophila* PKN gene (*pkn*) was first identified in 1997 and the study showed that the kinase is strongly expressed throughout development. During early embryogenesis PKN expression was first restricted to the mesoderm and later to the somatic musculature[151]. The first characterization of the biological functions of PKN was performed two years later using a loss-of-function PKN mutant. A specific role of PKN regulating dorsal closure was identified during early embryogenesis[130]. During dorsal closure (DC) the leading edge cells of the lateral epidermis accumulate Actin filaments and activated Myosin to their membranes, allowing cells to undergo extreme shape changes. They first elongate along the dorsal-ventral axis and finally the leading edge cells on both sides fuse. In this case, it was shown that PKN acts as a downstream target of Rho-1 and Rac-1, binding directly to the activated Rho-1 and Rac-1, regulating epidermal cell shape changes. A pathway involved in regulation of dorsal closure was previously identified, which involves activation of the c-Jun amino (N)-terminal kinase (JNK) via Rac-1. Subsequently, JNK kinase activates Decapenaplegic (Dpp), allowing extreme epidermal cell shape changes to occur. However, analysis of the Dpp expression in PKN mutant embryos showed no difference to wild type, indicating that PKN might regulate DC downstream of Rho-1 and Rac-1 but independently of Dpp signaling. This was the first work showing a possible role of PKN regulating reorganization of actomyosin network and so cell shape changes[130].

The same group was able to show also the first postembryonic biological function of PKN in *Drosophila*. After rescuing the PKN mutant lethality phenotype expressing different PKN transgenes, they identified that the majority of the flies showed wing morphogenetic and vein formation defects[152].

Another recent study also described Dpkn as a regulator of actomyosin contractility. In this case, the authors isolated and described the phenotype of two different PKN mutant alleles during *Drosophila* oogenesis. Nurse cell dumping is an actomyosin dependent process during oogenesis, which allows the nurse cells around the oocyte to contract and transfer proteins, organelles and mRNAs to the oocyte via cytoplasmic bridges. This so called cytoplasmic transfer was abolished in the PKN mutants due to excessive contractility. The authors conclude that PKN plays a role as a negative regulator of actomyosin contractility during nurse cell dumping[153].

Later, another PKN mutant allele, called the delorean (*pkn*^{dln}), which as a gain-of-function recessive mutation also shows wing morphogenesis phenotypes. The flies showed a dramatic change in the structure and position of the wings, which were strongly bent and held above the fly's body. In addition, the wings had reduced number of bristles, which were also positioned in larger spacing between each other[154].

However, it is not yet clear how PKN regulates actomyosin dynamics in these processes. Previously, it was proposed that the phosphorylation-dependent protein CPI-17 might act as a substrate of PKN. CPI-17 is known in smooth muscle tissue to be activated through phosphorylation at Thr38, which increases its inhibitory affinity towards the Myosin Phosphatase. In a biochemical study from Hamaguchi in 2000 it was shown that PKN can indeed phosphorylate and activate CPI-17 *in vitro*, which increases its potency as a Myosin Phosphatase inhibitor [105].

All these data taken together show that PKN plays a role in various biological processes and is involved in many different signaling pathways. Interestingly, PKN seems to be a downstream target of RhoA and further studies will be needed in order to fully understand its molecular mechanism of action.

IV. Rho-associated Kinase (Rock) as a Myosin regulator

Rho-associated Kinase (Rock) is a Serine/Threonine protein kinase, which is very well known to regulate actomyosin dynamics as a downstream effector of the GTPase RhoA. Rock was identified for the first time in 1996 from two independent groups, in a complex with the activated RhoA[155,156]. There are two known Rock isoforms in mammals, termed as Rock I (also known as Rockβ) and RockII (also known as Rockα)[157]. Northern blotting analysis showed that the mRNA of both isoforms was expressed ubiquitously in most mammalian tissues. Whereas Rockα is enriched in the brain and in the skeletal muscles, RockI was most abundant in the liver, spleen, kidney and testis[158]. Interestingly, RockII and RockI showed different cellular localization during cytokinesis of symmetrically dividing cultured cells. It was shown for the first time in different cell lines that RockII enriches at the cleavage furrow during late telophase, whereas RockI localized predominantly at the centrosomes[159,160]. In *Drosophila* there is only one Rock ortholog, called Drok.

1. Structure

Rock is a 160 kDa multi-domain protein kinase and is structurally similar to Citron kinase and the Cdc42-binding kinases MRCK. The structure of Rock is shown in Figure 9.

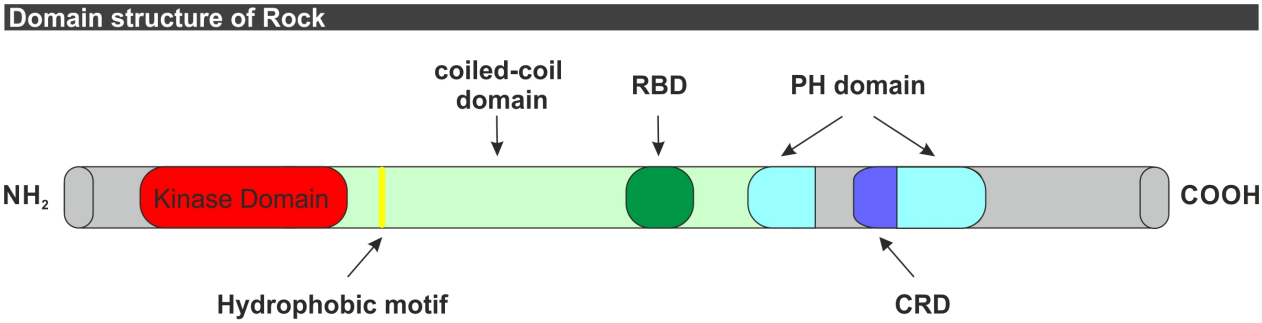

Figure 9: The domain structure of Rock. The N-terminal kinase domain is shown in red, followed by the coiled-coil domain shown in light green. The RhoA binding domain (RBD) is indicated in dark green. Rock contains a PH domain at the C-terminus (shown in cyan), which is interrupted by the Cysteine-rich domain (CRD), shown in dark blue. The hydrophobic motif is indicated in yellow.

Rock's N-terminus contains the conserved kinase domain, which shows strong homology between the two isoforms. It is followed by a coiled-coil region, which also contains the RhoA binding domain (RBD). Structural data indicates that the RBD is located at the C-terminal end of the coiled-coil region, which forms a parallel α-helical dimer and provides the interaction site for RhoA[161]. Furthermore, it was shown that the a 13 amino acid stretch within the RBD binds a hydrophobic patch assembled by the switch regions of RhoA[162]. The C-terminus of Rock contains a Pleckstrin homology (PH) domain, which is assumed to play a role for the correct localization of the kinase and is interrupted by a Cysteine-rich zinc-finger motif domain. Interestingly, a careful characterization of the PH domain showed that the interruption does not alter the correct folding of the PH domain[163]. Besides its role in protein localization it was also suggested that the PH domain might be negatively regulating the kinase activity via auto-inhibition[164,165]. Further structural information about the whole protein would be necessary in order to better understand the link between the structure and the function of Rock.

2. Regulation of Rock activity

Commonly, all Rho-associated Kinases are activated through interaction with RhoA[166]. Since the C-terminus of the kinase acts as an autoinhibitory region most probably through binding and inactivating the kinase domain, it was proposed that binding of Rock to RhoA could lead to conformational change[164]. Subsequently, this would release the kinase domain from the

inhibitory interaction with the C-terminal domains and increase the kinase activity of Rock (Figure 10). However, to date there are no structural studies to support this model. Interestingly, it was shown that the proteolytic cleavage of the C-terminus could generate a constitutively active form of Rock in a RhoA independent manner. During apoptosis it was shown that Rock is a target for proteolytic cleavage by Caspases, which activates the kinase[167,168]. Phosphorylation at other regions rather than the kinase domain has been indicated to fine-tune the kinase activity of Rock. For example, Polo-like-kinase-1 phosphorylates one of the conserved sites within Rockα Thr-967, Ser-1099, Ser-1133, or Ser-1374 in addition to RhoA interaction in order to further increase the Rock activity[169]. Also, phosphorylation or at Tyr-722 decreases the RhoA affinity for Rock and indirectly inhibits its kinase activity[170]. Dephosphorylation reverses this effect and brings back Rock in a high activation state[171].

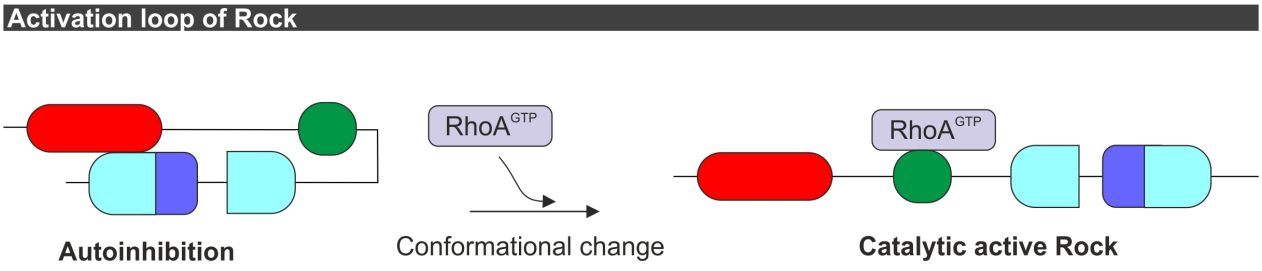

Figure 10: The activation loop of Rock. Rock exists in a closed and inactive conformation, where the kinase domain is blocked through binding with the PH domain. Upon binding of RhoA-GTP to the CRIB domain, Rocks change their conformation to a catalytically activated state.

Furthermore, negative regulation mechanisms were also reported through interaction with GTP-binding proteins such as Gem and Rad1, or the Colapsin response mediator protein-2 (Crmp-2), which binds the catalytic domain of Rock. The interaction in the presence of the bound RhoA-GTP reduces the kinase activity of Rock and leads to inhibition of Myosin activation and decreased actomyosin contractility[172,173]. Further studies in the future might reveal also other similar interaction partners, which regulate and fine-tune Rock activity in the context of different processes and model systems without interfering with the global signaling pathway.

3. Biological functions

One of the best-studied biological functions of Rock is the regulation of actomyosin contractility. As mentioned before (Introduction; chapter II.2) Rock can phosphorylate and therefore activate Myosin's RLC but also phosphorylate and inhibit MBS, both of which cause increased Myosin activation. Increased activation of Myosin leads to enhanced binding to Actin

filaments and bundling these into stress fibers focal adhesions. Rock, as an upstream activator of Myosin, is thus indirectly in establishment of cell adhesion, cell polarity, regulation of cell migration and cytokinesis.

In addition to Myosin, Rock is also known to phosphorylate other downstream targets thereby regulating other biological processes. As mentioned above Rock undergoes proteolytic cleavage through Caspase-3 and is involved in apoptosis. Increased activation of Rock leads to increased actomyosin constriction, membrane blebbing and formation of apoptotic bodies in a RhoA independent manner[167,174]. Activation of Rock was also shown to induce neurite retraction and growth clone collapse. Upon Rock inhibition, axonal outgrowth in cerebellar neurons was observed. On one hand, this is regulated through phosphorylation of Myosin and activation of actomyosin contractility and on the other hand, there were other downstream targets of Rock, which were also suggested to play a role in this process. The Phosphatidylinositol 4-phosphate 5-kinase (*PI*(*4*)P5K) was assumed to be a putative downstream target of Rock because the inhibition of its kinase activity blocked the Rock mediated neurite retraction and growth clone collapse[175]. Other studies proposed a role of LIMK and the cyclin dependent kinase inhibitor $p21^{Cip1}$. The kinase inactive form of LIMK showed suppression of the Rock-induced neurite outgrowth and the interaction of $p21^{Cip1}$ with LIMK showed to inhibit Rock activity[176].

Interestingly, a role of Rock in the regulation of cell size and cell differentiation was also proposed. Cell size is regulated through Insulin/Insulin like growth factor (IGF) signaling pathway, which increases the amount of proteins and therefore cell mass. Mice mutants for the p190B GAP, which inactivates RhoA, showed high RhoA activity and decreased cell size, which could be restored through inactivation of Rockα. This study proposes that Rock negatively regulates cell size by reducing the IGF induced phosphorylation and activation of the cyclic AMP response element-binding protein (CREB)[177]. Further studies showed fibroblasts from the same mutant mice with high RhoA activity were unable to undergo adipogenesis, but they undergo myogenesis. Furthermore, inhibition of Rock activity was able to reverse this phenotype[178].

In *Drosophila* the biological functions of Rock have also been extensively studied. Drok was shown to regulate different processes during development and to phosphorylate the two well established vertebrate targets, Myosin's RLC and MBS *in vivo* and *in vitro*[179]. One of the best-established examples is the role of Drok in the planar cell polarity (PCP) pathway during wing morphogenesis. Mostly epithelial cells establish an apical-basal polarity along an orthogonal line within the plane of the tissue. In the *Drosophila* wing, PCP is known to establish

the pattern of the hairs covering the dorsal and ventral surfaces. Extracellular signals are received and processed by the seven transmembrane proteins Frizzled (Fz) and downstream signals are processed through Dishevelled (Dsh). The Fz/Dsh pathway was shown to regulate PCP by reorganization of Actin filaments through RhoA and eventually Rac1. Drok was shown to be a downstream effector of RhoA in this signaling cascade, regulating the number and the rotation of the hairs upon phosphorylating and activating Myosin[180,181].

Similarly to PKN, Drok was also shown to play a role during oogenesis in some Actin dependent processes, such as nurse cell dumping, establishment of oocyte polarity and regulation of oocyte cortex integrity. This study used germ line clones of a *Drok* null allele and characterized the role of Drok as a novel regulator of oogenesis. It suggested that Drok is required for oocyte cortex integrity through regulation of its downstream effector at the oocyte cortex – DMoesin and also for establishing egg polarity[182]. The same authors performed another study overexpressing an activated Drok form and found that strict control of Drok's activity is necessary for photoreceptor maintenance, wing vein formation and central nervous system (CNS) development. Genetic interaction of Drok was found besides with Myosin, also with the *Drosophila* Lim-kinase (DLimk), which was suggested to play a role during early CNS development[183].

V. Mushroom body tiny as a putative Myosin regulator

The p-21-activated kinases (PAKs) are a Serine/Threonine kinase family, which was first identified in a screen as binding partners of the small GTPases Cdc42 and Rac1, but they do not bind RhoA. To date there are six known PAK isoforms in mammals (PAK1-PAK6) and they are subdivided into two classes of PAKs, conventional and non-conventional PAKs. PAK1-PAK3 belong to the conventional and PAK4-PAK6 to the non-conventional PAKs. All isoforms show high homology within their kinase domains, but both classes seem to be regulated differently. In *Drosophila* there are two members of the PAK class I, DPAK1 and DPAK3, whereas there is only one known member of the non-conventional PAKs, called Mushroom body tiny (Mbt), or also D-PAK2. As a downstream target of Rac1 and Cdc42 with an important role in regulation of the cytoskeleton, Mbt was studied as a putative regulator of Myosin in the current work[184].

1. Structure

All PAK family members show high homology within the kinase domain and some variability at the N-terminus. The conventional PAKs contain a Cdc42/Rac-interacting domain (CRIB) at the N-terminus, directly flanked by a Kinase Inhibitory domain (KI domain). Three proline-rich motifs regulate binding to the SH3 domain-containing proteins Nck and PIX (PAK-interacting exchange factor). The catalytic kinase domain is located at the C-terminus[184]. The domain structure of the conventional and non-conventional PAKs is shown in Figure 11.

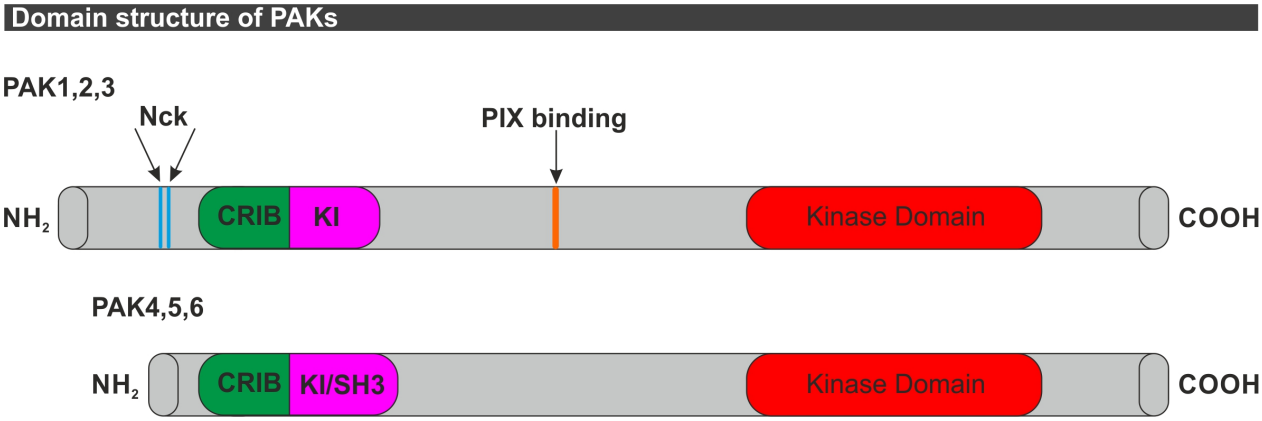

Figure 11: The domain structure of conventional and non-conventional PAKs (adapted from[184]). The conventional PAKs (upper panel) contain two SH3 binding sites for Nck at the N-terminus and one SH3 binding site for PIX in the central region. A CRIB domain followed by a kinase inhibitory domain is located also at the N-terminus. The non-conventional PAKs (lower panel) contain a CRIB domain, followed by a domain of unknown function at the N-terminus. Both the conventional and the non-conventional PAKs contain their kinase domain at the C-terminus.

The non-conventional PAKs are structurally similar to the conventional PAKs. They contain a C-terminal kinase domain and a N-terminal CRIB domain. Previously, it was assumed that the non-conventional PAKs lack the KI domain. However, recent studies have shown two different models where the CRIB domain of the non-conventional PAKs is followed either by a KI domain[185], or by a SH3 binding domain[186], which keep the protein in an inactive conformation prior to activation events. Furthermore, the non-conventional PAKs seem to lack the Nck and PIX binding motifs. These differences in the structure might be an indication for different regulation mechanisms of these two PAK classes.

2. Regulation of PAK activity

The conventional PAKs are activated through binding of Rac1 and Cdc42 to the CRIB domain. Structural studies have shown that the kinases exist as a trans-inhibited homodimer, where the KI domain is bound to the kinase domain and inhibits its catalytic activity[187]. This inhibitory state is further stabilized by the associated PIX dimer (Figure 12). Binding of GTPase triggers a conformational change leading to the release of the kinase domain from the KI domain. This allows a series of trans-autophosphorylation events, which are needed for the full activity of the kinase[188]. Firstly, a phosphorylation at one site within the kinase domain and another site within the KI domain, on one hand, activate the kinase and on the other hand, prevent the kinase domain to change back into an inactive conformation. Phosphorylation within the PIX binding site, disrupts the dimers and further stabilizes the active conformation. Furthermore, there are also other GTPase independent mechanisms proposed to activate the conventional PAKs. Similarly, as proposed for PKN and Rock, PAKs were also reported to undergo proteolytic cleavage by Caspase-3 generating a kinase active form of PAK during apoptosis. It was also suggested that a membrane recruitment of PAK via the interacting partners Nck and Grb2 can promote kinase activation in a GTPase independent manner[189]. This activation might be induced through phosphorylation of PAKs by PDK1 or by interaction with lipids such as sphingosine[190]. The activation mechanism of both conventional and non-conventional PAKs is shown in Figure 12.

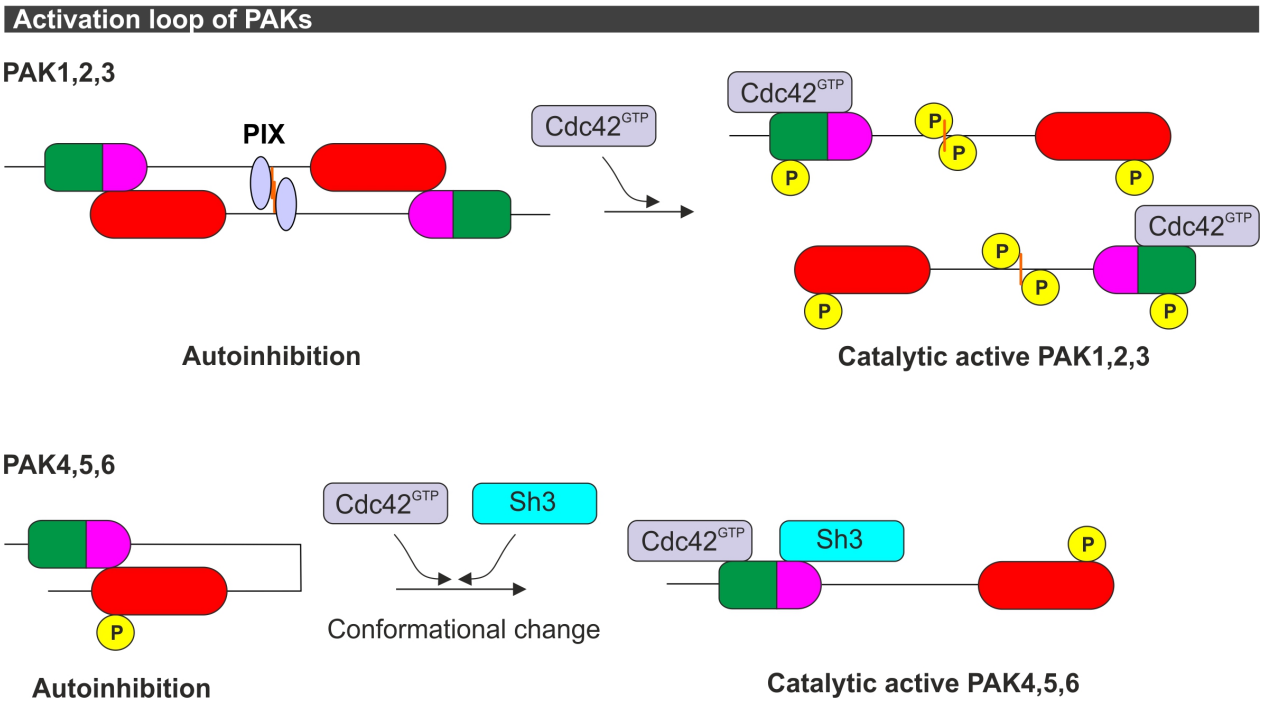

Figure 12: The activation loop of the conventional and non-conventional PAKs (adapted from[184,191]). The conventional PAKs (shown in the upper panel) exist in a trans-inhibited homodimer. Upon Cdc42-GTP binding to the CRIB domain, a conformational change and a series of autophosphorylation events take place, which activate and stabilize the active conformation of the kinase. The non-conventional PAKs (shown in the lower panel) exist as closed, inhibited monomers. Upon binding of Cdc42-GTP or SH3 containing proteins, a conformational change takes place and activates the kinase.

The activation mechanisms of the non-conventional PAKs are not well understood yet. Unlike the conventional PAKs, binding of Cdc42 or Rac1 to the class II PAKs does not lead to an increased kinase activity. However, it was shown that N-terminally truncated versions of both PAK4 and PAK6 lead to the generation of constitutively active forms. These results indicate that a similar inhibitory mechanism might also exist for the non-conventional PAK kinases. Recent studies have shown that the kinase domain of the non-conventional PAKs is constitutively phosphorylated. Prior to activation the kinase is found in a closed conformation, where the proposed KI, or SH3 binding domain blocks the kinase domain and keeps the protein in an inactive state. Both models propose that upon binding of either Cdc42-GTP, or SH3 domain containing proteins lead to conformational change and activation of the non-conventional PAKs. However further investigation is needed, in order to fully understand the process[185,186].

3. Biological functions

The class I and class II Pak kinases share some of their downstream effectors and play a role in the same biological processes. However, both classes also have unique targets and are required for some class-specific functions. One of the major functions of both class I and class II

PAKs is regulation of the cytoskeleton. Class I PAKs are mainly required to stabilize Actin polymerized filaments but they are also able to affect microtubule organization. Class II PAKs regulate the formation of filopodia and act predominantly in the nervous system. Many of the PAK targets are already known regulators of the cytoskeleton. In neuronal cells it was shown that PAK1 can directly phosphorylate the Myosin RLC at Ser-19 and induce Actin filament stabilization *in vivo*[192,193]. Through regulation of Actin filaments PAKs play a role in the formation of Actin structures such as lamellipodia and filopodia but also in the dissociation of stress fibers, which are also Actin-based structures, causing tension at the cell surface[194]. Stress fiber dissociation in fibroblasts, epithelial and endothelial cells is mediated through phosphorylation of MLCK by PAK1 and PAK2. This downregulates MLCK, decreases phosphorylation of the Myosin RLC, which triggers stress fiber dissolution[195,196].

Furthermore, the PAK class I role in Actin polymerization was also connected to the formation of dendritic spines in neurons. PAK activated Myosin was shown to localize to the dendritic spines, where it stabilizes Actin filaments, establishes contractility thereby promoting spine formation. Dendritic spines are key regulators of synaptic plasticity in most neurons, which is essential for cognitive functions such as learning and memory[197]. Apart form the direct activation of Myosin, PAKs are also known to regulate Actin polymerization through LIM kinase I (LIMK1)[198]. Phosphorylated LIMK1 can phosphorylate and inhibit its substrate, the Actin depolymerizing protein Cofilin[199,200]. In addition, the phosphorylation of LIMK1 is also established and stabilized indirectly through phosphorylation and inhibition of the LIMK1 phosphatase, SlingShot Phosphatase (SSH1)[201]. Further substrates are also been phosphorylated by PAKs and are involved in regulation and stabilization of Actin filaments, such as the Actin binding protein FilaminA (FLNa). FLNa is required to connect the Actin filaments to the cell membrane. Another interesting role for PAKs was reviled as a regulator of the mitotic spindle[202]. PAK1 was shown to phosphorylate the microtubule Cofactor B (TCoB), which is needed for the assembly of α/β-Tubulin[203]. PAK1 is also able to phosphorylate the centrosome localized Polo-like kinase 1 (Plk1) and AuroraA kinase. Phosphorylation of AuroraA leads to an increased activation of the kinase and to the formation of abnormal mitotic spindles as well as up-regulated cell growth of human breast epithelial cells[204].

In *Drosophila* the current work will concentrate on the role of the only member of the class II PAKs – Mushroom body tiny, or also called Mbt. Mbt was extensively studied in *Drosophila* in the context of neuronal developmental processes. The *mbt* mutant alleles were

first isolated and characterized in 1998[205]. The authors initially observed that *mbt* loss-of-function leads to significant reduction in the size of a neuropil structure called the mushroom body. This is a synaptic dense region in the fly's brain, which controls learning and memory, similar to the mammalian hippocampus. Since *mbt* mutants showed significantly reduced number of Kenyon neurons, it was suggested that the phenotype could be due to either loss of the mushroom body neuroblasts, or proliferation defects during development. Furthermore, the adult mutants had a rough eye phenotype. This study showed for the first time that Mbt might play an important role in the early development of the central brain of *Drosophila*[205]. Since a severe eye phenotype was observed previously, Schneeberger and Raabe analyzed the role of Mbt during photoreceptor cell development. Biochemical studies first showed that Mbt can bind to Cdc42-GTP, which leads to Mbt recruitment to the adherent junctions (AJs) and this is needed for the normal epithelial remodeling and finally normal photoreceptor terminal differentiation. Previous results from mammalian systems confirmed that the interaction between Cdc42 and the RAK class II does not induce catalytic activity of Mbt but only triggers its relocalization[206]. The Mbt signaling pathway during photoreceptor cell morphogenesis was addressed in another study from the same group later in 2007. There, the authors performed a genetic screen and found the Actin depolymerizing protein Twinstar/Cofilin might act downstream of Mbt to regulate cell adhesion during photoreceptor morphogenesis. Biochemical data suggests that Mbt interacts with Twinstar and upon co-expression of the catalytic active form of Mbt with Twinstar, phosphorylation of Twinstar can be induced. Together with genetic evidence showing that mutations in the *twinstar* gene lead to suppression of the *mbt* eye phenotype, this data suggests that Twinstar might be a downstream target of Mbt in regulation of the photoreceptor morphology. Further *in vitro* kinase assays and immunoprecipitation experiments showed the possible role of the *Drosophila* Lim protein kinase (D-Limk) as a mediator step between Mbt and Twinstar. Although this is well established in different mammalian systems, the careful genetic analysis of D-Limk and Mbt mutants in *Drosophila* leaves open questions about the molecular mechanism of the Mbt signaling pathway. On one hand, double mutants showed a strong synergistic effect on the *mbt* phenotype, and on the other hand the loss of D-Limk did not lead to a complete downregulation of Mbt signaling. This suggests that both proteins might have redundant functions during photocell receptor morphogenesis[207]. Based on the previously observed phenotype of the *mbt* mutants, showing significant loss of neurons in the fly's brain, a recent study has addressed the question about the role of Mbt during neuronal stem cell

division and proliferation. It was shown that stem cells in the larval brain, which are called neuroblasts and give rise to the neurons and glia cells in the brain, are severely affected in their proliferation rate and cell size in the *mbt* mutants. In addition, late apoptotic activity was detected, suggesting that the neuronal loss is due to the reduced proliferation rate leading subsequently to premature cell death. Apoptosis was assumed to be a consequence of the proliferation deficit rather than the primary cause for the adult brain mushroom body phenotype in this study[208].

VI. *Drosophila* neuroblasts

Drosophila neuroblasts (Nbs) are stem cells in the developing fly brain, which divide asymmetrically to give rise to all neurons and glia cells in the adult central nervous system. Based on their position in the brain there are different types of Nbs, the central brain Nbs, Ventral Nerve Cord (VNC) Nbs, the Mushroom body Nbs and the optic lobe Nbs. In the current work I will concentrate on central brain neuroblasts and refer to those as Nbs.

Central brain Nbs are first specified during embryonic stages 9 to 11 through lateral inhibition[209-211]. Notch/Delta signaling refines the expression of proneural genes such as *wingless* (*wnt* in vertebrates), *asense* (*asn*) or *scute* (*sc*) to individual cells of the proneural cluster within the embryonic neuroectoderm[212-215]. These defined Nbs later delaminate and start a series of asymmetric divisions, generating a self-renewing neuroblast and a smaller differentiating ganglion mother cell (GMC) (Figure 13)[216]. The embryonic neuroblasts will produce all 10 to 20 primary neurons in the larval central nervous system, which will make only up to 10 % of the neurons in the adult brain[217]. After completing their neuronal linages around the end of neurogenesis the Nbs in the central brain and in the thoracic region exit cell cycle and enter into a quiescent state, whereas the Nbs in the abdominal regions of the embryo undergo programmed cell death[218]. During the 1st instar stage of the larval development, around 8 - 10 h after hatching, Nbs exit quiescence and start a second round of asymmetric divisions, generating the remaining 90 % of the neurons and glia cells of the adult fly brain. Unlike embryonic Nbs, the larval Nbs are able to regrow to their original cell size after each round of division. The second wave of neurogenesis continues until pupal stages and then the Nbs exit the cell cycle again and disappear. This cell cycle exit was recently shown to be a result of a cell size reduction, leading to terminal differentiation[219-221]. The cell size reduction was suggested to be the result of a changed metabolic state, regulated through the steroid hormone Ecdysone[222].

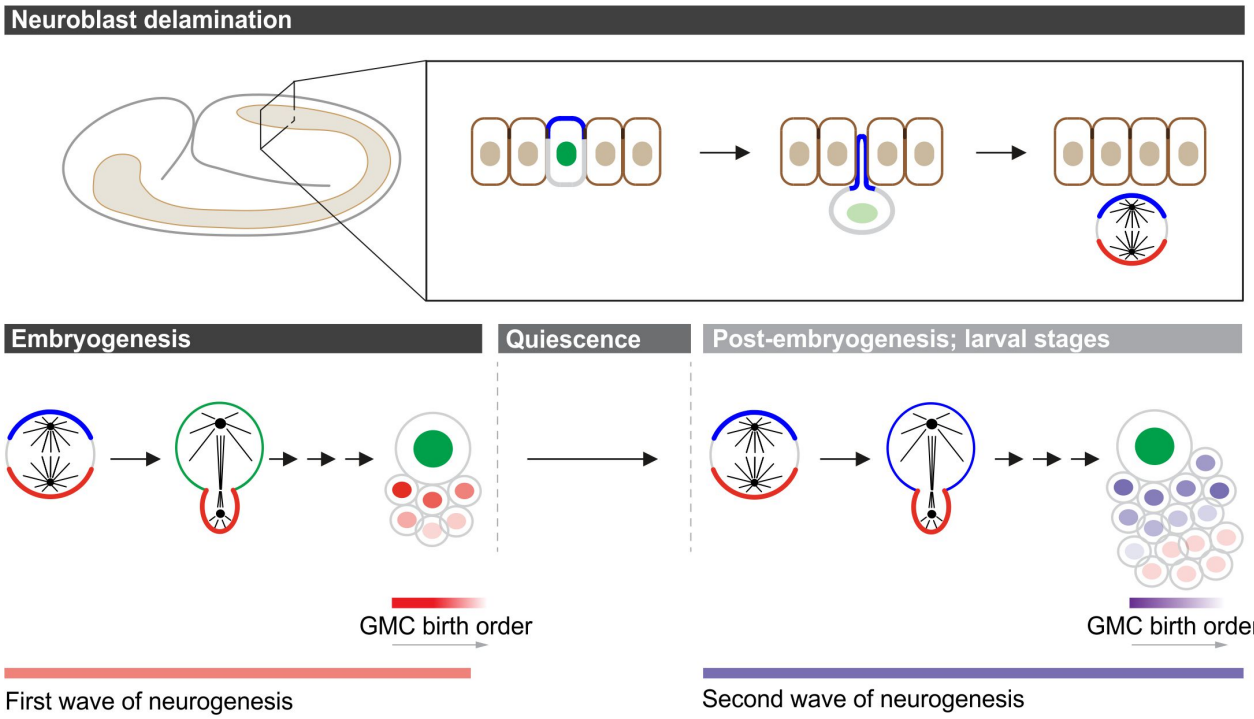

Figure 13: Upper panel: Neuroblast delamination. Specified neuroblasts undergo drastic cell shape changes and exclude from the neuroepithelium, inheriting apical (shown in blue) and establishing basal polarity later (shown in red). Lower panel: During embryogenesis, proliferating neuroblasts generate the neurons and glia cells of the larval brain. Later the neuroblasts enter into a quiescent state until larval stages. At this time they start proliferating again and generate the nervous system of the adult fly. Adapted from Gallaud et. al. (in revision).

There are two types of Nbs in the central brain, so-called type I and type II Nbs. Careful linage analysis has shown that there are around ninety type I Nbs located in the anterior and posterior of each brain lobe and only eight type II Nbs located only in the posterior of each brain lobe. On one hand, both Nb types show different division patterns[223-225]. Type I neuroblasts were shown to divide asymmetrically, giving rise to one self-renewing neuroblast and one GMC, which will divide once in a symmetric manner generating two postmitotic neurons, or glia cells (Figure 14). In contrast, the type II neuroblasts divide asymmetrically and generate an intermediate neural progenitor (INP), which first undergoes a maturation phase of four to six hours. The mature INP is then able to divide again in an asymmetric manner a defined number of times generating another mature INP and one GMC. This division mode allows the type II neuroblasts to generate a high neural diversity[223]. Both neuroblast linages were shown to express a different combination of transcription factors, which is important for the regulation of their division mode. Both type I and type II Nbs express the transcription factor Deadpan (Dpn). However, only the type I Nbs express the transcription factor Asense (Ase) and cytoplasmic Prospero (Pros). Only the type II Nbs express Pointed P1 (PntP1), which is an isoform of the transcription factor

Pointed[226]. After maturation, type II derived INPs start to re-express neuroblast-specific markers such as Ase, Dpn and Pros[227]. In contrast to the type I Nbs, the mature INPs also express the transcription factor Earmuff (Erm), which is an inhibitor of the Notch signaling pathway and insures that the mature INPs do not reenter the proliferation state and allows their terminal differentiation[228].

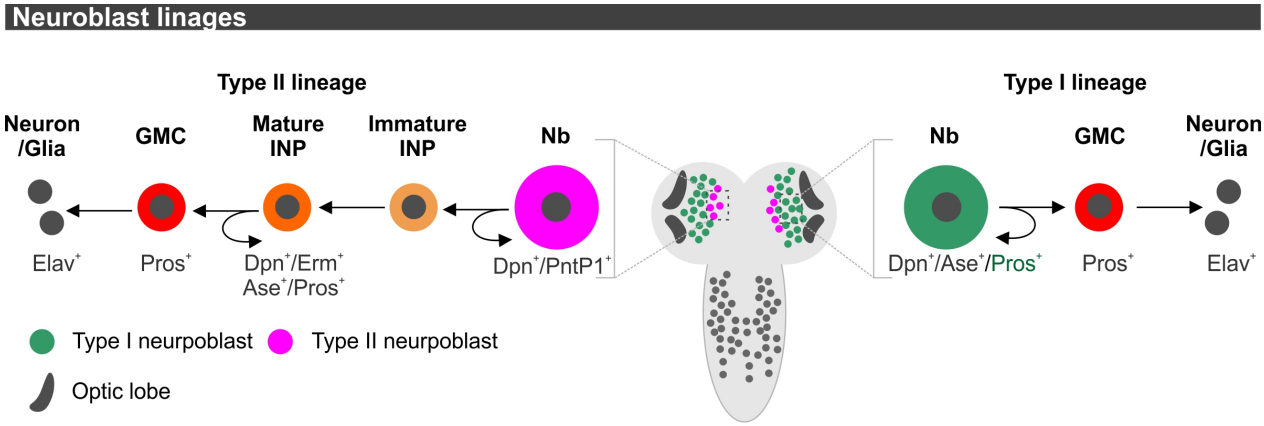

Figure 14: Neuroblast linages of the larval nervous system. There are type I (right part) and type II (left part) neuroblasts, which differ in their division mode and molecular identity. Type I neuroblasts divide asymmetrically to generate another neuroblast and a differentiating GMC. The type II neuroblasts generate an intermediate progenitor (INP), which is able to divide again asymmetrically generating a proliferating INP and a differentiating GMC.

In the recent years *Drosophila* neuroblasts have been a very useful tool to study different aspects of basic stem cell biology, cytokinesis and even tumor formation. They are very well suited for precise genetic manipulations and because of their location in the brain also for live imaging experiments. Since these central brain Nbs undergo repeated cycles of asymmetric divisions in a stem cell manner, they are a perfect model system for studying the establishment of physical and molecular asymmetry during cytokinesis.

VII. Asymmetric cell division (ACD)

1. Apical polarity in *Drosophila* neuroblasts

Drosophila neuroblasts are intrinsically polarized cells, which establish molecular asymmetry already during early metaphase, localizing cortical proteins and cell fate determinants exclusively either to the apical or to the basal cortex. Nbs then undergo asymmetric cell division along this apical-basal polarity axis, ensuring the correct segregation of the cell fate determinants either to the self-renewing neuroblast or to the differentiating daughter cell. The apical polarity domain is inherited from the neuroepithelia after Nb

delamination through the localization of the so-called Par complex[134,229]. The Par protein complex and thus the polarity axis are formed in early prophase (Figure 15). At this early mitotic stage the Par complex is composed of the atypical Protein kinase C (aPKC), Partitioning defective 6 (Par-6) and Lethal giant larvae (L(2)gl). During early mitosis, Aurora A phosphorylates Par-6, which activates aPKC. Active aPKC was shown to phosphorylate L(2)gl and to destabilize the binding of L(2)gl to the complex. This allows the exchange of L(2)gl with Bazooka (Baz; Par-3 in vertebrates) and the Par complex containing Baz forms a strong crescent during metaphase[230]. The components of the Par complex depend on each other for their correct localization at the apical cortex. Localization studies have suggested that Baz is the most upstream component of the apical polarity complex[231]. *Baz* mutants seem to mislocalize the remaining Par complex components[232]. Furthermore, it was also shown that Par-6 can bind to activated Cdc42 and Cdc42 is required for the correct cortical localization of both Par-6 and aPKC. In addition, Cdc42 is also mislocalized in *baz* mutants, supporting the hypothesis that Baz is also upstream of Cdc42[233]. Interestingly, the Dynamin-associated protein 160 (Dap160) was shown to be involved in regulation of the aPKC activity and correct apical localization, whereas the phosphatase PP2A might be involved in excluding aPKC from the basal cortex[234,235]. Once the Par complex forms apically, it is required for the correct basal localization of cell fate determinants (discussed in Introduction; chapter VII.2) and to correctly localize the second component of the apical domain (discussed below).

The second apically recruited complex contains Inscuteable (Insc; mInsc in mice), Partner of Inscuteable (Pins; LGN in vertebrates), the heterotrimeric G-protein alpha subunit (Gαi) and Mushroom body defect (Mud; NuMA in vertebrates). The Insc/Pins/Gαi complex is recruited to the apical cortex upon binding Pins, which is anchored to the membrane through Gαi-GDP[236]. Pins contains three C-terminal GoLoco motifs, which are the binding motifs for Gαi. Furthermore, the tetratricopeptide repeats (TPRs) at the N-terminus establish the interaction with Mud. Upon binding of the first GoLoco motif of Pins to Gαi, Pins undergoes a conformational change from a closed to an open conformation, allowing the further stabilization of the Gαi-Pins interaction with the other GoLoco motifs and allows binding of Mud to the TPRs. Both apical complexes are interconnected through Insc, which was shown to directly bind to both Baz and Pins and these are required for the apical recruitment of Insc[237-239]. The Insc/Pins/Gαi complex is required for proper spindle orientation during metaphase. This is established through the downstream effector Mud, which as mentioned above can directly bind

Pins and this interaction is required for the apical recruitment of Mud at metaphase. *Mud* mutants mislocalize the spindle but do not perturb apical-basal polarity. This then leads in some extreme cases to mispositioning the cleavage furrow and loss of physical asymmetry during cytokinesis[240-242]. Interestingly, Insc is also required for the correct localization of the Par complex, since the entire Par complex is mislocalized in *insc* mutants. Taken together this shows that Pins is required for both spindle orientation and establishment of the apical-basal polarity[243].

Further studies will be needed in order to fully understand the molecular mechanism involved in the correct localization of all apical domain components in intrinsically polarized *Drosophila* neuroblasts.

2. Localization of basal cell fate determinants

The cell fate determinants Prospero (Pros; Prox1 in vertebrates) and Brain tumor (Brat; Trim2, Trim3 and Trim32 in vertebrates) together with their adaptor protein Miranda (Mira) are localized specifically to the basal cortex at metaphase and are segregated to the GMC after cytokinesis[225,244-249]. The basal cortical enrichment of the transcription factor Pros and the transcription inhibitor Brat are regulated through their direct binding to Mira[244,250,251]. After completion of cytokinesis Mira is released from the GMC cortex and allows the relocalization of Brat and Pros to the nucleus, where they regulate other downstream targets to suppress proliferation and induce differentiation (Figure 15). This data showed that Mira is required for the recruitment and correct localization of basal cell fate determinants, and further *mira* mutants fail to localize correctly Brat and Pros at metaphase leading to loss of neural fate[252]. The N-terminus of Mira is necessary and sufficient for its correct basal localization and the central domains regulate the binding to Staufen and Pros. Interestingly, the C-terminus of Mira was suggested to play a key role for its release from the GMC cortex after cytokinesis and truncated versions of Mira lacking the C-terminus fail to release Miranda and also Pros from the cortex [253,254]. Thus, Pros fails to relocalize to the GMC nucleus and to induce differentiation[255]. Since Mira seems to be very important for the correct segregation of Pros and Brat, it is interesting to understand what is the regulatory mechanism for Mira enrichment at the basal cortex during metaphase. There are a number of studies suggesting different mechanisms for Mira recruitment and enrichment. Early studies have already shown that Mira is localized at the entire cell cortex during interphase. This early cortical recruitment is regulated through

dephosphorylation of the T591 site at the C-terminus of Mira by the Protein phosphatase 4 (PP4). The kinase, which is phosphorylating this site is unknown[256]. Subsequently, Mira is phosphorylated at five other sites through aPKC, which excludes Mira from the apical cortex and restricts its localization basally[257,258].

Further cell fate determinants, which show the same behavior, are Numb (Numb and Numb-like in vertebrates) and partner of Numb (Pon). Numb and Pon have been shown to directly interact in *vivo* and Pon is required for the basal recruitment of Numb[259]. Pon is relocalized to the basal cortex upon phosphorylation trough the mitotic kinase Polo[260]. During metaphase Baz can directly bind to Numb and bring it in physical proximity to aPKC, which phosphorylates Numb and excludes it from the apical cell membrane. This mechanism is very similar to the one proposed for regulating Mira's basal localization[230,261]. Once these cell fate determinants are in the GMC they act differently to inhibit self-renewal and promote cell cycle exit and differentiation. As mentioned above Pros acts as a transcription factor, repressing the expression of cell cycle genes such as *cyclin A*, *cyclin E* and *string* (*cdc25* in vertebrates). Pros also can induce the expression of pro-neural genes such as *fasciclin II* and *netrin B*[244,255,257]. Brat, on the other hand, is a posttranscriptional regulator, involved in the inhibition of the transcription factor Myc[262]. Furthermore, Numb has been shown to inhibit Notch signaling in the GMC by promoting the receptor endocytosis[247,262].

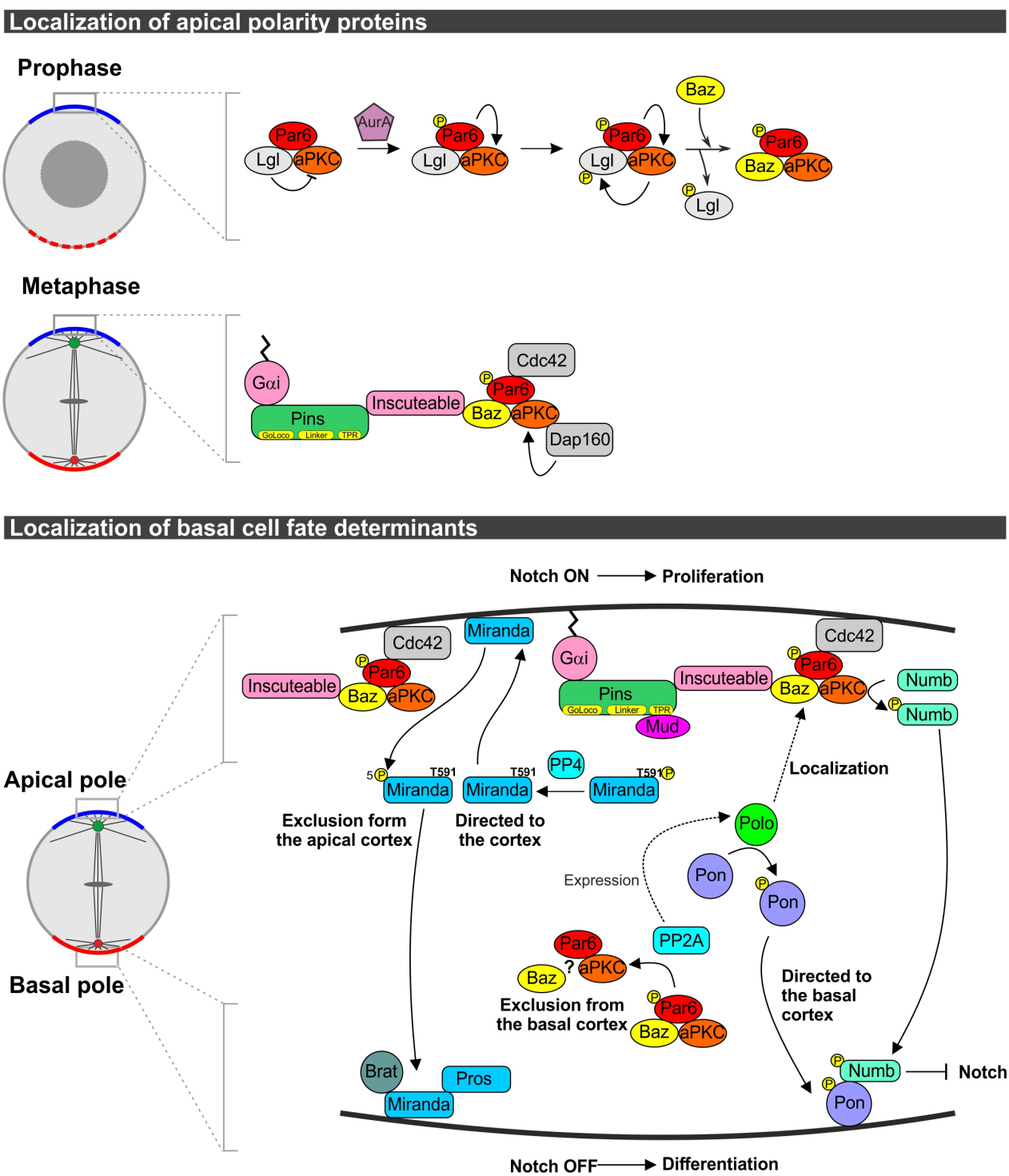

Figure 15: Establishment of polarity in *Drosophila* neuroblasts. Upper panel: Mechanism of establishment of the apical polarity domain. The Par-6 complex is localized at the apical cortex during prophase. The second apical complex containing Mud, Pins and Gαi is enriched at the apical cortex later during metaphase. Lower panel: Mechanism of segregation of basal cell fate determinants. Arrows indicate activation and the phosphorylation events at the components are also shown. Adapted from Gallaud et al. (in revision).

In conclusion, the correct segregation of apical polarity proteins and basal cell fate determinants, as the first aspect of ACD, is extremely important for stem cell self-renewal and differentiation[229]. A number of studies in the past have shown that mutants for the apical cortex components, which mislocalize basal cell fate determinants, can lead to loss of neural identity of

the GMC and de-differentiation (Brat, Numb, pros, Mira and Pon). This causes formation of massive tumors, consisting of stem cells, which can proliferate and form metastases even upon transplantation into a host organism[262-264]. Furthermore, physical mispositioning of the cleavage furrow also leads to an altered segregation of polarity proteins into the daughter cells. This can be achieved in mutants, which affect the spindle orientation without perturbing the apical-basal polarity. As mentioned above mutants such as *mud* can rotate the spindle perpendicular in relation to the polarity axis and these cells divide in a physically symmetric manner distributing the apical and basal components equally. This leads to the generation of two proliferating neuroblasts and might also generate stem cell containing tumors[265]. The mechanisms, which regulate the positioning of the cleavage furrow during ACD, are discussed below (Introduction; chapter VII.3).

3. Cleavage furrow positioning during ACD

Nuroblasts show not only molecular asymmetric during metaphase but show also physical asymmetry after cytokinesis; the proliferating neuroblast is two times larger compared to the differentiating GMC. This physical asymmetry of the two daughter cells is determined by the positioning of the cleavage furrow, which is shifted towards the basal cortex. As it was described for symmetrically dividing cells the spindle provides cues to the cell cortex at the site of constriction and determines the correct position of the furrow. However, it has recently been shown that for the asymmetrically dividing neuroblasts an additional polarity-dependent pathway exists, which regulates cleavage furrow positioning. The molecular mechanisms of both neuroblast cleavage furrow positioning pathways are discussed below.

a) Spindle-dependent cleavage furrow positioning pathway

Most of the symmetrically dividing cells define the cleavage furrow position through signals originating from the central spindle and the astral microtubules. This leads to a local activation of RhoA, Myosin enrichment and subsequently cortical constriction in the equatorial region of the cell at telophase. Assuming that the same pathway is also active in the asymmetrically dividing *Drosophila* neuroblasts, the question remains, how do the microtubules specify the division plane in a basally shifted position. Studies from Kaltschmidt and colleagues have shown that the spindle in these neuroblasts is asymmetric at anaphase[266]. In this case, live imaging experiments allowed to measure the distance between the centrosome and the midplane of the central spindle. The results suggested that the apical spindle arm is slightly

longer than the basal spindle arm[266,267]. This difference was a consequence of microtubule growth at the apical side and microtubule shrinking at the basal side. Furthermore, the entire spindle was shifted towards the basal cortex, generating a larger gap between the apical cortex and the centrosome compared to the gap between the cortex and centrosome at the basal side. In addition, mutants compromising spindle asymmetry during anaphase (eg. *mud* mutants) also generate equal size daughter cells.

In Nbs spindle geometry is regulated by Gβγ, which is a subunit of the heterotrimeric G proteins and is able to suppress spindle growth. Gβγ binds to GDP-Gαi at the apical cortex and inhibits its activity allowing the apical spindle arm and the astral microtubules to grow. Because of the lack of Gαi at the basal cortex, Gβγ is free to inhibit spindle growth thereby establishing spindle asymmetry (Figure 16)[267,268]. In addition to Gβγ, it has also been shown that components of the apical polarity domain can contribute to the generation of spindle asymmetry. Triple mutants for *dlg*/*scrib*/*lgl* can invert cell polarity and with this generate inverted spindles, where the apical spindle arm is significantly shorter than the basal[269,270]. However, it remains unclear whether Gβγ is also involved in this pathway. Furthermore, the hypothesis that centrosome size asymmetry might be involved in generating spindle geometry differences was discarded in a study from Cai and colleagues from 2001[271]. They found that inverting centrosome polarity though exchange of the positions between the apical and basal centrosome was not sufficient to invert spindle asymmetry. In addition, it has been shown that astral microtubules are also not involved in spindle asymmetry. Mutants for *asterless* (*asl*, *cep152* in humans) lack astral microtubules and centrosomes, but are still able to form asymmetric spindles[272-274]. The cleavage furrow positioning pathways are shown in Figure 16.

Taken together, all these data suggest that spindle asymmetry is an important factor for the generation of physical daughter cell size during ACD and is regulated through the polarity components.

b) Polarity-dependent cleavage furrow positioning pathway

Recent studies have shown for *Drosophila* Nbs the existence of a novel spindle-independent cleavage furrow positioning pathway. In these Nbs the cleavage furrow components Anillin and Myosin as well as the centralspindlin component Pavarotti showed an asymmetric distribution during early anaphase with enrichment at the lateral cortex at the site of the future cleavage furrow. This enrichment was observed around 40 s before establishment

of the spindle asymmetry[275]. In agreement with these results, another study showed live imaging data, where Survivin, a component of the centralspindlin complex, which marks the midzone of the central spindle is localized in an apically shifted position compared to the lateral enrichment of the cleavage furrow marker Myosin[276]. These observations taken together suggest that the spindle-dependent pathway cannot completely explain the cleavage furrow positioning in these asymmetrically dividing neuroblasts.

Furthermore, even after complete chemical depolymerization of all microtubules, Nbs still initiated basally shifted furrowing. Performing spindle rotation experiments in the presence of unperturbed polarity (*mud* mutants) two cleavage furrows were observed, where one furrow was aligned with the polarity and appeared in a basally shifted position in relation to the apical-basal axis. The second furrow was induced through the spindle pathway and appeared in the midplane of the cells, which divided in a physically symmetric manner. This indicates that in the asymmetrically dividing neuroblasts cleavage furrow positioning is regulated by two pathways – a spindle dependent and a spindle independent pathway.

The same work showed that the spindle-independent cleavage furrow positioning pathway is regulated by the polarity component Pins through the establishment of an asymmetric distribution of the cleavage furrow component Myosin[275]. During early anaphase Myosin clears from the apical cortex and only later clears from the basal cortex and enriches at the site of the division. Previous studies have shown that this asymmetric Myosin distribution could lead to unequal cortical tension at the apical and basal cortices allowing an early apical expansion and basally shifting of the cleavage furrow[277]. Furthermore, *pins* mutants compromise asymmetric Myosin localization and neuroblasts divide in a physically symmetric manner.

All these data taken together show that in *Drosophila* neuroblasts a second cleavage furrow positioning pathway exists, which is regulated through the polarity protein Pins and depends on the asymmetric distribution of Myosin at early anaphase. However, the detailed molecular mechanism underlying polarity-dependent cleavage furrow positioning and Myosin distribution remain elusive and require further investigation. Both pathways are summarized in Figure 16.

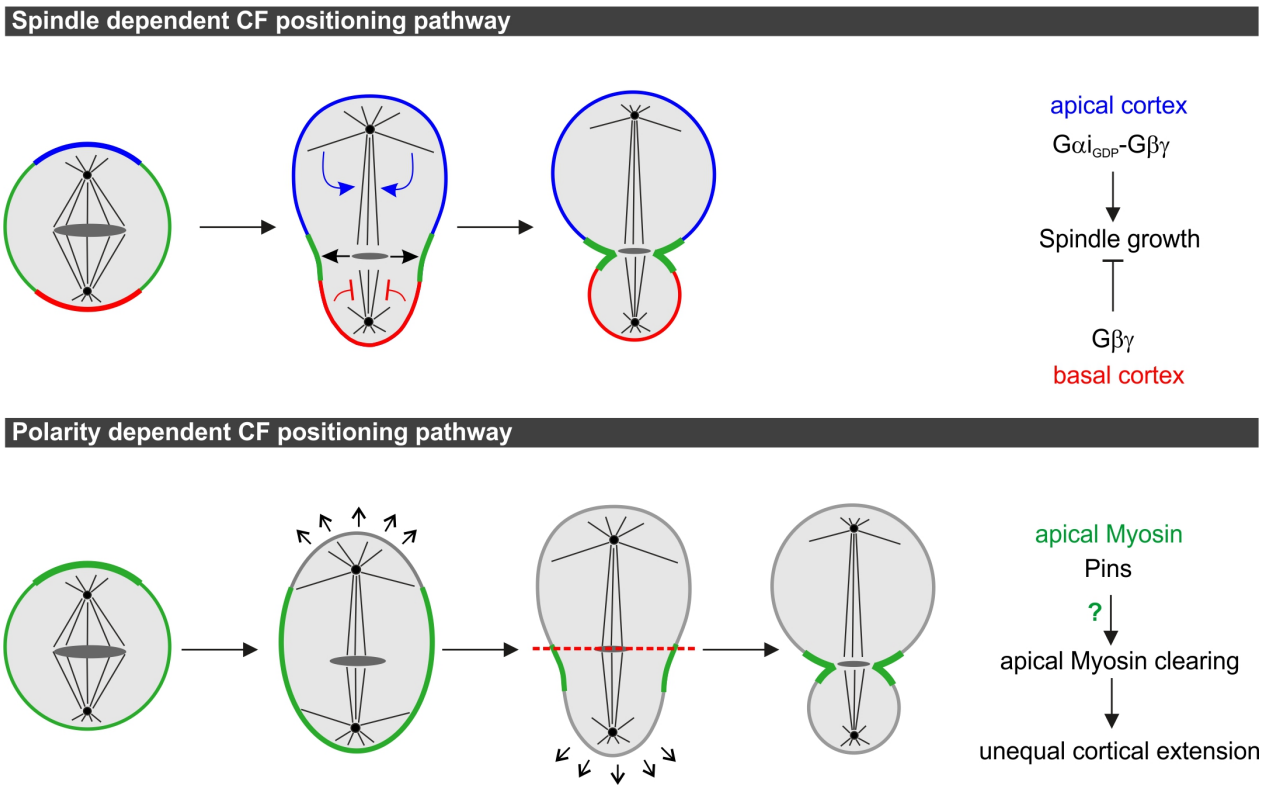

Figure 16: Spindle-dependent and polarity-dependent cleavage furrow positioning pathways. Upper panel: The spindle-dependent cleavage furrow positioning pathway. The apical and the basal domains of the neuroblast are indicated in blue and red respectively. The centralspindlin complex sends signals to establish the division plane (black arrows). Furthermore, active Gβγ at the basal cortex inhibit spindle growth (red arrows), whereas Gβγ is inactive at the apical side and this allows the spindle growth there (blue arrows). Lower panel: The polarity-dependent cleavage furrow positioning pathway. Myosin clears at early anaphase from the apical cortex and allows its expansion (arrows indicate the expansion direction). Later, Myosin clears basally and the cortex can expand also at the basal cortex (arrows). The position of the centralspindlin complex aligns only later with the division site (not shown).

Interestingly, a number of other studies showed that this process is not specific for *Drosophila* neuroblasts but might represent a general model for cleavage furrow positioning. Neuroblasts in *C.elegans* were shown to activate Myosin asymmetrically correlating with a smaller daughter cell after division. Laser induced Myosin inactivation specifically at the site of enrichment was able to invert the physical asymmetry and generate two daughter cells of similar size. Therefore, the authors conclude that physical daughter cell asymmetry might be regulated through Myosin asymmetric activation rather than the spindle[278]. Furthermore, a spindle-independent cleavage furrow positioning pathway is also required for the formation of primordial germ cells (PGC) during early *Drosophila* melanogaster embryogenesis[279]. Taken together the spindle-independent cleavage furrow positioning pathway might represent a more general biological processes for different model systems. However, the underlying molecular mechanisms remain to be elucidated.

Aim of the Thesis

The aim of the present study is to investigate the cellular and molecular mechanisms underlying Myosin localization during ACD. To this end, I used asymmetrically dividing *Drosophila* neuroblasts, stem cells in the *Drosophila* nervous system as a model system.

Previous studies have shown that shortly after anaphase onset, Myosin becomes asymmetrically localized. It first disappears from the apical cortex, followed by basal depletion and subsequent accumulation at the cleavage furrow. The mechanism of this dynamic localization remains elusive. To this end, I applied high-resolution live imaging and photoconversion techniques to follow specific sub-populations of Myosin at different cell cycle stages and cortical domains. I investigated the origin of Myosin molecules at the cleavage furrow. The accumulation is due either to a de-novo synthesis of Myosin or to an active redistribution. Since I confirmed an active redistribution, I further tested whether Myosin is transported via cortical flow or via lateral diffusion through the cytoplasm.

Furthermore, Myosin is activated through phosphorylation at two conserved sites within its RLC (Ser21 and Thr20). Firstly, I tested how phosphorylated and thus activated Myosin molecules are distributed in asymmetrically dividing neuroblasts and whether phosphorylation and thus activation is required for Myosin asymmetric distribution and cleavage furrow positioning. To this end, I performed immunohistochemistry in *Drosophila* neuroblasts using antibodies against phosphorylated Myosin in both wild type and symmetrically dividing *pins* mutant neuroblasts. Since Myosin localization is regulated through the apical polarity component Pins, I further screened for kinases specifically involved in Myosin regulation at the apical cortex during ACD. For the putative candidates, which regulate Myosin phosphorylation at the apical cortex, I investigated the regulatory mechanism underlying this phosphorylation. In particular, it would be interesting to address the question whether kinases regulating Myosin phosphorylation are involved in the novel polarity-dependent cleavage furrow positioning pathway, which was recently discovered[275].

Results

I. Myosin distribution during ACD

Myosin asymmetric distribution is established during early anaphase, when it first clears apically, later basally and finally accumulates at the cleavage furrow during telophase. However, the underlying mechanisms and the origin of the cleavage furrow Myosin molecules are not clear. In order to test whether Myosin is actively translocated to the cleavage furrow or it is de-novo synthetized there, we performed green-to red photoconversion experiments and high-resolution live imaging. This allowed us to follow the dynamic redistribution of specific sub-populations of Myosin at different cell cycle stages and cortical domains. In the following chapters we show data, explaining the mechanisms of Myosin relocalization and its contribution for correct cleavage furrow positioning and establishment of physical asymmetry.

1. Apical Myosin contributes to the accumulation at the cleavage furrow

In order to follow Myosin distribution during ACD, we generated transgenic flies expressing either the regulatory subunit of Myosin (encoded by *spaghetti squash*, *sqh),* or the MHC (encoded by *zipper, zip)*, both tagged with the photoconvertable fluorescent protein mDendra2. Both transgenes were endogenously expressed under the control of the regulatory elements of *sqh* and identical results were obtained using both transgenic lines. Thus, they will be referred as Myosin::Dendra hereafter. The structure of both transgenes is shown in Figure 17 and Figure 18.

Green-to-red photoconversion using UV light was first performed at the apical cortex at metaphase and the photoconverted Myosin molecules were followed over time. This allowed us to study the distribution mechanisms of specific sub-populations of Myosin at different cortical regions. Using this approach, two hypotheses were tested, in order to understand the origin of the cleavage furrow Myosin. On one hand, Myosin at the cleavage furrow might be de-novo synthetized as suggested for *Drosophila* S2 cells and the apical Myosin would be degraded ensuring apical clearing during anaphase onset[43]. In this case, photoconversion at the apical cortex during metaphase should result in loss of the photoconverted molecules and thus red fluorescence at the cleavage furrow. On the other hand, relocalization of the metaphase Myosin pool towards the cleavage furrow, should allow us to follow the red fluorescent Myosin

molecules and detect them at the furrow region during telophase. Both hypotheses are schematically shown in Figure 17.

Indeed, upon photoconversion of Myosin within a small region of interest at the apical cortex, Myosin relocalization towards the cleavage furrow was detected (Figure 17). Thus, these results suggest that apical Myosin depletion during anaphase can not only be explained by degradation and subsequent de-novo synthesis of Myosin, but rather by a relocalization mechanism. Furthermore, it was observed that also the basal pool of Myosin contributes to the forming cleavage furrow, supporting the existence of an active relocalization mechanism (Manuscript I; Roubinet et al.). A schematic representation of the Myosin photoconversion at different cortical regions and at different cytokinetic stages is shown in Figure 19.

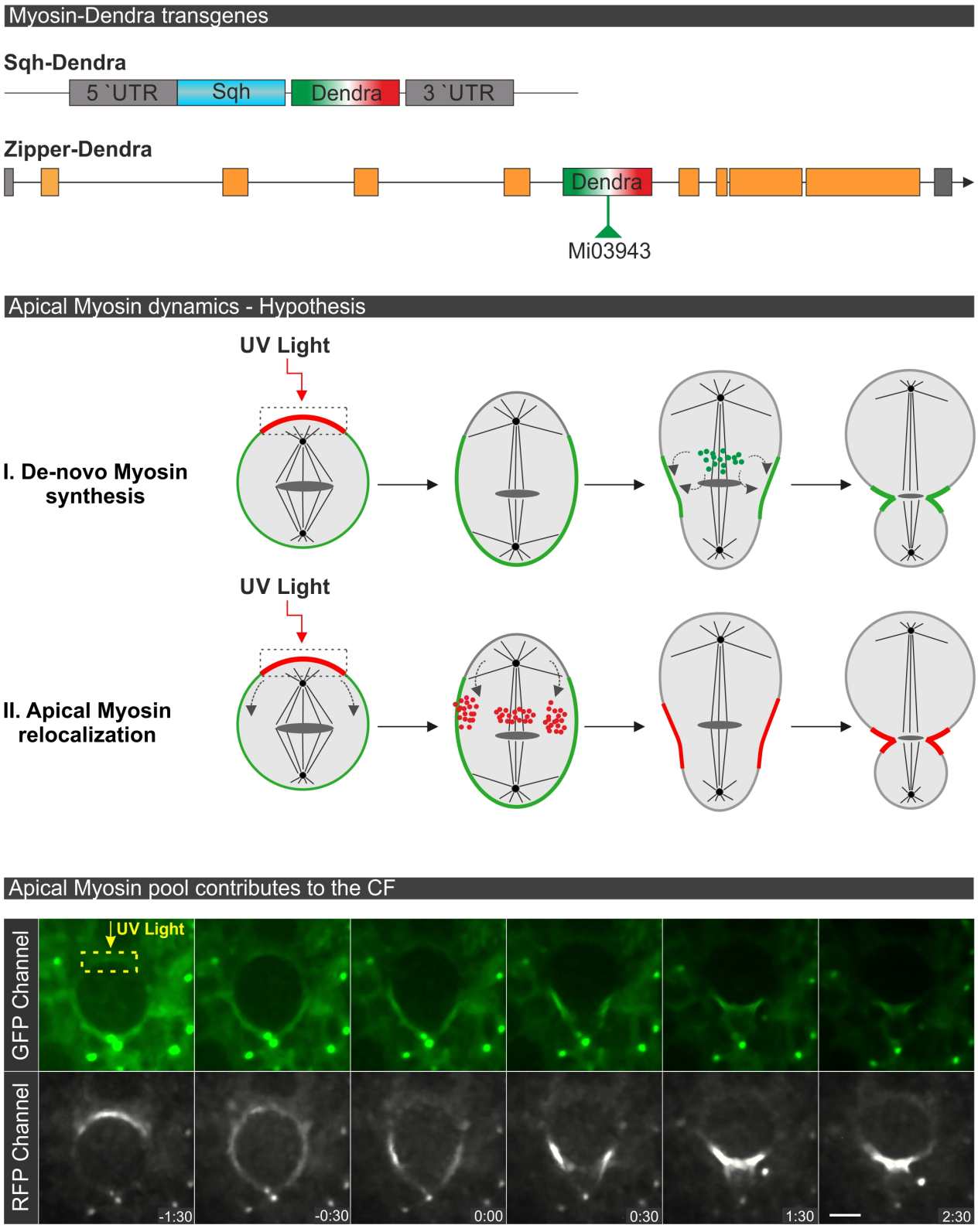

Figure 17: Photoconversion of apical Myosin shows active contribution to the cleavage furrow accumulation. Upper panel: Myosin::Dendra transgenes. The Myosin RLC and MHC (RMCE; see extended methods) were tagged with the photoconvertable fluorescent protein mDendra2. Middle panel: Both hypotheses for the origin of Myosin at the cleavage furrow are schematically shown. Lower panel: Photoconversion of Myosin at the apical cortex using UV light. Non-converted (green) and converted (red) Myosin molecules are shown in the GFP and the RFP channel respectively. The position of conversion is shown in yellow. The scale bar is 5 µm.

2. Myosin relocalizes towards the cleavage furrow via cortical flow

In order to understand how the relocalization of Myosin is regulated, photoconversion at the lateral cortex was performed at early anaphase after the onset of apical clearing and the photoconverted Myosin molecules were followed. For the active distribution mechanism two possible hypotheses were proposed. On one hand, Myosin filaments could locally disassemble and redistribute through the cytoplasm towards the cleavage furrow. This would suggest that upon lateral conversion, the cleavage furrow should be symmetrically labeled with the photoconverted red fluorescent Myosin molecules. Alternatively, Myosin could reach the furrow region through apical-basal oriented cortical flow. An apical-basal oriented cortical flow would result in an asymmetrically labeled cleavage furrow, where the photoconverted Myosin would remain predominantly at the side of conversion. The schematic representation of both hypotheses is shown in Figure 18.

Performing photoconversion at the lateral cortex after anaphase onset, when the apical Myosin pool already cleared, showed that indeed at early telophase only one side of the furrow region was labeled with the photoconverted Myosin molecules (Figure 18). These results strongly suggest that there is cortical flow, regulating the distribution of the apical Myosin molecules towards the cleavage furrow. Further results (see Mauscript I; Roubinet et al.) suggest that also the basal Myosin molecules reach the cleavage furrow via basal-apical cortical flow.

In addition, photoconversion was performed at early metaphase, resulting in a uniform cortical distribution of Myosin. This indicates that during these early stages Myosin undergoes non-directed cortical distribution. These results are in agreement with the observed behavior of Myosin, using live imaging of dividing neuroblasts expressing Sqh::GFP. During pro-metaphase Myosin pulsates along the entire neuroblast cortex and only at metaphase seems stabilized at the cortex. This might mean that the apical and basal cortical flows underlie a strict temporal control and their induction is tightly bound with the timing of anaphase onset. All observed Myosin behaviors upon photoconversion at different positions at the cell cortex and during different cell cycle stages are summarized in Figure 19. Some of the photoconversion data has been integrated in Manuscript I (Roubinet et al., submitted).

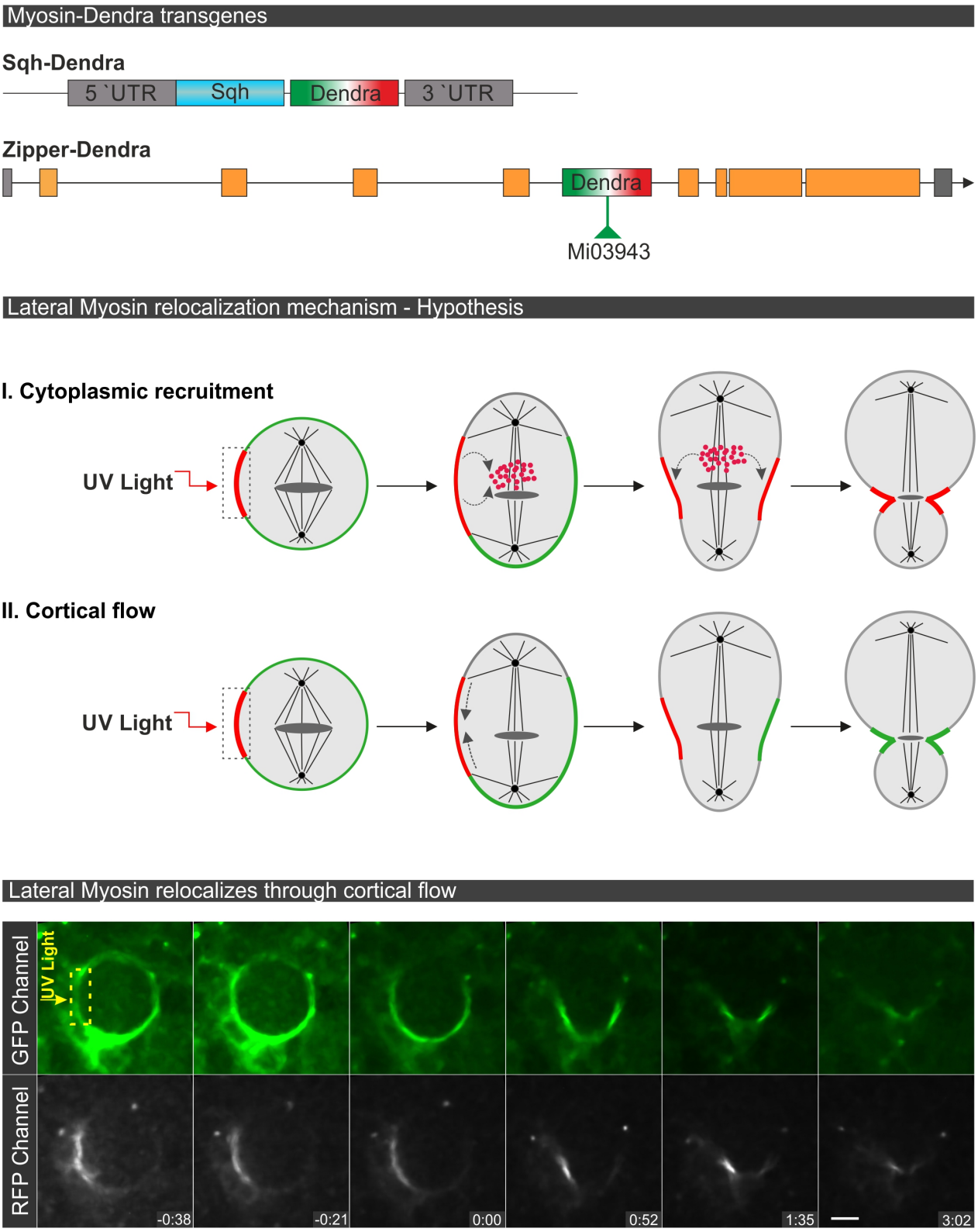

Figure 18: Lateral photoconversion shows cortical flow of Myosin towards the cleavage furrow. Upper panel: Myosin::Dendra transgenes as explained above. Middle panel: Both hypotheses for the redistribution of Myosin towards the cleavage furrow are shown. Lower panel: Photoconverted Myosin at the lateral side after the onset of apical clearing does not label the opposite side until late telophase, indicating the existence of cortical flow of Myosin towards the cleavage furrow. Non-converted (green) and converted (red) Myosin molecules are shown in the GFP and the RFP channel respectively. The position of conversion is shown in yellow. The scale bar is 5 µm.

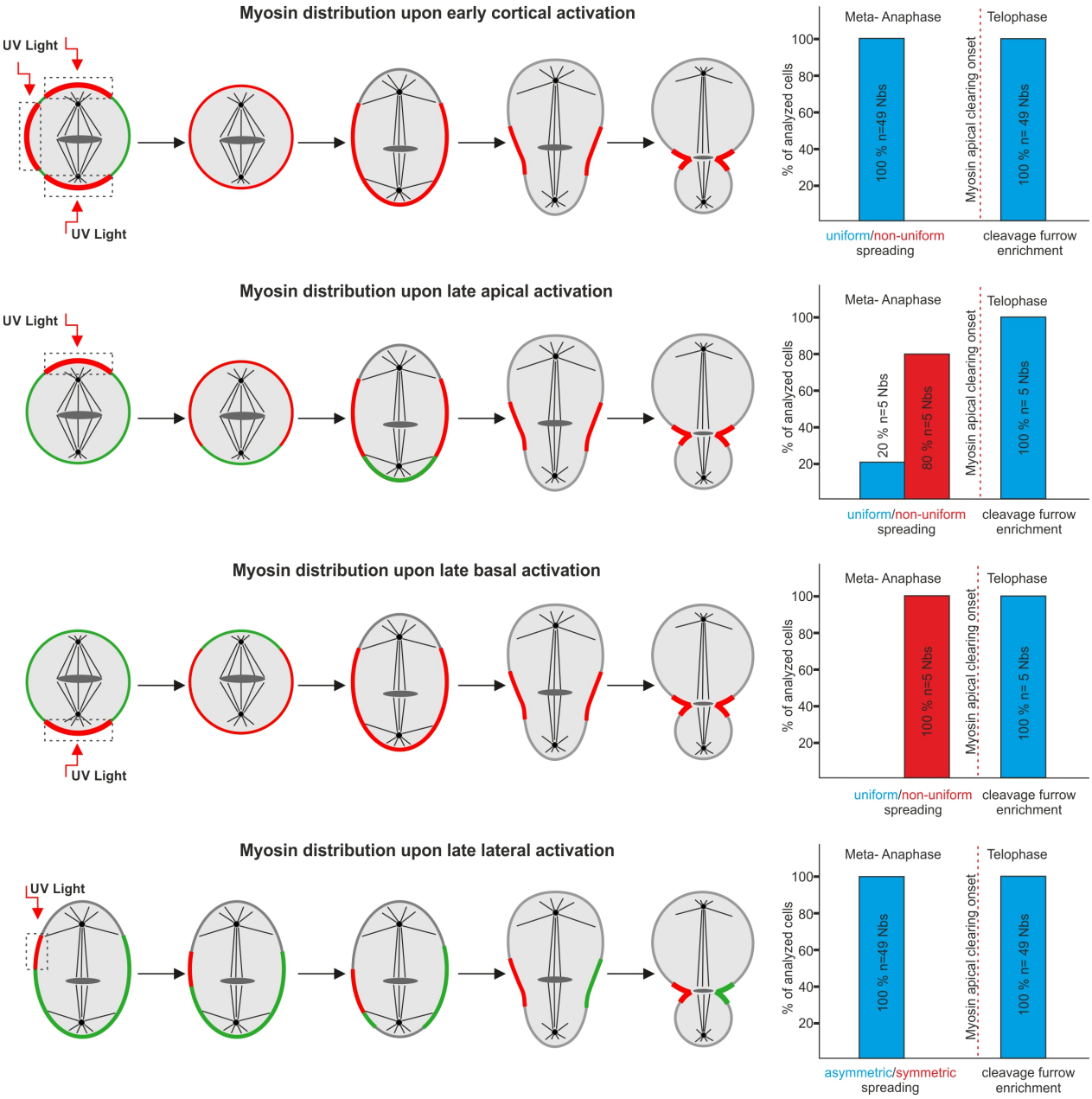

Figure 19: Summary of Myosin photoconversion at different cortical positions and different cell cycle stages. Upon early photoconversion a uniform distribution along the entire cortex was observed. Late apical or basal photoconversion resulted in relocalization towards the cleavage furrow without reaching the opposite tip of the cortex. The late lateral photoconversion showed asymmetric labeling of the cleavage furrow at telophase indicating an existing cortical flow. The non-converted Myosin is shown in green and the converted Myosin, as well as the position of the performed photoconversion are shown in red. The percentage of cells showing the indicated Myosin behavior is shown in the bar plots on the right.

3. Manuscript I: Spatiotemporally separated cortical flows and spindle-induced Myosin confinement coordinately acts to establish physical asymmetry in fly neural stem cells

In the following Manuscript I ("Spatiotemporally separated cortical flows and spindle-induced Myosin confinement coordinately acts to establish physical asymmetry in fly neural stem cells") we show how Myosin's cortical flows are regulated and how these together with cues from the spindle play a role for establishment of physical asymmetry under physiological conditions in *Drosophila* neuroblasts.

Spatiotemporally separated cortical flows and spindle-induced Myosin confinement coordinately act to establish physical asymmetry in fly neural stem cells

Chantal Roubinet[1], Anna Tsankova[1], Tri Than Pham[1] and Clemens Cabernard[2, #].

[1] Biozentrum, University of Basel

Klingelbergstrasse 50-70

CH-4056 Basel, Switzerland

[2] Department of Biology, University of Washington,

24 Kinkaid Hall

Seattle, WA 98105, USA

[#] Corresponding author: ccabern@uw.edu

Asymmetric cell division, creating sibling cells with distinct developmental potentials, can be manifested in physical asymmetry. This form of asymmetry occurs in a number of metazoan cells but the underlying mechanisms and function are incompletely understood. Here, we combine live cell imaging, photoconversion and laser cutting experiments in *Drosophila* neural stem cells to elucidate how physical asymmetry is established under physiological conditions. We show that Myosin relocalizes to the cleavage furrow via two distinct, spatiotemporally regulated cortical Myosin flows: a basally directed flow starting at anaphase onset followed by an opposing basal-to-apical flow. We show that the spindle-directed centralspindlin complex establishes a Myosin gradient at the lateral neuroblast cortex, necessary to trigger the second, apically directed flow. Based on this data, we propose that spatiotemporally controlled Myosin flows in conjunction with spindle positioning and spindle asymmetry are key determinants for correct cleavage furrow positioning and the establishment of physical asymmetry.

Introduction

Asymmetric cell division is an evolutionary conserved mechanism to create sister cells with different fate[1]. One manifestation of asymmetric cell division is the difference in sibling cell size and occurs in a number of different cell types and organisms[2]. Several mechanisms underlying the generation of physical asymmetry have been proposed but how they are spatiotemporally coordinated and molecularly controlled is incompletely understood[3]. Controlled cleavage furrow positioning can generate sibling cell size asymmetry by assembling an actomyosin-containing contractile ring at the correct position on the cell membrane. In most metazoan cells, the positional cues regulating ring positioning and assembly originate from the mitotic spindle in the form of the conserved Centralspindlin complex, composed of the mitotic kinesin-like protein 1 (MKLP1) (Pavarotti; Pav in *Drosophila*; Zen-4 in *C. elegans*) and MgcRacGAP (Tumbleweed; Tum in *Drosophila*; CYK-4 in *C. elegans*)[4,5,6]. It has been proposed that Pav travels along stable microtubules, delivering Tum to the cell equator where it activates the RhoGEF ECT2 (Pebble; Pbl in *Drosophila*; LET-21 in *C. elegans*)[7-9]. Equatorial localization of Pbl induces the activation of the small GTPase RhoA (Rho1 in *Drosophila*), promoting Actin polymerization and Myosin activation, resulting in the formation of the actomyosin-containing contractile ring[4,5].

This generalized model can explain equatorial Non-muscle Myosin II (Myosin, hereafter) localization in a number of cell types. However, cell type specific variations, highlighting fundamental mechanistic differences in Myosin dynamics, also exist. For instance, in Sea urchins phosphorylated Myosin is localized on the cell cortex until metaphase but subsequently disappears from the entire cortex and reappears in a confined spindle-induced band at the equatorial furrow[8]. In *Drosophila* neuroblasts, the neural stem cells in the developing fly brain, Myosin remains at the cell cortex throughout mitosis but the polarity proteins Discs large 1 (Dlg1; Dlg in vertebrates) and Partner of Inscuteable (Pins; LGN/AGS3) are used to transform Myosin from a uniform cortical distribution to an asymmetric localization before it enriches at the forming cleavage furrow[10]. Spindle-independent furrow positioning mechanisms are not confined to the neuroblast system but have also been reported in other organisms and cell types[11-15].

Myosin localization also influences the stability and dynamic behavior of the cell cortex. For instance, asymmetric Myosin localization regulates biased cortical expansion, shifting the cleavage furrow towards one cell pole, thereby generating unequal sized sibling cells and thus physical asymmetry[11,16]. However, how Myosin dynamics and activity are spatiotemporally regulated to ensure the correct establishment of physical asymmetry remains unclear.

Here, we use photoconversion, live cell imaging and laser cutting experiments in the *Drosophila* neuroblast system to specifically investigate the molecular mechanisms underlying sibling cell size asymmetry. We show that Myosin relocalizes to the cleavage furrow via two distinct cortical Myosin flows: a polarity induced, basally directed Myosin flow originating on the apical cortex and starting at anaphase onset. Subsequently, mitotic spindle cues establish a Myosin gradient at the lateral neuroblast cortex, necessary to trigger an apically directed flow, originating on the basal cortex. Based on data presented here, we propose that both spatiotemporally controlled Myosin flows in conjunction with spindle positioning and spindle asymmetry are key determinants for correct cleavage furrow placement and cortical expansion and thus the establishment of physical asymmetry.

Apical and basal Myosin filaments contribute to Myosin accumulation at the cleavage furrow

To learn how Myosin is regulated in asymmetrically dividing neuroblasts, we used live cell imaging and measured the relocalization dynamics of Non-muscle Myosin II (visualized with Sqh::GFP[17]; Myosin (Myo), hereafter) together with the cell cycle marker His2A::mRFP. We confirmed that by late metaphase Myosin was localized almost uniformly around the cortex[10,16,18]. Approximately 20 s after anaphase onset, Myosin first disappeared from the apical cortex and ~ 80 s later from the basal cortex, resulting in a ~ 1-minute delay between apical and basal Myosin depletion. Myosin also accumulated at the basally shifted cleavage furrow (Figure 1a-c).

We devised an *in vivo* pulse chase experiment to investigate the fate of apical and basal Myosin molecules. To this end, we generated transgenic flies, expressing either the regulatory subunit (encoded by *spaghetti squash; sqh*[19]) or the Myosin heavy chains (encoded by *zipper*; *zip*[20]) tagged with the photoconvertable fluorescent protein mDendra2[21]; both constructs are expressed by endogenous

regulatory elements (see methods). We obtained identical results with both lines and will collectively call these fusion proteins Myo::mDendra2 hereafter. We first photoconverted Myo::mDendra2 selectively on the apical cortex shortly before apical Myosin clearing and followed the subsequent relocalization of these photoconverted filaments with live cell imaging in intact fly larval brains or isolated neuroblasts (see methods). This pool of photoconverted Myosin spread almost over the entire cortex and subsequently focused at the cleavage furrow region (Figure 1d, Supplemental Figure 1a, movie S1 & movie S2). Similarly, Myo::mDendra2 filaments that were photoconverted on the basal cortex in early anaphase accumulated at the forming cleavage furrow later in anaphase (Figure 1e, movie S3). Thus, both pre-anaphase apical and early anaphase basal Myosin molecules contribute to the forming contractile ring.

Myosin filaments flow towards the cleavage furrow region

Apical and basal cortical Myosin filaments could locally disassemble and redistribute through the cytoplasm. Alternatively, actomyosin driven cortical flow could induce the onset of first an apical - basal and subsequently a basal - apical directed cortical flow[22]. To distinguish between these scenarios, we converted Myo::mDendra2 at the lateral cortex shortly after apical clearing. If cortical Myosin filaments would contribute to the cleavage furrow through cytoplasmic relocalization, we anticipated that Myosin would label the furrow symmetrically. Alternatively, laterally photoconverted Myosin filaments should predominantly stay at the lateral neuroblast cortex if cortical flow is the predominant mechanism (supplemental Figure 1b,c). In all cells (100 %; n = 49) we observed that photoconverted Myosin remains asymmetrically localized after photoconverting in early anaphase neuroblasts, labeling predominantly one side of the neuroblast cortex during anaphase and early telophase. Furthermore, laterally photoconverted Myo::mDendra2 flowed to the furrow region and became more confined towards the beginning of furrow ingression (Figure 1f & movie S4). The observed flows are not a consequence of cell shape changes since photoconverted Gap43::mEos[23] – a membrane marker - from the apical, basal or lateral neuroblast cortex distributed over the entire neuroblast membrane (Supplemental Figure 1d-g, movie S5 & movie S6). These results strongly suggest that Myosin's dynamic relocalization is due to two

opposing cortical flows: (1) an apical - basal flow, originating on the apical cortex shortly after anaphase onset and (2) a basal – apical flow, starting ~ 60 s later. We conclude that cortical flow is a major mechanism to relocalize Myosin filaments from both poles to the cleavage furrow in mitotic fly neuroblasts but do not exclude the contribution of cytoplasmic Myosin molecules to the cleavage furrow during anaphase (see also below).

Apical and Basal Myosin clearing is independent of Ran, Pp1-87B, Sds22 and other DNA derived cues

Next, we investigated the regulatory mechanisms underlying spatiotemporally controlled Myosin flows. Previously, we have shown that the polarity proteins Pins and Dlg1, as well as spindle-dependent cues are required for correct Myosin localization and cleavage furrow positioning[18,24]. Here, we focus on how the mitotic spindle induces or contributes to Myosin relocalization.

Neuroblasts lacking mitotic spindles (colcemid-treatment) and the spindle-assembly checkpoint component Rod[25], displayed a strong delay in basal Myosin clearing[10,16,18] (and Figure 2a-c) and also prevented the chromatin from reaching the basal cortex (Figure 2a). Since DNA-derived cues have recently been implicated in cortical remodeling[26,27], we investigated its role during asymmetric cell division in more detail. In wild type neuroblasts, chromatids approached the basal cortex more than the apical cortex (Figure 2d,f & Supplemental Figure 2a). In colcemid-treated *rod* mutant neuroblasts, the chromosomes stayed relatively close to the apical cortex, progressively moving away from the basal cortex during anaphase (Figure 2e,f & Supplemental Figure 2b).

Since these data showed a correlation between cortical Myosin clearing and chromatid proximity, we tested whether the small GTPase Ran, the phosphatase Pp1-87B and its regulatory subunit Sds22 – all of which were previously implicated in chromatid-associated cortex remodeling[26,27,28] - are required for apical and basal Myosin clearing. Ran accumulated around the chromatin in metaphase as reported for other cell types[29-31] but subsequently enriched on the sister chromatids, segregating into the neuroblast (Supplemental figure 2c). Pp1-87B was associated with neuroblast chromatin in interphase and late telophase but was widely distributed throughout the neuroblast's cytoplasm during anaphase when Myosin relocalization starts (Supplemental Figure 2f). Thus, neither Ran's nor Pp1-87B's localization

correlated with the sequence of basal Myosin clearing. Knocking-down *Ran, Pp1-87B* or *sds22* with inducible RNAi, expression of the dominant-negative $Ran^{T24N,\ 32}$ or using mutant alleles to remove *sds22* and *Pp1-87B*, respectively did neither compromise apical nor basal Myosin clearing (Supplemental Figure 2d,e). However, we noticed that sibling cell size asymmetry was perturbed after knocking-down Sds22 (see below).

Finally, to exclude the involvement of another chromosome-derived signal, we treated neuroblasts with colcemid to artificially push its chromatin close to the cell cortex but did not observe local Myosin depletion (100 %; n = 34; Figure 2g-j). Taken together, we conclude that neither Ran, Pp1-87B nor Sds22 are necessary to induce local Myosin relocalization. Furthermore, chromatin-derived cues are not sufficient to clear cortical Myosin in mitotic neuroblasts. Thus, the lack of basal Myosin clearing in colcemid treated neuroblasts is directly related to a lack of spindle-dependent cues.

The centralspindlin complex generates a lateral Myosin gradient, necessary for basal Myosin relocalization

We next asked how the mitotic spindle could induce a basal – apical Myosin flow. The equatorial stimulation model proposes that microtubules contacting the equatorial cortex (of central spindle or astral origin) lead to Myosin activation at the cell equator through centralspindlin-dependent activation of RhoA[4]. Due to the intrinsic contractile properties of Myosin, such an increase in activated Myosin generates a cortical flow towards the highest Myosin density[33]. To test whether this model could explain the basal – apical Myosin flow in neuroblasts, we first analyzed the localization of the centralspindlin complex using Tum::Venus[34]. From anaphase onset onwards, Tum was detected on bundled microtubules in the cell center, but also decorated microtubules contacting the lateral cortex (Figure 3a, b; Supplemental Figure 3a). Importantly, Tum preceded Myosin's enrichment on the lateral cortex (Figure 3b; compare 60 s vs. 90 s time point). Subsequently, both Tum and Myosin enrichment shifted closer to the basal cortex during anaphase (Figure 3b; Timepoints 60 s - 255 s). High temporal resolution imaging indicated that lateral Myosin accumulation always occurred prior to basal Myosin clearing (Figure 3c; n=10). Tum localization and subsequent Myosin enrichment agrees with the equatorial stimulation

model. To confirm it we (1) depleted the mitotic spindle completely (*rod*$^{H4.8}$ mutants treated with colcemid), (2) removed the centralspindlin components Tum and Pav and (3) knocked-down the chromosomal passenger complex component AurB, acting upstream of the centralspindlin complex[35]. Apical Myosin relocalization is not affected under these conditions[18] but lateral enrichment was abolished. Furthermore, Myosin enriched on the basal cortex and cleared with a significant delay (Figure 3d-g & Supplemental Figure 3b, c).

Since cortical Myosin is bound to filamentous Actin (F-Actin), Myosin's intrinsic contractility should induce an F-Actin flow. To test this hypothesis, we expressed Vinculin's Actin binding subunit (Vt)[36], tagged with the Fluorescence Resonance Energy Transfer (FRET) pair mTFP and Venus (mTFP1::Venus-Vt)[37] (and Tsankova A., et al., in preparation) and measured (1) F-Actin localization and (2) intermolecular FRET. We found that F-Actin intensity, and concomitantly also FRET ratios, increased prior to furrow formation, which was assayed by measuring curvature changes in the future furrow region (Figure 4a-c), suggesting that F-Actin crowding precedes furrow ingression. Furthermore, both lateral Myosin enrichment and subsequently basal Myosin clearing preceded furrow ingression. These data suggest that Myosin first accumulates at the lateral cortex, inducing an actomyosin flow, causing basal Myosin to clear (Figure 4d-f).

The mitotic spindle is necessary to confine Myosin to the lateral anaphase neuroblast cortex

Our photoconversion experiments showed that the apical – basal Myosin flow contributes to lateral Myosin enrichment but we wanted to know whether Myosin can also be recruited to the equatorial cortex from the cytoplasm. To this end, we used a pulsed UV laser (see methods) to induce local lesions in the neuroblast cortex (see methods). Cutting the cortex caused cortical Myosin to fall into the cytoplasm within ~ 40 s, thereby creating a neuroblast cortex that is essentially devoid of cortical Myosin. Under these conditions, the spatiotemporal relocalization of Myosin can be followed. Indeed, 1-2 minutes after the metaphase cortex was cut, cytoplasmic Myosin returned to the neuroblast cortex with a uniform cortical distribution (Figure 5a & Supplemental Figure 4a,b). However, if the cortex was cut in early anaphase (after apical Myosin depletion), Myosin also returned to the cortex but did not spread

uniformly anymore; Myosin was localized in a confined band, coinciding with the ingressing cleavage furrow (Figure 5b,d & movie S7). Surprisingly, in neuroblasts devoid of mitotic spindles (colcemid-treated *rod* mutants) Myosin was still able to return to the cortex after cutting. However, furrow confinement was lost and Myosin spread out on the basal cortex (Figure 5c, d, Supplemental Figure 4b and movie S8). We conclude that (1) cytoplasmic Myosin can be recruited to the equatorial cortex, independently of the mitotic spindle and (2) spindle-dependent cues are required to confine Myosin to the equatorial cleavage furrow region.

Spatiotemporally controlled Myosin flow onset contributes to furrow positioning and physical asymmetry

Since unequal cortical expansion is dependent on Myosin localization[16] the differential Myosin flow onset described here would provide an intuitive model for basal cleavage furrow positioning and thus physical asymmetry (Figure 6a). To test this hypothesis, we need to measure (1) Myosin flow velocity and (2) correlate Myosin flow onset with physical asymmetry. To this end, we used our photoconversion dataset and developed software to quantify Myosin flow velocity (see methods, Figure 6b and Supplemental Figure 5a). Velocity measurements were only performed until cell deformation set in to exclude an overestimation of Myosin flow speed. These measurements did not reveal a statistical significant difference between apical – basal and basal – apical flow, albeit some variability was detected (Figure 6c).

To correlate Myosin flow onset with physical asymmetry, we first identified mutant conditions, altering Myosin flow onset on both poles. In wild type neuroblasts, the temporal difference between the two flows is ~ 60 s (Mean: 65.56 s; +/- 13.33; n = 9). Neuroblasts depleted for intrinsic polarity such as *pins* single or *dlg;;pins* double mutants showed almost no delay between apical and basal Myosin clearing (Mean: 11 s; +/- 8.062; n = 15). *Rod* mutant neuroblasts treated with colcemid showed a strong delay in basal Myosin clearing, increasing the time between apical and basal Myosin flow onset to almost 3 minutes (Mean: 173.1 s; +/- 32.69; n = 13). Finally, we also found that Flavopiridol, a Cdk1 inhibitor, induced a premature Myosin flow from the basal to the apical cortex (data not shown). In this case, both

flows started with a minimal delay (Mean: 16.36 s; +/- 19.12; n = 11), mimicking *dlg;;pins* mutant neuroblasts (Figure 6d & Supplemental Figure 5b-e).

Myosin relocalization times also correlated well with cortical expansion. Wild type neuroblasts showed more apical than basal cortical expansion. In colcemid-treated neuroblasts only basal growth was reduced, also due to a retraction of the cortex. *dlg;;pins* double mutants and flavopiridol-treated cells showed comparable cortical expansion[16] (Supplemental Figure 6a,b and data not shown).

Next, we measured the distance from the cleavage furrow to the apical and basal cortex, respectively to determine an asymmetry ratio and plotted it against the individual clearing time delay. The measured clearing times showed a good correlation with the resulting asymmetry index; the larger the difference between apical and basal clearing, the bigger the asymmetry index. For instance, dlg;;pins double mutants showed an asymmetry index close to 1. Colcemid treated *rod* mutant neuroblasts delayed basal Myosin clearing considerably, resulting in an extreme asymmetry ratio. The calculated correlation (Pearson) coefficient is close to 1, suggesting that spatiotemporally regulated Myosin relocalization is a major contributor for basally shifted cleavage furrow positioning. However, although Flavopiridol-treated and *pins* single mutant neuroblasts had comparable Myosin clearing times to *dlg;;pins*, these conditions still showed partial physical asymmetry (Figure 6e). These measurements suggest that in addition to spatiotemporally regulated Myosin flow onset also other factors contribute to final furrow positioning and sibling cell size asymmetry.

Spindle asymmetry and positioning refine furrow placement to determine physical asymmetry

A prime suspect for this additional factor could be spindle geometry, prompting us to analyze both spindle positioning and spindle asymmetry by measuring the distance of the centrosomes to the cortex (positioning) and the length of the apical and basal spindle half at metaphase and telophase (asymmetry), respectively. We found that compared to wild type, flavopiridol-treated and *dlg;;pins* mutant neuroblasts showed normally positioned spindles in metaphase. However, metaphase neuroblasts lacking Sds22 displayed spindles that were shifted significantly towards the basal cortex (Figure 7a,b and supplemental Figure 5f and see above). Interestingly, metaphase spindle asymmetry was

normal in all conditions with the exception of *dlg;;pins* mutant neuroblasts, which displayed symmetric spindles (Figure 7a,c). Although we could not measure spindle asymmetry and positioning during anaphase, we found that in telophase, spindles of wild type, *sds22* mutants and neuroblasts treated with flavopiridol, were displaced towards the basal cortex (Figure 7d,e). Only *dlg;;pins* mutants contained centered telophase spindles (Figure 7d,e). However, telophase asymmetry was mostly affected in *dlg;;pins* and mildly compromised in Flavopiridol-treated or *sds22* deficient neuroblasts (Figure 6d,f). Spindle geometry correlated well with the shift in furrow positioning (Supplemental Figure 6c). We conclude that in addition to temporally regulated Myosin flow onset, spindle positioning and spindle asymmetry are important contributors to cleavage furrow positioning and final sibling cell size asymmetry.

Discussion

We have used asymmetrically dividing *Drosophila* neuroblasts to provide mechanistic insight into how physical asymmetry can be established. Previously, it has been shown that Myosin localization determines cortical expansion; cortical regions containing fewer Myosin filaments will be allowed to expand whereas regions containing high levels of Myosin are prevented to grow[16]. Unequal cortical expansion can thus be regulated through asymmetric Myosin localization. However, the spatiotemporal regulation controlling asymmetric Myosin localization and its dynamics remained elusive. Here, we have shown that two opposing cortical Myosin flows, starting at different times and locations, are a major mechanism to establish asymmetric Myosin distribution. For instance, shortly after anaphase onset, Myosin starts to flow towards the basal cortex, enabling the apical cortex to expand. With a delay of about 1 minute, Myosin subsequently flows from the basal cortex towards the apical pole. This spatiotemporal flow pattern ultimately regulates unequal cortical expansion, necessary for the establishment of physical asymmetry.

Cortical flow is triggered through Myosin contractility, pulling Actin filaments and associated proteins – such as non-contractile Myosin - towards the contractile Myosin filaments[33]. For cortical flow to start, Myosin contractility would need to be increased or inhibited locally[38]. Here, we propose that

Myosin flow onset on the basal cortex is induced through a lateral enhancement of Myosin activity, regulated through local delivery of the centralspindlin complex. This model is supported with the following data: (1) the centralspindlin complex component Tumbleweed is accumulating at the lateral neuroblast cortex in a confined position prior to lateral Myosin enrichment, which also precedes basal Myosin relocalization. (2) F-Actin localization and crowding increases at the lateral neuroblast cortex after lateral Myosin enrichment. (3) Removal of the mitotic spindle or kocking-down centralspindlin complex components such as *tum*, *pav*, or its upstream regulator *aurB*[18] compromise the establishment of a lateral Myosin gradient and perturb basal Myosin clearing. These results are consistent with a model, proposing that localized activation of the small GTPase Rho1 through the centralspindlin complex results in local Myosin filament formation and thus Myosin gradient formation (Figure 6g). Furthermore, our laser cutting experiments clearly show that the mitotic spindle is not required to bring Myosin to the cortex but to confine it to a focused region on the lateral cortex, corresponding to the furrow position. This result is consistent with our earlier observation, showing that the centralspindlin component Pav is already localized at the neuroblast cortex by metaphase (similar to Myosin)[39]. Thus, we conclude that the mitotic neuroblast cortex is primed to bind Myosin filaments already before anaphase but that spindle-dependent cues build up a lateral Myosin gradient specifically from early anaphase onwards. It is important to note that Myosin flow onset on the apical cortex is independent of both chromatin and spindle cues[18,24] (data shown here); the molecular nature of its onset will be described elsewhere (Tsankova, A., et al., in preparation).

Our results also imply that spindle geometry is an important factor in determining the lateral position of the Myosin gradient, providing an additional layer of regulation which influences how far apical and basal Myosin filaments are flowing before they reach the furrow region. Our data are consistent with this notion, showing that compromising either spindle positioning, spindle asymmetry or both have an influence on the site of cleavage furrow formation (supplemental Figure 6c) and subsequent physical asymmetry (supplemental Figure 6d,e). Thus, mutant conditions such as *dlg;;pins,* affecting both Myosin flow onset and spindle positioning/geometry will divide in a perfectly symmetrical manner whereas *sds22* mutants, shifting the spindle cue basally increase physical asymmetry. Having identified

mechanisms to establish physical asymmetry, it will be interesting to test how they will affect cell behavior and fate in fly and other metazoan cells.

Figure legends

Figure 1: Myosin filaments from the apical and basal neuroblast cortex flow to the cleavage furrow.

(a) Representative image sequence showing a wild type neuroblast expressing Sqh::GFP (Myosin) (white; top row, green; bottom row) and the DNA marker His2A::mRFP (red; bottom row). Cortical Myosin intensity was measured at the apical (dark green dashed box) and basal cortex (light green dashed box) throughout mitosis and plotted in **(b)**. Chromatid segregation starts at "0 s". **(c)** Mean apical and basal Myosin clearing time and standard deviation in relation to chromatid segregation. The blue and orange numbers represent the mean value. Myosin::Dendra2 was photoconverted on the **(d)** apical, **(e)** basal and **(f)** lateral neuroblast cortex. Top row: Photoconverted Myosin. Bottom row: overlay between Non-photoconverted (green) and photoconverted Myosin (red). The purple dashed box represents the photoconverted ROI. For this and all subsequent figures, asterisk denote statistical significance, derived from unpaired t-tests: *; $p \leq 0.05$, **; $p \leq 0.01$, ***; $p \leq 0.001$, ****; $P \leq 0.0001$, ns; not significant.

Time: seconds (s). Scale bar: 5 μm.

Figure 2: Chromatid-derived cues are insufficient to induce Myosin relocalization in fly neuroblasts.

(a) Representative image sequence showing a *rod* mutant neuroblast expressing Sqh::GFP (Myosin, top row; white, bottom row; green) and His2A::mRFP (DNA, bottom row; red) exposed to colcemid. Cortical Myosin intensity was measured at the apical and basal cortex, respectively (dark and light green dashed boxes) and plotted in **(b)**. **(c)** Graph showing the mean and standard deviation of basal Myosin clearing in relation to apical depletion (timepoint "0") for wild-type and colcemid-treated neuroblasts. Kymographs obtained from wild type **(d)** and *rod* mutant neuroblasts exposed to colcemid **(e)** showing Myosin (green) and DNA (red). The white dashed line indicates the region represented in the kymograph. Kymographs were used to measure the distance between the chromosomes and the apical (yellow arrows) or basal cortex (white arrows). **(f)** Scatter plot representing the distance between chromosomes and the basal cortex at the onset of apical Myosin depletion (0 s), at the onset of basal Myosin clearing (60 s) and once

basal Myosin depletion is completed (120 s). **(g)** Representative colcemid-treated neuroblast expressing Sqh::GFP (white; top panel, green; merge) and His2A::mRFP1 (red). Myosin and His2A intensity are shown in the 3D graph, corresponding to the ROI represented by the white dashed box. **(h)** Radar graph showing the distance of the neuroblast's chromatid to the cortex and **(i)** Myosin intensity for each of the 16 represented sectors. Yellow sectors represent areas with high DNA-cortex proximity. **(j)** Bar graph showing the percentage of *rod* mutant, colcemid treated neuroblasts displaying cortical Myosin depletion when the proximity of the DNA with the cortex is less than 2 µm.

Time: seconds (s). Scale bar: 5 µm.

Scale bar: 5 µm.

Figure 3: The centralspindlin complex induces basolateral Myosin enrichment, necessary for basal Myosin relocalization.

(a) Representative wild type neuroblasts expressing Tum::Venus (white; middle row, green; overlay), and stained for alpha-Tubulin (aTub; red) and phospho-Histone3 (PH3; white in first and third row). Higher magnification images correspond to regions highlighted with yellow and blue squares. **(b)** Representative image sequence of a wild type neuroblast expressing Myosin (white; top row, red; overlay in third row) and Tumbleweed (white; second row, green; overlay in third row). Higher magnification pictures were taken from the regions highlighted with white dashed boxes and shown as a merge (third row). Myosin (red) and Tumbleweed (green) intensity plots, obtained from the apical to the basal cortex, are shown for each time point. **(c)** Kymographs showing Myosin intensity at the lateral (green boxes) and at the basal neuroblast cortex (orange boxes) for one representative wild type neuroblast. Kymographs were generated from high temporal resolution time-lapse movies (2 second acquisition time). The graph shows Myosin intensity at the lateral (green plot) and basal cortex (orange plot). Representative image sequences of third instar neuroblasts expressing Sqh::GFP (green) and Cherry::Jupiter (MTs; purple) for **(d)** wild type, **(e)** colcemid-treated *rod* mutant **(f)**, Tum or **(g)** Pavarotti depleted neuroblast. Myosin intensity measurements were performed from the apical to the basal neuroblast cortex at three different

time points and shown below the image sequences. The star corresponds to the restrained lateral Myosin enrichment detected in early anaphase in WT neuroblast. Scale bars: 5 µm.

Figure 4: Lateral Myosin enrichment precedes lateral F-Actin crowding and basal Myosin clearing.

(a) Representative image sequence of a wild type neuroblast expressing the F-Actin probe and intramolecular FRET sensor TSmod-VT. The color in the images represents the FRET ratio (1st row). Curvature and F-Actin intensity were determined along the curved yellow line (2nd and 3rd row, respectively). Positive curvature is indicated with a "+", negative curvature (furrowing) with a "-". The horizontal dashed line represents the change from negative to positive curvature values. The region corresponding to the future cleavage furrow is indicated in red and highlighted in the graphs below. Blue arrows emphasize furrowing. **(b)** Graph showing F-Actin intensity (teal) and mean curvature (dark blue) changes from the furrow region (red line in (a)). For this and subsequent graphs, the time before and after cleavage furrow ingression is plotted along the X axis. The horizontal dashed line represents the change from negative to positive curvature values. Onset of furrowing corresponds to the timepoint "0". **(c)** Graph showing intramolecular F-Actin FRET index (magenta) and curvature (dark blue). **(d)** Graph showing Myosin intensity on the lateral (green) and basal (orange) neuroblast cortex. **(e)** Summary plot and **(f)** cartoon, derived from individual measurements, showing the temporal sequence between lateral Myosin enrichment, lateral F-Actin enrichment (F-Actin crowding) and basal Myosin clearing in relation to furrowing. Each dot represents the measurement of one cell. Scale bars: 5 µm.

Figure 5: The anaphase spindle is necessary for confined Myosin localization at the cleavage furrow

(a) Laser-induced cortical cutting experiments performed on third instar wild type neuroblasts expressing Sqh::GFP (Myosin) (white; upper panel, green; lower panel) and Cherry::Jupiter (magenta) in metaphase, or **(b)** anaphase. For this and subsequent panels the cortical cutting site is highlighted with yellow arrowheads. Orange arrowheads highlight Myosin recruitment. Myosin intensity profiles, measured from the apical to the basal cortex, are shown underneath the corresponding image. **(c)** Laser-induced cortical

cutting experiments performed on third instar *rod* mutant neuroblasts exposed to colcemid in anaphase. Only Sqh::GFP (white) is shown. **(d)** Experimental summary.

Time is shown as seconds before and after cortical cutting. Scale bars: 5 µm.

Figure 6: Cortical Myosin flow is a major mechanism for the generation of physical asymmetry

(a) Schematic illustration of the model to be tested: if cleavage furrow positioning and thus physical asymmetry depends on Myosin flows, then altering Myosin flow onset on the apical and/or basal cortex will misposition the cleavage furrow, if Myosin flow velocities on both cortices are similar. **(b)** Representative wild type neuroblasts showing photoconverted Myosin at the apical (left) or basal cortex (right). Myosin flow velocity was determined with custom-made software and stamped onto the images. **(c)** Relative apical – basal and basal – apical Myosin flow speed in third instar wild type neuroblasts. In most cases, averaged values were plotted. **(d)** Scatter plot showing basal Myosin clearing time after apical depletion for wild-type, flavopiridol- or colcemid-treated neuroblasts, *dlg;;pins* and *pins* mutant neuroblasts. **(e)** Scatter plot showing the correlation between Myosin clearing on the apical and basal cortex and the final furrow position in late anaphase/early telophase. A Pearson coefficient of "1" indicates a perfect correlation between Myosin clearing and furrow positioning. Scale bars: 5 µm.

Figure 7: Spindle asymmetry and positioning contribute to confined cleavage furrow placement and physical asymmetry.

Representative snapshots for wild-type, flavopiridol-treated, *dlg;;pins* and *sds22* mutant **(a)** metaphase and **(d)** telophase neuroblasts. Myosin is shown in green and MTs in magenta. **(b, e)** Scatter plot showing spindle position and **(c, f)** spindle asymmetry for each genotype at metaphase and telophase, respectively.

(g) Model. In *Drosophila* neuroblasts, polarity cues are used to initiate an apical – basal Myosin flow. Apical clearing of Myosin allows apical cortical expansion. Subsequently, Myosin flows from the basal towards the apical neuroblast cortex induced through a lateral Myosin gradient, which is established through anaphase spindle cues. The centralspindlin complex is required to enrich for Myosin on the

lateral cortex, initiating basal Myosin clearing. Spindle positioning and geometry are key factors to confine Myosin enrichment to the lateral cortex. See text for details.

Scale bars: 5 μm.

Supplemental Figure 1: Myosin relocalizes to the cleavage furrow through cortical flow

(a) Neuroblasts from intact brains, expressing Myo::mDendra2 (Myosin's heavy chains, encoded by *zipper*, fused to the photoconvertable fluorescent protein mDendra2) were photoconverted in a confined region (purple dashed box) on the apical cortex. In this and all subsequent panels, non-photoconverted and photoconverted Myosin are represented in green and red, respectively. Time is shown as seconds after the photoconversion. **(b, c)** Cartoons representing two possible distributions after lateral photoconversion of Myo::mDendra2. If Myosin reaches the cleavage furrow through cytoplasmic distribution, converting Myosin on the lateral cortex should result in labelling both sides of the cleavage furrow with almost equal probability. Alternatively, if Myosin flows on the lateral cortex to the cleavage furrow, the photoconverted side should remain labeled predominantly.

(d) Apical, **(e)** basal and **(f)** lateral control photoconversion experiments with the membrane receptor Gap43 fused to the photo-switchable protein mEos (Gap43::mEos). Time is shown as seconds after the photoconversion and the purple dashed box represents the photoconverted ROI. **(g)** Quantification of the observed phenotype for the indicated markers. Scale bars: 5 μm.

Supplemental Figure 2: Ran, Pp1-87B and Sds22 are not required for basal Myosin clearing.

Plots showing the distance between chromatids and the apical (top graph) and the basal cortex (bottom graph) throughout mitosis in wild type **(a)** and colcemid-treated *rod* mutant **(b)** neuroblasts. **(c)** Dividing neuroblasts immunostained for microtubules (alpha-Tubulin; white in first and third row), DNA (DAPI; red in first and third row) and Ran (white in second row; green in third row). Yellow arrows highlight Ran localization from metaphase to telophase. **(d)** Image sequence of a representative neuroblast expressing Sqh::GFP (Myosin, white; top panel, green; bottom), Cherry::Jupiter (MTs, magenta in bottom row) and RNAi against Ran. **(e)** Summary of phenotypes. Ran was knocked-down using two independent RNAi lines.

Ran^{T24N} is a dominant-negative. **(f)** Dividing neuroblasts immunostained for alpha-Tubulin (white in first and third row) and Pp1-87B (Pp1-87B-HA; white in middle row, green in third row), from interphase to telophase. Representative Image sequences of neuroblasts expressing Sqh::GFP (white; top row, green; bottom row) and Cherry::Jupiter (magenta in overlay) and **(g)** RNAi against *pp1-87B* or **(h)** mutant for *sds22* (*sds22*^{PB1173}). **(i)** Quantification of apical and basal Myosin clearing in neuroblasts lacking Pp1-87B (*pp1-87B*^{Bg3} and *pp1-87B*^{Bg6} are amorphs) or **(j)** Sds22. Scale bars: 5 µm.

Supplemental Figure 3: The centralspindlin complex is localized to the lateral neuroblast cortex and is necessary for basal Myosin clearing.

(a) Representative third instar wild type neuroblast expressing the centralspindlin component Tumbleweed fused to Venus (Tum::Venus, white; top row, green; second row) and the spindle marker Cherry::Jupiter (magenta) from anaphase onset until telophase. Third row shows a higher magnification image of the region, highlighted with the yellow dashed box. From these regions, Tum intensity was measured and plotted as a 3D graph (bottom row). Blue and yellow arrows highlight Tum accumulations at the lateral cortex and on centralspindle microtubules. **(b)** Time-lapse of a representative third instar neuroblast, expressing Sqh::GFP (green), Cherry::Jupiter (magenta) and RNAi against *aurB*. Myosin intensity measurements were performed from the apical to the basal neuroblast cortex at three different time points and shown below the image sequence. **(c)** Graph representing basal Myosin clearing time after apical Myosin depletion in wild-type, colcemid-treated *rod* mutant neuroblasts or after expression of RNAi against tumbleweed. Scale bars: 5 µm.

Supplemental Figure 4: The mitotic spindle is not required for cortical Myosin recruitment in metaphase.

(a) Graph showing cortical Myosin *versus* cytoplasmic Myosin intensity, before and after laser-induced cortical cut in metaphase. Quantifications are performed on the cell shown in Figure 4a. **(b)** Summary of cortical cut experiments performed in metaphase.

Supplemental Figure 5: Myosin flow, spindle geometry and positioning contribute to cleavage furrow placement and physical asymmetry

(a) Apical – basal and basal – apical Myosin flow were calculated by assigning a centroid to the photoconverted signal. The position of the centroid in relation to the apical and/or basal neuroblast cortex was used to determine flow velocity. Representative image sequence of a **(b)** *dlg;;pins* double mutant or **(d)** Flavopiridol-treated wild type neuroblast, expressing Myosin (white on the upper panel, green on the merge) and Cherry::Jupiter (magenta on the merge). Cortical Myosin intensity was measured on the apical (dark green dashed box) and basal cortex (light green dashed box) throughout mitosis and plotted in **(c)** for *dlg;;pins* and **(e)** flavopiridol-treated wild type neuroblast. **(f)** Scatter plot representing the proximity of apical and basal centrosomes to the apical and basal cortex, respectively in control, flavopiridol-treated, *dlg;;pins* and *sds22* mutant neuroblasts. Scale bars: 5 µm.

Supplemental Figure 6: Cortical extension and cleavage furrow shift contribute to physical asymmetry.

Scatter plots showing **(a)** apical and **(b)** basal cortical extension in wild type, flavopiridol-treated, colcemid-treated, *dlg;;pins* and *sds22* mutant neuroblasts. Since polarity is lost in *dlg;;pins* mutants, the cortex associated with the slightly bigger cell is defined as “apical”, whereas the cortex, associated with the slightly smaller cell “basal”. **(c)** Scatter plot showing cleavage furrow shift and **(d)** physical asymmetry for the indicated genotypes. **(e)** Summary of phenotypes. An increase in asymmetry can be obtained by shifting the spindle basally and/or increasing its asymmetry. Changes in cortical flow onset, affecting cortical expansion also contribute to increased or reduced physical sibling cell size asymmetry.

Movie legends

Movie S1: Apical Myosin filaments contribute to the cleavage furrow in telophase in intact larval fly brains.

Third instar larval wild type neuroblast of an intact brain lobe, expressing the photoconvertable fluorescent protein mDendra2, fused with Myosin's regulatory subunit, encoded by *spaghetti squash* (*sqh::mDendra2*; white). Myosin was photoconverted on the apical cortex. The movie starts with the first frame after photoconversion. The neuroblast was imaged every 30 s. Time scale is h:mm:ss:ms. The scale bar is 5 μm.

Movie S2: Apical Myosin filaments contribute to the cleavage furrow in telophase in isolated neuroblasts.

Third instar larval wild type neuroblast from a primary culture expressing the photoconvertable fluorescent protein mDendra2, fused with Myosin's heavy chain, encoded by *zipper* (*zip::mDendra2*; white). Myosin was photoconverted on the apical cortex (purple box). Unconverted Myosin (white) is shown on the left, converted Myosin (white) in the middle and both unconverted (green) and converted Myosin (red) are shown to the left. The neuroblast was imaged every 9.9 s. Time is in seconds. The scale bar is 5 μm.

Movie S3: Basal Myosin filaments contribute to the cleavage furrow in telophase in isolated neuroblasts.

Third instar larval wild type neuroblast from a primary culture expressing *zip::mDendra2* (white). Myosin was photoconverted on the basal cortex (purple box). Unconverted Myosin (white) is shown on the left, converted Myosin (white) in the middle and both unconverted (green) and converted Myosin (red) are shown to the left. The neuroblast was imaged every 10 s. Time is in seconds. The scale bar is 5 μm.

Movie S4: Myosin filaments reach the cleavage furrow through cortical flow.

Third instar larval wild type neuroblast of an intact brain lobe, expressing photoconvertable Sqh::mDendra2. Myosin was photoconverted laterally in early anaphase. Note that photoconverted Myosin remains confined to the lateral region and moves towards the cleavage furrow. The neuroblast was imaged every 0.43 s before photoconversion and every 4.3 s after photoconversion. Time scale is h:mm:ss:ms. The scale bar is 5 μm.

Movie S5: Apically photoconverted Gap43 spreads over the entire neuroblast cortex.

Isolated and cultured third instar larval wild type neuroblast expressing Gap43 fused to the photoconvertable fluorescent protein mEos (Gap43::mEos). Photoconversion was performed on the apical neuroblast cortex (purple box) and imaged every 9.6 s. Unconverted Gap43 is shown on the left (white), converted Gap43 in the middle (white) and both unconverted (green) and converted (red) Gap43 to the right. Time is in seconds (s). The scale bar is 5 μm.

Movie S6: Laterally photoconverted Gap43 does not flow to the cleavage furrow.

Isolated and cultured third instar larval wild type neuroblast expressing Gap43::mEos. Photoconversion was performed on the lateral neuroblast cortex (purple box) and imaged every 10.5 s. Note that photoconverted Gap43 does not remain confined to the lateral region but spreads all over the membrane. Unconverted Gap43 is shown on the left (white), converted Gap43 in the middle (white) and both unconverted (green) and converted (red) Gap43 to the right. Time is in seconds. The scale bar is 5 μm.

Movie S7: Myosin relocalizes to the cleavage furrow after lesion-induced cortical delocalization.

Third instar larval wild type neuroblast of an intact brain lobe, expressing Sqh::GFP (Myosin ; white) and imaged every 10 s. A UV laser pulse was used to cut the cortex in anaphase. The yellow arrow refers to the laser-cutting site and the yellow box highlights the cortical lesion after the cut. Note that Myosin is

completely removed from the neuroblast cortex after the cut but relocalizes to the cleavage furrow subsequently. Time is in seconds. The scale bar is 5 μm.

Movie S8: Spindle cues are not required to relocalize Myosin to the anaphase cortex but necessary for confined recruitment.

Third instar larval *rod* mutant, colcemid-treated neuroblast of an intact brain lobe, expressing Sqh::GFP (Myosin ; white) and imaged every 10 s. A UV laser pulse was used to cut the cortex in anaphase (yellow arrow; yellow box). Note that Myosin is completely removed from the neuroblast cortex and is not restricted to the cleavage furrow when it relocalizes. Time is in seconds. The scale bar is 5 μm.

Methods

Fly strains and genetics

All mutant chromosomes were balanced over FM7actin::GFP, CyO actin::GFP or TM6B, Tb. The following mutant alleles and RNAi lines were used: *pins*^{P89} [40], *dlg*^{m52} [41], *FRT82B sas4*^{M} [42], *rod*$^{H4.8}$ [25], *pav* RNAi (v46137; VDRC), *tum* RNAi (BL28982; Bloomington; v106850; VDRC), *aurB* RNAi (VDRC), *sds22* RNAi (IR GD11788)[43], *sds22*^{PB1173} [43], *pp1-87B* RNAi (v35025; VDRC), *pp1-87B*^{Bg3} (BL23696; Bloomington), *pp1-87B*^{Bg6} [44], *Df(3R)Exel6164* (removes Pp1-87B; Bloomington).

Transgenes and fluorescent markers:

worGal4, UAS-cherry::Jupiter, Sqh::GFP[24], *Histone2A::mRFP1* (Bloomington stock center), *UAS-Tum::Venus*[34]. UAS-Ran-Q69L, UAS-Ran-T24N[45]. UAS-Gap43::mEos[23]. Sqh::mCherry [46].

Transgenes were expressed using the neuroblast specific driver *worGal4*[47].

Zipper::mDendra2 MiMIC[48] line: Mi02518 was crossed to phiC31 integrase (expressed under the vasa promotor; Bloomington stock center) and the resulting progeny were injected with mDendra2 exchange cassette[48]. Injections were performed by BestGene. Positive lines were initially screened for loss of yellow body marker and tested for the expression of Zipper::mDendra2

Generation of constructs

Sqh::mDendra2: The mDendra2 coding sequence was PCR amplified and inserted into AscI and NotI restriction sites of attP-Sqh. attP-Sqh was generated by removing EGFP with AscI and NotI (Tsankova, A., et al., in preparation). The construct was injected into attP (VK00033 and VK00037).

pUAST-attP-TSmod-Vt: The *TSmod-Vt*[49] fragment, consisting of mTFP1, the spinder silk protein SSP, Venus and the F-Actin binding domain of Vinculin (Vt) was PCR amplified from the *VinTS* cDNA obtained from addgene (Plasmid #26019) and subcloned into pUAST-attP between EcoR1 (5') and Kpn1 (3') using In-Fusion technology (Takara, Clontech). The construct was inserted at VK00033.

Antibodies

The following primary antibodies were used for this study: rat anti-a-Tub (Serotec; 1:500), mouse anti-a-Tub (DM1A, Sigma; 1:2500), rabbit anti-phospho-Histone 3 (Abcam; 1:1000), chicken anti-GFP (abcam; 1/1000), rabbit anti-Ran (Abcam; 1/100). Secondary antibodies were from Molecular Probes and the Jackson Immuno laboratory.

Immunostaining

96h larval brains were dissected in Schneider's insect medium (Sigma-Aldrich S0146) and fixed for 20 min in 4 % paraformaldehyde in PEM (100 mM PIPES pH 6.9, 1 mM EGTA and 1 mM MgSO4). After fixing, the brains were washed with PBSBT (1X PBS (pH7.4), 0.1 % Triton-X-100 and 1 % BSA) and then blocked with 1X PBSBT for 1h. Primary antibody dilution was prepared in 1X PBSBT and brains were incubated 48 h at 4°C. Brains were washed with 1X PBSBT four times for 30 min each and then incubated with secondary antibodies diluted in 1X PBSBT at 4 °C, overnight. The next day, brains were washed with 1X PBST (1x PBS, 0.1 % Triton-X-100) four times for 20 minutes each and kept in Vectashield (Vector laboratories) mounting media at 4 °C.

Live imaging sample preparation

Imaging medium (Schneider's insect medium (Sigma-Aldrich S0146) mixed with 10 % FBS (Sigma), 2 % PenStrepNeo (Sigma), 0.02 mg/mL insulin (Sigma), 20 mM L-glutamine (Sigma), 0.04 mg/mL L-glutathione (Sigma) and 5 µg/mL 20-hydroxyecdysone (Sigma)) was warmed up to room temperature before use.

96h after egg laying, larval brains were dissected in imaging medium and transferred onto a gas-permeable membrane (YSI Life Sciences 5793) fitted on a metallic slide. Brains were oriented with the brain lobes facing the coverslip. Excess media was removed until the brain lobes were in contact with the coverslip. The sample was sealed with Vaseline. A detailed protocol can be found here[50].

Primary neuroblast cultures

For photoconversion experiments, 96h larval brains were dissected in Chang & Gerhing solution (3.2 g/L NaCl, 3 g/L KCL, 0.69 g/L CaCl2-2H2O, 3.7 g/L MgSO4-7H2O, 1.79 g/L tricine buffer pH 7; 3.6 g/L glucose, 17.1 g/L sucrose, 1 g/L BSA) at room temperature. Brains were then dissociated in Chang & Gerhing solution supplemented in collagenase from Clostridium histolyticum (Sigma) and papain from papaya latex (Sigma) at a final concentration of 1 mg/mL each, during 30 minutes at 30 °C. Brains were washed with imaging medium (see above) and then dissociated in imaging medium by pipetting 20 - 30 times.

Imaging

Fixed samples were imaged using an inverted Leica TSC SPE confocal microscope. For representative images a 60X/1.40NA oil immersion objective was used. For 4X scans a z-step size of 0.3 µm was used.
Live samples were imaged with an Andor revolution spinning disc confocal system, consisting of a Yokogawa CSU-X1 spinning disk unit and two Andor iXon3 DU-897-BV EMCCD cameras. A 60X/1.4NA oil immersion objective mounted on a Nikon Eclipse Ti microscope was used. Live imaging voxels sizes are 0.22 X 0.22 X 0.5 µm (60x/1.4NA spinning disc).

Laser cutting experiments

For laser cutting experiments, Andor's Micropoint system, consisting of a pulsed nitrogen pumped tunable dye laser was used. Ablation was performed using a power of 72 %. Imaging was performed before and after ablation using a 60x oil immersion lens (NA 1.4) that was also used to focus the Micropoint laser.

Photoconversion

96 h larval brains expressing Zipper::mDendra2 were used after their dissociation (see above). Photoconversion experiments were performed on an Andor Revolution spinning disc system containing Andor's FRAPPA unit. Several regions of interests (ROIs) were manually chosen in the GFP channel and Zipper::mDendra2 was irradiated with 405 nm on either the apical, basal or lateral cortex just after

anaphase onset. Before photoconversion, single Z planes containing ROIs were scanned for ten time points with maximum speed. Subsequently, ROIs were irradiated with 405 nm (10 %; 50 repeats; 50 µs dwell time). After photoconversion, the entire neuroblast was scanned with a z-step size of 0.65 µm. Converted and unconverted mDendra2 emission were merged in AndorIQ2 and converted into Imaris.

Colcemid and flavopiridol experiments

For colcemid and flavopiridol experiments, the following strains were used

+; worGal4, UAS-Cherry::Jupiter, Sqh::GFP; + [24]

+; worGal4, UAS-Cherry::Jupiter, Sqh::GFP; rodH4.8[24]

+; His2A::mRFP1; rod$^{H4.8}$ (this work)

Wild-type or *rod*$^{H4.8}$ mutant neuroblasts were incubated with colcemid (Sigma) in live imaging medium at a final concentration of 5 µg/ml, or with flavopiridol hydrochloride (Sigma) at a final concentration of 5 µM. Live imaging was started without delay. Complete spindle depolymerization was seen ~ 30-60 min after colcemid addition.

Image processing and calculations

Images were processed using Imaris x64 7.5.2 and ImageJ. Andor IQ2 files were converted into Imaris files using Imaris File Converter. Measurements of apical and basal Myosin intensity were obtained by using the oblique slicer in Imaris oriented along the apico-basal polarity axis, with a thickness of ~ 3.5 µm. The corresponding image sequences were exported as TIFF files and opened with ImageJ to measure Myosin intensity along the apical and basal cortex. Due to the cellular size, which differs from one neuroblast to another, the apical and basal cortical regions used for intensity measurement correspond to ¼ of the diameter of the cell in metaphase. Background corrections were performed by measuring Myosin intensity in the media. Myosin flow velocity was obtained using a custom-made Matlab code. Kymographs, made in ImageJ using the pluggin "MultipleKymograph", were used to analyze the distribution of Sqh and chromosomes. Myosin intensity profiles were established in ImageJ by measuring Sqh::GFP intensities along a line from the apical to the basal cortex (after background correction). Cortical

expansion was obtained by measuring the length between the center of the cell in metaphase (used as spatial reference) and the apical/basal cortex in metaphase (=A1) and anaphase (=A2). From these values, the ratio was calculated (A2/A1 and B2/B1, respectively). For laser cutting experiments, Myosin intensity was measured both at the cortex and in the cytoplasm before and after cortical cuts were performed using a line on the entire cortex or a circle in the cytoplasm.

Pictures were cropped in Photoshop and assembled in Illustrator. Quantifications and graphical representations were generated in Microsoft Excel, and Graphpad Prism.

Curvature and furrow initiation analysis

To determine the curvature along the cell cortex, a line was manually drawn in ImageJ from the apical to the basal cortex on the mid-plane. Cortical curvature *K* can be determined via the following formula: $K = \frac{f''(x)}{(1+f'^2(x))^{3/2}}$, where x and $f(x)$ are the horizontal and vertical position of the drawn cortex, respectively. The first and second derivatives ($f'(x)$ and$f''(x)$) of the curve were calculated numerically using second order difference methods. Custom-written Matlab codes were used to determine curvature values for all points on the curve. To determine furrow initiation, we first determined the average curvature value for the furrow site. Since curvature value at the furrow site will change its sign (from positive to negative or vice versa) when the furrow starts to ingress, the furrow site can be detected by determining the position of the cortex with the highest sign change in the curvature value. Average furrow curvature values were calculated from an average of five nearest points around the peak of the sign change. Furrow initiation (*T* =0) is defined as the first time point that the average curvature value changes in sign value. For all time points that furrow ingression was not yet observed, the furrow position at *T*=0 was used to determine average value at the furrow.

Furrow Myosin quantification

Cell mid-planes were first generated using the Oblique Slicer tool in Imaris (Bitplane) and the entire image volume was then resliced along the direction of this plane for all time points. Using ImageJ, an average intensity projection was generated from three selected planes closest to the mid-plane. This procedure was done for all acquired time points. To determine cortical intensity signal for both Myosin and polymerized actin markers, a spline curve was drawn along the cell cortex on the average intensity projection image and the XY coordinates of this curve were exported to a text file. Custom made Matlab codes were written to extract the exact XY coordinates of the drawn curve from the text file. Intensity signal of the drawn curve was calculated from the image using an average intensity of the three pixels, closest to the curve. Average furrow Myosin was calculated in the same way as the average curvature described above.

FRET Imaging and quantifications

Live samples of cultured neuroblasts were placed in a ibidi 8-well glass bottom 1 µ-slide and imaged on a 3i spinning disk confocal microscope equipped with a Photometrics Evolve 512 back-illuminated EMCCD camera, using a X63 1.4 numerical aperture oil-immersion objective. Both donor (mTFP1) and acceptor/FRET (Venus) fluorophores were excited by a diode laser with 440nm wavelength at 40 % power and 200 ms exposure time. Donor and FRET signals were detected using standard CFP (482 / 35-25) and YFP (542 / 27-25) emission filter set. The FRET index was determined using custom-written Matlab code. First, a background subtraction was performed for both donor and FRET detected signals using a background averaged noise obtained from 50 different images acquired with the same imaging conditions. Then, the FRET index was calculated by calculating the ratio between the FRET acceptor and FRET donor intensity after subtracting background noise. A cut-off threshold (range 700-1100 a.u.) was used for the donor intensity such that only pixels with intensity above the cut-off are used for FRET index calculations. This cut-off threshold step was required to eliminate artificially high FRET index pixels in the medium due to fluctuating noises. The FRET index was determined for all slices in the z-stack at all acquired time points. 3D images with FRET index distribution was reconstructed in Imaris. The Oblique

Slicer tool was used to view FRET index distribution at the cell mid-plane. To determine average FRET index for the furrow site, a z-focal plane which best represents the furrow site was selected for every time point for the analysis. Average FRET index around the furrow site was calculated by averaging the FRET index along the cortex with 30 pixels long and 5 pixels thick centered at the furrow site. Average actin intensity, which can be represented by mTFP1 signal, was determined with a line of 5 pixels long and 3 pixels thick around the furrow site.

Statistics and sample number

Statistical significance was calculated using the unpaired samples t-test. For each experiment, the data was collected from at least 3 independent experiments.

Acknowledgements

We thank members of the Cabernard lab for helpful discussions and Emmanuel Gallaud, François Payre and Linda Wordeman for critical reading of the manuscript. We are also grateful to Barry Thompson and David Glover for flies and antibodies. We would also like to thank the Imaging Core Facility (IMCF) at the Biozentrum for technical support. This work was supported by the Swiss National Science Foundation (SNSF) and Worldwide Cancer Research. C.R was supported with an EMBO long-term postdoctoral fellowship. Stocks obtained from the Bloomington Drosophila Stock Center (NIH P40OD018537) and the Vienna Drosophila Resource Center (VDRC) were used in this study.

Author contributions

The majority of the study was conceived by C.R and C.C and C.R performed most of the experiments. A.T and C.C conceived, designed and performed the initial Myo::mDendra2 experiments, resulting in some of the main conclusions. T.T.P performed the F-Actin localization, FRET and curvature experiments and wrote custom-made Matlab codes for data analysis. All authors contributed to data interpretation. C.R and C.C wrote the paper with help from T.T.P.

References

1. Horvitz, H. R. & Herskowitz, I. Mechanisms of asymmetric cell division: two Bs or not two Bs, that is the question. *Cell* **68,** 237–255 (1992).
2. Li, R. The art of choreographing asymmetric cell division. *Dev. Cell* **25,** 439–450 (2013).
3. Roubinet, C. & Cabernard, C. Control of asymmetric cell division. *Curr. Opin. Cell Biol.* **31,** 84–91 (2014).
4. Green, R. A., Paluch, E. & Oegema, K. Cytokinesis in Animal Cells. *Annu. Rev. Cell Dev. Biol.* **28,** 120717164503001 (2011).
5. D'Avino, P. P., Giansanti, M. G. & Petronczki, M. Cytokinesis in animal cells. *Cold Spring Harb Perspect Biol* **7,** a015834 (2015).
6. White, E. A. & Glotzer, M. Centralspindlin: at the heart of cytokinesis. *Cytoskeleton (Hoboken)* **69,** 882–892 (2012).
7. Odell, G. M. & Foe, V. E. An agent-based model contrasts opposite effects of dynamic and stable microtubules on cleavage furrow positioning. *J. Cell Biol.* **183,** 471–483 (2008).
8. Foe, V. E. & Dassow, von, G. Stable and dynamic microtubules coordinately shape the myosin activation zone during cytokinetic furrow formation. *J. Cell Biol.* **183,** 457–470 (2008).
9. Somers, W. G. & Saint Robert. A RhoGEF and Rho family GTPase-activating protein complex links the contractile ring to cortical microtubules at the onset of cytokinesis. *Dev. Cell* **4,** (2003).
10. Cabernard, C., Prehoda, K. E. & Doe, C. Q. A spindle-independent cleavage furrow positioning pathway. *Nature* **467,** 91–94 (2010).
11. Ou, G., Stuurman, N., D'Ambrosio, M. & Vale, R. D. Polarized myosin produces unequal-size daughters during asymmetric cell division. *Science* **330,** 677–680 (2010).
12. Sedzinski, J. *et al.* Polar actomyosin contractility destabilizes the position of the cytokinetic furrow. *Nature* **476,** 462–466 (2011).
13. Cinalli, R. M. & Lehmann, R. A spindle-independent cleavage pathway controls germ cell formation in Drosophila. *Nat. Cell Biol.* **15,** 839–845 (2013).
14. Pacquelet, A., Uhart, P., Tassan, J.-P. & Michaux, G. PAR-4 and anillin regulate myosin to coordinate spindle and furrow position during asymmetric division. *J. Cell Biol.* **210,** 1085–1099 (2015).
15. Jordan, S. N. *et al.* Cortical PAR polarity proteins promote robust cytokinesis during asymmetric cell division. *J. Cell Biol.* **212,** 39–49 (2016).
16. Connell, M., Cabernard, C., Ricketson, D., Doe, C. Q. & Prehoda, K. E. Asymmetric cortical extension shifts cleavage furrow position in Drosophila neuroblasts. *Mol. Biol. Cell* **22,** 4220–4226 (2011).
17. Royou, A., Sullivan, W. & Karess, R. Cortical recruitment of nonmuscle myosin II in early syncytial Drosophila embryos: its role in nuclear axial expansion and its regulation by Cdc2 activity. *J Cell Biol* **158,** 127–137 (2002).
18. Roth, M., Roubinet, C., Iffländer, N., Ferrand, A. & Cabernard, C. Asymmetrically dividing Drosophila neuroblasts utilize two spatially and temporally independent cytokinesis pathways. *Nat Commun* **6,** 6551 (2015).
19. Karess, R. E. *et al.* The regulatory light chain of nonmuscle myosin is encoded by spaghetti-squash, a gene required for cytokinesis in Drosophila. *Cell* **65,** 1177–1189 (1991).
20. Edwards, K. A., Chang, X. J. & Kiehart, D. P. Essential light chain of Drosophila nonmuscle myosin II. *J. Muscle Res. Cell. Motil.* **16,** 491–498 (1995).
21. Chudakov, D. M., Lukyanov, S. & Lukyanov, K. A. Tracking intracellular protein movements using photoswitchable fluorescent proteins PS-CFP2 and Dendra2. *Nat Protoc* **2,** 2024–2032 (2007).
22. Yumura, S., Ueda, M., Sako, Y., Kitanishi-Yumura, T. & Yanagida, T. Multiple mechanisms for accumulation of myosin II filaments at the equator during cytokinesis. *Traffic* **9,** 2089–2099 (2008).
23. Mavrakis, M., Rikhy, R. & Lippincott-Schwartz, J. Plasma membrane polarity and

compartmentalization are established before cellularization in the fly embryo. *Dev. Cell* **16,** 93–104 (2009).
24. Cabernard, C., Prehoda, K. E. & Doe, C. Q. A spindle-independent cleavage furrow positioning pathway. *Nature* **467,** 91–94 (2010).
25. Basto, R., Gomes, R. & Karess, R. E. Rough deal and Zw10 are required for the metaphase checkpoint in Drosophila. *Nat. Cell Biol.* **2,** 939–943 (2000).
26. Kiyomitsu, T. & Cheeseman, I. M. Cortical Dynein and Asymmetric Membrane Elongation Coordinately Position the Spindle in Anaphase. *Cell* **154,** 391–402 (2013).
27. Rodrigues, N. T. L. *et al.* Kinetochore-localized PP1-Sds22 couples chromosome segregation to polar relaxation. *Nature* **524,** 489–492 (2015).
28. Ramkumar, N. & Baum, B. Coupling changes in cell shape to chromosome segregation. *Nat. Rev. Mol. Cell Biol.* **17,** 511–521 (2016).
29. Kaláb, P., Pralle, A., Isacoff, E. Y., Heald, R. & Weis, K. Analysis of a RanGTP-regulated gradient in mitotic somatic cells. *Nature* **440,** 697–701 (2006).
30. Kaláb, P., Weis, K. & Heald, R. Visualization of a Ran-GTP gradient in interphase and mitotic Xenopus egg extracts. *Science* **295,** 2452–2456 (2002).
31. Cao, Y.-K. *et al.* Cell cycle-dependent localization and possible roles of the small GTPase Ran in mouse oocyte maturation, fertilization and early cleavage. *Reproduction* **130,** 431–440 (2005).
32. Kornbluth, S., Dasso, M. & Newport, J. Evidence for a Dual Role for Tc4 Protein in Regulating Nuclear-Structure and Cell-Cycle Progression. *J Cell Biol* **125,** 705–719 (1994).
33. Mayer, M., Depken, M., Bois, J. S., Jülicher, F. & Grill, S. W. Anisotropies in cortical tension reveal the physical basis of polarizing cortical flows. *Nature* **467,** 617–621 (2010).
34. Goldstein, A. Y., Jan, Y.-N. & Luo, L. Function and regulation of Tumbleweed (RacGAP50C) in neuroblast proliferation and neuronal morphogenesis. *Proc. Natl. Acad. Sci. U.S.A.* **102,** (2005).
35. Carmena, M., Wheelock, M., Funabiki, H. & Earnshaw, W. C. The chromosomal passenger complex (CPC): from easy rider to the godfather of mitosis. *Nat. Rev. Mol. Cell Biol.* **13,** 789–803 (2012).
36. Ziegler, W. H., Gingras, A. R., Critchley, D. R. & Emsley, J. Integrin connections to the cytoskeleton through talin and vinculin. *Biochem. Soc. Trans.* **36,** 235–239 (2008).
37. Day, R. N., Booker, C. F. & Periasamy, A. Characterization of an improved donor fluorescent protein for Forster resonance energy transfer microscopy. *J Biomed Opt* **13,** –031203–9 (2008).
38. Munro, E. & Bowerman, B. Cellular symmetry breaking during Caenorhabditis elegans development. *Cold Spring Harb Perspect Biol* **1,** a003400–a003400 (2009).
39. Cabernard, C., Prehoda, K. E. & Doe, C. Q. A spindle-independent cleavage furrow positioning pathway. *Nature* (2010).
40. Yu, F., Morin, X., Cai, Y., Yang, X. & Chia, W. Analysis of partner of inscuteable, a Novel Player of Drosophila Asymmetric Divisions, Reveals Two Distinct Steps in Inscuteable Apical Localization. *Cell* **100,** 399–409 (2000).
41. Woods, D. F. & Bryant, P. J. The discs-large tumor suppressor gene of Drosophila encodes a guanylate kinase homolog localized at septate junctions. *Cell* (1991). doi:10.1016/0092-8674(81)90009-X
42. Basto, R. *et al.* Flies without centrioles. *Cell* **125,** 1375–1386 (2006).
43. Grusche, F. A. *et al.* Sds22, a PP1 phosphatase regulatory subunit, regulates epithelial cell polarity and shape [Sds22 in epithelial morphology]. **9,** 14 (2009).
44. Axton, J. M., Dombrádi, V., COHEN, P. & Glover, D. M. One of the Protein Phosphatase-1 Isoenzymes in Drosophila Is Essential for Mitosis. *Cell* **63,** 33–46 (1990).
45. Cesario, J. & McKim, K. S. RanGTP is required for meiotic spindle organization and the initiation of embryonic development in Drosophila. *Journal of cell science* **124,** 3797–3810 (2011).
46. Martin, A. C., Kaschube, M. & Wieschaus, E. F. Pulsed contractions of an actin-myosin network drive apical constriction. *Nature* **457,** 495–499 (2009).
47. Albertson, R. & Doe, C. Q. Dlg, Scrib and Lgl regulate neuroblast cell size and mitotic spindle asymmetry. *Nat. Cell Biol.* **5,** 166–170 (2003).
48. Venken, K. J. T. *et al.* MiMIC: a highly versatile transposon insertion resource for engineering Drosophila melanogaster genes. *Nat. Methods* **8,** 737–743 (2011).

49. Grashoff, C. *et al.* Measuring mechanical tension across vinculin reveals regulation of focal adhesion dynamics. *Nature* **466,** 263–266 (2010).
50. Cabernard, C. & Doe, C. Q. Live Imaging of Neuroblast Lineages within Intact Larval Brains in Drosophila. *Cold Spring Harbor Protocols* **2013,** 970–977 (2013).

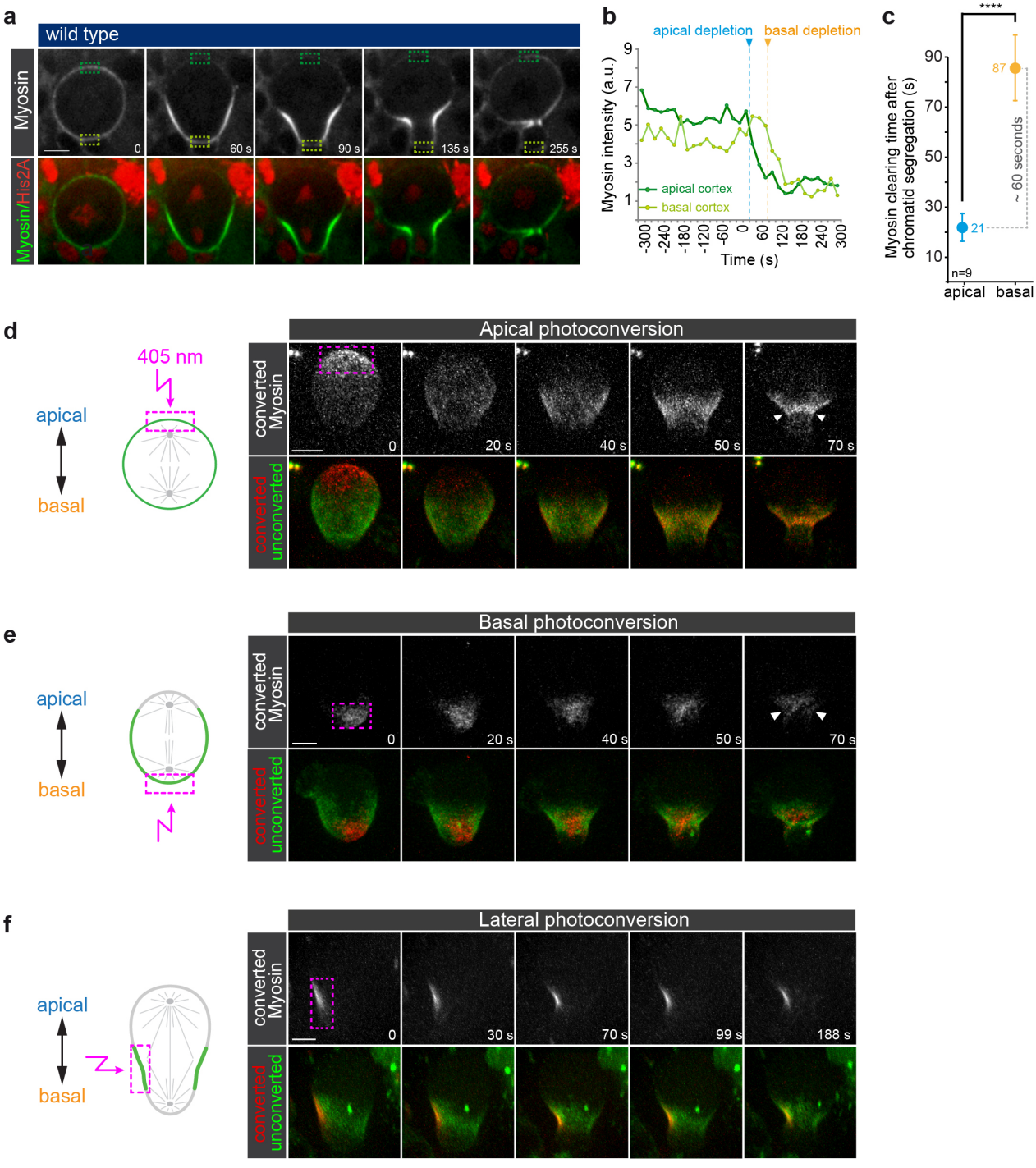
a
wild type
Myosin
Myosin/His2A
0
60 s
90 s
135 s
255 s
b
apical depletion
basal depletion
Myosin intensity (a.u.)
apical cortex
basal cortex
Time (s)
c
****
Myosin clearing time after chromatid segregation (s)
87
~ 60 seconds
21
n=9
apical
basal
d
405 nm
apical
basal
Apical photoconversion
converted Myosin
converted unconverted
0
20 s
40 s
50 s
70 s
e
apical
basal
Basal photoconversion
converted Myosin
converted unconverted
0
20 s
40 s
50 s
70 s
f
apical
basal
Lateral photoconversion
converted Myosin
converted unconverted
0
30 s
70 s
99 s
188 s

Figure 1

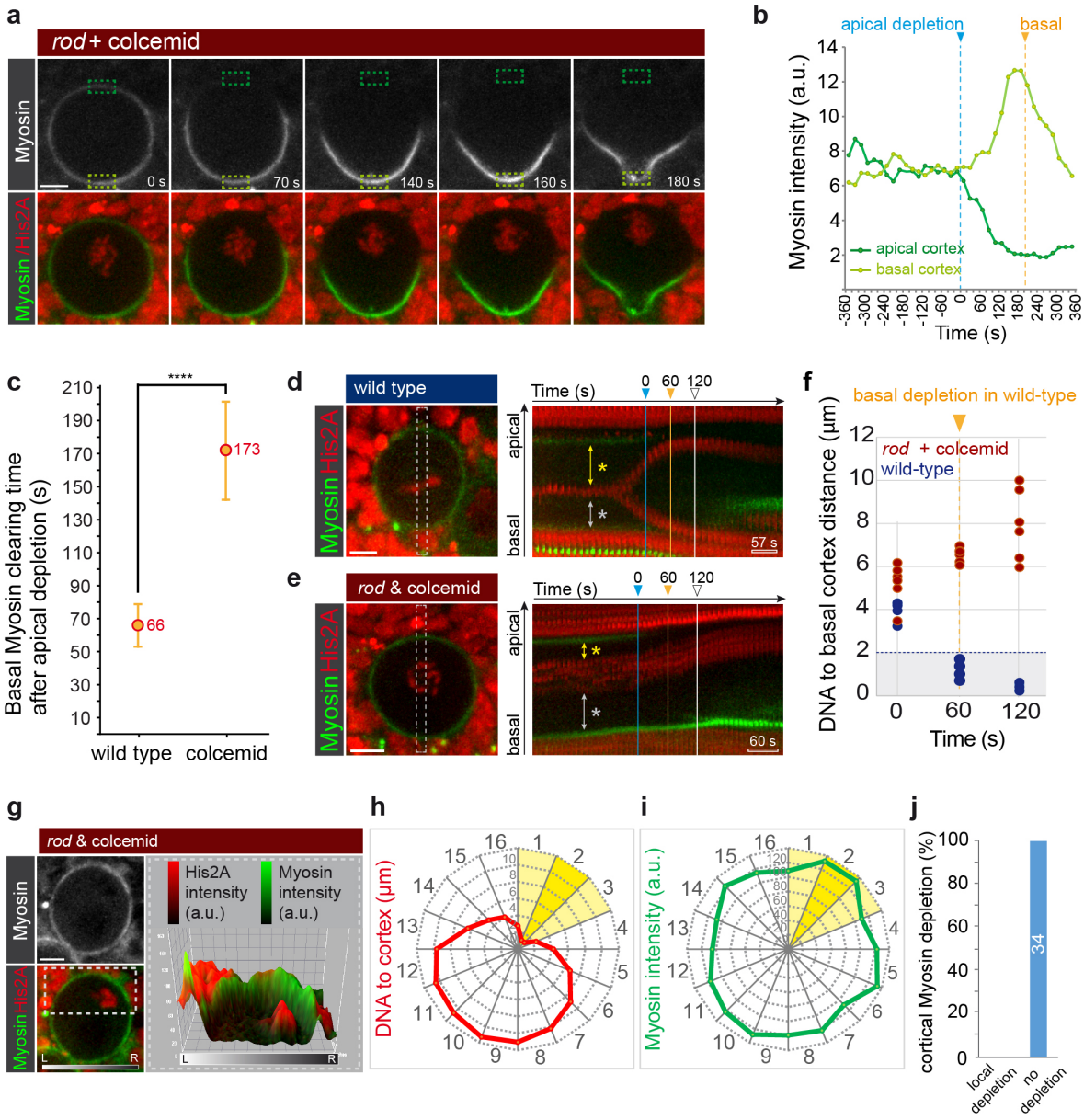
a
rod+ colcemid
Myosin
Myosin/His2A
0 s
70 s
140 s
160 s
180 s
b
apical depletion
basal
Myosin intensity (a.u.)
apical cortex
basal cortex
Time (s)
c
Basal Myosin clearing time after apical depletion (s)
****
173
66
wild type
colcemid
d
wild type
Myosin His2A
Time (s)
0 60 120
apical
basal
57 s
e
rod & colcemid
60 s
f
basal depletion in wild-type
rod + colcemid
wild-type
DNA to basal cortex distance (µm)
Time (s)
g
rod & colcemid
His2A intensity (a.u.)
Myosin intensity (a.u.)
h
DNA to cortex (µm)
i
Myosin intensity (a.u.)
j
cortical Myosin depletion (%)
34
local depletion
no depletion

Figure 2

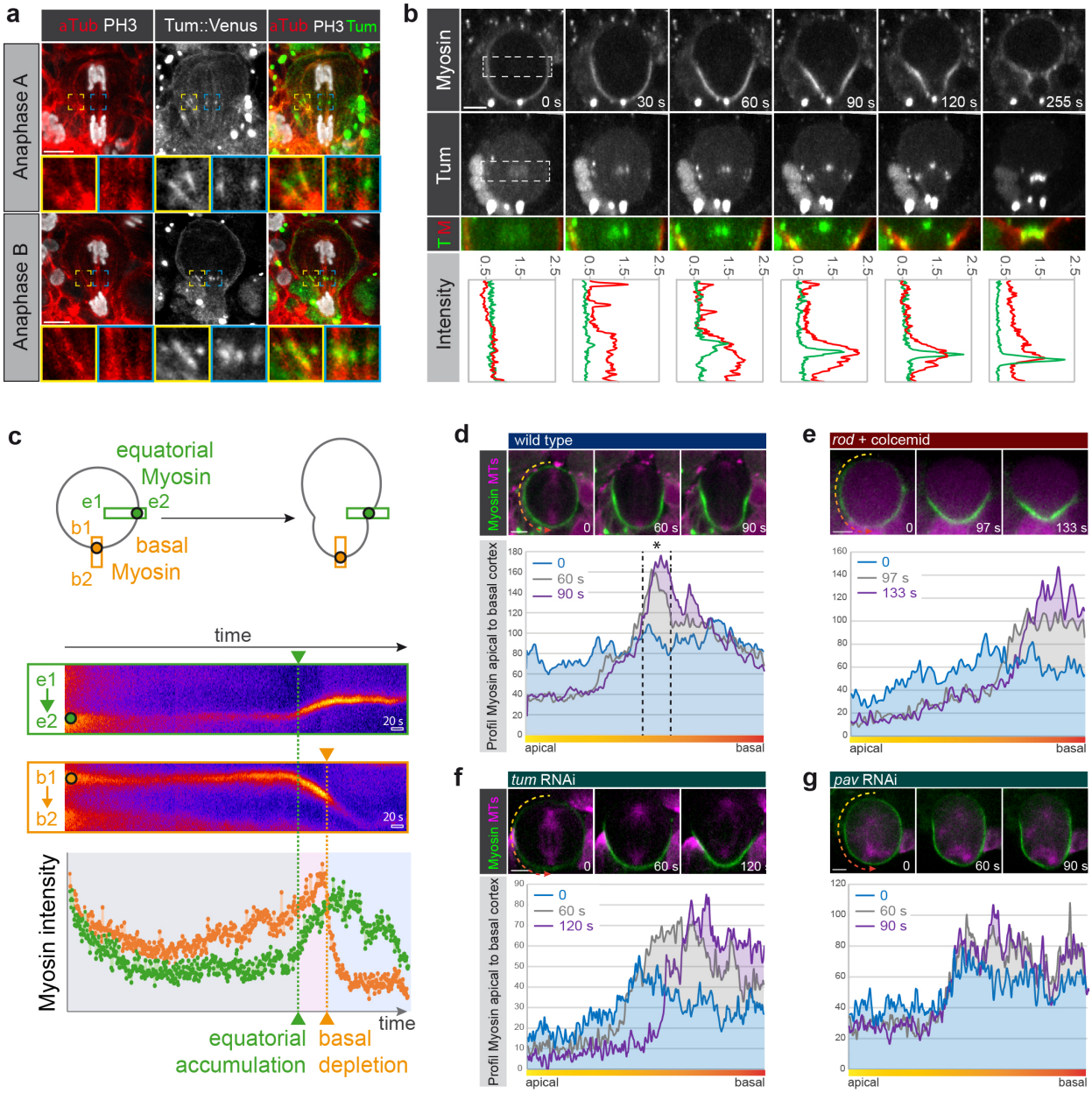
a
aTub PH3
Tum::Venus
aTub PH3 Tum
Anaphase A
Anaphase B
b
Myosin
Tum
TM
Intensity
0 s
30 s
60 s
90 s
120 s
255 s
c
equatorial
Myosin
e1
e2
b1
basal
Myosin
b2
time
e1
e2
20 s
b1
b2
20 s
Myosin intensity
time
equatorial
accumulation
basal
depletion
d
wild type
Myosin MTs
0
60 s
90 s
Profil Myosin apical to basal cortex
0
60 s
90 s
apical
basal
e
rod + colcemid
0
97 s
133 s
0
97 s
133 s
apical
basal
f
tum RNAi
Myosin MTs
0
60 s
120 s
Profil Myosin apical to basal cortex
0
60 s
120 s
apical
basal
g
pav RNAi
0
60 s
90 s
0
60 s
90 s
apical
basal

Figure 3

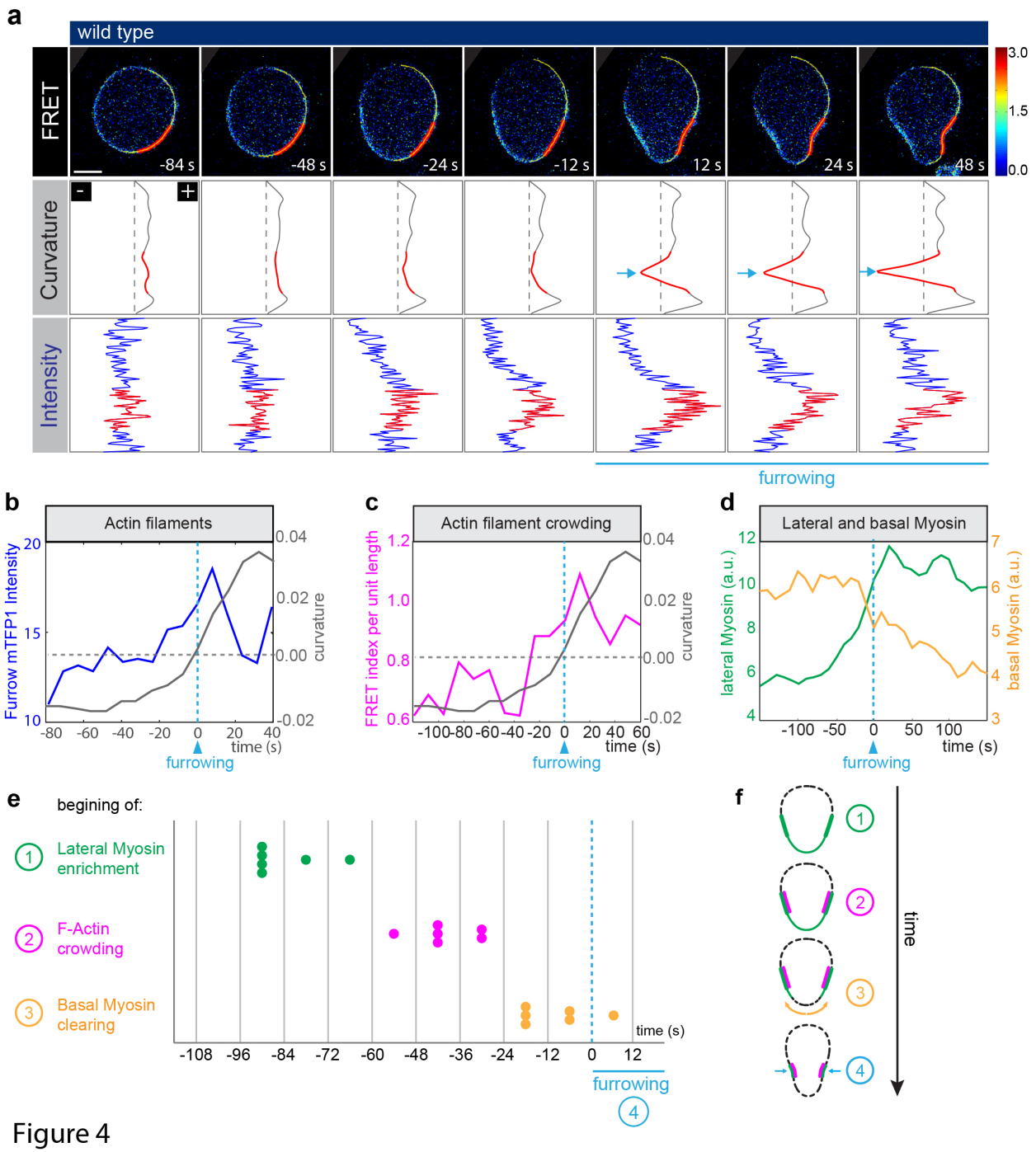
a
wild type
FRET
-84 s
-48 s
-24 s
-12 s
12 s
24 s
48 s
3.0
1.5
0.0
Curvature
Intensity
furrowing
b
Actin filaments
Furrow mTFP1 Intensity
curvature
time (s)
furrowing
c
Actin filament crowding
FRET index per unit length
curvature
time (s)
furrowing
d
Lateral and basal Myosin
lateral Myosin (a.u.)
basal Myosin (a.u.)
time (s)
furrowing
e
begining of:
1 Lateral Myosin enrichment
2 F-Actin crowding
3 Basal Myosin clearing
time (s)
furrowing
4
f
time

Figure 4

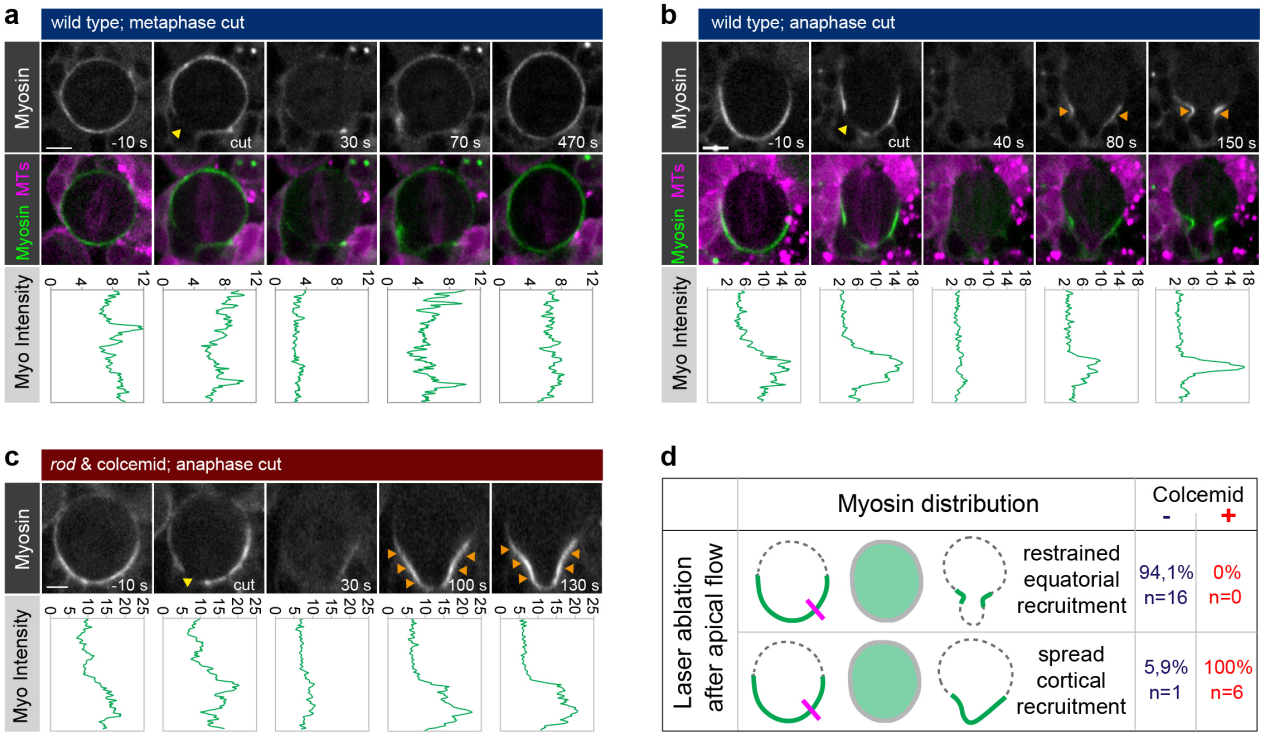
a
wild type; metaphase cut
Myosin
Myosin MTs
Myo Intensity
-10 s
cut
30 s
70 s
470 s
b
wild type; anaphase cut
-10 s
cut
40 s
80 s
150 s
c
rod & colcemid; anaphase cut
-10 s
cut
30 s
100 s
130 s
d
Myosin distribution
Colcemid
-
+
Laser ablation after apical flow
restrained equatorial recruitment
94,1% n=16
0% n=0
spread cortical recruitment
5,9% n=1
100% n=6

Figure 5

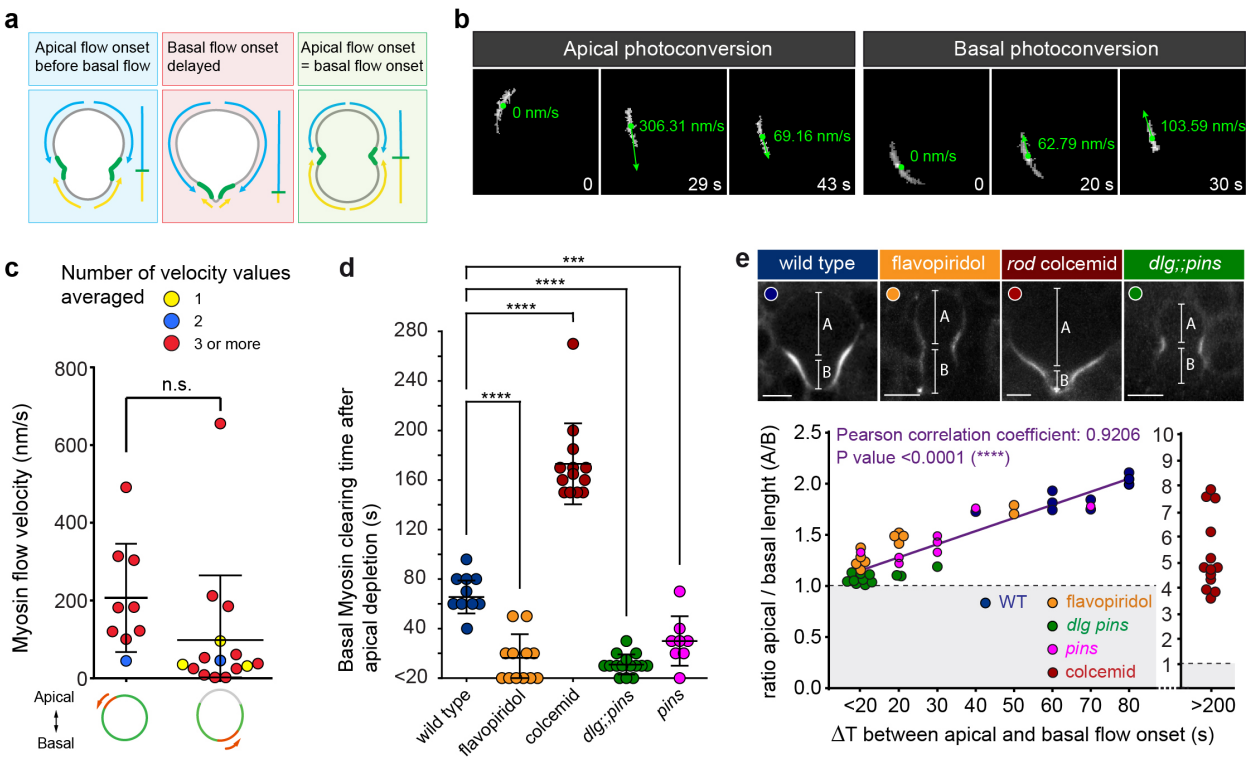
a
Apical flow onset before basal flow
Basal flow onset delayed
Apical flow onset = basal flow onset
b
Apical photoconversion
Basal photoconversion
0 nm/s
0
306.31 nm/s
29 s
69.16 nm/s
43 s
0 nm/s
0
62.79 nm/s
20 s
103.59 nm/s
30 s
c
Number of velocity values averaged
1
2
3 or more
n.s.
Myosin flow velocity (nm/s)
800
600
400
200
0
Apical
Basal
d
Basal Myosin clearing time after apical depletion (s)
280
240
200
160
120
80
40
<20
***
****
****
****
wild type
flavopiridol
colcemid
dlg;;pins
pins
e
wild type
flavopiridol
rod colcemid
dlg;;pins
A
B
Pearson correlation coefficient: 0.9206
P value <0.0001 (****)
ratio apical / basal lenght (A/B)
2.5
2.0
1.5
1.0
0.5
0.0
10
9
8
7
6
5
4
3
2
1
WT
flavopiridol
dlg pins
pins
colcemid
<20
20
30
40
50
60
70
80
>200
ΔT between apical and basal flow onset (s)

Figure 6

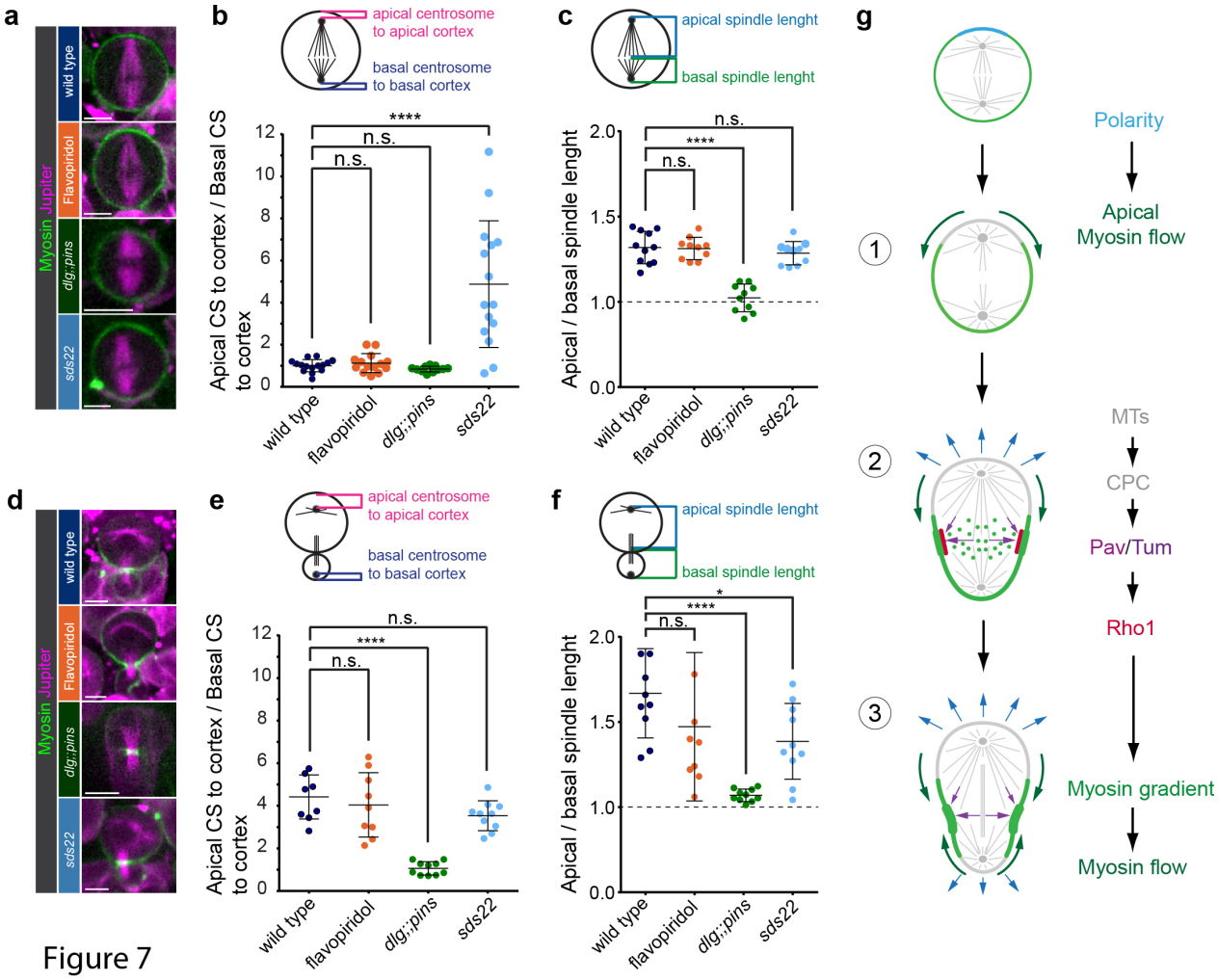
a
Myosin Jupiter
wild type
Flavopiridol
dlg::pins
sds22
b
apical centrosome to apical cortex
basal centrosome to basal cortex
Apical CS to cortex / Basal CS to cortex
****
n.s.
n.s.
wild type
flavopiridol
dlg::pins
sds22
c
apical spindle lenght
basal spindle lenght
Apical / basal spindle lenght
n.s.
****
n.s.
wild type
flavopiridol
dlg::pins
sds22
g
Polarity
Apical Myosin flow
MTs
CPC
Pav/Tum
Rho1
Myosin gradient
Myosin flow
1
2
3
d
Myosin Jupiter
wild type
Flavopiridol
dlg::pins
sds22
e
apical centrosome to apical cortex
basal centrosome to basal cortex
Apical CS to cortex / Basal CS to cortex
n.s.
****
n.s.
wild type
flavopiridol
dlg::pins
sds22
f
apical spindle lenght
basal spindle lenght
Apical / basal spindle lenght
*
****
n.s.
wild type
flavopiridol
dlg::pins
sds22

Figure 7

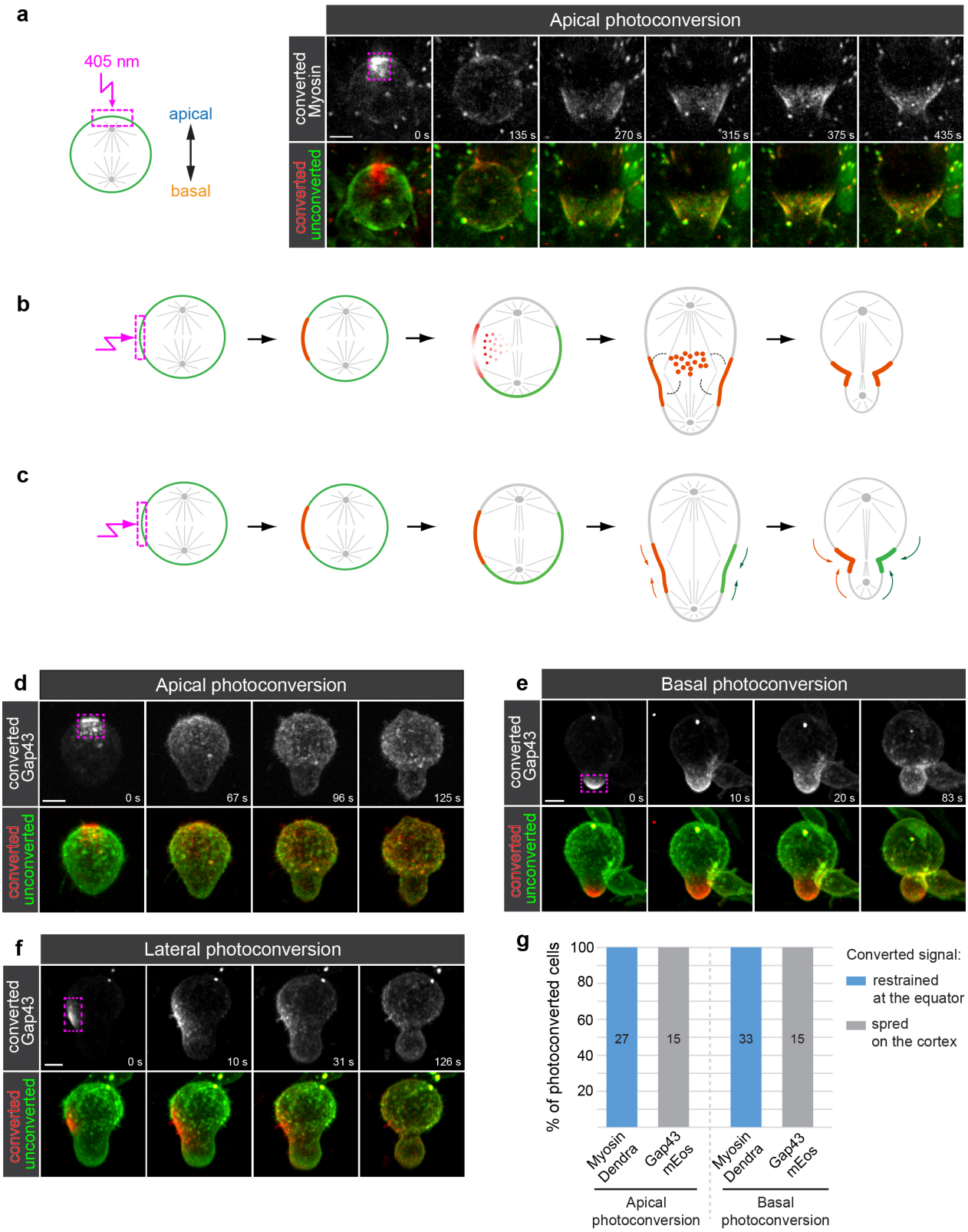

Supplemental Figure 1

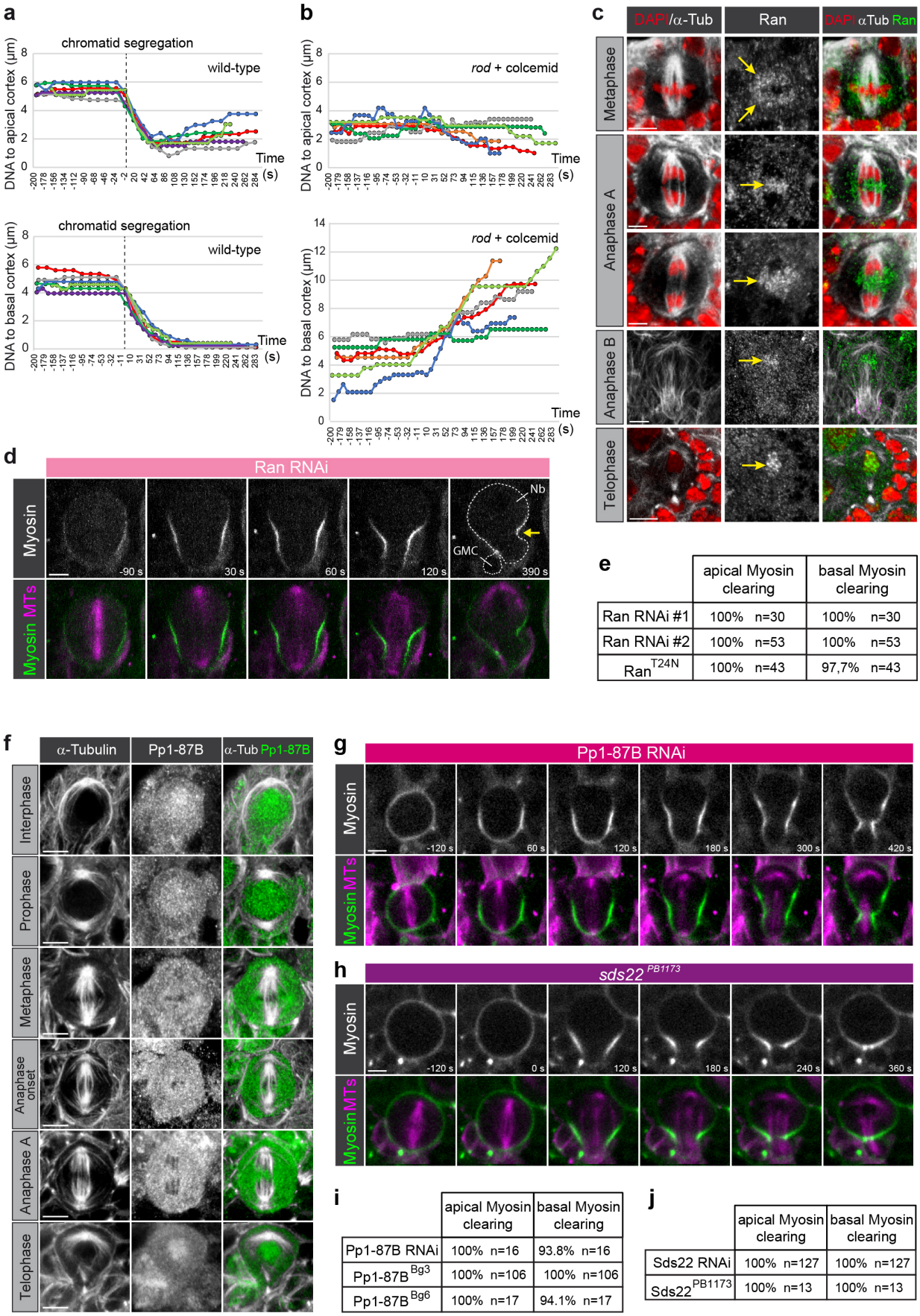

	apical Myosin clearing	basal Myosin clearing
Ran RNAi #1	100% n=30	100% n=30
Ran RNAi #2	100% n=53	100% n=53
Ran^{T24N}	100% n=43	97,7% n=43

i

	apical Myosin clearing	basal Myosin clearing
Pp1-87B RNAi	100% n=16	93.8% n=16
Pp1-87B^{Bg3}	100% n=106	100% n=106
Pp1-87B^{Bg6}	100% n=17	94.1% n=17

j

	apical Myosin clearing	basal Myosin clearing
Sds22 RNAi	100% n=127	100% n=127
Sds22^{PB1173}	100% n=13	100% n=13

Supplemental Figure 2

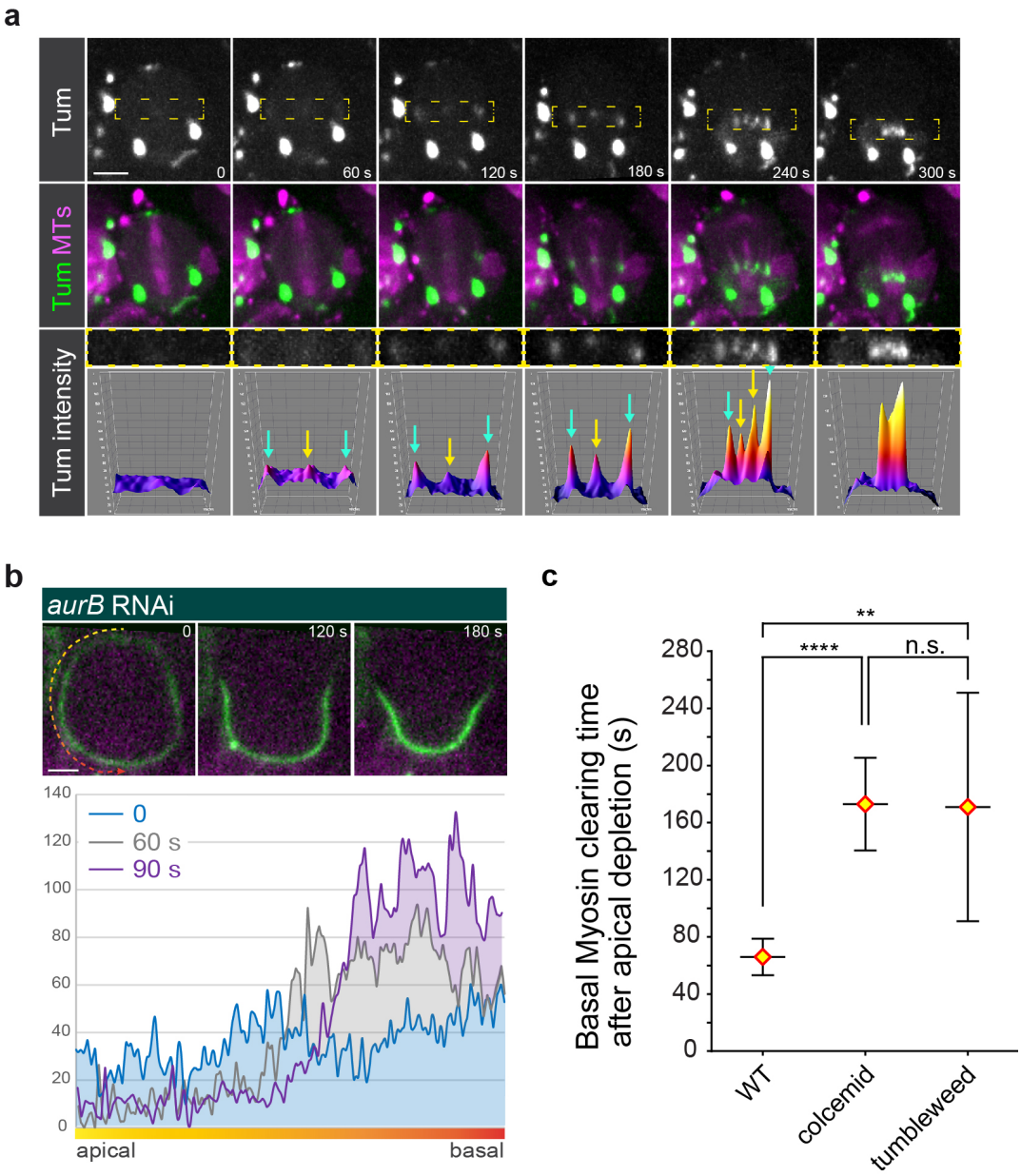

Supplemental Figure 3

a

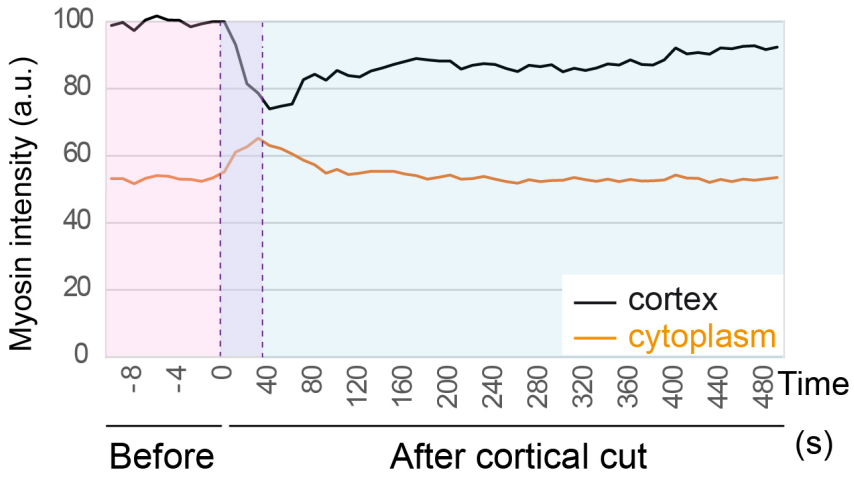

b

Laser ablation		Myosin distribution		Colcemid -	Colcemid +
	before apical flow		Uniform cortical recruitment	78,6% n=22	91,7% n=11
			No cortical recruitment	21,4% n=6	8,3% n=1

Supplemental Figure 4

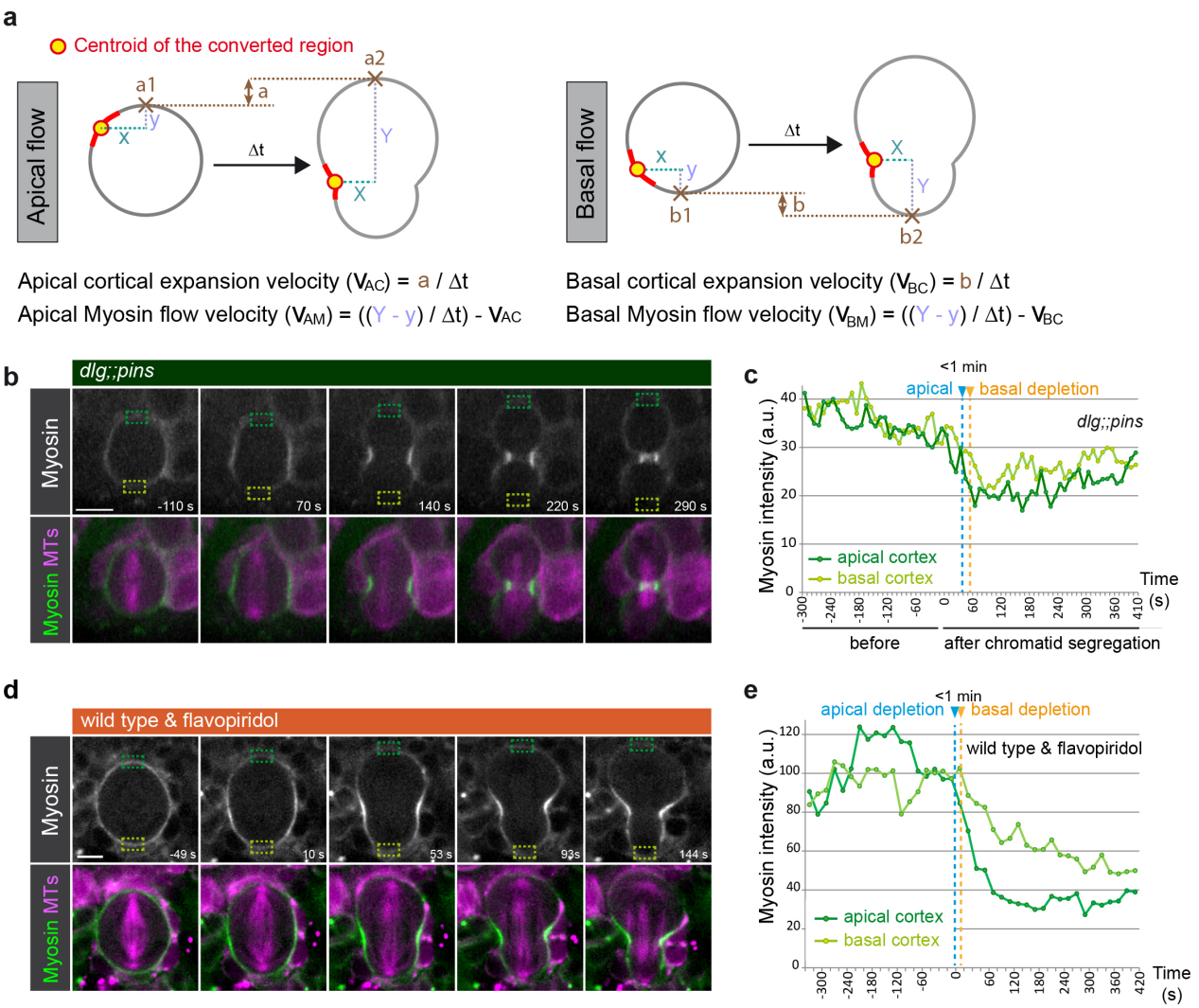

Supplemental Figure 5

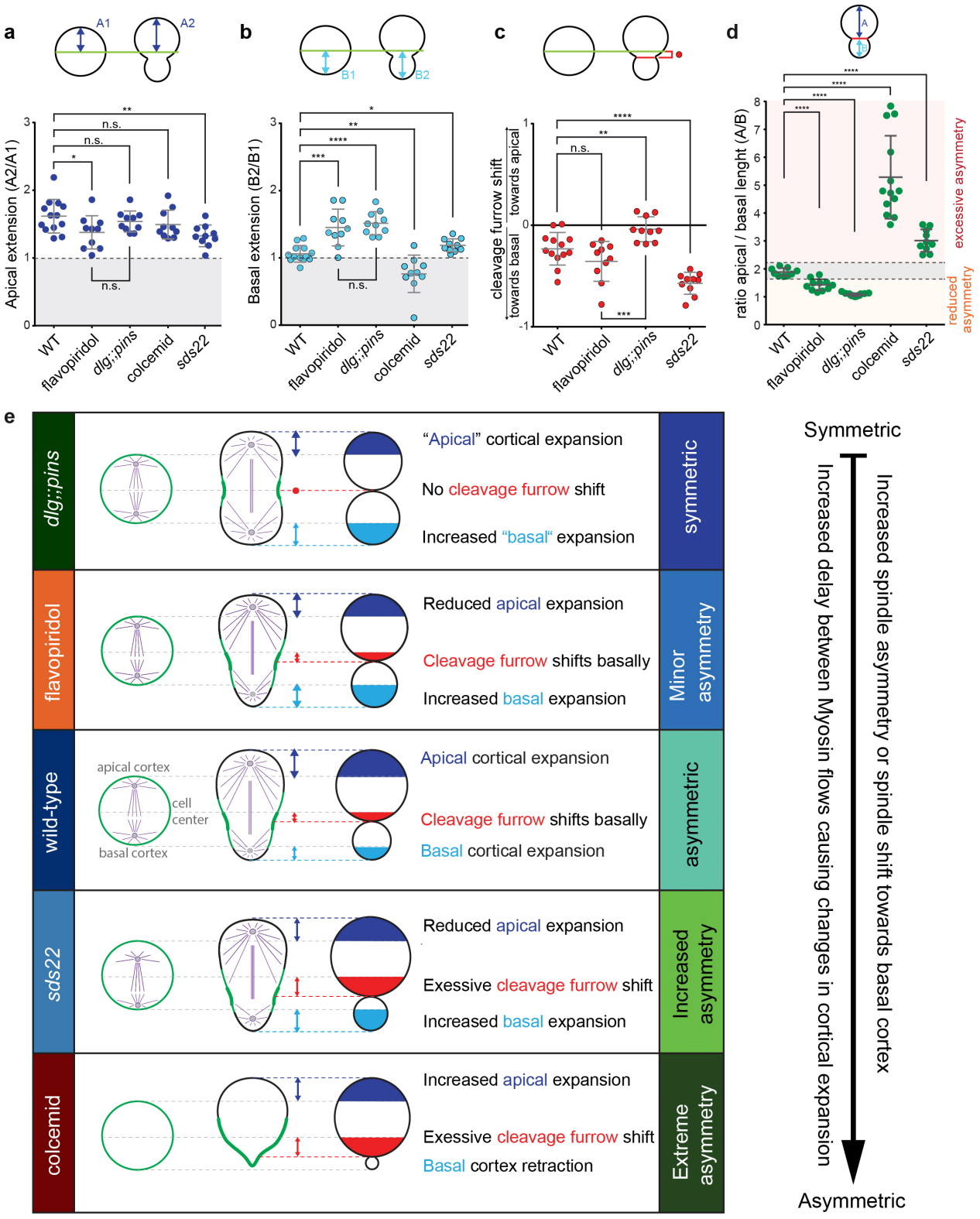

Supplemental Figure 6

II. Spatiotemporal regulation of Myosin activity during ACD

Myosin is activated through phosphorylation at Ser21 and Thr20 within its RLC and to date not much is known about the phosphorylation profile of Myosin during ACD of *Drosophila* neuroblasts. In the second part of the current work we used phospho-specific antibodies in order to understand how activated Myosin is distributed in asymmetrically dividing neuroblasts. Furthermore, we test kinases, which might act as putative Myosin regulators specifically at the apical cortex triggering the polarity-dependent asymmetric Myosin clearing during early anaphase and thus basally shifted cleavage furrow positioning.

1. Manuscript II: Cell cycle and polarity cues regulate biased Myosin activity and dynamics via Drosophila Rho kinase/Drok and Protein Kinase N/Pkn during asymmetric cell division

In the following Manuscript II ("Cell cycle and polarity cues regulate biased Myosin activity and dynamics via Drosophila Rho kinase/Drok and Protein Kinase N/Pkn during asymmetric cell division") we show that Myosin activity plays a key role in the asymmetrically dividing neuroblasts for establishment of cortical stability, cell shape and correct cleavage furrow positioning. The activation profile of Myosin during ACD is tightly controlled through two kinases; Drok and PKN. Initially, Drok responds to cell cycle and polarity cues to recruit Myosin to the neuroblast cortex and to enrich it apically during early metaphase. Later the polarity component Pins recruits a second kinase to the apical cortex, PKN, which inhibits Drok apically and gradually decreases Myosin's activity there. This leads to apical Myosin depletion and to the induction of an apical-basal cortical flow enriching Myosin at the cleavage furrow.

Cell cycle and polarity cues regulate biased Myosin activity and dynamics via Drosophila Rho kinase/Drok and Protein Kinase N/Pkn during asymmetric cell division

Anna Tsankova[1], Tri Thanh Pham[1], David Salvador Garcia[1], Fabian Otte[1] & Clemens Cabernard [2,#]

[1] Biozentrum, University of Basel
Klingelbergstrasse 50-70
CH-4056 Basel, Switzerland

[2] Department of Biology, University of Washington,
Seattle, WA 98105, USA

[#] Corresponding author: ccabern@uw.edu

Running head: Cleavage furrow positioning during asymmetric cell division

Cell and tissue morphogenesis depends on the correct regulation of Non-muscle Myosin II but how this motor protein is spatiotemporally controlled is incompletely understood. Here, we show that in asymmetrically dividing *Drosophila* neural stem cells both cell cycle and cell intrinsic polarity cues provide spatial and temporal information to regulate biased Myosin activity. Using live cell imaging and a genetically encoded Myosin activity sensor, we found that Drosophila Rho Kinase (Drok) enriches for activated Myosin on the neuroblast cortex prior to nuclear envelope breakdown (NEB). After NEB, the conserved polarity protein Partner of Inscuteable (Pins) sequentially enriches Drok and recruits Protein Kinase N (Pkn) to the apical neuroblast cortex; Drok further increases phospho-Myosin whereas Pkn downregulates it on the apical cortex by inhibiting Drok. We propose that the sequential activity of these kinases is important for unequal cortical expansion, ensuring correct cleavage furrow positioning and the establishment of physical asymmetry.

Introduction

Cell shape changes, instrumental in driving tissue morphogenesis, depend to a large extend on the dynamic behavior of the actomyosin cytoskeleton[1]. The motor protein Non-muscle Myosin II (Myosin hereafter) provides the necessary force to pull Actin filaments together. This intrinsic property is utilized during cell division, enabling cells to undergo dramatic cell shape changes, such as cell rounding, elongation and polar expansion. Furthermore, Myosin dynamics are also instrumental during cytokinesis, the process that ensures the physical separation of both cytoplasmic, cortical and nuclear contents[2]. The site on the cell membrane where an actomyosin-containing contractile ring - necessary for cleavage furrow formation and cytokinesis - will be positioned has to be determined with great precision. In asymmetrically dividing stem cells, cleavage furrow mispositioning can result in defective segregation of cell fate determinants and to changes in cell fate and cell behavior[3,4]. Thus, during cell division both spatial and temporal cues are necessary to correctly regulate Myosin localization and activity in order to prevent tetraploidy, tumor formation and cancer[5]. However, the underlying molecular mechanisms are incompletely understood.

In metazoan cells the positional cues for contractile ring placement and assembly originate from astral microtubules, the central spindle, or both (reviewed in[2,6,7]). Recent findings also implicated spindle-independent furrow positioning pathways in a number of different experimental systems[8-14]. For instance, in asymmetrically dividing fly neural stem cells, called neuroblasts, it has been shown that polarity cues are required for the positioning of the cleavage furrow by regulating the localization of Myosin, a central component of the actomyosin contractile ring[8,9]. *Drosophila* neuroblasts are the precursors of the fly's central nervous system and undergo repeated rounds of physical and molecular asymmetric cell divisions, generating differentiating ganglion mother cells (GMCs) while self-renewing the neuroblast[15]. Neuroblasts are intrinsically polarized, consisting of an apically localized Par complex, instrumental in confining cell fate determinants to the opposite basal cell cortex. Inscuteable connects the apical Par complex with the Pins complex, composed of Partner of Inscuteable (Pins; LGN/AGS3 in vertebrates), Gαi and Mushroom body defects (Mud; NuMA in vertebrates, Lin-5 in *C. elegans*)[15,16]. Shortly after anaphase onset, Myosin relocalizes first from the apical neuroblast cortex, giving rise to an

asymmetric distribution. Subsequently, Myosin clears from the basal cortex and accumulates at the cleavage furrow. This dynamic Myosin redistribution causes unequal cortical expansion, shifting the cleavage furrow towards the basal cortex[9,14]. The spatiotemporal regulation of Myosin activity, a requirement for the establishment of sibling cell size asymmetry, is regulated by neuroblast intrinsic polarity cues. In particular, Pins and Dlg are important for correct Myosin relocalization and subsequent cleavage furrow positioning[8,9,17]. However, how cells integrate both cell cycle and polarity cues to regulate and coordinate actomyosin cytoskeleton dynamics is incompletely understood.

Here we show that the polarity protein Pins is regulating Myosin dynamics and activity through the spatiotemporal regulation of Drosophila Rho Kinase (Drok; Rock1,2 in vertebrates) and Protein Kinase N (Pkn; Pkn1-3 in vertebrates). We find that Drok is required to localize Myosin to the neuroblast cortex before neuroblasts enter mitosis and, in response to Pins, also to enrich it apically in early metaphase. Pkn is recruited to the apical cortex during metaphase through Pins and is required to induce apical Myosin relocalization, necessary for timely apical Myosin clearing, which precedes basal Myosin clearing. Thus, our data is consistent with a model proposing that cell cycle and polarity cues regulate Myosin dynamics and activity through the sequential activation of two distinct kinases.

Pins biases Myosin localization and activity

To learn how polarity cues regulate Myosin localization and activity, we used live cell imaging, measuring the dynamics of Sqh::GFP (*spaghetti squash* encodes for Myosin's regulatory subunit) ([18] & methods) from prophase onwards until telophase. As previously noted, we confirmed that Myosin was enriched on the apical neuroblast cortex prior to apical clearing[19,20]. Using Kymograph analysis (see methods) we determined that this apical enrichment started immediately before and peaked shortly after NEB (Figure 1a-c). Apical Myosin enrichment at NEB was significantly reduced in symmetrically dividing *pins* mutants (Figure 1d-f, k). Similarly, neuroblast specific expression of Gai relocalized Pins uniformly on the neuroblast cortex[21] and prevented biased Myosin enrichment; Myosin peaked everywhere on the neuroblast cortex at NEB (Figure 1g-i). We quantified peak Myosin intensity at or after NEB on the apical cortex, basal cortex and cytoplasm in wild type, *pins* mutant and Gai expressing

neuroblasts. Interestingly, Myosin levels in *pins* mutants were comparable to basal cortical levels in wild type neuroblasts but Gαi expressing neuroblasts showed slightly higher cortical Myosin than basal cortical wild type Myosin levels (Figure 1j). Finally, we found that *pins* mutant and Gαi expressing neuroblasts significantly reduced asymmetrically localized Myosin (Figure 1k).

Myosin's activity is regulated through phosphorylation and dephosphorylation[22], prompting us to investigate how phosphorylated Myosin is distributed in mitotic neuroblasts. Using Sqh-1P, an antibody specifically recognizing the monophosphorylated form of Myosin's regulatory light chain (recognizing phospho-Ser21 in Sqh)[23], we found that wild type neuroblasts show transient apical enrichment of activated Myosin in early metaphase. This apical enrichment was gone in early metaphase *pins* mutant neuroblasts (Figure 1l,m & Supplemental Figure 1a,b). These data show that polarity cues are required to increase activated Myosin on the apical neuroblast cortex.

Pins is necessary for apical Pkn localization

To identify a kinase that could provide a spatiotemporal link between neuroblast intrinsic polarity and Myosin, we performed a candidate screen and identified Pkn as a potential regulator of biased Myosin phosphorylation. Using a protein trap line (see methods), containing a GFP cassette inserted in-frame with *pkn's* coding region[24], we performed live cell imaging to determine its localization dynamics. In interphase neuroblasts, Pkn::GFP was predominantly localized in the cytoplasm. During prophase, Pkn::GFP was weakly associated with the apical cortex. Apical localization increased after NEB and peaked during metaphase. Subsequently, Pkn disappeared from the apical cortex and relocalized to the cleavage furrow (Figure 2a & Supplement Figure 2a). We confirmed Pkn's localization with two independent protein trap lines (data not shown). The start of Pkn's apical localization coincided with apical Myosin enrichment. However, apical Pkn reached peak levels in late metaphase, whereas apical Myosin enrichment is highest just after NEB (Figure 2b-d). Pkn and Pins also colocalized on the apical neuroblast cortex from prometaphase until early anaphase. Pins then spread on the apical cortex during anaphase whereas Pkn relocalized to the cleavage furrow (Figure 2a, Supplemental Figure 2a and data not shown).

Pkn's apical localization is independent of the spindle-dependent pathway; chemical spindle ablation experiments using colcemid and spindle rotation experiments using *mud* mutants[25-27] – both conditions retain normal apical – basal polarity - did not alter the apical localization of Pkn (Supplemental Figure 2b,c). However, apical Pkn localization is compromised in *pins* mutants; Pkn is weakly retained on the cortex, resembling non-apical cortical Pkn levels in wild type. Furthermore, uniform cortical localization of Pins using forced expression of Gαi[21] also enriched Pkn uniformly on the cortex with no apical bias (Figure 2e-g). We conclude that Pins is necessary for apical Pkn localization but not required for its localization to the cleavage furrow.

Pkn is required for spatiotemporal correct Myosin phosphorylation and localization

Pkn has been implicated in actomyosin dependent processes such as dorsal closure during embryogenesis or nurse cell dumping[28,29]. We used the previously isolated loss of function allele *pkn*^{06736}[,30] to assay whether Pkn is required for Myosin activity and dynamics during asymmetric neuroblast division (see methods and legends for exact genotype). We stained larval brains, expressing Sqh::GFP with the cell cycle marker DAPI and Sqh1P[23] antibody to investigate the localization of phosphorylated and thus activated Myosin. *Pkn* mutants retained patches of apical Sqh::GFP at comparable levels to wild type neuroblasts. However, Sqh::GFP was significantly reduced on the basal or lateral cortex (Figure 3a,b). Similarly, monophosphorylated Myosin was either restricted to the apical neuroblast cortex or, in 30 % of all *pkn* mutant neuroblasts, significantly reduced from the entire neuroblast cortex. In general, basal and overall cortical Myosin phosphorylation was markedly diminished (Figure 3a-c).

We performed live cell imaging on third instar *pkn* mutant neuroblasts to assay how these changes in Myosin phosphorylation affect Myosin dynamics. Prior to NEB, Myosin was mostly localized uniformly around the neuroblast cortex (Figure 3d; timepoint -2:56) but diminished on the basal and lateral neuroblast cortex after NEB and until late metaphase; apical Myosin was retained on the apical cortex (Figure 3d). In contrast to wild type cells, apical Myosin enrichment was shifted towards anaphase onset and significantly prolonged in *pkn* mutant neuroblasts (Figure 3e-h).

We also observed characteristic changes in neuroblast shape; whereas wild type neuroblasts expanded the apical cortex, *pkn* mutants showed an expanding basal cortex first (Figure 3d; timepoint 8:22). Subsequently, the basal cortex retracted and the apical cortex enlarged, causing a temporarily inverted asymmetric, followed by a symmetric, and then normal asymmetric anaphase figure (Figure 3d; time point 8:22, 9:58 and 12:19). These changes in cortical domain size were accompanied by Myosin accumulations at cortical ingression sites, shifting basally during anaphase (see also below). The same defects were observed with the independent pkn^{3} allele[31] (data not shown). We conclude that Pkn is required for the correct spatiotemporal phosphorylation of Myosin, necessary for its timely relocalization from the apical neuroblast cortex to ensure normal physical asymmetric cell division.

Drok is necessary for cortical Myosin localization and Pins-mediated apical enrichment

The conserved Ser-21 residue (Ser-19 in vertebrates) in Sqh is the primary target for Drok[32], prompting us to test whether Pkn could affect Myosin phosphorylation through Drok. We first analyzed Drok localization and found it to be almost identical to Myosin; unlike Pkn, Drok was already robustly localized at the neuroblast cortex in prophase and prometaphase. Shortly after NEB, Drok showed a brief window of apical enrichment, followed by a more uniform cortical localization during metaphase and early anaphase (Figure 4a). Kymograph analysis revealed that the timing and duration of Drok's apical enrichment coincided with apical Myosin enrichment but differed significantly from Pkn; the peak of apically localized Drok occurred significantly earlier and was shorter compared to Pkn (Figure 4b-d). Thus, Drok's spatiotemporal localization pattern is very similar to Myosin in wild type neuroblasts and we assayed whether Drok's apical enrichment is also dependent on Pins. Indeed, in neuroblasts with uniform cortical Pins (*UAS-Gαi*), Drok was localized mostly uniform cortical with no apical bias (Figure 4e,f).

Drok is required to recruit Myosin to the neuroblast cortex before and after NEB since in *drok* mutants, cortical Myosin levels were significantly reduced[20] (Figure 5a-c). However, in late metaphase *pkn* mutants Drok levels were enriched on the apical cortex but significantly decreased at the lateral and basal cortex. During anaphase, Drok was associated with the shifting cleavage furrow similar to Myosin (Figure 5d,e). This data suggests that in *pkn* mutants phospho-Myosin is retained on the apical cortex due

to a lack of Drok relocalization, causing aberrant cell shape changes. Taken together, we conclude that Drok is required for cortical Myosin localization before NEB independently of Pins but at and after NEB, Drok induces apical Myosin enrichment in a Pins-dependent manner. Furthermore, compromising Drok downregulation from the apical neuroblast cortex perturbs timely apical cortical expansion and physical asymmetry.

Apically mislocalized Myosin causes ectopic contractions and cell shape changes

We next investigated the consequences of misregulated Myosin activity and dynamics during mitosis in more detail. Actomyosin contraction is causing cells to round up early in mitosis[33,34]. We reasoned that compromised Myosin activity could affect cell rounding and cell shape before anaphase onset already. To test this hypothesis, we first measured the curvature of the apical neuroblast cortex in wild type and *pkn* mutant neuroblasts in metaphase (see methods). Wild type neuroblasts showed very little changes in curvature during metaphase (Figure 6a,b,d). *Pkn* mutants, however, displayed both negative and positive changes in curvature, indicating that the apical cortex is subject to significant deformations (Figure 6c,d). Since these apical deformations could induce the aforementioned inversion in cortical expansion (see Figure 3d) we also measured cell curvature along the apical-basal neuroblast cortex from early anaphase until telophase (Figure 6e). Wild type neuroblasts showed a cortical ingression (manifested in negative curvature) in early anaphase in a basally shifted position. This ingression developed into a pronounced cleavage furrow; it mostly remained at the same location but increased during anaphase (Figure 6f,h). *Pkn* mutant neuroblasts showed furrowing closer to the apical side and these furrows shifted basally (Figure 6g,h). We conclude that Myosin misregulation compromises cell rounding and cleavage furrow positioning.

Cortical deformations in *pkn* mutants are due to Myosin contractions on the apical neuroblast cortex

To better understand how Myosin activity influences cell shape and furrow positioning, we developed a genetically encoded live sensor that monitors Myosin activity. Myosin can bind to and pull Actin filaments together based on its inherent motor activity[35]. Taking advantage of this property, we

constructed a Myosin activity sensor by adding two Vinculin domains that bind filamentous Actin (F-Actin) and a FRET module, separated by a flexible spider silk protein[36]. If Actin filaments are pulled together due to Myosin motor activity the sensor will respond with high FRET signals (Supplemental Figure 3a,b). We expressed this sensor in larval neuroblasts and reliably found high FRET signals on the apical neuroblast cortex in early metaphase. High apical Myosin activity is in agreement with the observed enrichment of Sqh::GFP and phospho-Myosin on the apical neuroblast cortex. Subsequently, FRET signals were high at the ingressing cleavage furrow (Figure 7a and Supplemental Figure 3e,f). A control sensor containing only one F-Actin binding domain (Supplemental Figure 3c,d) or neuroblasts expressing the Myosin activity sensor and treated with the Rok inhibitor Y27632 showed a significant reduction in apical and cleavage furrow FRET signals (Supplemental figure 3g,h). Having shown that this sensor reliably monitors Myosin activity, we used it to test whether cortical deformations in *pkn* mutants were due to local constrictions. In this case, we would expect high FRET ratios whenever cortical deformations occur. Indeed, in *pkn* mutants, we found high FRET signals associated with apical ingressions before anaphase onset. These contractions relaxed and shifted further basally during anaphase. Furthermore, other regions on the neuroblast cortex in *pkn* mutants showed dramatically reduced FRET signals compared to wild type neuroblasts (Figure 7a,b). These results suggest that *pkn* mutant neuroblasts contain an inherently weak cortex, but apical accumulation of activated Myosin is causing ectopic cortical contractions and pseudo cleavage furrows. In wild type neuroblasts, apical Myosin activity is also higher compared to other cortical regions but since the entire cortex is under active tension, this elevated Myosin activity is too weak to cause furrowing on the apical neuroblast cortex because lateral and basal Myosin is counteracting this apical pulling force.

Biased Myosin activity influences furrow positioning and physical asymmetry

To directly test the influence of local and enhanced Myosin activity on cell shape and furrow positioning, we tethered a constitutively active version of Myosin's regulatory subunit (SqhEE) either to the apical or basal neuroblast cortex using Inscuteable's apical localization domain (ALD[37]; Figure 8a) and Staufen's basal localization domain (BLD[38]; Figure 8c), respectively. ALD-SqhEE::mCherry and BLD-

SqhEE::GFP were expressed with the neuroblast specific WorGal4 driver and the cortical behavior was subsequently monitored from early anaphase until telophase (see methods). Forcing constitutively activated Sqh to the apical neuroblast cortex caused a phenotype similar to *pkn* mutants, albeit weaker; furrowing was initiated closer to the apical cortex than in wild type and shifted basally (Figure 8b). Tethering constitutively active Myosin on the basal neuroblast cortex caused the opposite phenotype: furrowing initiated closer to the basal cortex and then shifted apically (Figure 8d). In both instances, the final cleavage furrow was mildly misplaced in comparison to wild type neuroblasts (Figure 8g). We further manipulated Myosin activity by compromising Myosin light chain phosphatase (MLCP), using a mutant allele of *myosin binding subunit* (*mbs; mbs^{3}/Def*); Mbs targets MLCP to its substrates and removal of this subunit has been shown to increase Myosin phosphorylation in imaginal discs[39,40]. Interestingly, *mbs* mutant neuroblasts showed a mix of the aforementioned BLD-SqhEE and ALD-SqhEE phenotype; similar to BLD::SqhEE, furrowing initiated in extreme basal positions. However, these furrows shifted apically, extending past the normal wild type furrow position, causing a slight reduction in physical asymmetric cell divisions (Figure 8e-g). Thus, changing Myosin activity locally or globally can reposition the cleavage furrow and compromise physical asymmetric cell division. However, backup mechanisms, most likely dependent on spindle geometry (Roubinet et al., submitted), can correct final furrow positioning.

Polarity proteins dynamically respond to changes in cortical domain sizes

Biasing Myosin activity to either the apical or basal cell pole provides an opportunity to assay how asymmetrically localized polarity proteins respond to changes in cortical domain size. To this end, we assayed how changes in Myosin dynamics - due to loss of Pkn - affect neuroblast polarization and the segregation of cell fate determinants. *Pkn* mutants showed normal apical-basal polarity since Pins, aPKC and Miranda were correctly localized at metaphase (Figure 8h and data not shown). However, 2/3's (n = 17) of *pkn* mutant neuroblasts showed defects in cortical domain size during anaphase and early telophase; either both cortices were equal in size or the basal cortex was dramatically enlarged at the expense of the apical domain, causing an inversion of cell polarity (Figure 8h,i). Interestingly, we have not observed any spilling of polarity proteins into the adjacent domain, suggesting that polarity proteins

anchored to the membrane or cell cortex dynamically respond to the changes in cortical domain size. Indeed, live cell imaging with Pins::EGFP, tagging Pins endogenously (see methods), confirmed that in contrast to wild type neuroblasts, the apical polarity domain in *pkn* mutants first shrunk at the expense of the basal domain before it expanded as in wild type anaphase neuroblasts (Supplemental Figure 4a,b). These data show that inverted polarity is a transient phenotype, suggesting the presence of spindle-dependent backup mechanisms (see above and Roubinet et al., submitted), allowing cortical domains to revert back to wild type sizes. Taken together, we conclude that polarity boundaries and polarity domain size is determined by Myosin activity and local Myosin contractions.

Discussion

Here, we have shown that in asymmetrically dividing fly neural stem cells, the protein kinases Drok and Pkn respond to cell cycle and polarity cues to regulate Myosin activity and dynamics in a stereotypic spatiotemporal manner. The sequential regulation mediated by these two kinases is necessary to control actomyosin dynamics, triggering stereotypic cell shape changes at various steps in the neuroblast cell cycle; first to induce cell rounding as neuroblasts enter mitosis, to permit cell elongation and unequal cortical expansion during anaphase and finally to complete cytokinesis and the establishment of physical asymmetry.

Myosin recruitment before NEB is mediated by Drok. This kinase, implicated in Myosin phosphorylation[22], is already localized at the neuroblast cortex before NEB and in *rok* mutants, Myosin remains cytoplasmic (Supplemental Figure 5a,b). At NEB both Drok and Myosin enrich on the apical neuroblast cortex. This apical enrichment - but not cortical localization - depends on the polarity protein Pins since in *pins* mutants only apical Drok and Myosin enrichment is lost. Based on these data, we propose that Drok responds to cell cycle cues, presumably through the small GTPase Rho1[41], to phosphorylate Myosin's regulatory subunit, enabling activated Myosin to engage with F-Actin at the cell cortex. Subsequently, polarity cues enhance Drok on the apical cortex, resulting in the elevation of phosphorylated and thus activated Myosin on the apical neuroblast cortex.

With Pkn we have identified a second kinase, responding to polarity cues since its apical localization, starting at NEB and peaking by the end of metaphase, is dependent on Pins. Pkn is not absolutely necessary for cortical Myosin enrichment; *pkn* mutant neuroblasts still retain apical Myosin, although elsewhere on the cortex its localization is dramatically reduced. However, Pkn is required for Myosin's timely relocalization from the apical cortex. Wild type neuroblasts clear Myosin from the apical cortex in early anaphase, creating an asymmetric distribution that is necessary for the unequal cortical expansion[9]. In *pkn* mutants, however, both Drok and Myosin dynamics are changed, retaining both on the apical neuroblast cortex, causing aberrant cortical constrictions and concomitantly inverted polar expansion (Supplemental Figure 5c).

Based on these results, we propose the following model: (1) Myosin accumulates at the neuroblast cortex through Drok before NEB. (2) Shortly before and after NEB, apically localized Pins induces apical Myosin enrichment and activity through Drok. (3) Pins also induces the apical enrichment of Pkn, which is necessary for the timely relocalization of Myosin from the apical neuroblast during metaphase. We further propose that Pkn is downregulating Myosin activity through inhibiting and or downregulating apical Drok activity (Figure 8j). Whether Pkn downregulates Drok activity by direct phosphorylation remains an attractive hypothesis, since vertebrate Rock2 has recently been identified as a Pkn target[42].

This sequential regulation of Myosin dynamics seems to be a key regulatory mechanism underlying physical asymmetric cell divisions. For instance, apical Myosin relocalization always precedes basal Myosin clearing in wild type neuroblasts[9,17,43]. We hypothesize that polarity cues provide a cell intrinsic timer, priming Myosin relocalization on the apical cortex, thereby ensuring the generation of physical asymmetry through unequal cortical extension. Consistent with this model is the finding that *pins* mutants, or uniform cortical localization of Pins, cause Myosin to clear from both poles at the same time and divide symmetrically by size[8,9,17].

Tissue and organ growth critically depends on the correct spatiotemporal regulation of cell division. Here, we provide a conceptual framework of how Drok and Pkn respond to both cell cycle and polarity cues, ensuring correct physical asymmetric cell division, necessary for stem cell homeostasis and

cell differentiation[3]. Drok and Pkn play important roles during vertebrate development and morphogenesis[44-46], and it will be interesting to see how spatiotemporal cues, affecting local cell shape changes, are coordinated with overall tissue morphogenesis in flies and beyond.

Figure legends

Figure 1: Biased Myosin localization is dependent on Pins.

Representative image sequence of a (a) wild type third instar neuroblast expressing Sqh::GFP (Myosin; green in overlay) and Cherry::Jupiter (Microtubules (MTs); white overlay) in (top row), (d) *pins*$^{P89/}$*pins*^{P62} (middle row) and (g) *UAS-G*α*i* (bottom row), respectively. Representative kymographs from (b) wild type, (e) *pins*$^{P89/}$*pins*^{P62} and (h) *UAS-G*α*i* expressing neuroblasts, derived from a line along the apical to basal cortex. Arrowheads highlight the apical (blue in *wild type*, grey in the symmetrically dividing cells) and the basal (red in *wild type*, grey in symmetrically dividing cells) cortex, respectively. The vertical dashed lines refer to the Nuclear Envelope Break (NEB) and Anaphase Onset (AO), respectively. (c), (f) and (i) Intensity plots measured along the apical and basal cortex from the respective kymographs. The values were normalized over the global maximal intensity. (j) Normalized cortical Sqh intensities are plotted for the indicated genotypes (blue; apical. red; basal. grey; apical or basal since polarity is lost). (k) The difference between the apical and basal normalized intensity, at the averaged time of the peak, for each cell is plotted as an asymmetry coefficient. (l) Representative wild type metaphase and *pins*$^{P89/}$*pins*^{P62} neuroblasts stained against monophosphorylated Myosin (Sqh-1P antibody) and the cell cycle marker DAPI. (m) Ratio of apical/basal Sqh-1P intensity for *wild type* and *pins*$^{P89/}$*pins*^{P62}. For this and all subsequent figures, asterisk denote statistical significance, derived from two-sample equal or unequal variance t-test: *; $p < 0.05$, **; $p < 0.005$, ***; $p < 0.0005$. ns; not significant.

Scale bar 5: μm; time in min:sec; NEB; nuclear envelope breakdown (= 0:00), MTs; microtubules.

Figure 2: Asymmetric Pkn localization depends on Pins

(a) Representative image sequence of a third instar wild type neuroblast, expressing Pkn::GFP (top row) and Sqh::Cherry (bottom row). (b) Kymographs along a line from the apical to the basal cortex. Red and blue arrowheads indicate the apical cortex of Pkn and Sqh respectively. (c) Representative Intensity plot along the apical cortex, showing Pkn (red) and Sqh (blue). The time between NEB and the apical Pkn and Sqh peak was measured and plotted in (d). (e) Representative neuroblast metaphase and anaphase

images, showing Pkn::GFP localization in wild type (blue), *pins*$^{P89/}$*pins*^{P62} (magenta) and *UAS-Gαi* (orange). (f) Scatter plot showing apical/basal cortical Pkn::GFP intensity ratios at metaphase for the indicated genotypes. (g) Scatter plot showing the cortical enrichment of Pkn::GFP on the non-apical cortex, in relation to cytoplasmic Pkn::GFP (ratio).

Scale bar 5: μm; time in min:sec; NEB; nuclear envelope breakdown (= 0:00).

Figure 3: Pkn is required for the correct spatiotemporal localization and phosphorylation of Myosin

(a) Representative images of prometaphase and metaphase wild type and *pkn*^{06736}*/Def* neuroblasts expressing Sqh::GFP and stained against monophosphorylated Myosin (Sqh-1P antibody) and DAPI. Sqh::GFP (b) and Sqh-1P (c) intensities were measured at the apical (green), basal (blue) and whole cortex (red) for wild type and *pkn*^{06736}*/Def* mutant neuroblasts. (d) Representative image sequence of a *pkn*^{06736}*/Def* mutant neuroblast expressing Sqh::GFP (single channel; white. merged channel; green) and Cherry::Jupiter (MTs, merged channel; white). (e) Kymograph along a line from the apical towards the basal cortex of a *pkn*^{06736}*/Def* mutant neuroblast. The apical and basal cortices are highlighted with a blue and red arrowhead, respectively. (f) Normalized intensity plot, showing the intensities along the apical (blue) and basal (red) cortex. (g) Scatter plot showing the duration of apical Sqh enrichment in wild type (blue) and *pkn*^{06736}*/Def* (grey) and (h) the temporal delay between apical peak of Sqh in relation to NEB for wild type and *pkn*^{06736}*/Def*.

Scale bar 5: μm; time in min:sec; NEB; nuclear envelope breakdown (= 0:00), MTs; microtubules.

Figure 4: Apical Drok localization depends on polarity cues and precedes Pkn localization

(a) Representative image sequence of a wild type neuroblast expressing Drok::GFP (top; white; merged channel; green) and Cherry::Zeus (white in merged channel). (b) Kymograph along a line from the apical towards the basal cortex. Apical and basal cortices are highlighted with a blue and red arrowhead, respectively. (c) Scatter plot showing the duration of apical Sqh (blue), Pkn (red) and Drok (green) enrichment in wild type neuroblasts. (d) Scatter plot showing the temporal delay between NEB and the apical peak of Sqh (blue), Pkn (red) and Drok (green) in wild type neuroblasts. The values in (c) and (d) are

normalized to the total time between NEB and AO for each cell. (e) Image sequence showing a neuroblast expressing Drok::GFP (white; top, green; merged channel), Gαi (unmarked) and Cherry::Juptier (white in overlay). Drok::GFP intensity along a line from the apical – basal Nb cortex is shown underneath the individual time points. (f) Scatter plot showing apical (blue) and basal (red) or cortical (grey) Drok::GFP intensity ratios in relation to cytoplasmic Drok::GFP for wild type and UAS-Gαi expressing neuroblasts.
Scale bar 5: μm; time in min:sec; NEB; nuclear envelope breakdown (= 0:00), MTs; microtubules.

Figure 5: Rok is required for cortical Myosin localization.

Representative prometaphase (prometa) and metaphase (meta) images of a (a) wild type and (b) *rok*^{2} mutant neuroblast expressing Sqh::GFP (white in the single channel image and green in the merged channel) and Cherry::Jupiter (MTs; white in the merged channel). (c) The cortical Myosin intensities were normalized to the cytoplasm and plotted for wild type (blue) and *rok*^{2} (green) at prophase and metaphase. (d) Image sequence showing a *pkn*^{06736}*/Def* neuroblast expressing Drok::GFP (white on top, green in the merged channel) and Cherry::Jupiter (white in overlay). (e) Apical (blue) and basal (red) intensity ratios for wild type and *pkn*^{06736}*/Def* mutant neuroblasts, in relation to cytoplasmic Drok levels.
Scale bar 5: μm; time in min:sec, referenced to NEB (nuclear envelope breakdown; 0:00), MTs; microtubules.

Figure 6: Pkn mutant neuroblasts show ectopic contractions and cell shape changes.

(a) Curvature measurements were performed during prometaphase and metaphase on the apical neuroblast cortex. (b) Representative curvature measurement for a wild type and (c) *pkn*^{06736}*/Def* mutant neuroblast. (d) Scatter plot showing the maximal curvature values (h) for wild type (blue) and *pkn*^{06736}*/Def* (beige) mutant neuroblasts. (e) Curvature was measured along the apical – basal neuroblast tip from anaphase until telophase (f) Representative wild type and (g) *pkn*^{06736}*/Def* mutant neuroblast. Colored lines in the curvature plot correspond to the represented time points. (h) Scatter plot showing the maximal distance between the first and final furrow. The cortical position for all curvature measurements was normalized on the respective measured distance.

Scale bar 5 μm; time is in min:sec. NEB; nuclear envelope breakdown (0:00 in (b) and (c)), AO; Anaphase onset (0:00 in (f) and (g)), MTs; microtubules.

Figure 7: Apical cortical constrictions are causing ectopic furrowing

Representative images of a (a) wild type and (b) *pkn*^{06736}*/Def* mutant neuroblast expressing the Myosin activity sensor (Vt-TS-Vt). FRET histograms, showing normalized FRET ratios are shown below the image sequences. FRET ratios were plotted for apical cortex (orange box), furrow or ectopic furrow regions (red box) and basal cortex (magenta).

Figure 8: Biased Myosin activity regulates cleavage furrow positioning.

Constitutively activated Sqh (SqhEE) was localized to the (a) apical or (c) basal neuroblast cortex. (b) Representative image sequence and curvature measurement along the apical – basal cortex for a neuroblast, expressing ALD-SqhEE::mCherry (not shown) and Sqh::GFP (white) or (d) BLD-SqhEE and Sqh::mCherry (white). (e) Curvature measurements were also performed in *mbs*^{3}*/Def* mutant neuroblasts; a representative image sequence and measurement is shown in (f). (g) Scatter plot of final furrow positioning for the indicated genotypes. (h) Representative images of wild type and *pkn*^{06736}*/Def* mutant neuroblasts at anaphase and telophase stained for the polarity protein Pins (red in merged image), Miranda (green in merged image; white in single channel) and Ph3 or DAPI. (i) Quantification of neuroblasts showing normal asymmetric, symmetric or inverted asymmetric anaphase figures. (j) Model. Scale bar 5 μm; time is in min:sec. Time stamps are in relation to anaphase onset (=0:00). ALD; apical localization domain, BLD; basal localization domain, Asym; asymmetric. Sym; symmetric.

Supplemental Figure 1: Myosin phosphorylation profile in wild type neuroblasts

(a) Representative wild type neuroblasts stained with Sqh-1P antibody, (red in overlay; white in single channel), Miranda (Mira; shown in white in the overlay) and PH3 (shown in green in the overlay). (b) Quantification of cortical Sqh-1P levels for metaphase wild type and *pins*$^{P89/}$*pins*^{P62} mutant neuroblasts.

Apical (shown in green), basal (shown in red) and whole cortex (shown in blue) intensities were normalized to the cytoplasm.

Scale bar is 5 μm.

Supplemental Figure 2: Apical Pkn localization is independent of the mitotic spindle

Representative image sequences of a (a) wild type (b), *rod*$^{H4.8}$ and (c) *mud*^{4} mutant neuroblast expressing Pkn::GFP (green in overlay) and Cherry::Zeus (MTs; white in overlay). Note that *rod* mutant neuroblasts treated with colcemid show complete depolymerization of the microtubules. *mud* mutant neuroblasts display spindle orientation defects, uncoupling the mitotic spindle from the apical – basal polarity axis. Scale bar 5 μm. Time is min:sec.

Supplemental Figure 3: Myosin activity sensor monitors active tension

(a) Schematic representation of the Myosin activity sensor, consisting of two Vinculin tail (VT) domains, binding to filamentous Actin and a FRET module, consisting of the FRET donor mTFP, the FRET acceptor Venus and a stretchable spider silk protein (modified from[36]). (b) The Myosin control sensor contains only one Vt domain. (c) The Myosin activity sensor responds with high FRET ratios if F-Actin is pulled together. The control sensor is used to determine baseline FRET signal since it will bind to F-Actin but does not respond to pulling and stretching of F-Actin filaments. (d) Wild type neuroblast expressing Sqh::GFP to show the localization of Myosin at early metaphase and telophase. (e) Wild type neuroblast expressing the Myosin activity sensor. Note that regions of high FRET ratios correlate well with Myosin localization. (f) Wild type neuroblasts expressing either the control sensor or (g) the Myosin activity sensor, treated with the Rok inhibitor Y-27632 show reduced FRET ratios on the apical and furrow region in metaphase and late anaphase, respectively.

Supplemental Figure 4: Apical polarity domain obeys membrane ingression boundaries.

(a) Representative Image sequence of a wild type and (b) *pkn*^{06736}*/Def* mutant neuroblasts expressing Pins::EGFP (green in overlay) and Cherry::Zeus (MTs; white in overlay). Time is in mins:sec. Time stamps are in relation to anaphase onset (=0:00). Scale bar is 5 μm

Supplemental Figure 5: Schematic summary of Myosin dynamics in (a) wild type, (b) *rok* and (c) *pkn* mutant neuroblasts.

Movie legends

Movie 1: Myosin shows a transient apical enrichment prior to apical clearing in wild type neuroblasts

Wild type larval neuroblast expressing Myosin (Sqh::EGFP; white in the single channel movie on the left and green in the merged channel movie on the right) and the microtubule marker Cherry::Jupiter (white in the merged movie on the right). The neuroblast shows a transient apical enrichment of Myosin just as the nuclear envelope breaks down (0:02:47.737). The temporal resolution is 8 s, the time scale is h:mm:ss.ms and the scale bar is 5 μm.

Movie 2: Protein Kinase N (Pkn) and Myosin colocalize at the apical cortex during early metaphase

Wild type larval neuroblast expressing Pkn::GFP (white in the movie on the left) and Myosin (Sqh::mCherry; green in the movie on the right). Pkn becomes enriched on the apical cortex shortly before nuclear envelope breakdown (NEB) and increases during metaphase. The neuroblast shows a short window of apical enrichment for Myosin (from 0:02:29.960 until 0:05:59.904) and a longer persisting apical enrichment for Pkn. The temporal resolution is 30 s, the time scale is h:mm:ss.ms and the scale bar is 5 μm.

Movie 3: Gαi expressing neuroblasts show loss of apical Myosin enrichment.

A representative neuroblast expressing Gαi (*UAS-Gαi*; unmarked), Myosin (Sqh::EGFP; white in the single channel movie on the left and green in the merged channel movie on the right) and the microtubule marker Cherry::Jupiter (white in the merged movie on the right). Note that apical Myosin enrichment just after NEB is no longer visible. Instead, Myosin shows a uniform cortical localization. The temporal resolution is 5 s, the time scale is h:mm:ss.ms and the scale bar is 3 μm.

Movie 4: Pins is necessary for apical Pkn localization.

A representative *pins* mutant neuroblast expressing Pkn::GFP (white in the movie on the left) and Myosin (Sqh::mCherry; white in the movie on the right). The neuroblast shows loss of apical Pkn enrichment and loss of asymmetric Myosin localization during prometaphase. Note that Pkn is still present at the cleavage furrow in anaphase. The temporal resolution is 10 s, the time scale is h:mm:ss.ms and the scale bar is 3 μm.

Movie 5: Mislocalization of Pins compromises apical Pkn localization.

A representative neuroblast expressing Gαi (*UAS-Gαi*; unmarked), Pkn::GFP (white in the movie on the left) and the microtubule marker Cherry::Jupiter (green in the merged movie on the right). The neuroblast shows increased uniform cortical Pkn localization compared to wild type but no biased apical enrichment. The temporal resolution is 10 s, the time scale is h:mm:ss.ms and the scale bar is 3 μm.

Movie 6: Pkn is required for correct spatiotemporal regulation of Myosin dynamics.

A representative *pkn* mutant neuroblast expressing Myosin (Sqh::EGFP; white in the single channel movie on the right) and the microtubule marker Cherry::Jupiter (white in the movie on the left). The neuroblast shows a premature furrow formed on the apical cortex, which is shifting basally. The temporal resolution is 7.5 s, the time scale is h:mm:ss.ms and the scale bar is 5 μm.

Movie 7: Drok localization is similar to Myosin in wild type neuroblasts.

Wild type larval neuroblast expressing Drok::EGFP (white in the single channel movie on the left and green in the merged channel movie on the right) and the microtubule marker Cherry::Jupiter (white in the merged movie on the right). The neuroblast shows a transient apical enrichment of Drok at NEB. The temporal resolution is 10 s.

Movie 8: *pkn* mutants enrich for Drok on the apical neuroblast cortex.

A representative *pkn* mutant neuroblast expressing Drok::EGFP (white in the single channel movie on the left, green in the merged movie on the right) and the microtubule marker Cherry::Jupiter (white in the merged movie on the right). The neuroblast shows enrichment of Drok on the apical cortex. Drok is reduced at the basal and lateral cortex. The temporal resolution is 10 s.

Movie 9: Anchoring activated Myosin on the basal neuroblast cortex pulls the cleavage furrow basally.

Wild type larval neuroblast expressing activated Myosin, trapped on the basal neuroblast cortex (BLD-SqhEE::EGFP; white in the single channel movie on the left and green in the merged channel movie on the right) and the microtubule marker Cherry::Jupiter (white in the merged movie on the right). The forming cleavage furrow is formed too close to the basal cortex but shifts slightly apically during late anaphase. The final furrow is mispositioned. The temporal resolution is 10 s.

Methods

Fly strains and genetics

All mutant chromosomes were balanced over FM7Actin::GFP, CyOactin::GFP or TM6B, Tb. The following alleles and deficiencies were used: *pkn*^{06736} [30], *pkn*^{3} [31], *Df(2R)w73-1* (removes *pkn*; Bloomington stock center), *pins*^{P89,47}, *pins*^{P62,47}, *mud*^{4,48}, *rod*$^{H4.8,49}$, *Df(3L)Exel6127* (removes *mbs*; Bloomington stock center), *mbs*^{3} (Bloomington stock center), *rok*^{2,32}. Mutants were crossed over the corresponding deficiency and analyzed in a heteroallelic combination.

Transgenes and fluorescent markers: *worGal4, UAS-Cherry::Jupiter, Sqh::GFP*[8], *ALD-Sqh*^{EE}*::EGFP* (this work), *BLD-Sqh*^{EE}*::EGFP* (this work), *Pkn::GFP* (CC01654)[24], *ubi–Rok::GFP*[50], *worGal4, UAS-Cherry::Jupiter*[3], *Sqh::mCherry*[51], *worGal4, UAS-cherry::Jupiter; Sqh::EGFP* (this work), UAS-Gαi[47].

The following recombinant chromosomes were generated using standard genetic procedures: Pkn::GFP, worGal4, UAS-Cherry::Jupiter (this work). WorGal4, UAS Cherry::Jupiter, Sqh::EGFP (3rd chromosome; this work), *Df(2R)w73-1*, worGal4, pUAST-Cherry::Jupiter.

Generation of transgenic lines

Sqh^{EE}::mCherry: The coding sequence of the constitutively active form of Sqh (Sqh^{EE}) and the fluorescent protein mCherry were PCR amplified and cloned into the XbaI and NotI restriction sites of the pUAST-attB vector. The mCherry sequence was flanked additionally with two unique restriction sites MluI and KpnI. The construct was injected into pUAST-attP (VK00005 and VK00037). All cloning procedures were performed using the In-Fusion technology (Takara, Clontech).

ALD-Sqh^{EE}::EGFP/Cherry: The coding sequence of *inscuteable's* Apical Localization Domain (ALD)[37], *sqh*^{EE}, EGFP or mCherry were PCR amplified and cloned into the NotI and XbaI restriction sites of the pUAST-attB vector. *ALD-Sqh*^{EE}*::EGFP* was injected into attP (VK00005 and VK00037). *ALD-Sqh*^{EE}*::mCherry* was injected into attP (VK00005).

BLD-Sqh^{EE}::EGFP: The coding sequence of *staufen's* Basal Localization Domain (BLD)[38], *sqh^{EE}* and EGFP were PCR amplified and cloned into the NotI and XbaI restriction sites of the pUAST-attB vector. The construct was injected into attP (VK00005 and VK00037).

Sqh::EGFP: The Sqh coding sequence, together with its 3` UTR, 5` UTR and the EGFP coding sequence were PCR amplified and cloned into the BglII and XbaI sites of the pattB transformation vector using In-Fusion technology (Takara, Clontech). The unique restriction sites AscI and NotI were introduced at the N- and C-terminal end of EGFP, respectively. The construct was injected into attP (VK00033).

Pins::EGFP: CRISPR target sites close to the Pins' C-terminus were selected using http://www.flyrnai.org/crispr2/index.html (for 5' sites) and http://tools.flycrispr.molbio.wisc.edu/targetFinder/ (for 3' sites). A donor plasmid, containing an EGFP::DsRed cassette and 1 kb homology arms to integrate EGFP at the C-terminus of Pins was generated. The template's PAM site was mutated to prevent cutting of the donor construct. The cutting vectors, containing the CRISPR target sites and the donor plasmid were injected into nosCas9 embryos. Survivors were crossed to an appropriate balancer line and the F1 progeny screened for DsRed positives and outcrossed to established stable lines. Integration events were verified by sequencing. Finally, DsRed was removed by crossing to Cre expressing flies (BL851).

Myosin sensor

***pUAST-attP-Vt-TSmod-Vt*:** *Vt* and *TSmod-Vt* fragments were PCR amplified and subcloned into pUAST-attP between EcoR1 (5') and Kpn1 (3') using In-Fusion technology (Takara, Clontech).

***pUAST-attP-TSmod-Vt* (control):** The *TSmod-Vt* fragment was PCR amplified from the *VinTS* cDNA obtained from addgene (Plasmid #26019) and subcloned into pUAST-attP between EcoR1 (5') and Kpn1 (3') using In-Fusion technology (Takara, Clontech). Both constructs were inserted at VK00033.

Antibodies Used

The following primary antibodies were used: mouse anti-Tubulin (Roche, 1:1000), chicken anti-GFP (abcam, 1:500), rabbit anti-aPKC (Santa Cruz Biotechnology, 1:1000), rabbit anti-P-Histone H3 (Santa Cruz Biotechnology 1:1000), rabbit anti-Pins (gift from Fumio Matsuzaki 1:500), DAPI (Sigma 32670, 5 μg/ml), guinea pig anti-Sqh1P (gift from R. Ward, 1:500), rabbit anti-Sqh-1P (Ser19, Cell Signaling, 1:500), rat anti-Miranda (gift from Chris Doe, 1:1000). Secondary antibodies were from Jackson Immuno Laboratory and Molecular Probes.

Immunohistochemistry

Third instar larval brains were dissected in S2 medium (Invitrogen) and fixed for 20 min in 4 % paraformaldehyde in PEM (100 mM PIPES pH 6.9, 1 mM EGTA and 1 mM $MgSO_4$). After fixing, the brains were washed with PBSBT (1X PBS, 0.5 % Triton-X-100 and 1 % BSA) and then blocked in 1X PBSBT, supplemented with 10 mM Glycine for 1 h. The primary antibodies were diluted in 1X PBSBT and the brains were incubated overnight at 4 °C. The brains were washed in 1X PBSBT 3 x 15 min and then incubated with the respective secondary antibodies (diluted in 1X PBSBT) at 4 °C overnight. Next, the brains were washed with 1X PBST (1x PBS, 0.5 % Triton-X-100) 3 x 15 min and were incubated in Vectashield (Vector laboratories) mounting media at 4 °C.

Fixed samples were imaged using an inverted Leica TSC SPE confocal microscope. For representative images a 60X/1.40NA oil immersion objective was used. For 4X scans a z-step size of 0.3 μm and for 1X scans a z-step size of 0.5 μm was used.

Live Cell Imaging

For all live imaging experiments second or third instar larvae were used. The live imaging procedure was performed as described previously[52] with the following minor modifications: S2 Media (Invitrogen) was supplemented with 10 % HyClone Bovine Growth Serum (BGS, Thermo Scientific SH3054102). The larval brains were dissected in the supplemented S2 media and transferred into a μ-slide angiogenesis (ibidi). Live samples were imaged with an Andor revolution spinning disc confocal system, consisting of a

Yokogawa CSU-X1 spinning disk unit and two Andor iXon3 DU-897-BV EMCCD cameras. A 60X/1.4NA oil immersion objective mounted on a Nikon Eclipse Ti microscope was used for most images. Live imaging voxels sizes are 0.22 X 0.22 X 1 μm (60x/1.4NA spinning disc).

UAS-ALD-Sqh^{EE}::Cherry larvae were incubated at 29 °C up to 72 h prior to imaging.

Colcemid treatment: larval brains were incubated during the imaging in the supplemented S2 media with colcemid in a final concentration of 10 μg/ml.

Image Processing and Measurements

Live imaging data was processed using Imaris x64 7.5.4 and ImageJ. Andor IQ2 files were converted into Imaris files using a custom-made Matlab code. Maximal intensity projections were generated in ImageJ. All Kymographs were generated along a 5 pixel wide line from the apical to the basal cortex. The intensity values at the apical and basal cortex, as well as in the cytoplasm were extracted using a custom made Matlab code. For the intensity plots the cytoplasmic values were subtracted from the cortical intensities and then normalized on the maximum value. The cortical enrichment was calculated by averaging 5 time points at the peak and was normalized to the corresponding cytoplasmic intensity value. Peak Myosin intensity was taken as the global maximal value for symmetrically dividing cells.

Pkn::GFP enrichment was calculated as a mean intensity value at one timepoint (60 - 120 s before anaphase onset) using a 2 pixel wide line along the respective cortical area and the values were normalized on the cytoplasmic intensities. The curvature analysis was performed in ImageJ, using a custom made Matlab code.

Fixed imaging data was processed using Imaris 7.5.4 and ImageJ. All intensity measurements were performed along a 2 pixel wide line at the respective cortical area and average values were normalized on the average values along a line in the cytoplasm. Figures were assembled using Adobe Illustrator CS6 and all quantifications were performed in Microsoft Excel.

Primary larval neuroblasts culture procedure

FRET experiments with the Myosin sensor were performed on isolated neuroblasts, derived from primary neuroblast cultures[53]. Wild-type brains expressing the Myosin sensor were dissected in Chan and Gehring's medium and incubated with Collagenase Type I (Sigma) and Papain (Sigma) at 30 °C for 30 min at a final concentration of 1 mg/ml. The brains were gently washed twice with 400 µl of supplemented Schneider's medium and then transferred to a 1.5 ml tube. Neuroblasts were dissociated by repeatedly pipetting the brains with 200 µl of supplemented Schneider's medium until the solution looked homogenous.

Curvature analysis

To determine the curvature along the cell cortex, a line was manually drawn in ImageJ from the apical to the basal cortex on the mid-plane. Cortical curvature *K* was calculated with the following formula: $K = \frac{f''(x)}{(1+f'^2(x))^{3/2}}$, where x and $f(x)$ are the horizontal and vertical position of the drawn cortex, respectively. The first and second derivatives ($f'(x)$ and$f''(x)$) of the curve were calculated numerically using second order difference methods. Custom-written Matlab codes were used to determine curvature values for all points on the curve.

Kymograph quantification

Cell mid-planes were first generated using the Oblique Slicer tool in Imaris (Bitplane) and the entire image volume was then resliced along the direction of this plane for all timepoints. Using ImageJ, a Maximal intensity projection was generated from three selected planes closest to the mid-plane. This procedure was done for all acquired time points. Kymographs were then generated by drawing a five pixel wide straight line from the apical to the basal cortex for all timepoints. To determine cortical intensity signal from a kymograph, a spline curve was drawn along the cortex on the kymograph and the XY coordinates of this curve were exported to a text file. Custom made Matlab codes were written to extract the exact XY coordinates of the drawn curve from the text file without any repetitive timepoints by using a

standard interpolation method. Intensity signal of the drawn curve was calculated from the grayscale kymograph image using an average intensity of the three pixels, closest to the curve.

FRET Imaging and quantifications

Live samples of cultured neuroblasts were placed in a 8-well glass bottom μ-slide (iBidi) and imaged on a 3i spinning disk confocal microscope equipped with a Photometrics Evolve 512 back-illuminated EMCCD camera, using a X63 1.4 numerical aperture oil-immersion objective. Both donor (mTFP1) and acceptor/FRET (Venus) fluorophores were excited by a diode laser with 440 nm wavelength at 36 % power and 200 ms exposure time. Donor and FRET signals were detected using standard CFP (482 / 35-25) and YFP (542 / 27-25) emission filter set. The FRET index was determined using custom-written Matlab code. First, a background subtraction was performed for both donor and FRET detected signals using a background-averaged noise obtained from 50 different images acquired with the same imaging conditions. Then, the FRET index was calculated by calculating the ratio between the FRET acceptor and FRET donor intensity after subtracting background noise. A cut-off threshold (range 700-1100 a.u.) was used for the donor intensity such that only pixels with intensity above the cut-off are used for FRET index calculations. This cut-off threshold step was required to eliminate pixels with artificially high FRET index in the medium due to fluctuating noises. The FRET index was determined for all slices in the z-stack at all acquired time points. 3D images with FRET index distribution were reconstructed in Imaris. The Oblique Slicer tool was used to view FRET index distribution at the cell mid-plane. A square patch of 15x15 pixels was placed on the cell cortex to collect the FRET index of all pixels within that region of interest (ROI) for histogram analysis. Histograms of calculated FRET indices were accumulated from five planes closest to the mid-plane of the cell with the same box position and plotted as normalized frequency for easy comparison.

Acknowledgements

We thank members of the Cabernard lab for helpful discussions. We are also grateful to Robert E. Ward, Fumio Matsuzaki and Chris Doe for flies and antibodies. We would also like to thank the Imaging Core Facility (IMCF) at the Biozentrum for technical support. This work was supported by the Swiss National Science Foundation (SNSF). Stocks were obtained from the Bloomington Drosophila Stock Center (NIH P40OD018537).

Author contributions

The study was conceived by A.T and C.C. The majority of the experiments were performed by A.T. T.T.P generated the Myosin activity sensor, performed the FRET experiments and provided custom-made matlab codes for data analysis. D.S.G generated the Pins::EGFP CRISPR line and F. O. provided the *mbs* data. A.T and C.C interpreted the data and wrote the paper with help from T.T.P.

References

1. Munjal, A. & Lecuit, T. Actomyosin networks and tissue morphogenesis. *Development* **141,** 1789–1793 (2014).
2. D'Avino, P. P., Giansanti, M. G. & Petronczki, M. Cytokinesis in animal cells. *Cold Spring Harb Perspect Biol* **7,** a015834 (2015).
3. Cabernard, C. *et al.* Apical/basal spindle orientation is required for neuroblast homeostasis and neuronal differentiation in Drosophila. *Dev. Cell* **17,** 134–141 (2009).
4. Cabernard, C. Cytokinesis in Drosophila melanogaster. *Cytoskeleton* (2012).
5. Lacroix, B. & Maddox, A. S. Cytokinesis, ploidy and aneuploidy. *J. Pathol.* **226,** 338–351 (2012).
6. Green, R. A., Paluch, E. & Oegema, K. Cytokinesis in Animal Cells. *Annu. Rev. Cell Dev. Biol.* **28,** 120717164503001 (2011).
7. White, E. A. & Glotzer, M. Centralspindlin: at the heart of cytokinesis. *Cytoskeleton (Hoboken)* **69,** 882–892 (2012).
8. Cabernard, C., Prehoda, K. E. & Doe, C. Q. A spindle-independent cleavage furrow positioning pathway. *Nature* (2010).
9. Connell, M., Cabernard, C., Ricketson, D., Doe, C. Q. & Prehoda, K. E. Asymmetric cortical extension shifts cleavage furrow position in Drosophila neuroblasts. *Mol. Biol. Cell* **22,** 4220–4226 (2011).
10. Pacquelet, A., Uhart, P., Tassan, J.-P. & Michaux, G. PAR-4 and anillin regulate myosin to coordinate spindle and furrow position during asymmetric division. *J. Cell Biol.* **210,** 1085–1099 (2015).
11. Jordan, S. N. *et al.* Cortical PAR polarity proteins promote robust cytokinesis during asymmetric cell division. *J. Cell Biol.* **212,** 39–49 (2016).
12. Cinalli, R. M. & Lehmann, R. A spindle-independent cleavage pathway controls germ cell formation in Drosophila. *Nat. Cell Biol.* **15,** 839–845 (2013).
13. Sedzinski, J. *et al.* Polar actomyosin contractility destabilizes the position of the cytokinetic furrow. *Nature* **476,** 462–466 (2011).
14. Ou, G., Stuurman, N., D'Ambrosio, M. & Vale, R. D. Polarized myosin produces unequal-size daughters during asymmetric cell division. *Science* **330,** 677–680 (2010).
15. Homem, C. C. F. & Knoblich, J. A. Drosophila neuroblasts: a model for stem cell biology. *Development* **139,** 4297–4310 (2012).
16. Knoblich, J. A. Asymmetric cell division: recent developments and their implications for tumour biology. *Nat. Rev. Mol. Cell Biol.* **11,** 849–860 (2010).
17. Roth, M., Roubinet, C., Iffländer, N., Ferrand, A. & Cabernard, C. Asymmetrically dividing Drosophila neuroblasts utilize two spatially and temporally independent cytokinesis pathways. *Nat Commun* **6,** 6551 (2015).
18. Royou, A., Sullivan, W. & Karess, R. Cortical recruitment of nonmuscle myosin II in early syncytial Drosophila embryos: its role in nuclear axial expansion and its regulation by Cdc2 activity. *J Cell Biol* **158,** 127–137 (2002).
19. Albertson, R. & Doe, C. Q. Dlg, Scrib and Lgl regulate neuroblast cell size and mitotic spindle asymmetry. *Nat. Cell Biol.* **5,** 166–170 (2003).
20. Barros, C. S., Phelps, C. B. & Brand, A. H. Drosophila nonmuscle myosin II promotes the asymmetric segregation of cell fate determinants by cortical exclusion rather than active transport. *Dev. Cell* **5,** 829–840 (2003).
21. Cai, Y., Yu, F., Lin, S., Chia, W. & Yang, X. Apical complex genes control mitotic spindle geometry and relative size of daughter cells in Drosophila neuroblast and pI asymmetric divisions. *Cell* **112,** 51–62 (2003).
22. Matsumura, F., Yamakita, Y. & Yamashiro, S. Myosin light chain kinases and phosphatase in mitosis and cytokinesis. *Arch. Biochem. Biophys.* **510,** 76–82 (2011).
23. Zhang, L. & Ward, R. E. Distinct tissue distributions and subcellular localizations of differently phosphorylated forms of the myosin regulatory light chain in Drosophila. *Gene Expr. Patterns* **11,**

93–104 (2011).
24. Buszczak, M. *et al.* The carnegie protein trap library: a versatile tool for Drosophila developmental studies. *Genetics* **175,** 1505–1531 (2007).
25. Siller, K. H., Cabernard, C. & Doe, C. Q. The NuMA-related Mud protein binds Pins and regulates spindle orientation in Drosophila neuroblasts. *Nat. Cell Biol.* **8,** 594–600 (2006).
26. Izumi, Y., Ohta, N., Hisata, K., Raabe, T. & Matsuzaki, F. Drosophila Pins-binding protein Mud regulates spindle-polarity coupling and centrosome organization. *Nat. Cell Biol.* **8,** 586–593 (2006).
27. Bowman, S. K., Neumüller, R. A., Novatchkova, M., Du, Q. & Knoblich, J. A. The Drosophila NuMA Homolog Mud regulates spindle orientation in asymmetric cell division. *Dev. Cell* **10,** 731–742 (2006).
28. Betson, M. & Settleman, J. A Rho-Binding Protein Kinase C-Like Activity Is Required for the Function of Protein Kinase N in Drosophila Development. *Genetics* **176,** 2201–2212 (2007).
29. Ferreira, T., Prudêncio, P. & Gonçalo Martinho, R. Drosophila protein kinase N (Pkn) is a negative regulator of actin–myosin activity during oogenesis. *Dev. Biol.* (2014). doi:10.1016/j.ydbio.2014.08.008
30. Lu, Y. & Settleman, J. The Drosophila Pkn protein kinase is a Rho/Rac effector target required for dorsal closure during embryogenesis. *Genes Dev.* **13,** 1168–1180 (1999).
31. Konev, A. Y., VARENTSOVA, E. P., LEVINA, V. V., SARANTSEVA, S. V. & Khromykh, Y. M. Cytogenetic Analysis of the Chromosome Region Containing Radiosensitivity Gene in Drosophila .1. a Cytogenetic Mapping of Radiosensitivity Gene. *Genetika* **30,** 192–200 (1994).
32. Winter, C. G. *et al.* Drosophila Rho-associated kinase (Drok) links Frizzled-mediated planar cell polarity signaling to the actin cytoskeleton. *Cell* **105,** 81–91 (2001).
33. Stewart, M. P. *et al.* Hydrostatic pressure and the actomyosin cortex drive mitotic cell rounding. *Nature* **469,** 226–230 (2011).
34. Rosa, A., Vlassaks, E., Pichaud, F. & Baum, B. Ect2/Pbl Acts via Rho and Polarity Proteins to Direct the Assembly of an Isotropic Actomyosin Cortex upon Mitotic Entry. *Dev. Cell* **32,** 604–616 (2015).
35. Clark, A. G., Wartlick, O., Salbreux, G. & Paluch, E. K. Stresses at the Cell Surface during Animal Cell Morphogenesis. *Current Biology* **24,** R484–R494 (2015).
36. Grashoff, C. *et al.* Measuring mechanical tension across vinculin reveals regulation of focal adhesion dynamics. *Nature* **466,** 263–266 (2010).
37. Knoblich, J. A., Jan, L. Y. & Jan, Y. N. Deletion analysis of the Drosophila Inscuteable protein reveals domains for cortical localization and asymmetric localization. *Curr. Biol.* **9,** 155–158 (1999).
38. Fuerstenberg, S., Peng, C. Y., Alvarez-Ortiz, P., Hor, T. & Doe, C. Q. Identification of Miranda protein domains regulating asymmetric cortical localization, cargo binding, and cortical release. *Mol. Cell. Neurosci.* **12,** 325–339 (1998).
39. Mitonaka, T., Muramatsu, Y., Sugiyama, S., Mizuno, T. & Nishida, Y. Essential roles of myosin phosphatase in the maintenance of epithelial cell integrity of Drosophila imaginal disc cells. *Dev. Biol.* **309,** 78–86 (2007).
40. Lee, A. & Treisman, J. E. Excessive Myosin activity in mbs mutants causes photoreceptor movement out of the Drosophila eye disc epithelium. *Mol Biol Cell* **15,** 3285–3295 (2004).
41. David, M., Petit, D. & Bertoglio, J. Cell cycle regulation of Rho signaling pathways. *Cell Cycle* **11,** 3003–3010 (2012).
42. Amano, M. *et al.* Kinase-interacting substrate screening is a novel method to identify kinase substrates. *J. Cell Biol.* **209,** 895–912 (2015).
43. Cabernard, C., Prehoda, K. E. & Doe, C. Q. A spindle-independent cleavage furrow positioning pathway. *Nature* **467,** 91–94 (2010).
44. Mukai, H. *et al.* PKN3 is the major regulator of angiogenesis and tumor metastasis in mice. *Sci Rep* **6,** 18979 (2016).
45. Quétier, I. *et al.* Knockout of the PKN Family of Rho Effector Kinases Reveals a Non-redundant Role for PKN2 in Developmental Mesoderm Expansion. *Cell Rep* **14,** 440–448 (2016).
46. Loirand, G. Rho Kinases in Health and Disease: From Basic Science to Translational Research. *Pharmacol Rev* **67,** 1074–1095 (2015).
47. Yu, F., Morin, X., Cai, Y., Yang, X. & Chia, W. Analysis of partner of inscuteable, a Novel Player of

Drosophila Asymmetric Divisions, Reveals Two Distinct Steps in Inscuteable Apical Localization. *Cell* **100,** 399–409 (2000).
48. Guan, Z. *et al.* Mushroom body defect, a gene involved in the control of neuroblast proliferation in Drosophila, encodes a coiled-coil protein. *Proceedings of the National Academy of Sciences* **97,** 8122–8127 (2000).
49. Basto, R., Gomes, R. & Karess, R. E. Rough deal and Zw10 are required for the metaphase checkpoint in Drosophila. *Nat. Cell Biol.* **2,** 939–943 (2000).
50. Kerridge, S. *et al.* Modular activation of Rho1 by GPCR signalling imparts polarized myosin II activation during morphogenesis. *Nat. Cell Biol.* **18,** 261–270 (2016).
51. Martin, A. C., Kaschube, M. & Wieschaus, E. F. Pulsed contractions of an actin-myosin network drive apical constriction. *Nature* **457,** 495–499 (2009).
52. Cabernard, C. & Doe, C. Q. Live Imaging of Neuroblast Lineages within Intact Larval Brains in Drosophila. *Cold Spring Harbor Protocols* **2013,** 970–977 (2013).
53. Berger, C. *et al.* FACS Purification and Transcriptome Analysis of Drosophila Neural Stem Cells Reveals a Role for Klumpfuss in Self-Renewal. *Cell Rep* **2,** 407–418 (2012).

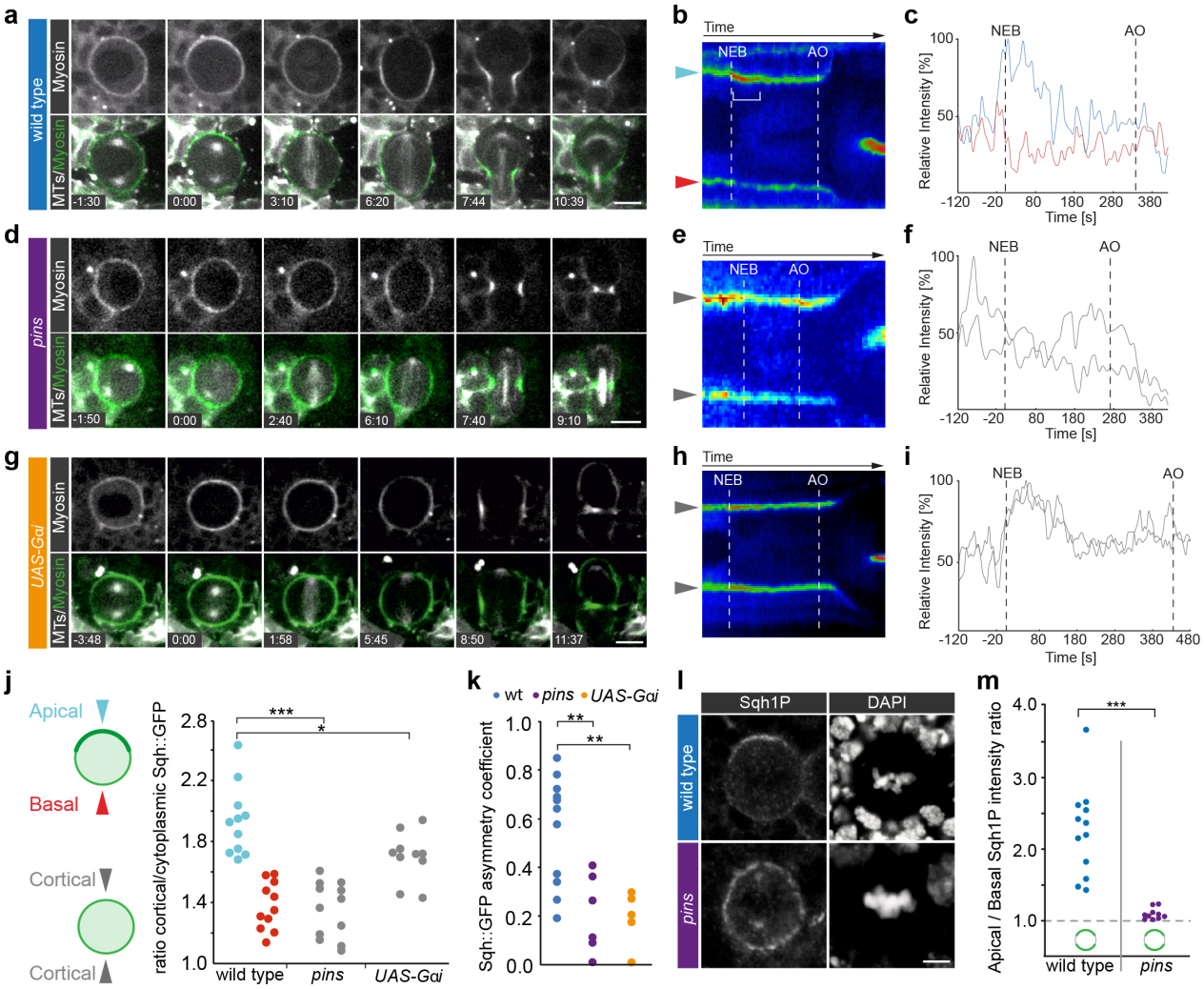
a
wild type
Myosin
MTs/Myosin
-1:30
0:00
3:10
6:20
7:44
10:39
b
Time
NEB
AO
c
NEB
AO
Relative Intensity [%]
100
50
-120
-20
80
180
280
380
Time [s]
d
pins
Myosin
MTs/Myosin
-1:50
0:00
2:40
6:10
7:40
9:10
e
Time
NEB
AO
f
NEB
AO
Relative Intensity [%]
100
50
-120
-20
80
180
280
380
Time [s]
g
UAS-Gαi
Myosin
MTs/Myosin
-3:48
0:00
1:58
5:45
8:50
11:37
h
Time
NEB
AO
i
NEB
AO
Relative Intensity [%]
100
50
-120
-20
80
180
280
380
480
Time [s]
j
Apical
Basal
Cortical
Cortical
ratio cortical/cytoplasmic Sqh::GFP
2.8
2.2
1.8
1.4
1.0
***
*
wild type
pins
UAS-Gαi
k
wt
pins
UAS-Gαi
Sqh::GFP asymmetry coefficient
1.0
0.8
0.6
0.4
0.2
0.0
**
**
l
Sqh1P
DAPI
wild type
pins
m
Apical / Basal Sqh1P intensity ratio
4.0
3.0
2.0
1.0
***
wild type
pins

Figure 1

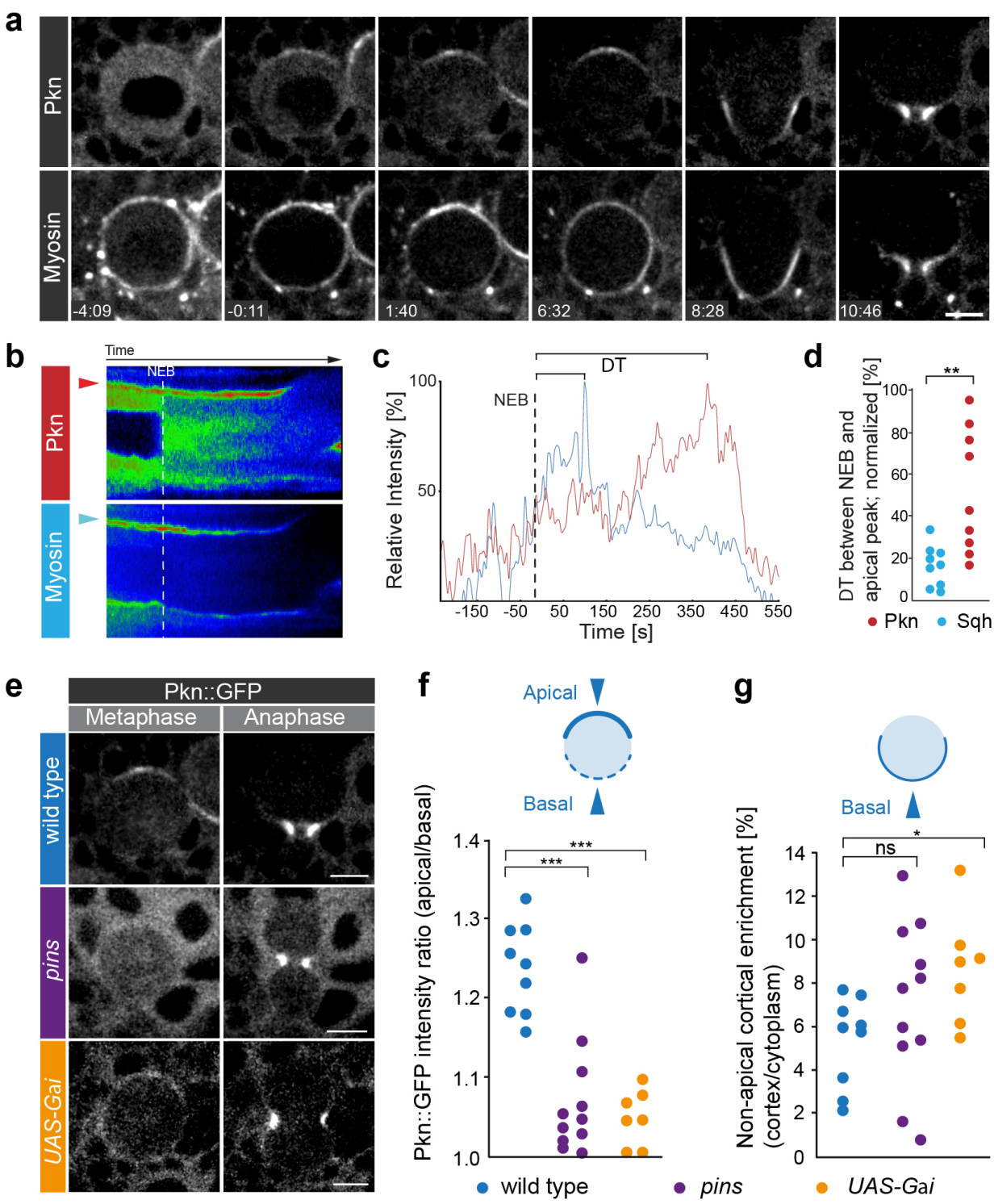
a
Pkn
Myosin
-4:09
-0:11
1:40
6:32
8:28
10:46
b
Time
NEB
Pkn
Myosin
c
DT
NEB
Relative Intensity [%]
100
50
-150 -50 50 150 250 350 450 550
Time [s]
d
DT between NEB and apical peak; normalized [%]
**
100
80
60
40
20
0
Pkn
Sqh
e
Pkn::GFP
Metaphase
Anaphase
wild type
pins
UAS-Gai
f
Apical
Basal
Pkn::GFP intensity ratio (apical/basal)
***
***
1.4
1.3
1.2
1.1
1.0
wild type
pins
UAS-Gai
g
Basal
Non-apical cortical enrichment [%] (cortex/cytoplasm)
ns
*
14
12
10
8
6
4
2
0
wild type
pins
UAS-Gai

Figure 2

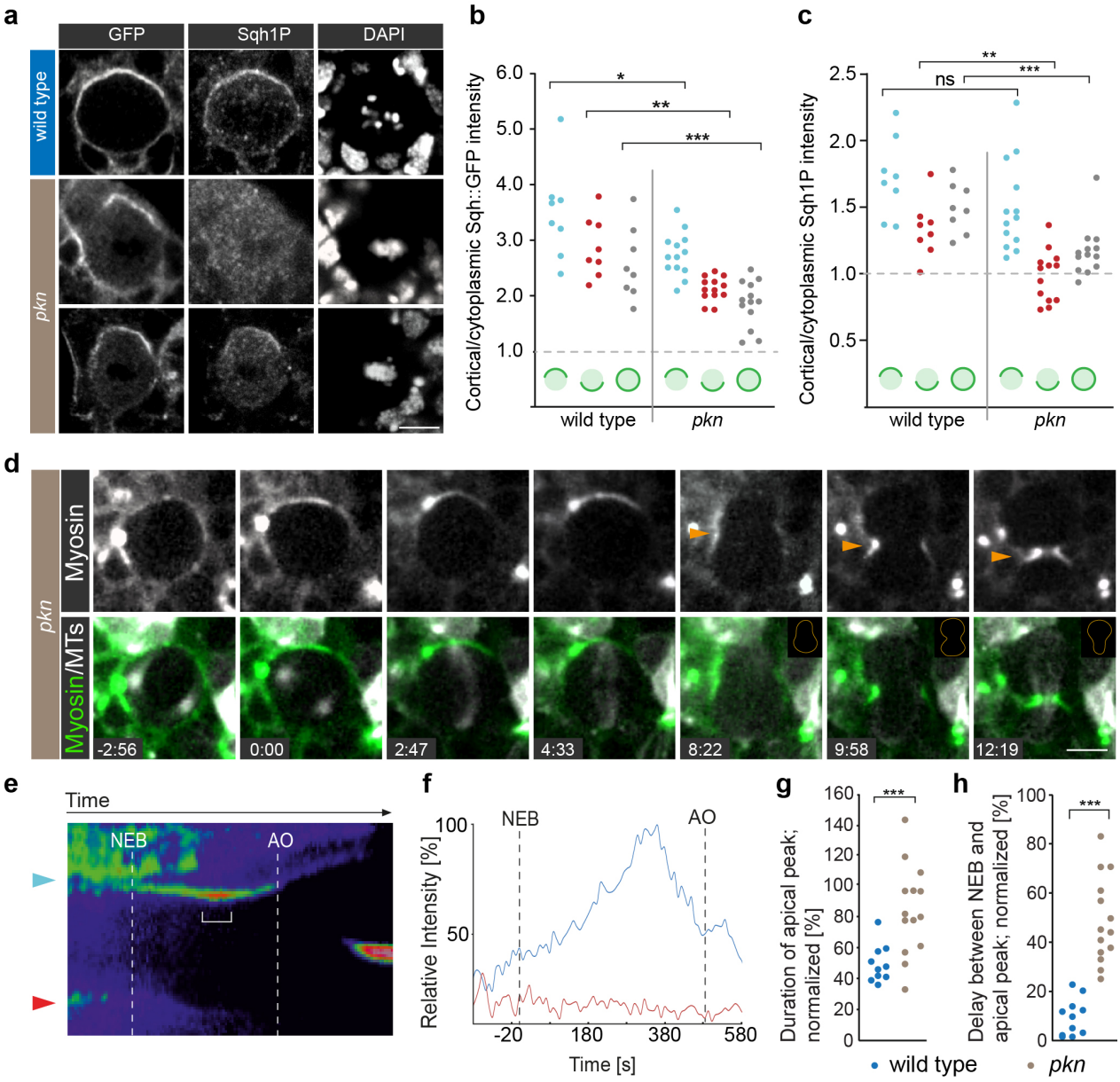
a
GFP
Sqh1P
DAPI
wild type
pkn
b
Cortical/cytoplasmic Sqh::GFP intensity
wild type
pkn
c
Cortical/cytoplasmic Sqh1P intensity
ns
wild type
pkn
d
pkn
Myosin
Myosin/MTs
-2:56
0:00
2:47
4:33
8:22
9:58
12:19
e
Time
NEB
AO
f
Relative Intensity [%]
NEB
AO
Time [s]
g
Duration of apical peak; normalized [%]
wild type
h
Delay between NEB and apical peak; normalized [%]
pkn

Figure 3

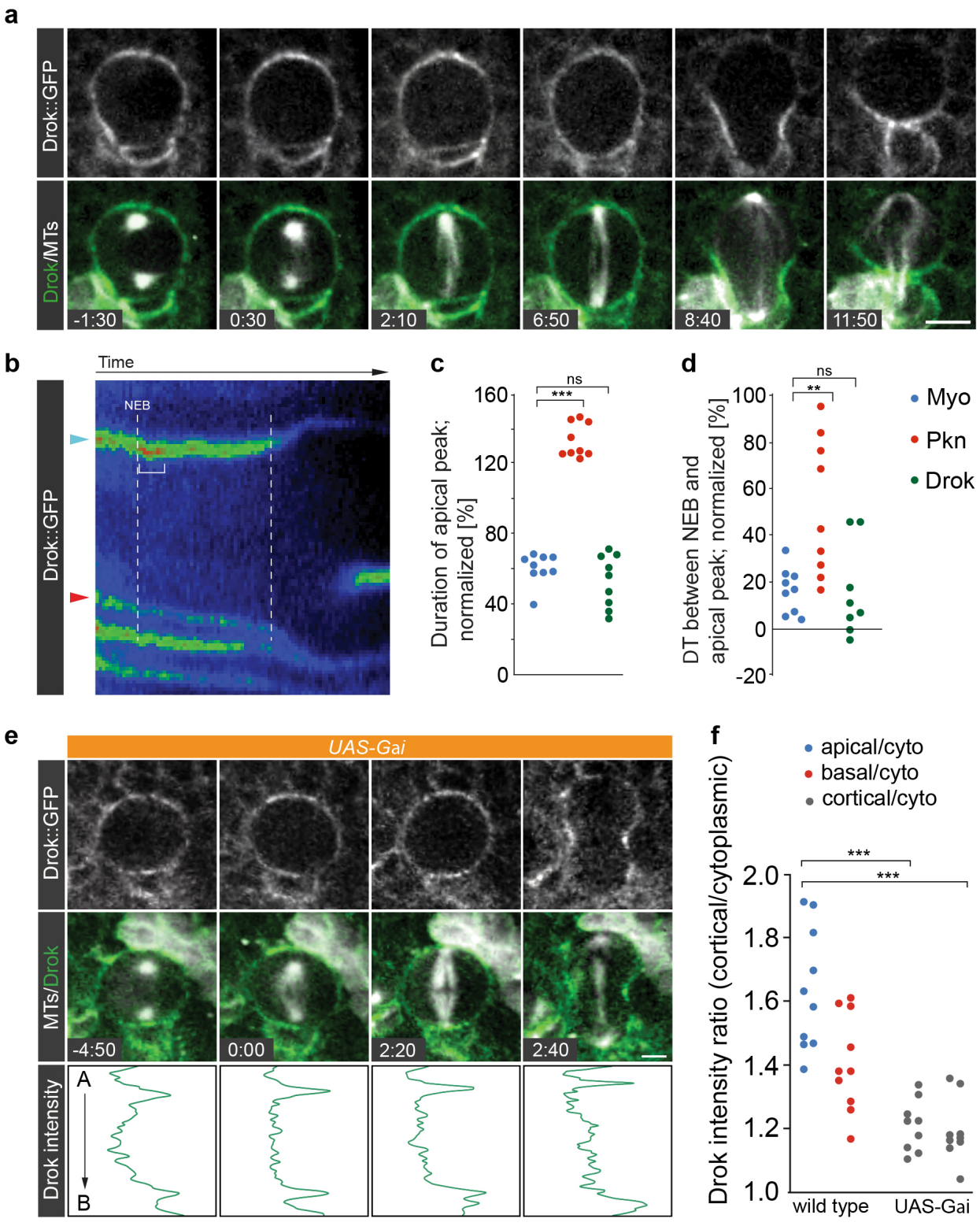
a
Drok::GFP
Drok/MTs
-1:30
0:30
2:10
6:50
8:40
11:50
b
Time
Drok::GFP
NEB
c
Duration of apical peak; normalized [%]
ns
***
160
120
80
40
0
d
DT between NEB and apical peak; normalized [%]
ns
**
100
80
60
40
20
0
-20
Myo
Pkn
Drok
e
UAS-Gai
Drok::GFP
MTs/Drok
-4:50
0:00
2:20
2:40
Drok intensity
A
B
f
apical/cyto
basal/cyto
cortical/cyto
***
***
Drok intensity ratio (cortical/cytoplasmic)
2.0
1.8
1.6
1.4
1.2
1.0
wild type
UAS-Gai

Figure 4

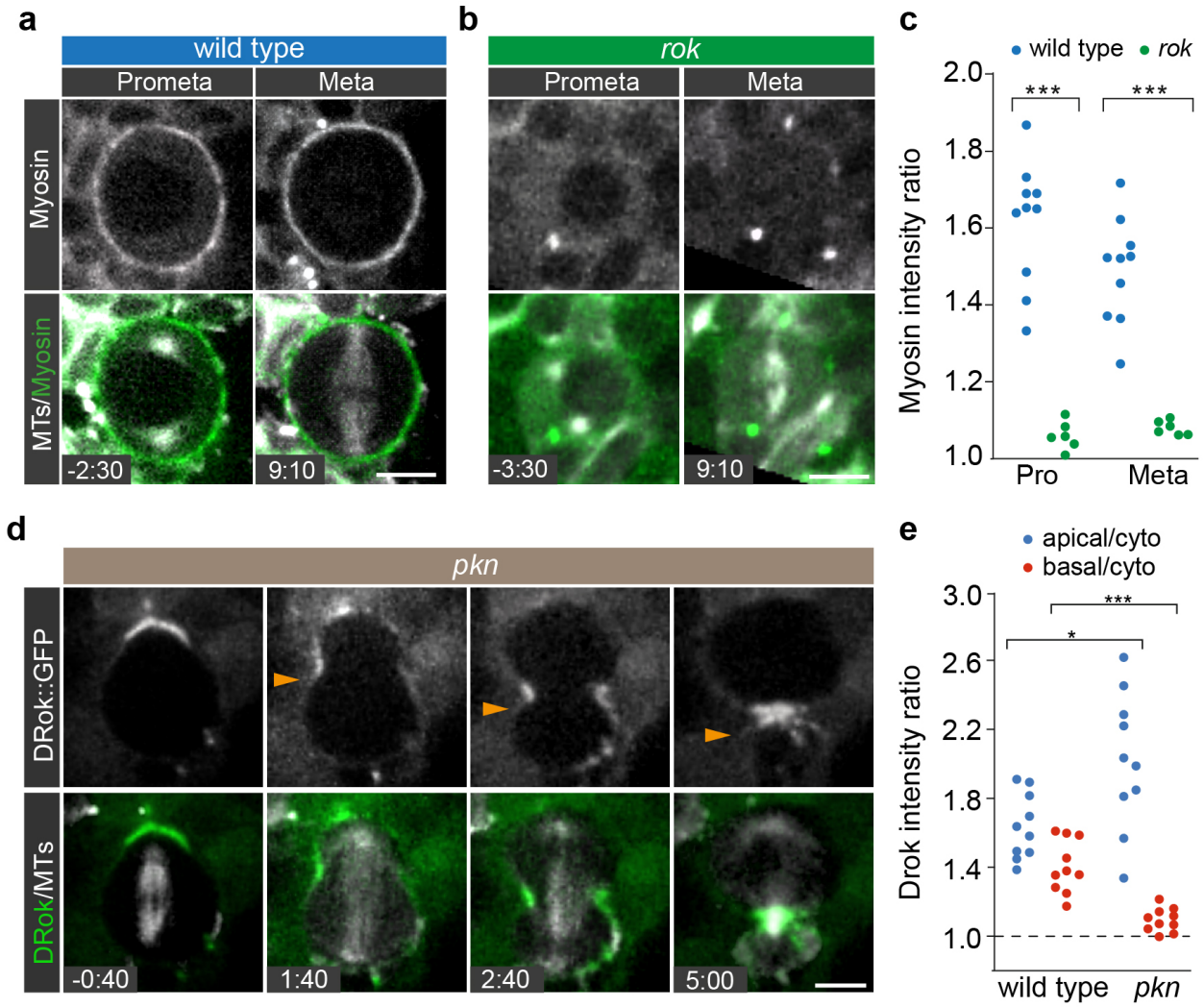
a
wild type
Prometa
Meta
Myosin
MTs/Myosin
-2:30
9:10
b
rok
Prometa
Meta
-3:30
9:10
c
wild type
rok
Myosin intensity ratio
2.0
1.8
1.6
1.4
1.2
1.0
***
***
Pro
Meta
d
pkn
DRok::GFP
DRok/MTs
-0:40
1:40
2:40
5:00
e
apical/cyto
basal/cyto
Drok intensity ratio
3.0
2.6
2.2
1.8
1.4
1.0
*
***
wild type
pkn

Figure 5

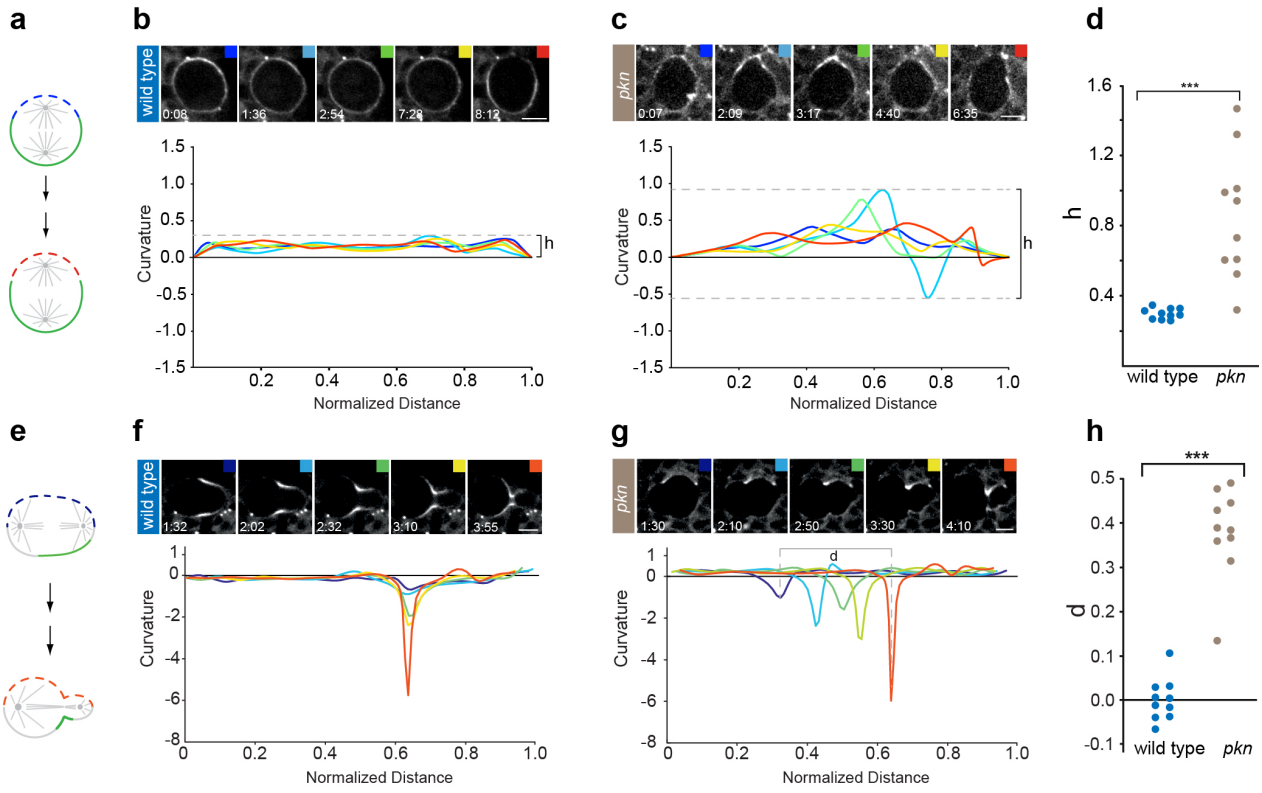
a
b
c
d
wild type
pkn
0:08
1:36
2:54
7:28
8:12
0:07
2:09
3:17
4:40
6:35
Curvature
Normalized Distance
h
***
wild type
pkn
e
f
g
h
1:32
2:02
2:32
3:10
3:55
1:30
2:10
2:50
3:30
4:10
d

Figure 6

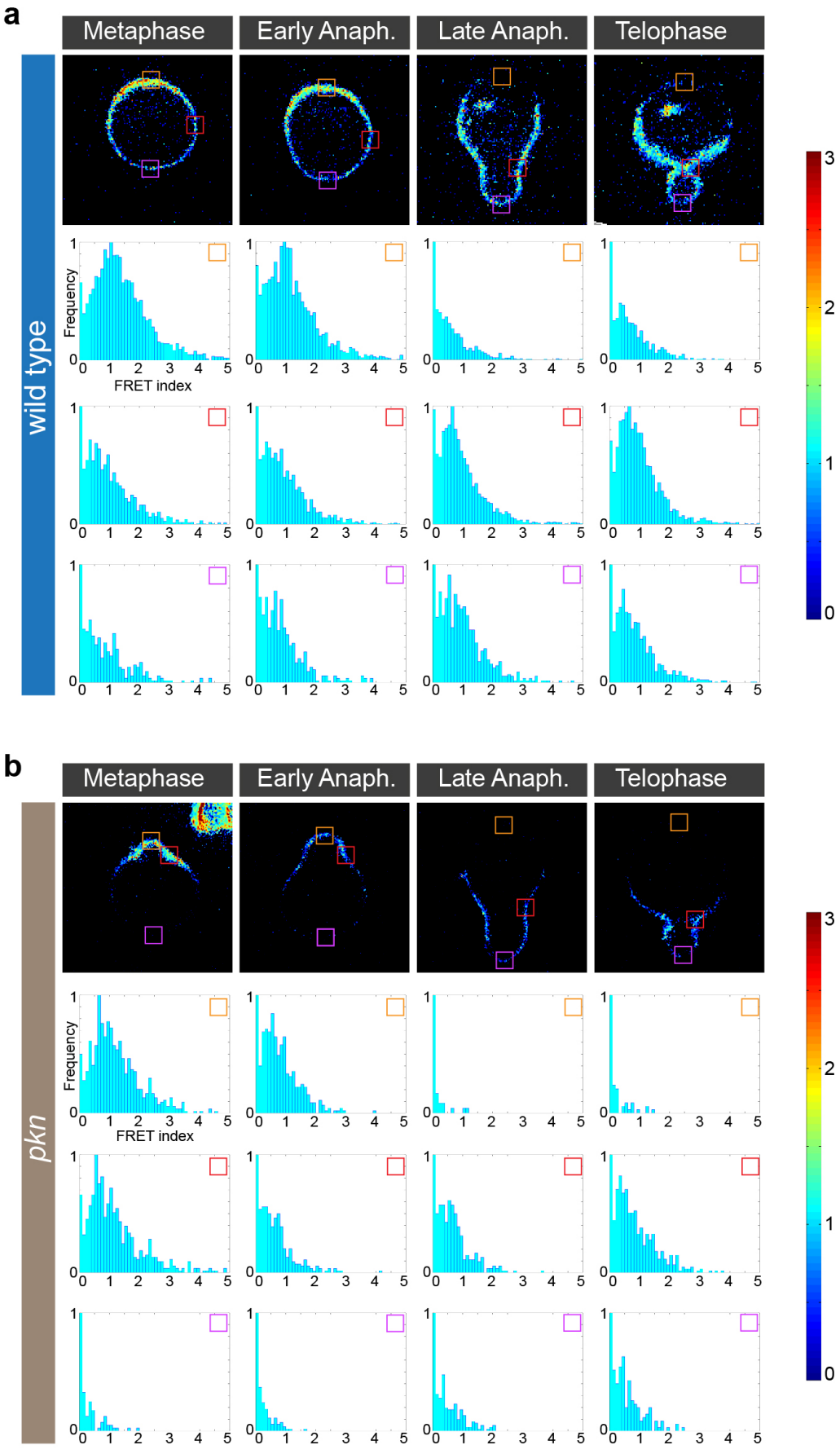
a
Metaphase
Early Anaph.
Late Anaph.
Telophase
wild type
Frequency
FRET index
b
Metaphase
Early Anaph.
Late Anaph.
Telophase
pkn
Frequency
FRET index

Figure 7

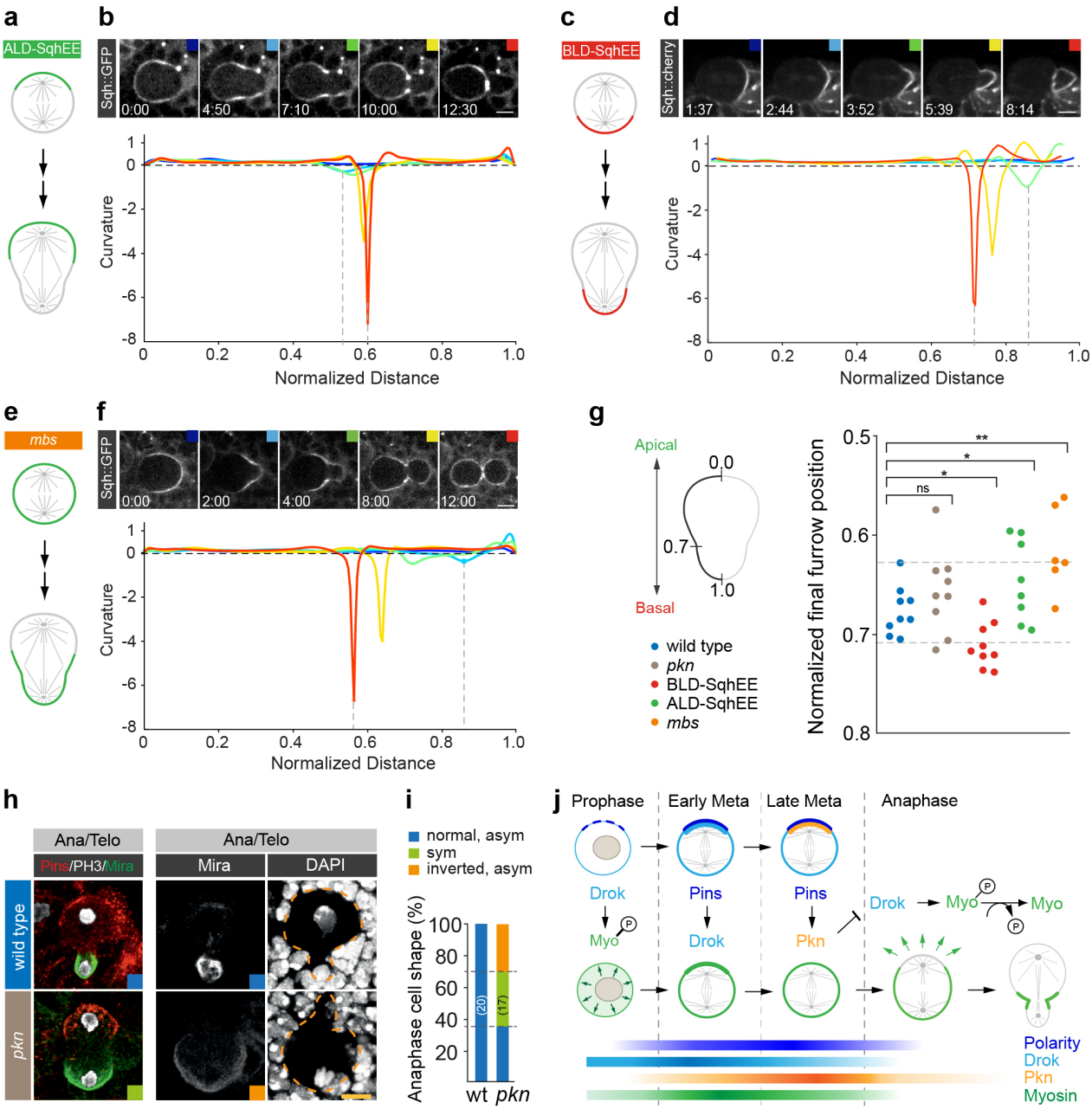
a
b
ALD-SqhEE
Sqh::GFP
0:00
4:50
7:10
10:00
12:30
Curvature
Normalized Distance
c
d
BLD-SqhEE
Sqh::cherry
1:37
2:44
3:52
5:39
8:14
e
f
mbs
0:00
2:00
4:00
8:00
12:00
g
Apical
Basal
0.0
0.7
1.0
wild type
pkn
BLD-SqhEE
ALD-SqhEE
mbs
Normalized final furrow position
ns
*
**
h
Ana/Telo
Pins/PH3/Mira
Mira
DAPI
wild type
pkn
i
normal, asym
sym
inverted, asym
Anaphase cell shape (%)
wt
pkn
(20)
(17)
j
Prophase
Early Meta
Late Meta
Anaphase
Drok
Myo
Pins
Pkn
Polarity
Drok
Pkn
Myosin

Figure 8

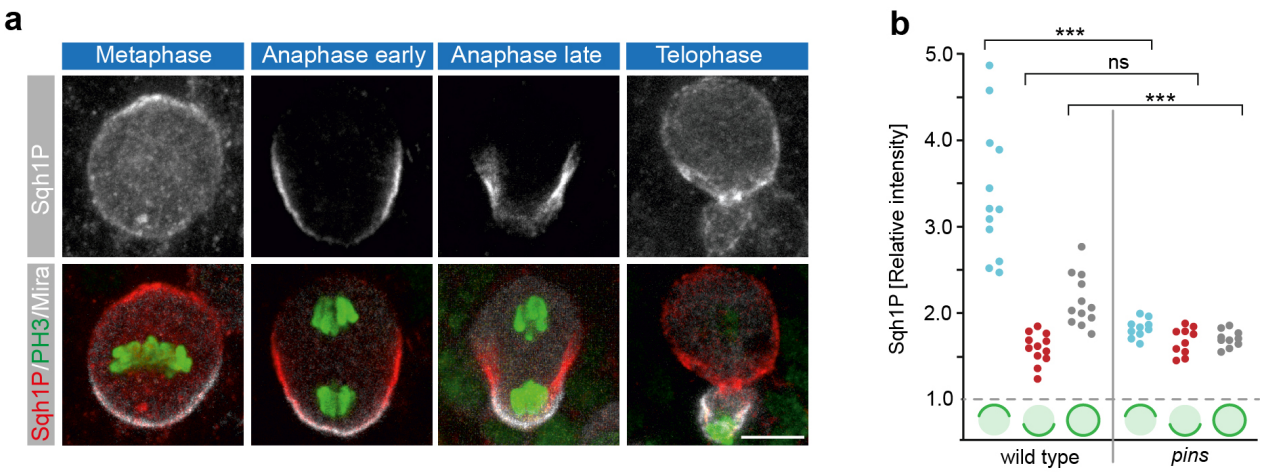

Supplemental Figure 1

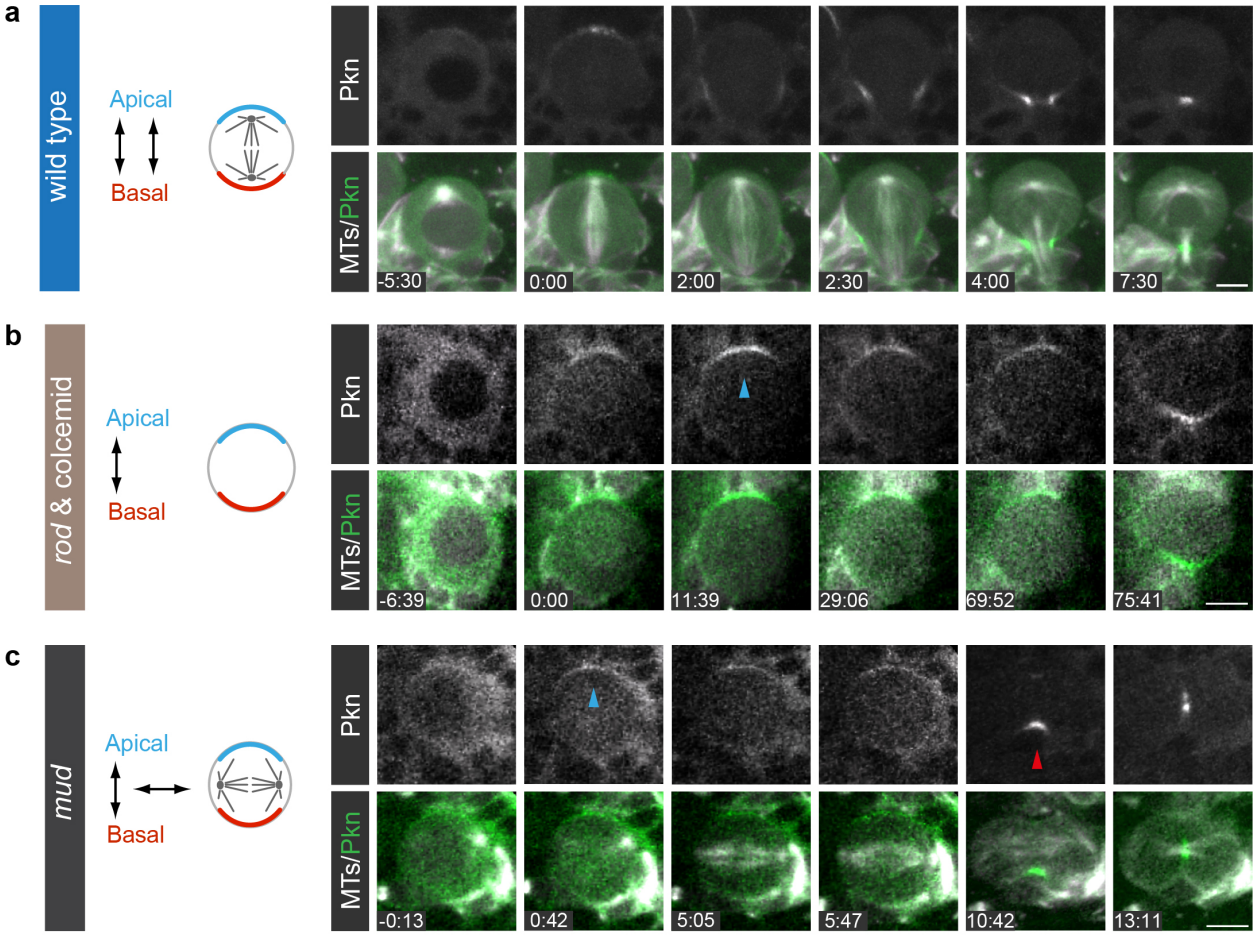

Supplemental Figure 2

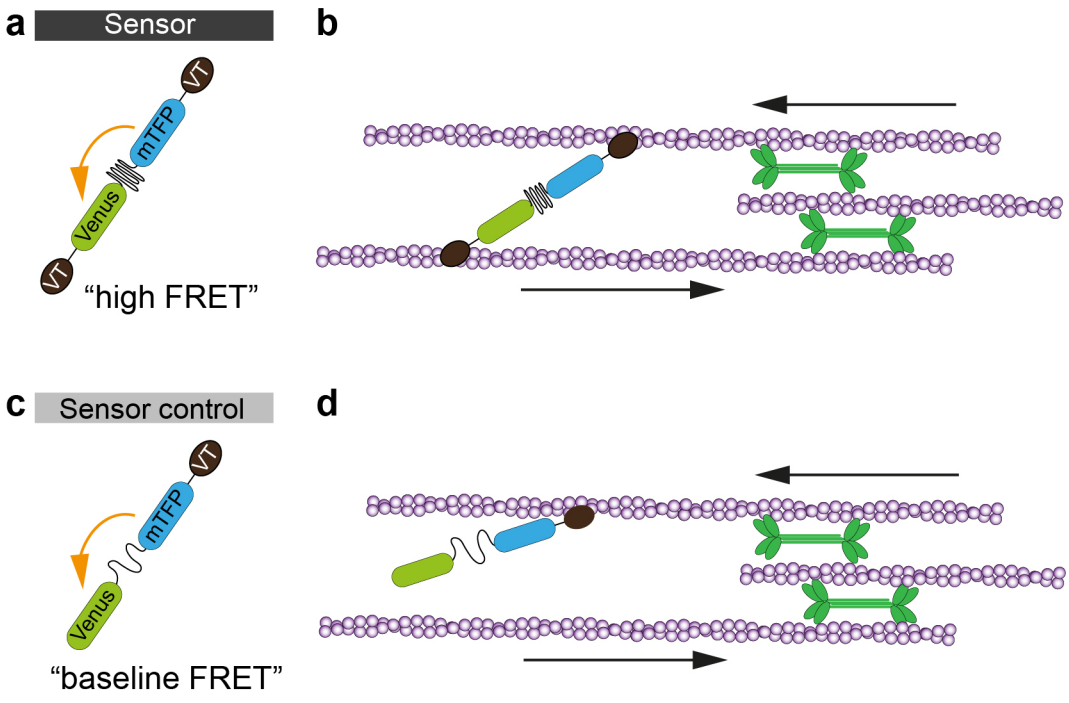

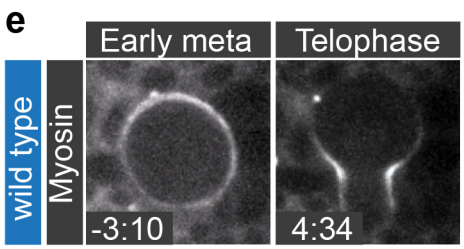

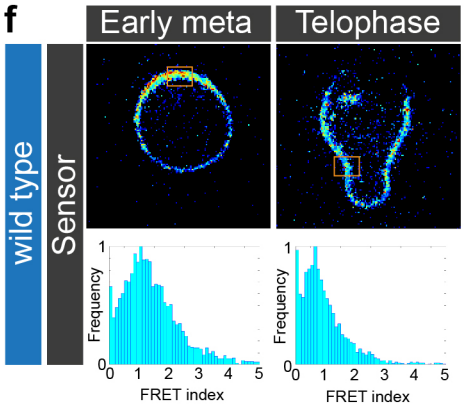

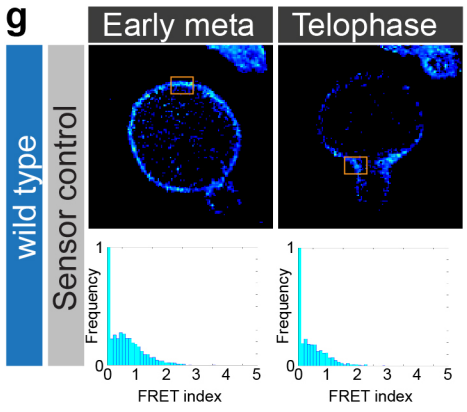

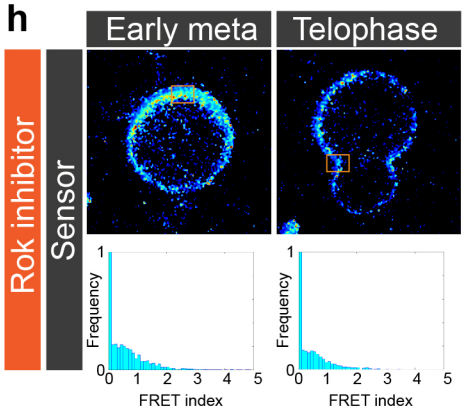

Supplemental Figure 3

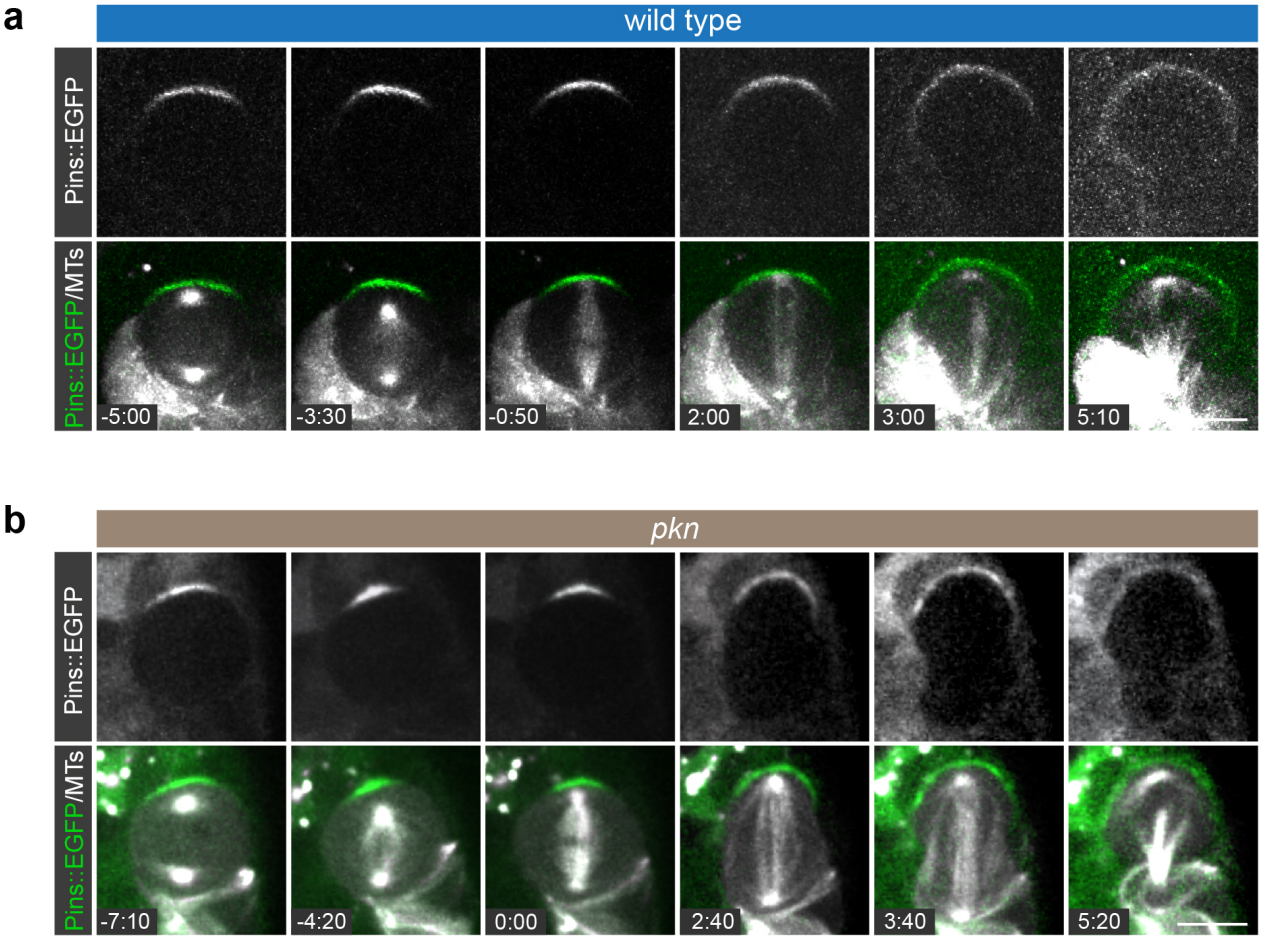

Supplemental Figure 4

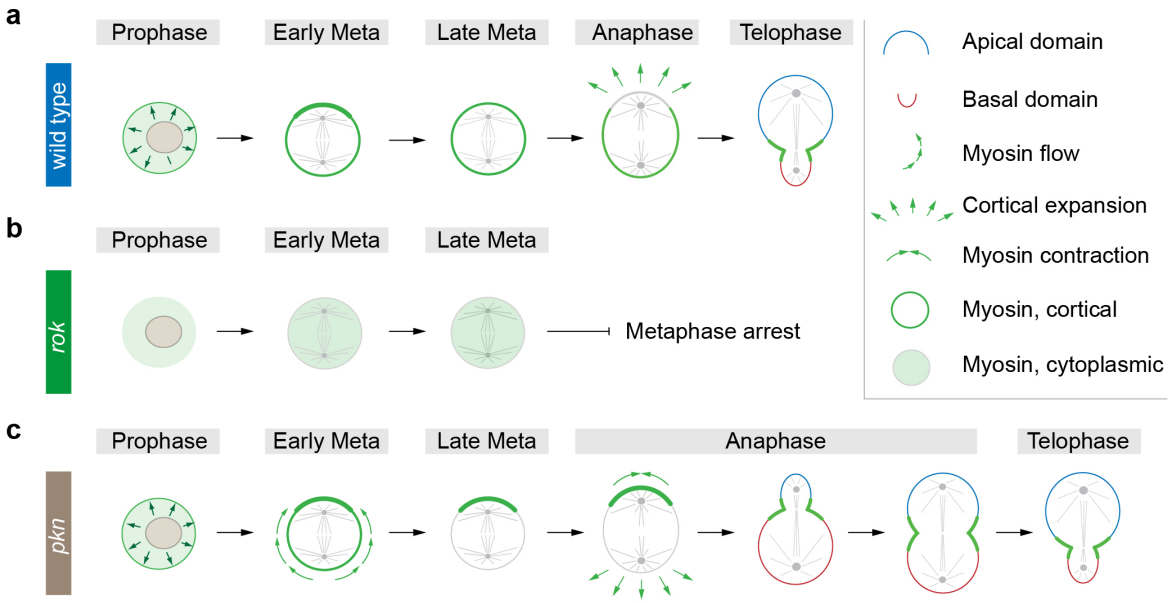

Supplemental Figure 5

2. PKN localization is dependent on aPKC

Since it has been shown that the apical PKN enrichment is dependent on the polarity protein Pins, we further tested whether other apically localized components regulate PKN localization. Indeed PKN::GFP expression in an *aPKC* RNAi background led to a complete loss of apical PKN at metaphase in the majority of the analyzed cells (Figure 20). At this stage only cytoplasmic PKN was detected. However, during telophase PKN still enriched at the cleavage furrow. These results are similar to the PKN localization obtained in the symmetrically dividing *pins* mutants and indicate that also aPKC is required for apical enrichment of PKN. However, we conclude that neither Pins, nor aPKC are required for the accumulation of PKN at the cleavage furrow. Since these experiments were performed in an *aPKC* knock-down background, they need to be confirmed in a mutant background.

Furthermore, we tested whether aPKC is also sufficient for PKN localization by imaging PKN::GFP in neuroblasts expressing an aPKC targeted to the plasma membrane using a caax phenylation motif (*UAS-aPKCcaax*)[280]. Upon expression of UAS-aPKCcaax, ectopic cortical localization of aPKC has been detected, whereas Miranda was entirely cytoplasmic[280]. However, targeting aPKC to the neuroblast cortex lead to normal apical enrichment of PKN at metaphase and enrichment at the furrow during telophase in the majority of the analyzed cells. This indicates that aPKC is not sufficient for the apical PKN recruitment at metaphase.

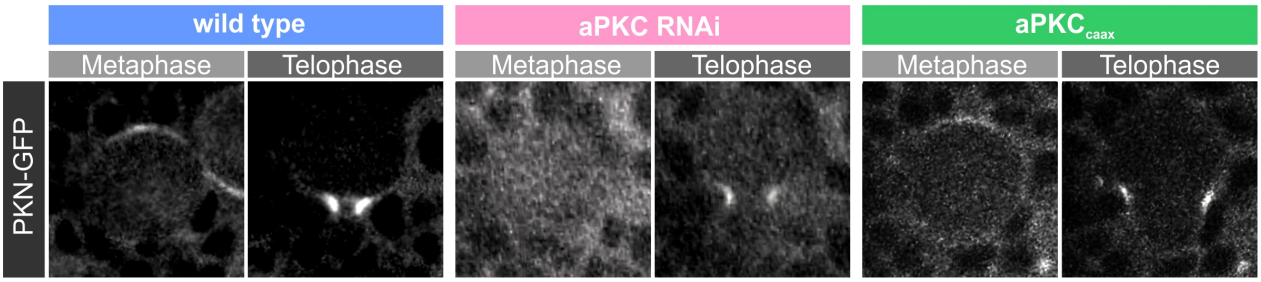

Figure 20: aPKC is required, but not sufficient for the apical PKN enrichment during metaphase. PKN localization is shown for *wt* (blue), *aPKC* RNAi (pink) and UAS-aPKCcaax (green) neuroblasts. Apical PKN enrichment is compromised in 85 % of all analyzed *aPKC* RNAi metaphase neuroblasts (n=48), whereas normal apical PKN was detected in 88 % of all metaphase neuroblasts expressing aPKCcaax (n=50).

3. Mbt as putative Myosin regulator

Mbt is another kinase, which was tested as a putative regulator of the apical Myosin enrichment during metaphase in asymmetrically dividing neuroblasts. Mbt is apically enriched at metaphase, similarly to PKN and is also a known regulator of actomyosin contractility[208]. Since the apical Myosin enrichment is polarity dependent, we first tested whether Mbt is enriched apically also in a polarity dependent manner. Staining of Mbt in wild type and *pins* mutants showed that during metaphase the apical Mbt crescent, which was detected in all wild type neuroblasts, is compromised in all analyzed *pins* mutant cells (Figure 21). Furthermore, during telophase Mbt was detected in both wild type and *pins* mutants at the apical cortex. Miranda was used as a polarity marker in this case. As it has already been shown, here we can also detect the majority of *pins* mutant neuroblasts showing mislocalization of Miranda[280].

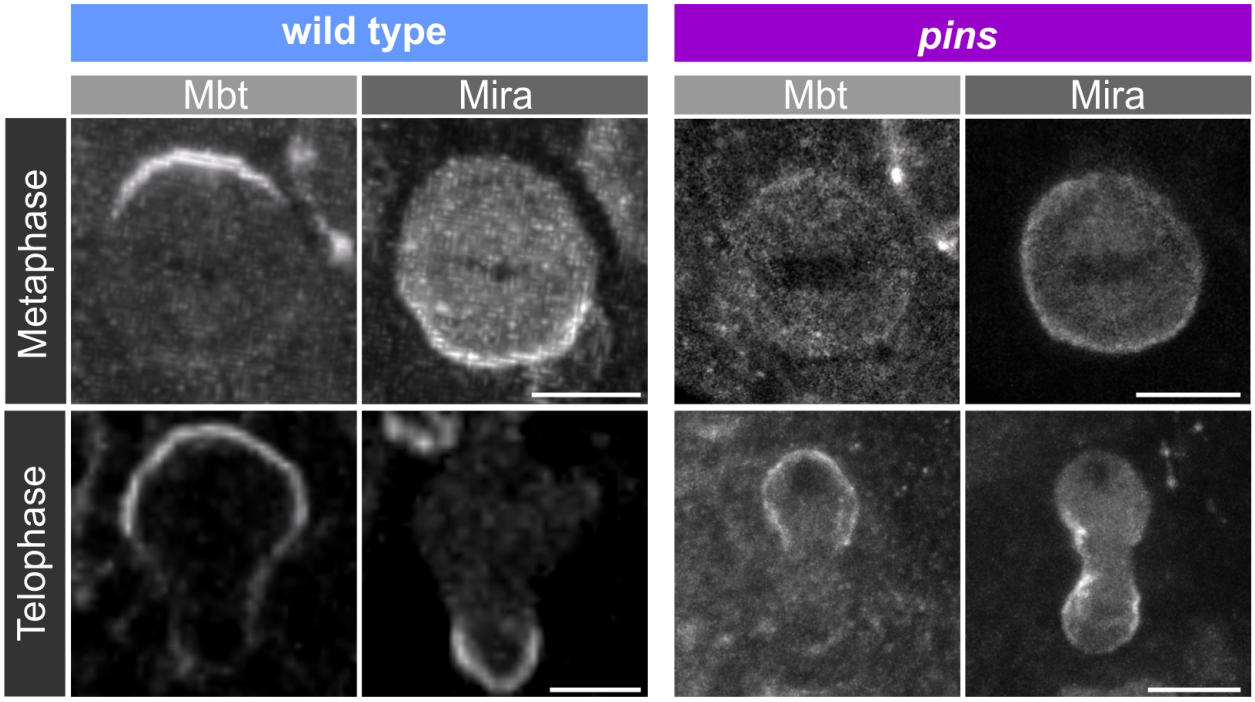

Figure 21: Mbt localization in wild type and *pins* mutants. All wt neuroblasts show apical enrichment of Mbt during metaphase (n=14; upper panel) and telophase (lower panel). However, all *pins* mutants show loss of apical Mbt during metaphase (n=7). During telophase *pins* mutants recruit Mbt at the cortex. The scale bar is 5 µm.

In order to test the role of Mbt for apical recruitment of Myosin during metaphase and later for the correct cleavage furrow positioning we performed live imaging experiments in *mbt* mutant neuroblasts expressing Sqh::EGFP (encodes the Myosin regulatory subunit). All analyzed cells were comparable to wild type. Myosin showed transient enrichment during metaphase and cleared first from the apical and later from the basal cortex during anaphase. This resulted in a

basally shifted cleavage furrow. Thus, abnormalities were detected neither in the distribution of Myosin, nor in the physically asymmetric division of the analyzed neuroblasts (upper panel Figure 22).

Furthermore, we performed immunohistochemistry, staining wild type and *mbt* mutant neuroblasts using an antibody specifically recognizing the monophosphorylated form of Myosin's regulatory light chain (Sqh-1P; recognizing phospho-Ser21 in Sqh). We previously have shown that wild type neuroblasts enrich phospho-Myosin at metaphase apically (see Manuscript II). *Mbt* mutants did not show compromised Myosin phosphorylation compared to the wild type controls (lower panel Figure 22). These data suggest that besides PKN, Mbt is another kinase, showing asymmetric localization during metaphase, which is dependent on the polarity protein Pins. However, Mbt does not seem to regulate, neither the transient Myosin enrichment during metaphase, nor its initial depletion at anaphase. We conclude, that Mbt is not required for Myosin phosphorylation during ACD.

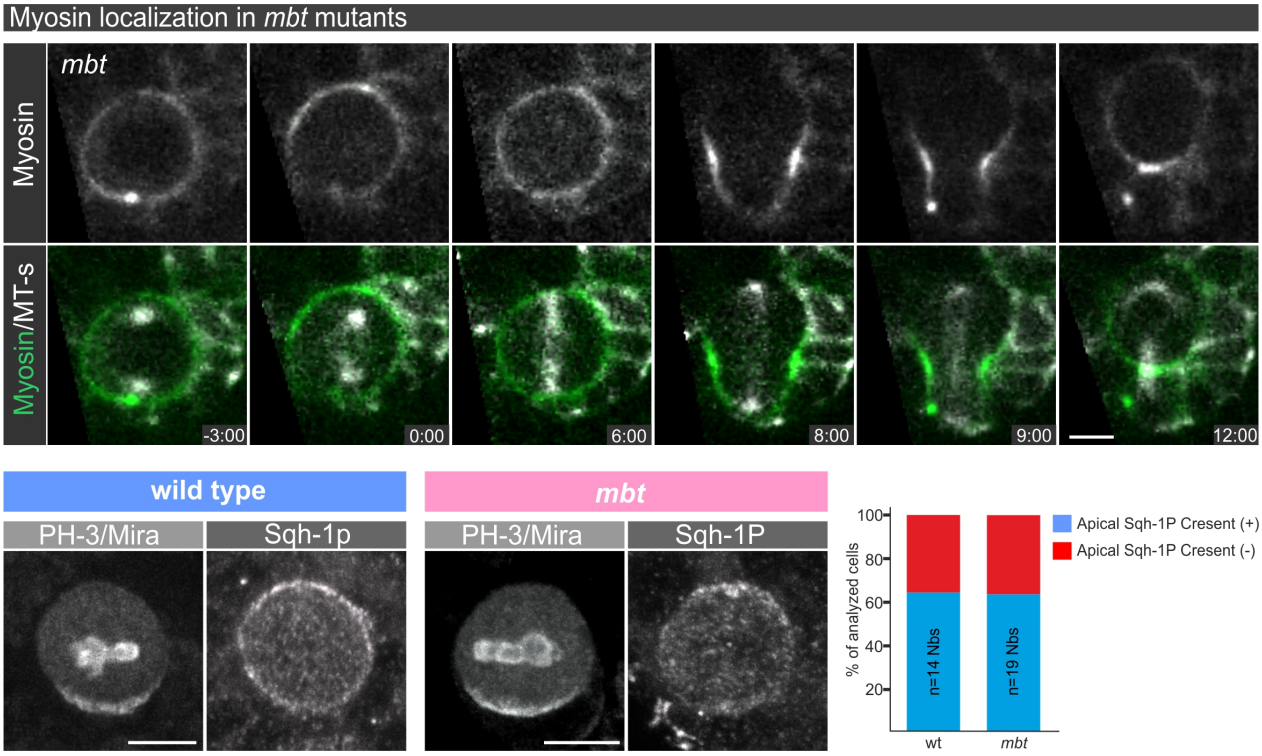

Figure 22: *Mbt* mutants show normal Myosin distribution. Upper panel: Timelaps of a *mbt* mutant neuroblast expressing Myosin::EGFP (white in the single channel and green in the merged channel) and Cherry::Jupiter (microtubules; MT-s; white in the merged channel). The temporal resolution is 1 min and the scale bar is 5 μm. All analyzed neuroblasts show normal Sqh localization. Lower panel: A wild type (wt; shown in blue) and a *mbt* mutant (shown in pink) neuroblast stained against the monophosphorylated form of Sqh (Sqh-1P) at Ser21. Miranda (Mira, white in the merged channel) is used as a polarity marker and phosphor-Histon-H3 (PH-3; white in the merged channel) as a cell cycle marker. The scale bar is 5 μm. The quantification of the analyzed cells for wt and the *mbt* mutant is shown at the right. In blue is shown the percentage of metaphase cells showing apical Sqh-1p enrichment and in red the percentage of analyzed metaphase cells lacking the apical Sqh-1p enrichment.

Extended Methods

I. Generation of constructs and transgenic flies

Sqh::mDendra2: The *mDendra2* coding sequence was PCR amplified and inserted into AscI and NotI restriction sites of attP-Sqh. AttP-Sqh was generated by removing EGFP with AscI and NotI (Tsankova, A., et al., in preparation). The construct was injected into attP (VK00033 and VK00037).

Zipper::mDendra2 MiMIC line: Mi02518 was crossed to phiC31 integrase (expressed under the vasa promotor; Bloomington stock center) and the resulting progeny were injected with mDendra2 exchange cassette. Injections were performed by BestGene. Positive lines were initially screened for loss of yellow body marker and tested for the expression of Zipper::mDendra2

II. Photoconversion

96h larval brains expressing Zipper::mDendra2 or Sqh::Dendra (will be referred as Myosin::Dendra) were used for all photoconversion experiments. Photoconversion experiments were performed on an Andor Revolution spinning disc system containing Andor's FRAPPA unit. A region of interests (ROI) was manually chosen in the GFP channel and Myosin::Dendra was irradiated with 405 nm on either the apical, basal or lateral cortex just after anaphase onset. Before photoconversion, single Z planes containing ROIs were scanned for ten time points with maximum speed. Subsequently, the ROI was irradiated with 405 nm (10 %; 50 repeats; 50 µs dwell time). After photoconversion, the entire neuroblast was scanned with a z-step size of 0.65 µm. Converted and unconverted mDendra2 emission were merged in AndorIQ2 and converted into Imaris.

Discussion

Previous studies have shown that Myosin is asymmetrically distributed during ACD of *Drosophila* neuroblasts, established through apical Myosin clearing prior to basal clearing after anaphase onset. This leads to an unequal cortical expansion and basally shifted cleavage furrow. The asymmetric localization of Myosin is dependent on the polarity protein Pins[275,277]. However, the mechanism regulating Myosin activity and its localization during ACD and thus the polarity dependent cues for cleavage furrow positioning are not fully understood.

In the present work we provide evidence that cell cycle and polarity cues regulate Myosin's activity and asymmetric distribution in a tight spatial and temporal manner. This ensures the cortical stability and cell shape during cytokinesis, as well as the correct furrow positioning and polarity domain size.

We first have shown that during prophase Drok recruits Myosin to the cell cortex, which is essential to complete cytokinesis. Thus, *rok* mutants show significant reduction of cortical Myosin, which in most extreme cases leads to complete loss of Myosin and to cytokinesis failure. Later during metaphase, neuroblasts enrich for activated Myosin at the apical cortex, which is regulating cell shape and actomyosin constriction. We show that the spatiotemporal regulation of Myosin's asymmetry at this cell cycle stage is dependent on Pins, biasing Myosin's activity through locally enriching for the *Drosophila* Rho kinase (Drok).

Our data suggest that also the second step of Myosin's asymmetry is regulated through Pins-dependent recruitment of a second kinase. PKN is recruited to the apical cortex, which inhibits Drok there and allows the initial apical clearing of Myosin. In agreement with this, *pkn* mutants still show recruitment of activated Myosin apically, reducing the overall cortical levels already at metaphase, and fail to clear apical Myosin at anaphase. This leads to reversed basal cortical expansion and mispositioning the cleavage furrow. We further show that ectopic activation of Myosin leads to drastic cell shape changes and ectopic formation of cleavage furrows, which form altered cortical domains. These changes are a transient phenotype and are corrected during cell cycle progression.

I. Myosin distribution during ACD

There has been a debate about the origin of the cleavage furrow Myosin molecules during telophase. Recent studies in *Drosophila* S2 cells have indicated that Myosin is degraded from the apical cortex and de-novo synthetized at the furrow region later during telophase[43]. However, our photoconversion experiments clearly show that asymmetrically dividing *Drosophila* neuroblasts redistribute the apical and basal pools of Myosin towards the cleavage furrow via two opposing cortical flows of Myosin. However, we cannot exclude the possibility that in addition to the cortical flow of Myosin there is also recruitment of cytoplasmic Myosin to the cleavage furrow region. In order to address the contribution of cytoplasmic and cortical Myosin to the cleavage furrow pool, we performed primed photoconversion experiments, which aimed to photoconvert specifically the cytoplasmic pool of Myosin without affecting the cortical Myosin molecules. This method was recently published and showed that dual-wavelength illumination of the photoconvertable tag Dendra2, using low intensity laser, results in its pronounced green-to red conversion. This dual-wavelength illumination was implemented on a confocal microscopy system and allowed performing confined photoconversion in complex 3D structures[281]. We performed the experiment at metaphase before the onset of the apical-basal flow and in addition at a later timepoint after the apical flow already had started. During early metaphase we observed a very dynamic exchange of cortical and cytoplasmic Myosin molecules, although at this cell cycle stage live imaging experiments show a non-pulsatile cortical Myosin. Furthermore, it would be possible that cytoplasmic Myosin would not be distributed to the cortex at later stages after apical redistribution already had started. We addressed this question by photoconverting cytoplasmic Myosin at anaphase after apical clearing onset. However, due to the short time window of anaphase and the drastic cell shape changes at this stage, we were not able to convert specifically the cytoplasmic pool of Myosin without affecting the cortical regions. Another drawback of the technique was the low temporal resolution. Taken together, we were not able to obtain conclusive results answering the question whether cytoplasmic Myosin molecules contribute to the cleavage furrow population.

Since Drok is involved in enrichment of activated Myosin at the apical cortex during metaphase, we addressed another hypothesis that the PKN induced reduction of Myosin phosphorylation might also be regulated through Drok. Indeed *pkn* mutants show changed Drok dynamics very similar to Myosin. Therefore, we propose here a model, which suggests that PKN initiates apical Myosin cortical flow through inhibition of the apically enriched Drok and thus

decreasing Myosin phosphorylation specifically at the apical cortex. Further experiments would be needed in order to understand whether PKN directly inhibits Drok, or whether this is mediated through another protein. In order to test this, we could use a constitutively active form of PKN targeted to the apical cortex at early metaphase. If PKN is indeed involved in Drok inhibition and Myosin relocalization, this should lead to premature apical clearing, basally enriched active Myosin and cleavage furrow shifted in an extreme basal position.

Furthermore, the question how does the PKN dependent inhibition of Drok lead to onset of cortical Myosin flow remains unclear. In this case, it is possible that gradual inhibition of Myosin leads to an unequal Myosin distribution. An increased amount of activated Myosin at the basal cortex might cause cortical constriction pulling the remaining Myosin from the apical cortex towards the cleavage furrow. This model would be in agreement with the observed *pkn* mutant phenotype where apical Myosin enrichment is retained but overall Myosin levels are significantly reduced. Lack of Drok inhibition at the apical cortex through lack of PKN might lead to an excessive apical activation of Myosin pulling the remaining molecules to this side. Furthermore, this would indicate the existence of a different pathway regulating Myosin clearing from the basal cortex and initiating the basal-apical opposing cortical flow. In this regard further work (Roubinet et. at., Manuscript I; submitted) showed that apical directed cortical flow is dependent on spindle cues establishing a Myosin gradient at the cleavage furrow and pulling the basally located Myosin molecules.

II. Molecular mechanisms of Myosin's activity during ACD

We show that Drok responds to both cell cycle and polarity cues and regulates the early cortical recruitment of Myosin and the initial establishment of Myosin's asymmetric activation during metaphase. Drok recruits Myosin to the cortex before nuclear envelope breakdown in a polarity-independent manner. Neuroblasts mutant for the polarity protein Pins are still able to recruit cortical Myosin, however, they lack apical bias. The underlying molecular mechanism for Drok-dependent Myosin cortical recruitment remains unclear. Since Rock is a known downstream target of the GTAase RhoA in other model systems, it is possible that also for the *Drosophila* neuroblasts Drok responds at early prometaphase to cell cycle cues through Rho1, which should lead to its recruitment to the cortex, where Drok can phosphorylate and activate Myosin. In this case Drok should be mislocalized in a *rho1* mutant background. Live imaging experiments of neuroblasts expressing Drok::GFP in a *rho1* mutant background could answer this

question. Also, expressing a Rho GDP dissociation inhibitor (GDI) could stabilize the Rho-GDP complex and keep Rho1 in an inactive state[282]. In this genetic background we could check whether Drok localization is dependent on the Rho activity. Furthermore, we have shown that the detected apical Myosin enrichment during metaphase is dependent on the polarity protein Pins through biased recruitment of Drok there. However, the mechanism of Drok enrichment and thus Myosin activation remains unclear. Biochemical experiments such as immunoprecipitations and mass spectroscopy could show whether Pins and Drok exist in the same complex and directly interact. It remains possible that also other apical components play a role in this process.

What is the biological function of the transient apical enrichment of Myosin during metaphase is still not clear. Interestingly, *pins* mutants, which loose apical Myosin bias divide in a physical symmetric manner. This indicates that there might be a mechanism, connecting the temporal regulation of Myosin activity with the physical asymmetry in wild type neuroblasts. This is further supported by our data, showing that misregulated Myosin activity leads to ectopic cortical constrictions and formation of mispositioned cleavage furrows. These cells, however, correct the cleavage furrow positioning at the end of cytokinesis suggesting that a possible complementary function of the spindle pathway might be involved. The question, whether the spindle can correct the mispositioned cleavage furrow, due to misregulation of Myosin's activity, could also be addressed. To this end, we performed live imaging experiments of *pkn* mutants expressing the basal polarity protein Miranda in the complete absence of microtubules (colcemid treatment, data not shown). Since these mutants combined with the chemical microtubule-depolymerization did not survive long enough, the performed experiments remained inconclusive. An easier possibility would be using the constitutively active forms of Sqh (SqhEE). Fused to a basal or apical localization domain (BLD/ALD) activated Myosin initiated the cleavage furrows in an extreme, either basally shifted, or apically shifted position, which was later corrected. If the spindle plays a role in the correction pathway, the depolymerization of the microtubules in these cases should lead to final cleavage furrow at the site where it is initially placed. Such mechanism was also observed in asymmetrically dividing QR.aa neuroblasts in *C. elegans*. Their asymmetric Myosin localization during anaphase triggers cortical constriction at the site of the accumulation and allows cortical expansion on the opposite site, generating daughter cells of different size. Furthermore, chromophore-assisted laser inactivation (CALI) experiments degraded Myosin's accumulation and this reversed the physical asymmetry[278]. This

approach might be another possibility to test whether the metaphase enrichment of Myosin in *Drosophila* neuroblasts is required to generate unequal cell size of the daughter cells.

Furthermore, it is possible that biased apical Myosin enrichment is involved in establishing the position for initial Myosin clearing during anaphase, which is the second step of Myosin asymmetric distribution during ACD. As mentioned above Myosin clears first apically and only later basally allowing unequal cortical expansion on both sides and forming two cortical domains of different sizes. This asymmetry is compromised in the symmetrically dividing *pins* mutants, which clear apical and basal Myosin at the same time. This suggests that the temporal regulation of apical and basal Myosin clearing is important for establishment of correct furrow positioning and daughter cell size. The current results indicate that a polarity-dependent recruitment of PKN is involved in the correct timing for apical clearing of Myosin during anaphase. Thus, the apical enrichment might act as a polarity-dependent cell intrinsic timer, ensuring the correct Myosin relocalization from the apical cortex, generating physically asymmetric cell division.

Since Pins is also involved in regulating the spindle alignment with the apical-basal polarity axis, a possible role of the apical Myosin enrichment for spindle positioning should also be tested. In this regard, depleting or relocalizing the enrichment to the lateral cortex should either alter the correct spindle positioning, or lead to orthogonal rotation of the spindle similarly, as shown for *mud* mutants. This should lead to formation of two cleavage furrows and symmetric divisions. However, the technical approach in order to perform such experiments might be challenging. A recent study in *C. elegans* 1-cell embryos has shown that centrosome separation at early prophase is dependent on actomyosin cortical flows[283]. The pulling force would be transmitted via the cross-linker Dynein, which pulls the centrosomes away from each other. This indicates that during the early cell cycle steps actomyosin dynamics might play a direct role in regulation of centrosome separation, spindle assembly and orientation.

We further found that PKN also responds to polarity cues and enriches at the apical neuroblast cortex in a Pins dependent manner. However, it remains unclear what are the upstream regulators involved in PKN apical recruitment. We performed RNAi knock-down of the small GTPase *rho1* specifically in the *Drosophila* neuroblasts and assayed PKN localization in this genetic background. We observed cells with multiple defects, most of them were multinucleated and were not able to divide. Furthermore, knock-down of *rho1* induced complete loss of cortical PKN. Our data strongly suggests that Rho1 is involved in the cortical recruitment of PKN. Since,

Rho1 has multiple cellular functions and is a known activator of Rock also in other model systems, the additional observed cell cycle defects are not surprising. However, in order to confirm these results PKN localization should be assayed also in a *rho1* mutant background.

Assuming that both Rho1 and Pins are upstream regulators involved in recruiting PKN to the neuroblast cortex during ACD, it would be interesting to address the question whether the polarity cues through Pins are required for regulation the GTPase Rho1 or vice versa. This would mean that the polarity components might play a role in much broader biological processes than previously known. Live imaging of Rho1::GFP in a *pins* mutant background might be an easy experimental setup to address this question.

There might also be other polarity proteins involved in Myosin regulation trough the PKN pathway. Our preliminary results show that *aPKC* knock-down also lead to compromised apical enrichment similar to what was already observed in the *pins* mutants. However, in both cases PKN was recruited to the cleavage furrow during telophase. These results, however, need to be confirmed using *aPKC* mutants. Furthermore, we tested whether aPKC is also sufficient for PKN localization. It has been shown that neuroblasts expressing aPKCcaax target aPKC ectopically to the cortex, which should lead to relocalization of the apical PKN crescent. However, we were still able to detect normal apical enrichment of PKN and subsequent accumulation at the cleavage furrow suggesting that aPKC is not sufficient for apical PKN enrichment[280]. Since, the *aPKCcaax* transgene does not lead to complete relocalization of the aPKC apical crescent but to an additional increase of overall cortical aPKC levels, our results might need to be reanalyzed. In addition to the apical PKN enrichment, we should assay whether the aPKCcaax expressing neuroblasts increase the PKN levels overall at the cortex. Indeed, aPKC might be involved in PKN and thus Myosin regulation. Biochemical analysis would be helpful to understand whether there is physical interaction between PKN and the components of the apical polarity complexes.

Since *pkn* mutants showed a significant reduction of Myosin phosphorylation, we addressed the question about the underlying molecular mechanism. For muscle cells it has been shown that CPI-17 is an inhibitor of the Myosin phosphatase. *In vitro* biochemical studies have also shown that PKN can phosphorylate and activate CPI-17[105]. In the current study we addressed the role of CPI-17 for non-muscle Myosin activation in neuroblasts. To this end, David Salvador Garcia generated CPI-17 mutants and tested whether these show defects in Myosin's activation profile. However, we did not find changes of phospho-Myosin levels suggesting that, although CPI-17 is expressed in non-muscle cells, it is not involved in regulation of non-muscle

Myosin in *Drosophila* neuroblasts. These results indicate that, although muscle and non-muscle Myosins show significant conservation degree, the regulatory mechanisms might differ. However, we cannot exclude that CPI-17 might be involved in Myosin regulation in other non-muscle tissues.

Furthermore, besides PKN and Drok there are also other kinases showing apical enrichment, which is established in a polarity dependent manner. We found Mbt, which showed similarly to PKN and Drok apical enrichment during metaphase, which was regulated through Pins. However, *mbt* mutants did not alter Myosin localization and activation, indicating that Mbt might have other functions during cytokinesis. Mushroom body neuroblasts mutant for *Mbt* have been previously shown to have a reduced mitotic index and to undergo apoptosis. To this end, polarity proteins might regulate Mbt in the central brain neuroblasts in order to ensure cell cycle timing and proliferation. Further experiments would be needed in order to fully understand the role of the biased Mbt localization during ACD of central brain neuroblasts.

A connection between actomyosin regulation and cell polarity components is not only restricted to *Drosophila,* but has been studied also in other model systems in the context of various biological processes. Asymmetric Myosin distribution and activation has been shown to play a key role in establishing polarity during early *C. elegans* embryogenesis. Near the end of meiosis, a centrosome triggered actomyosin flow causes an asymmetric cortical contractions. The actomyosin cortical flow transports the polarity proteins Par-3, Par-6 and PKC-3 to the anterior cap. This allows the accumulation of Par-1 and Par-2 at the posterior[284]. Furthermore, as previously discussed, biased Myosin activity is also involved in establishing polarity of migrating cells (Introduction; chapter II.3).

Furthermore, Myosin activity is not only associated with establishment of cell polarity but is known to be regulated through polarity cues in some model systems. A well-established example of polarity dependent Myosin regulation is through the Planar Cell Polarity (PCP) pathway. This pathway was discovered during *Drosophila* wing morphogenesis and it is conserved across organisms. In this case, cells undergo dramatic cell shape changes and align polarity of neighboring cells to form a single layered tissue. In intercalating neuroepithelia cells, asymmetrically localized PCP components have been show to recruit both Myosin and RhoA. This triggers local activation of Myosin and constriction of the actomyosin network, resulting in a medial-directed cell intercalation and bending of the neural plate. Furthermore, a similar mechanism was observed to drive the intercalation of mesenchymal cells during *Xenopus*

gastrulation. In this case PCP components were required for the asymmetric recruitment of Septins, which inhibit actomyosin activity and trigger cell intercalation[285,286].

All these data taken together shows that the mechanisms of Myosin activation and the connection with polarity components plays an important role for different biological processes during development in various model organisms. However, the details of this regulation remain elusive and many open questions need to be addressed in the future.

References

1. Fededa, J. P. & Gerlich, D. W. Molecular control of animal cell cytokinesis. *Nat. Cell Biol.* **14,** 440–447 (2012).
2. Uehara, R. *et al.* The augmin complex plays a critical role in spindle microtubule generation for mitotic progression and cytokinesis in human cells. *Proc. Natl. Acad. Sci. U.S.A.* **106,** 6998–7003 (2009).
3. Uehara, R. & Goshima, G. Functional central spindle assembly requires de novo microtubule generation in the interchromosomal region during anaphase. *J. Cell Biol.* **191,** 259–267 (2010).
4. Subramanian, R. *et al.* Insights into antiparallel microtubule crosslinking by PRC1, a conserved nonmotor microtubule binding protein. *Cell* **142,** 433–443 (2010).
5. Bieling, P., Telley, I. A. & Surrey, T. A minimal midzone protein module controls formation and length of antiparallel microtubule overlaps. *Cell* **142,** 420–432 (2010).
6. Pavicic-Kaltenbrunner, V., Mishima, M. & Glotzer, M. Cooperative assembly of CYK-4/MgcRacGAP and ZEN-4/MKLP1 to form the centralspindlin complex. *Mol. Biol. Cell* **18,** 4992–5003 (2007).
7. Mishima, M., Kaitna, S. & Glotzer, M. Central spindle assembly and cytokinesis require a kinesin-like protein/RhoGAP complex with microtubule bundling activity. *Dev. Cell* **2,** 41–54 (2002).
8. Hutterer, A., Glotzer, M. & Mishima, M. Clustering of centralspindlin is essential for its accumulation to the central spindle and the midbody. *Curr. Biol.* **19,** 2043–2049 (2009).
9. Mishima, M., Pavicic, V., Grüneberg, U., Nigg, E. A. & Glotzer, M. Cell cycle regulation of central spindle assembly. *Nature* **430,** 908–913 (2004).
10. Guse, A., Mishima, M. & Glotzer, M. Phosphorylation of ZEN-4/MKLP1 by aurora B regulates completion of cytokinesis. *Curr. Biol.* **15,** 778–786 (2005).
11. Carmena, M., Wheelock, M., Funabiki, H. & Earnshaw, W. C. The chromosomal passenger complex (CPC): from easy rider to the godfather of mitosis. *Nat. Rev. Mol. Cell Biol.* **13,** 789–803 (2012).
12. Glotzer, M. The 3Ms of central spindle assembly: microtubules, motors and MAPs. *Nat. Rev. Mol. Cell Biol.* **10,** 9–20 (2009).
13. Ban, R., Irino, Y., Fukami, K. & Tanaka, H. Human mitotic spindle-associated protein PRC1 inhibits MgcRacGAP activity toward Cdc42 during the metaphase. *J. Biol. Chem.* **279,** 16394–16402 (2004).
14. Motegi, F., Velarde, N. V., Piano, F. & Sugimoto, A. Two phases of astral microtubule activity during cytokinesis in C. elegans embryos. *Dev. Cell* **10,** 509–520 (2006).
15. Foe, V. E. & Dassow, von, G. Stable and dynamic microtubules coordinately shape the myosin activation zone during cytokinetic furrow formation. *J. Cell Biol.* **183,** 457–470 (2008).
16. Odell, G. M. & Foe, V. E. An agent-based model contrasts opposite effects of dynamic and stable microtubules on cleavage furrow positioning. *J. Cell Biol.* **183,** 471–483 (2008).
17. Werner, M., Munro, E. & Glotzer, M. Astral signals spatially bias cortical myosin recruitment to break symmetry and promote cytokinesis. *Curr. Biol.* **17,** 1286–1297 (2007).
18. Dechant, R. & Glotzer, M. Centrosome separation and central spindle assembly act in

redundant pathways that regulate microtubule density and trigger cleavage furrow formation. *Dev. Cell* **4,** 333–344 (2003).
19. Bement, W. M., Benink, H. A. & Dassow, von, G. A microtubule-dependent zone of active RhoA during cleavage plane specification. *J. Cell Biol.* **170,** 91–101 (2005).
20. Yüce, O., Piekny, A. & Glotzer, M. An ECT2-centralspindlin complex regulates the localization and function of RhoA. *J. Cell Biol.* **170,** 571–582 (2005).
21. Burkard, M. E. *et al.* Plk1 self-organization and priming phosphorylation of HsCYK-4 at the spindle midzone regulate the onset of division in human cells. *PLoS Biol.* **7,** e1000111 (2009).
22. Petronczki, M., Glotzer, M., Kraut, N. & Peters, J.-M. Polo-like kinase 1 triggers the initiation of cytokinesis in human cells by promoting recruitment of the RhoGEF Ect2 to the central spindle. *Dev. Cell* **12,** 713–725 (2007).
23. Wolfe, B. A., Takaki, T., Petronczki, M. & Glotzer, M. Polo-like kinase 1 directs assembly of the HsCyk-4 RhoGAP/Ect2 RhoGEF complex to initiate cleavage furrow formation. *PLoS Biol.* **7,** e1000110 (2009).
24. Miller, A. L. & Bement, W. M. Regulation of cytokinesis by Rho GTPase flux. *Nat. Cell Biol.* **11,** 71–77 (2009).
25. Canman, J. C. *et al.* Inhibition of Rac by the GAP activity of centralspindlin is essential for cytokinesis. *Science* **322,** 1543–1546 (2008).
26. Loria, A., Longhini, K. M. & Glotzer, M. The RhoGAP domain of CYK-4 has an essential role in RhoA activation. *Curr. Biol.* **22,** 213–219 (2012).
27. Joo, E., Surka, M. C. & Trimble, W. S. Mammalian SEPT2 is required for scaffolding nonmuscle myosin II and its kinases. *Dev. Cell* **13,** 677–690 (2007).
28. Neufeld, T. P. & Rubin, G. M. The Drosophila peanut gene is required for cytokinesis and encodes a protein similar to yeast putative bud neck filament proteins. *Cell* **77,** 371–379 (1994).
29. Mavrakis, M. *et al.* Septins promote F-actin ring formation by crosslinking actin filaments into curved bundles. *Nat. Cell Biol.* **16,** 322–334 (2014).
30. Piekny, A. J. & Maddox, A. S. The myriad roles of Anillin during cytokinesis. *Semin. Cell Dev. Biol.* **21,** 881–891 (2010).
31. Field, C. M. & Alberts, B. M. Anillin, a contractile ring protein that cycles from the nucleus to the cell cortex. *J. Cell Biol.* **131,** 165–178 (1995).
32. Kee, Y.-S. & Robinson, D. N. Motor proteins: myosin mechanosensors. *Curr. Biol.* **18,** R860–2 (2008).
33. Sweeney, H. L. & Houdusse, A. Structural and functional insights into the Myosin motor mechanism. *Annu Rev Biophys* **39,** 539–557 (2010).
34. Maupin, P. & Pollard, T. D. Arrangement of actin filaments and myosin-like filaments in the contractile ring and of actin-like filaments in the mitotic spindle of dividing HeLa cells. *J. Ultrastruct. Mol. Struct. Res.* **94,** 92–103 (1986).
35. Reichl, E. M. *et al.* Interactions between myosin and actin crosslinkers control cytokinesis contractility dynamics and mechanics. *Curr. Biol.* **18,** 471–480 (2008).
36. Kamasaki, T., Osumi, M. & Mabuchi, I. Three-dimensional arrangement of F-actin in the contractile ring of fission yeast. *J. Cell Biol.* **178,** 765–771 (2007).
37. Cramer, L. P., Siebert, M. & Mitchison, T. J. Identification of novel graded polarity actin filament bundles in locomoting heart fibroblasts: implications for the generation of motile force. *J. Cell Biol.* **136,** 1287–1305 (1997).
38. Watanabe, S. *et al.* mDia2 induces the actin scaffold for the contractile ring and stabilizes its position during cytokinesis in NIH 3T3 cells. *Mol. Biol. Cell* **19,** 2328–2338

(2008).
39. Castrillon, D. H. & Wasserman, S. A. Diaphanous is required for cytokinesis in Drosophila and shares domains of similarity with the products of the limb deformity gene. *Development* **120,** 3367–3377 (1994).
40. Severson, A. F., Baillie, D. L. & Bowerman, B. A Formin Homology protein and a profilin are required for cytokinesis and Arp2/3-independent assembly of cortical microfilaments in C. elegans. *Curr. Biol.* **12,** 2066–2075 (2002).
41. Matsumura, F. Regulation of myosin II during cytokinesis in higher eukaryotes. *Trends Cell Biol.* **15,** 371–377 (2005).
42. Yumura, S., Ueda, M., Sako, Y., Kitanishi-Yumura, T. & Yanagida, T. Multiple mechanisms for accumulation of myosin II filaments at the equator during cytokinesis. *Traffic* **9,** 2089–2099 (2008).
43. Vale, R. D., Spudich, J. A. & Griffis, E. R. Dynamics of myosin, microtubules, and Kinesin-6 at the cortex during cytokinesis in Drosophila S2 cells. *J. Cell Biol.* **186,** 727–738 (2009).
44. Schroeder, T. E. The contractile ring. II. Determining its brief existence, volumetric changes, and vital role in cleaving Arbacia eggs. *J. Cell Biol.* **53,** 419–434 (1972).
45. Carvalho, A., Desai, A. & Oegema, K. Structural memory in the contractile ring makes the duration of cytokinesis independent of cell size. *Cell* **137,** 926–937 (2009).
46. Calvert, M. E. K. *et al.* Myosin concentration underlies cell size-dependent scalability of actomyosin ring constriction. *J. Cell Biol.* **195,** 799–813 (2011).
47. Ma, X. *et al.* Nonmuscle myosin II exerts tension but does not translocate actin in vertebrate cytokinesis. *Proc. Natl. Acad. Sci. U.S.A.* **109,** 4509–4514 (2012).
48. Pelham, R. J. & Chang, F. Actin dynamics in the contractile ring during cytokinesis in fission yeast. *Nature* **419,** 82–86 (2002).
49. Zumdieck, A., Kruse, K., Bringmann, H., Hyman, A. A. & Jülicher, F. Stress generation and filament turnover during actin ring constriction. *PLoS ONE* **2,** e696 (2007).
50. Biron, D., Alvarez-Lacalle, E., Tlusty, T. & Moses, E. Molecular model of the contractile ring. *Phys. Rev. Lett.* **95,** 098102 (2005).
51. Carlsson, A. E. Contractile stress generation by actomyosin gels. *Phys Rev E Stat Nonlin Soft Matter Phys* **74,** 051912 (2006).
52. Dickinson, R. B., Caro, L. & Purich, D. L. Force generation by cytoskeletal filament end-tracking proteins. *Biophys. J.* **87,** 2838–2854 (2004).
53. Mierzwa, B. & Gerlich, D. W. Cytokinetic abscission: molecular mechanisms and temporal control. *Dev. Cell* **31,** 525–538 (2014).
54. Green, R. A., Paluch, E. & Oegema, K. Cytokinesis in animal cells. *Annu. Rev. Cell Dev. Biol.* **28,** 29–58 (2012).
55. Amine, El, N., Kechad, A., Jananji, S. & Hickson, G. R. X. Opposing actions of septins and Sticky on Anillin promote the transition from contractile to midbody ring. *J. Cell Biol.* **203,** 487–504 (2013).
56. Gai, M. *et al.* Citron kinase controls abscission through RhoA and anillin. *Mol. Biol. Cell* **22,** 3768–3778 (2011).
57. Bassi, Z. I., Audusseau, M., Riparbelli, M. G., Callaini, G. & D'Avino, P. P. Citron kinase controls a molecular network required for midbody formation in cytokinesis. *Proc. Natl. Acad. Sci. U.S.A.* **110,** 9782–9787 (2013).
58. Grüneberg, U. *et al.* KIF14 and citron kinase act together to promote efficient cytokinesis. *J. Cell Biol.* **172,** 363–372 (2006).
59. Kurasawa, Y., Earnshaw, W. C., Mochizuki, Y., Dohmae, N. & Todokoro, K. Essential roles of KIF4 and its binding partner PRC1 in organized central spindle midzone formation.

EMBO J. **23,** 3237–3248 (2004).
60. Somma, M. P., Fasulo, B., Cenci, G., Cundari, E. & Gatti, M. Molecular dissection of cytokinesis by RNA interference in Drosophila cultured cells. *Mol. Biol. Cell* **13,** 2448–2460 (2002).
61. Echard, A., Hickson, G. R. X., Foley, E. & O'Farrell, P. H. Terminal cytokinesis events uncovered after an RNAi screen. *Curr. Biol.* **14,** 1685–1693 (2004).
62. Hu, C.-K., Coughlin, M. & Mitchison, T. J. Midbody assembly and its regulation during cytokinesis. *Mol. Biol. Cell* **23,** 1024–1034 (2012).
63. Carlton, J. G. & Martin-Serrano, J. Parallels between cytokinesis and retroviral budding: a role for the ESCRT machinery. *Science* **316,** 1908–1912 (2007).
64. Fielding, A. B. *et al.* Rab11-FIP3 and FIP4 interact with Arf6 and the exocyst to control membrane traffic in cytokinesis. *EMBO J.* **24,** 3389–3399 (2005).
65. Gromley, A. *et al.* Centriolin anchoring of exocyst and SNARE complexes at the midbody is required for secretory-vesicle-mediated abscission. *Cell* **123,** 75–87 (2005).
66. Kouranti, I., Sachse, M., Arouche, N., Goud, B. & Echard, A. Rab35 regulates an endocytic recycling pathway essential for the terminal steps of cytokinesis. *Curr. Biol.* **16,** 1719–1725 (2006).
67. Guizetti, J. *et al.* Cortical constriction during abscission involves helices of ESCRT-III-dependent filaments. *Science* **331,** 1616–1620 (2011).
68. Hurley, J. H. & Hanson, P. I. Membrane budding and scission by the ESCRT machinery: it's all in the neck. *Nat. Rev. Mol. Cell Biol.* **11,** 556–566 (2010).
69. Carlton, J. G., Agromayor, M. & Martin-Serrano, J. Differential requirements for Alix and ESCRT-III in cytokinesis and HIV-1 release. *Proc. Natl. Acad. Sci. U.S.A.* **105,** 10541–10546 (2008).
70. Morita, E. *et al.* Human ESCRT and ALIX proteins interact with proteins of the midbody and function in cytokinesis. *EMBO J.* **26,** 4215–4227 (2007).
71. Yang, D. *et al.* Structural basis for midbody targeting of spastin by the ESCRT-III protein CHMP1B. *Nat. Struct. Mol. Biol.* **15,** 1278–1286 (2008).
72. Connell, J. W., Lindon, C., Luzio, J. P. & Reid, E. Spastin couples microtubule severing to membrane traffic in completion of cytokinesis and secretion. *Traffic* **10,** 42–56 (2009).
73. Lacroix, B. *et al.* Tubulin polyglutamylation stimulates spastin-mediated microtubule severing. *J. Cell Biol.* **189,** 945–954 (2010).
74. Bastos, R. N. & Barr, F. A. Plk1 negatively regulates Cep55 recruitment to the midbody to ensure orderly abscission. *J. Cell Biol.* **191,** 751–760 (2010).
75. Carlton, J. G., Caballe, A., Agromayor, M., Kloc, M. & Martin-Serrano, J. ESCRT-III governs the Aurora B-mediated abscission checkpoint through CHMP4C. *Science* **336,** 220–225 (2012).
76. Capalbo, L. *et al.* The chromosomal passenger complex controls the function of endosomal sorting complex required for transport-III Snf7 proteins during cytokinesis. *Open Biol* **2,** 120070–120070 (2012).
77. Adell, M. A. Y. *et al.* Coordinated binding of Vps4 to ESCRT-III drives membrane neck constriction during MVB vesicle formation. *J. Cell Biol.* **205,** 33–49 (2014).
78. Boura, E. *et al.* Solution structure of the ESCRT-I and -II supercomplex: implications for membrane budding and scission. *Structure* **20,** 874–886 (2012).
79. Saksena, S., Wahlman, J., Teis, D., Johnson, A. E. & Emr, S. D. Functional reconstitution of ESCRT-III assembly and disassembly. *Cell* **136,** 97–109 (2009).
80. Golomb, E. *et al.* Identification and characterization of nonmuscle myosin II-C, a new member of the myosin II family. *J. Biol. Chem.* **279,** 2800–2808 (2004).

81. Bao, J., Jana, S. S. & Adelstein, R. S. Vertebrate nonmuscle myosin II isoforms rescue small interfering RNA-induced defects in COS-7 cell cytokinesis. *J. Biol. Chem.* **280,** 19594–19599 (2005).
82. Kawamoto, S. & Adelstein, R. S. Chicken nonmuscle myosin heavy chains: differential expression of two mRNAs and evidence for two different polypeptides. *J. Cell Biol.* **112,** 915–924 (1991).
83. Murakami, N., Mehta, P. & Elzinga, M. Studies on the distribution of cellular myosin with antibodies to isoform-specific synthetic peptides. *FEBS Lett.* **288,** 247 (1991).
84. Ma, X. *et al.* Ablation of nonmuscle myosin II-B and II-C reveals a role for nonmuscle myosin II in cardiac myocyte karyokinesis. *Mol. Biol. Cell* **21,** 3952–3962 (2010).
85. Kovács, M., Wang, F., Hu, A., Zhang, Y. & Sellers, J. R. Functional divergence of human cytoplasmic myosin II: kinetic characterization of the non-muscle IIA isoform. *J. Biol. Chem.* **278,** 38132–38140 (2003).
86. Wang, F. *et al.* Kinetic mechanism of non-muscle myosin IIB: functional adaptations for tension generation and maintenance. *J. Biol. Chem.* **278,** 27439–27448 (2003).
87. Kim, K.-Y., Kovács, M., Kawamoto, S., Sellers, J. R. & Adelstein, R. S. Disease-associated mutations and alternative splicing alter the enzymatic and motile activity of nonmuscle myosins II-B and II-C. *J. Biol. Chem.* **280,** 22769–22775 (2005).
88. Vicente-Manzanares, M., Ma, X., Adelstein, R. S. & Horwitz, A. R. Non-muscle myosin II takes centre stage in cell adhesion and migration. *Nat. Rev. Mol. Cell Biol.* **10,** 778–790 (2009).
89. Burgess, S. A. *et al.* Structures of smooth muscle myosin and heavy meromyosin in the folded, shutdown state. *J. Mol. Biol.* **372,** 1165–1178 (2007).
90. Ikebe, M., Hartshorne, D. J. & Elzinga, M. Identification, phosphorylation, and dephosphorylation of a second site for myosin light chain kinase on the 20,000-dalton light chain of smooth muscle myosin. *J. Biol. Chem.* **261,** 36–39 (1986).
91. Jung, H. S., Komatsu, S., Ikebe, M. & Craig, R. Head-head and head-tail interaction: a general mechanism for switching off myosin II activity in cells. *Mol. Biol. Cell* **19,** 3234–3242 (2008).
92. Ikebe, M. & Reardon, S. Phosphorylation of smooth muscle caldesmon by calmodulin-dependent protein kinase II. Identification of the phosphorylation sites. *J. Biol. Chem.* **265,** 17607–17612 (1990).
93. Komatsu, S. & Ikebe, M. The phosphorylation of myosin II at the Ser1 and Ser2 is critical for normal platelet-derived growth factor induced reorganization of myosin filaments. *Mol. Biol. Cell* **18,** 5081–5090 (2007).
94. Yamashiro, S. *et al.* Citron kinase, a Rho-dependent kinase, induces di-phosphorylation of regulatory light chain of myosin II. *Mol. Biol. Cell* **14,** 1745–1756 (2003).
95. Murata-Hori, M., Suizu, F., Iwasaki, T., Kikuchi, A. & Hosoya, H. ZIP kinase identified as a novel myosin regulatory light chain kinase in HeLa cells. *FEBS Lett.* **451,** 81–84 (1999).
96. Goeckeler, Z. M. & Wysolmerski, R. B. Myosin light chain kinase-regulated endothelial cell contraction: the relationship between isometric tension, actin polymerization, and myosin phosphorylation. *J. Cell Biol.* **130,** 613–627 (1995).
97. Totsukawa, G. *et al.* Distinct roles of ROCK (Rho-kinase) and MLCK in spatial regulation of MLC phosphorylation for assembly of stress fibers and focal adhesions in 3T3 fibroblasts. *J. Cell Biol.* **150,** 797–806 (2000).
98. Totsukawa, G. *et al.* Distinct roles of MLCK and ROCK in the regulation of membrane protrusions and focal adhesion dynamics during cell migration of fibroblasts. *J. Cell Biol.* **164,** 427–439 (2004).

99. Clark, K., Langeslag, M., Figdor, C. G. & van Leeuwen, F. N. Myosin II and mechanotransduction: a balancing act. *Trends Cell Biol.* **17,** 178–186 (2007).
100. Nishikawa, M., Sellers, J. R., Adelstein, R. S. & Hidaka, H. Protein kinase C modulates in vitro phosphorylation of the smooth muscle heavy meromyosin by myosin light chain kinase. *J. Biol. Chem.* **259,** 8808–8814 (1984).
101. Yamakita, Y., Yamashiro, S. & Matsumura, F. In vivo phosphorylation of regulatory light chain of myosin II during mitosis of cultured cells. *J. Cell Biol.* **124,** 129–137 (1994).
102. Komatsu, S., Yano, T., Shibata, M., Tuft, R. A. & Ikebe, M. Effects of the regulatory light chain phosphorylation of myosin II on mitosis and cytokinesis of mammalian cells. *J. Biol. Chem.* **275,** 34512–34520 (2000).
103. Beach, J. R., Licate, L. S., Crish, J. F. & Egelhoff, T. T. Analysis of the role of Ser1/Ser2/Thr9 phosphorylation on myosin II assembly and function in live cells. *BMC Cell Biol.* **12,** 52 (2011).
104. Kimura, K. *et al.* Regulation of myosin phosphatase by Rho and Rho-associated kinase (Rho-kinase). *Science* **273,** 245–248 (1996).
105. Hamaguchi, T. *et al.* Phosphorylation of CPI-17, an inhibitor of myosin phosphatase, by protein kinase N. *Biochem. Biophys. Res. Commun.* **274,** 825–830 (2000).
106. Conti, M. A., Sellers, J. R., Adelstein, R. S. & Elzinga, M. Identification of the serine residue phosphorylated by protein kinase C in vertebrate nonmuscle myosin heavy chains. *Biochemistry* **30,** 966–970 (1991).
107. Ludowyke, R. I. *et al.* Phosphorylation of nonmuscle myosin heavy chain IIA on Ser1917 is mediated by protein kinase C beta II and coincides with the onset of stimulated degranulation of RBL-2H3 mast cells. *J. Immunol.* **177,** 1492–1499 (2006).
108. Clark, K. *et al.* TRPM7 regulates myosin IIA filament stability and protein localization by heavy chain phosphorylation. *J. Mol. Biol.* **378,** 790–803 (2008).
109. Li, Z.-H. & Bresnick, A. R. The S100A4 metastasis factor regulates cellular motility via a direct interaction with myosin-IIA. *Cancer Res.* **66,** 5173–5180 (2006).
110. Kiss, B. *et al.* Crystal structure of the S100A4-nonmuscle myosin IIA tail fragment complex reveals an asymmetric target binding mechanism. *Proc. Natl. Acad. Sci. U.S.A.* **109,** 6048–6053 (2012).
111. Strand, D. *et al.* The Drosophila lethal(2)giant larvae tumor suppressor protein forms homo-oligomers and is associated with nonmuscle myosin II heavy chain. *J. Cell Biol.* **127,** 1361–1373 (1994).
112. Dahan, I., Yearim, A., Touboul, Y. & Ravid, S. The tumor suppressor Lgl1 regulates NMII-A cellular distribution and focal adhesion morphology to optimize cell migration. *Mol. Biol. Cell* **23,** 591–601 (2012).
113. Cabernard, C. Cytokinesis in Drosophila melanogaster. *Cytoskeleton (Hoboken)* **69,** 791–809 (2012).
114. Heath, J. P. & Holifield, B. F. Cell locomotion: new research tests old ideas on membrane and cytoskeletal flow. *Cell Motil. Cytoskeleton* **18,** 245–257 (1991).
115. Etienne-Manneville, S. & Hall, A. Integrin-mediated activation of Cdc42 controls cell polarity in migrating astrocytes through PKCzeta. *Cell* **106,** 489–498 (2001).
116. Cai, Y. *et al.* Nonmuscle myosin IIA-dependent force inhibits cell spreading and drives F-actin flow. *Biophys. J.* **91,** 3907–3920 (2006).
117. Ponti, A., Machacek, M., Gupton, S. L., Waterman-Storer, C. M. & Danuser, G. Two distinct actin networks drive the protrusion of migrating cells. *Science* **305,** 1782–1786 (2004).
118. Kolega, J. Asymmetry in the distribution of free versus cytoskeletal myosin II in

locomoting microcapillary endothelial cells. *Exp. Cell Res.* **231,** 66–82 (1997).
119. Eddy, R. J., Pierini, L. M., Matsumura, F. & Maxfield, F. R. Ca2+-dependent myosin II activation is required for uropod retraction during neutrophil migration. *J. Cell. Sci.* **113 (Pt 7),** 1287–1298 (2000).
120. Gomes, E. R., Jani, S. & Gundersen, G. G. Nuclear movement regulated by Cdc42, MRCK, myosin, and actin flow establishes MTOC polarization in migrating cells. *Cell* **121,** 451–463 (2005).
121. Shewan, A. M. *et al.* Myosin 2 is a key Rho kinase target necessary for the local concentration of E-cadherin at cell-cell contacts. *Mol. Biol. Cell* **16,** 4531–4542 (2005).
122. Ivanov, A. I. *et al.* A unique role for nonmuscle myosin heavy chain IIA in regulation of epithelial apical junctions. *PLoS ONE* **2,** e658 (2007).
123. Conti, M. A., Even-Ram, S., Liu, C., Yamada, K. M. & Adelstein, R. S. Defects in cell adhesion and the visceral endoderm following ablation of nonmuscle myosin heavy chain II-A in mice. *J. Biol. Chem.* **279,** 41263–41266 (2004).
124. Shutova, M., Yang, C., Vasiliev, J. M. & Svitkina, T. Functions of nonmuscle myosin II in assembly of the cellular contractile system. *PLoS ONE* **7,** e40814 (2012).
125. Kerridge, S. *et al.* Modular activation of Rho1 by GPCR signalling imparts polarized myosin II activation during morphogenesis. *Nat. Cell Biol.* **18,** 261–270 (2016).
126. Hashimoto, T. *et al.* Localization of PKN mRNA in the rat brain. *Brain Res. Mol. Brain Res.* **59,** 143–153 (1998).
127. Quilliam, L. A. *et al.* Isolation of a NCK-associated kinase, PRK2, an SH3-binding protein and potential effector of Rho protein signaling. *J. Biol. Chem.* **271,** 28772–28776 (1996).
128. Oishi, K., Mukai, H., Shibata, H., Takahashi, M. & Ona, Y. Identification and characterization of PKNbeta, a novel isoform of protein kinase PKN: expression and arachidonic acid dependency are different from those of PKNalpha. *Biochem. Biophys. Res. Commun.* **261,** 808–814 (1999).
129. Mukai, H. *et al.* Translocation of PKN from the cytosol to the nucleus induced by stresses. *Proc. Natl. Acad. Sci. U.S.A.* **93,** 10195–10199 (1996).
130. Lu, Y. & Settleman, J. The Drosophila Pkn protein kinase is a Rho/Rac effector target required for dorsal closure during embryogenesis. *Genes Dev.* **13,** 1168–1180 (1999).
131. Maesaki, R. *et al.* The structural basis of Rho effector recognition revealed by the crystal structure of human RhoA complexed with the effector domain of PKN/PRK1. *Mol. Cell* **4,** 793–803 (1999).
132. Takahashi, M. *et al.* Characterization of a novel giant scaffolding protein, CG-NAP, that anchors multiple signaling enzymes to centrosome and the golgi apparatus. *J. Biol. Chem.* **274,** 17267–17274 (1999).
133. Mukai, H. The structure and function of PKN, a protein kinase having a catalytic domain homologous to that of PKC. *J. Biochem.* **133,** 17–27 (2003).
134. Yoshinaga, C., Mukai, H., Toshimori, M., Miyamoto, M. & Ono, Y. Mutational analysis of the regulatory mechanism of PKN: the regulatory region of PKN contains an arachidonic acid-sensitive autoinhibitory domain. *J. Biochem.* **126,** 475–484 (1999).
135. Mukai, H. & Ono, Y. A novel protein kinase with leucine zipper-like sequences: its catalytic domain is highly homologous to that of protein kinase C. *Biochem. Biophys. Res. Commun.* **199,** 897–904 (1994).
136. Palmer, R. H. *et al.* Activation of PRK1 by phosphatidylinositol 4,5-bisphosphate and phosphatidylinositol 3,4,5-trisphosphate. A comparison with protein kinase C isotypes. *J. Biol. Chem.* **270,** 22412–22416 (1995).
137. Amano, M. *et al.* Identification of a putative target for Rho as the serine-threonine

kinase protein kinase N. *Science* **271,** 648–650 (1996).
138. Watanabe, G. *et al.* Protein kinase N (PKN) and PKN-related protein rhophilin as targets of small GTPase Rho. *Science* **271,** 645–648 (1996).
139. Flynn, P., Mellor, H., Palmer, R., Panayotou, G. & Parker, P. J. Multiple interactions of PRK1 with RhoA. Functional assignment of the Hr1 repeat motif. *J. Biol. Chem.* **273,** 2698–2705 (1998).
140. Dong, L. Q. *et al.* Phosphorylation of protein kinase N by phosphoinositide-dependent protein kinase-1 mediates insulin signals to the actin cytoskeleton. *Proc. Natl. Acad. Sci. U.S.A.* **97,** 5089–5094 (2000).
141. Flynn, P., Mellor, H., Casamassima, A. & Parker, P. J. Rho GTPase control of protein kinase C-related protein kinase activation by 3-phosphoinositide-dependent protein kinase. *J. Biol. Chem.* **275,** 11064–11070 (2000).
142. Sun, W., Vincent, S., Settleman, J. & Johnson, G. L. MEK kinase 2 binds and activates protein kinase C-related kinase 2. Bifurcation of kinase regulatory pathways at the level of an MAPK kinase kinase. *J. Biol. Chem.* **275,** 24421–24428 (2000).
143. Calautti, E. *et al.* Fyn tyrosine kinase is a downstream mediator of Rho/PRK2 function in keratinocyte cell-cell adhesion. *J. Cell Biol.* **156,** 137–148 (2002).
144. Torbett, N. E., Casamassima, A. & Parker, P. J. Hyperosmotic-induced protein kinase N 1 activation in a vesicular compartment is dependent upon Rac1 and 3-phosphoinositide-dependent kinase 1. *J. Biol. Chem.* **278,** 32344–32351 (2003).
145. Takahashi, M., Mukai, H., Toshimori, M., Miyamoto, M. & Ono, Y. Proteolytic activation of PKN by caspase-3 or related protease during apoptosis. *Proc. Natl. Acad. Sci. U.S.A.* **95,** 11566–11571 (1998).
146. Koh, H. *et al.* Inhibition of Akt and its anti-apoptotic activities by tumor necrosis factor-induced protein kinase C-related kinase 2 (PRK2) cleavage. *J. Biol. Chem.* **275,** 34451–34458 (2000).
147. Misaki, K. *et al.* PKN delays mitotic timing by inhibition of Cdc25C: possible involvement of PKN in the regulation of cell division. *Proc. Natl. Acad. Sci. U.S.A.* **98,** 125–129 (2001).
148. Schmidt, A., Durgan, J., Magalhaes, A. & Hall, A. Rho GTPases regulate PRK2/PKN2 to control entry into mitosis and exit from cytokinesis. *EMBO J.* **26,** 1624–1636 (2007).
149. Kawamata, T. *et al.* A protein kinase, PKN, accumulates in Alzheimer neurofibrillary tangles and associated endoplasmic reticulum-derived vesicles and phosphorylates tau protein. *J. Neurosci.* **18,** 7402–7410 (1998).
150. Taniguchi, T. *et al.* Phosphorylation of tau is regulated by PKN. *J. Biol. Chem.* **276,** 10025–10031 (2001).
151. Ueno, N. *et al.* Identification of a novel Drosophila protein kinase highly homologous to protein kinase N (PKN). *Biochem. Biophys. Res. Commun.* **232,** 126–129 (1997).
152. Betson, M. & Settleman, J. A rho-binding protein kinase C-like activity is required for the function of protein kinase N in Drosophila development. *Genetics* **176,** 2201–2212 (2007).
153. Ferreira, T., Prudêncio, P. & Martinho, R. G. Drosophila protein kinase N (Pkn) is a negative regulator of actin-myosin activity during oogenesis. *Dev. Biol.* **394,** 277–291 (2014).
154. Sass, G. L. & Ostrow, B. D. Disruption of the protein kinase N gene of drosophila melanogaster results in the recessive delorean allele (pkndln) with a negative impact on wing morphogenesis. *G3 (Bethesda)* **4,** 643–656 (2014).
155. Leung, T., Manser, E., Tan, L. & Lim, L. A novel serine/threonine kinase binding the Ras-related RhoA GTPase which translocates the kinase to peripheral membranes. *J. Biol.*

Chem. **270,** 29051–29054 (1995).
156. Matsui, T. *et al.* Rho-associated kinase, a novel serine/threonine kinase, as a putative target for small GTP binding protein Rho. *EMBO J.* **15,** 2208–2216 (1996).
157. Leung, T., Chen, X. Q., Manser, E. & Lim, L. The p160 RhoA-binding kinase ROK alpha is a member of a kinase family and is involved in the reorganization of the cytoskeleton. *Mol. Cell. Biol.* **16,** 5313–5327 (1996).
158. Nakagawa, O. *et al.* ROCK-I and ROCK-II, two isoforms of Rho-associated coiled-coil forming protein serine/threonine kinase in mice. *FEBS Lett.* **392,** 189–193 (1996).
159. Kosako, H. *et al.* Specific accumulation of Rho-associated kinase at the cleavage furrow during cytokinesis: cleavage furrow-specific phosphorylation of intermediate filaments. *Oncogene* **18,** 2783–2788 (1999).
160. Chevrier, V. *et al.* The Rho-associated protein kinase p160ROCK is required for centrosome positioning. *J. Cell Biol.* **157,** 807–817 (2002).
161. Shimizu, T. *et al.* Parallel coiled-coil association of the RhoA-binding domain in Rho-kinase. *J. Biol. Chem.* **278,** 46046–46051 (2003).
162. Dvorsky, R., Blumenstein, L., Vetter, I. R. & Ahmadian, M. R. Structural insights into the interaction of ROCKI with the switch regions of RhoA. *J. Biol. Chem.* **279,** 7098–7104 (2004).
163. Wen, W., Liu, W., Yan, J. & Zhang, M. Structure basis and unconventional lipid membrane binding properties of the PH-C1 tandem of rho kinases. *J. Biol. Chem.* **283,** 26263–26273 (2008).
164. Amano, M. *et al.* The COOH terminus of Rho-kinase negatively regulates rho-kinase activity. *J. Biol. Chem.* **274,** 32418–32424 (1999).
165. Chen, X.-Q. *et al.* Characterization of RhoA-binding kinase ROKalpha implication of the pleckstrin homology domain in ROKalpha function using region-specific antibodies. *J. Biol. Chem.* **277,** 12680–12688 (2002).
166. Ishizaki, T. *et al.* The small GTP-binding protein Rho binds to and activates a 160 kDa Ser/Thr protein kinase homologous to myotonic dystrophy kinase. *EMBO J.* **15,** 1885–1893 (1996).
167. Sebbagh, M. *et al.* Caspase-3-mediated cleavage of ROCK I induces MLC phosphorylation and apoptotic membrane blebbing. *Nat. Cell Biol.* **3,** 346–352 (2001).
168. Coleman, M. L. *et al.* Membrane blebbing during apoptosis results from caspase-mediated activation of ROCK I. *Nat. Cell Biol.* **3,** 339–345 (2001).
169. Lowery, D. M. *et al.* Proteomic screen defines the Polo-box domain interactome and identifies Rock2 as a Plk1 substrate. *EMBO J.* **26,** 2262–2273 (2007).
170. Sinning, J.-M. *et al.* Circulating CD31+/Annexin V+ microparticles correlate with cardiovascular outcomes. *Eur. Heart J.* **32,** 2034–2041 (2011).
171. Lee, H.-H. & Chang, Z.-F. Regulation of RhoA-dependent ROCKII activation by Shp2. *J. Cell Biol.* **181,** 999–1012 (2008).
172. Ward, Y. *et al.* The GTP binding proteins Gem and Rad are negative regulators of the Rho-Rho kinase pathway. *J. Cell Biol.* **157,** 291–302 (2002).
173. Hall, C. *et al.* Collapsin response mediator protein switches RhoA and Rac1 morphology in N1E-115 neuroblastoma cells and is regulated by Rho kinase. *J. Biol. Chem.* **276,** 43482–43486 (2001).
174. Croft, D. R. *et al.* Actin-myosin-based contraction is responsible for apoptotic nuclear disintegration. *J. Cell Biol.* **168,** 245–255 (2005).
175. Yamazaki, M. *et al.* Phosphatidylinositol 4-phosphate 5-kinase is essential for ROCK-mediated neurite remodeling. *J. Biol. Chem.* **277,** 17226–17230 (2002).

176. Tanaka, H. *et al.* Cytoplasmic p21(Cip1/WAF1) regulates neurite remodeling by inhibiting Rho-kinase activity. *J. Cell Biol.* **158,** 321–329 (2002).
177. Sordella, R. *et al.* Modulation of CREB activity by the Rho GTPase regulates cell and organism size during mouse embryonic development. *Dev. Cell* **2,** 553–565 (2002).
178. Sordella, R., Jiang, W., Chen, G.-C., Curto, M. & Settleman, J. Modulation of Rho GTPase signaling regulates a switch between adipogenesis and myogenesis. *Cell* **113,** 147–158 (2003).
179. Mizuno, T., Amano, M., Kaibuchi, K. & Nishida, Y. Identification and characterization of Drosophila homolog of Rho-kinase. *Gene* **238,** 437–444 (1999).
180. Strutt, D. I., Weber, U. & Mlodzik, M. The role of RhoA in tissue polarity and Frizzled signalling. *Nature* **387,** 292–295 (1997).
181. Winter, C. G. *et al.* Drosophila Rho-associated kinase (Drok) links Frizzled-mediated planar cell polarity signaling to the actin cytoskeleton. *Cell* **105,** 81–91 (2001).
182. Verdier, V. *et al.* Drosophila Rho-kinase (DRok) is required for tissue morphogenesis in diverse compartments of the egg chamber during oogenesis. *Dev. Biol.* **297,** 417–432 (2006).
183. Verdier, V., Guang-Chao-Chen & Settleman, J. Rho-kinase regulates tissue morphogenesis via non-muscle myosin and LIM-kinase during Drosophila development. *BMC Dev. Biol.* **6,** 38 (2006).
184. Zhao, Z.-S. & Manser, E. PAK and other Rho-associated kinases--effectors with surprisingly diverse mechanisms of regulation. *Biochem. J.* **386,** 201–214 (2005).
185. Baskaran, Y., Ng, Y.-W., Selamat, W., Ling, F. T. P. & Manser, E. Group I and II mammalian PAKs have different modes of activation by Cdc42. *EMBO Rep.* **13,** 653–659 (2012).
186. Ha, B. H. *et al.* Type II p21-activated kinases (PAKs) are regulated by an autoinhibitory pseudosubstrate. *Proc. Natl. Acad. Sci. U.S.A.* **109,** 16107–16112 (2012).
187. Lei, M. *et al.* Structure of PAK1 in an autoinhibited conformation reveals a multistage activation switch. *Cell* **102,** 387–397 (2000).
188. Buchwald, G. *et al.* Conformational switch and role of phosphorylation in PAK activation. *Mol. Cell. Biol.* **21,** 5179–5189 (2001).
189. Fryer, B. H. *et al.* cGMP-dependent protein kinase phosphorylates p21-activated kinase (Pak) 1, inhibiting Pak/Nck binding and stimulating Pak/vasodilator-stimulated phosphoprotein association. *J. Biol. Chem.* **281,** 11487–11495 (2006).
190. Strochlic, T. I., Viaud, J., Rennefahrt, U. E. E., Anastassiadis, T. & Peterson, J. R. Phosphoinositides are essential coactivators for p21-activated kinase 1. *Mol. Cell* **40,** 493–500 (2010).
191. Radu, M., Semenova, G., Kosoff, R. & Chernoff, J. PAK signalling during the development and progression of cancer. *Nat. Rev. Cancer* **14,** 13–25 (2014).
192. Ramos, E., Wysolmerski, R. B. & Masaracchia, R. A. Myosin phosphorylation by human cdc42-dependent S6/H4 kinase/gammaPAK from placenta and lymphoid cells. *Recept Signal Transduct* **7,** 99–110 (1997).
193. Chew, T. L., Masaracchia, R. A., Goeckeler, Z. M. & Wysolmerski, R. B. Phosphorylation of non-muscle myosin II regulatory light chain by p21-activated kinase (gamma-PAK). *J. Muscle Res. Cell. Motil.* **19,** 839–854 (1998).
194. Qu, J. *et al.* Activated PAK4 regulates cell adhesion and anchorage-independent growth. *Mol. Cell. Biol.* **21,** 3523–3533 (2001).
195. Sanders, L. C., Matsumura, F., Bokoch, G. M. & de Lanerolle, P. Inhibition of myosin light chain kinase by p21-activated kinase. *Science* **283,** 2083–2085 (1999).
196. Goeckeler, Z. M. *et al.* Phosphorylation of myosin light chain kinase by p21-activated

kinase PAK2. *J. Biol. Chem.* **275,** 18366–18374 (2000).
197. Zhang, H., Webb, D. J., Asmussen, H., Niu, S. & Horwitz, A. F. A GIT1/PIX/Rac/PAK signaling module regulates spine morphogenesis and synapse formation through MLC. *J. Neurosci.* **25,** 3379–3388 (2005).
198. Edwards, D. C., Sanders, L. C., Bokoch, G. M. & Gill, G. N. Activation of LIM-kinase by Pak1 couples Rac/Cdc42 GTPase signalling to actin cytoskeletal dynamics. *Nat. Cell Biol.* **1,** 253–259 (1999).
199. Arber, S. *et al.* Regulation of actin dynamics through phosphorylation of cofilin by LIM-kinase. *Nature* **393,** 805–809 (1998).
200. Yang, N. *et al.* Cofilin phosphorylation by LIM-kinase 1 and its role in Rac-mediated actin reorganization. *Nature* **393,** 809–812 (1998).
201. Soosairajah, J. *et al.* Interplay between components of a novel LIM kinase-slingshot phosphatase complex regulates cofilin. *EMBO J.* **24,** 473–486 (2005).
202. Vadlamudi, R. K. *et al.* Filamin is essential in actin cytoskeletal assembly mediated by p21-activated kinase 1. *Nat. Cell Biol.* **4,** 681–690 (2002).
203. Vadlamudi, R. K. *et al.* p21-activated kinase 1 regulates microtubule dynamics by phosphorylating tubulin cofactor B. *Mol. Cell. Biol.* **25,** 3726–3736 (2005).
204. Maroto, B., Ye, M. B., Lohneysen, von, K., Schnelzer, A. & Knaus, U. G. P21-activated kinase is required for mitotic progression and regulates Plk1. *Oncogene* **27,** 4900–4908 (2008).
205. Melzig, J. *et al.* A protein related to p21-activated kinase (PAK) that is involved in neurogenesis in the Drosophila adult central nervous system. *Curr. Biol.* **8,** 1223–1226 (1998).
206. Schneeberger, D. & Raabe, T. Mbt, a Drosophila PAK protein, combines with Cdc42 to regulate photoreceptor cell morphogenesis. *Development* **130,** 427–437 (2003).
207. Menzel, N., Schneeberger, D. & Raabe, T. The Drosophila p21 activated kinase Mbt regulates the actin cytoskeleton and adherens junctions to control photoreceptor cell morphogenesis. *Mech. Dev.* **124,** 78–90 (2007).
208. Melzer, J., Kraft, K. F., Urbach, R. & Raabe, T. The p21-activated kinase Mbt is a component of the apical protein complex in central brain neuroblasts and controls cell proliferation. *Development* **140,** 1871–1881 (2013).
209. Taghert, P. H. & Goodman, C. S. Cell determination and differentiation of identified serotonin-immunoreactive neurons in the grasshopper embryo. *J. Neurosci.* **4,** 989–1000 (1984).
210. Fehon, R. G. *et al.* Molecular interactions between the protein products of the neurogenic loci Notch and Delta, two EGF-homologous genes in Drosophila. *Cell* **61,** 523–534 (1990).
211. Kunisch, M., Haenlin, M. & Campos-Ortega, J. A. Lateral inhibition mediated by the Drosophila neurogenic gene delta is enhanced by proneural proteins. *Proc. Natl. Acad. Sci. U.S.A.* **91,** 10139–10143 (1994).
212. Skeath, J. B. & Carroll, S. B. The achaete-scute complex: generation of cellular pattern and fate within the Drosophila nervous system. *FASEB J.* **8,** 714–721 (1994).
213. García-Bellido, A. Genetic Analysis of the Achaete-Scute System of DROSOPHILA MELANOGASTER. *Genetics* **91,** 491–520 (1979).
214. Ghysen, A. & Dambly-Chaudière, C. From DNA to form: the achaete-scute complex. *Genes Dev.* **2,** 495–501 (1988).
215. Chu-LaGraff, Q. & Doe, C. Q. Neuroblast specification and formation regulated by wingless in the Drosophila CNS. *Science* **261,** 1594–1597 (1993).

216. Hartenstein, V., Younossi-Hartenstein, A. & Lekven, A. Delamination and division in the Drosophila neurectoderm: spatiotemporal pattern, cytoskeletal dynamics, and common control by neurogenic and segment polarity genes. *Dev. Biol.* **165,** 480–499 (1994).
217. Prokop, A. & Technau, G. M. The origin of postembryonic neuroblasts in the ventral nerve cord of Drosophila melanogaster. *Development* **111,** 79–88 (1991).
218. White, K. *et al.* Genetic control of programmed cell death in Drosophila. *Science* **264,** 677–683 (1994).
219. White, K. & Kankel, D. R. Patterns of cell division and cell movement in the formation of the imaginal nervous system in Drosophila melanogaster. *Dev. Biol.* **65,** 296–321 (1978).
220. Truman, J. W. & Bate, M. Spatial and temporal patterns of neurogenesis in the central nervous system of Drosophila melanogaster. *Dev. Biol.* **125,** 145–157 (1988).
221. Maurange, C., Cheng, L. & Gould, A. P. Temporal transcription factors and their targets schedule the end of neural proliferation in Drosophila. *Cell* **133,** 891–902 (2008).
222. Homem, C. C. F. *et al.* Ecdysone and mediator change energy metabolism to terminate proliferation in Drosophila neural stem cells. *Cell* **158,** 874–888 (2014).
223. Bello, B. C., Izergina, N., Caussinus, E. & Reichert, H. Amplification of neural stem cell proliferation by intermediate progenitor cells in Drosophila brain development. *Neural Dev* **3,** 5 (2008).
224. Boone, J. Q. & Doe, C. Q. Identification of Drosophila type II neuroblast lineages containing transit amplifying ganglion mother cells. *Dev Neurobiol* **68,** 1185–1195 (2008).
225. Bowman, S. K. *et al.* The tumor suppressors Brat and Numb regulate transit-amplifying neuroblast lineages in Drosophila. *Dev. Cell* **14,** 535–546 (2008).
226. Zhu, S., Barshow, S., Wildonger, J., Jan, L. Y. & Jan, Y.-N. Ets transcription factor Pointed promotes the generation of intermediate neural progenitors in Drosophila larval brains. *Proc. Natl. Acad. Sci. U.S.A.* **108,** 20615–20620 (2011).
227. Bayraktar, O. A. & Doe, C. Q. Combinatorial temporal patterning in progenitors expands neural diversity. *Nature* **498,** 449–455 (2013).
228. Weng, M., Golden, K. L. & Lee, C.-Y. dFezf/Earmuff maintains the restricted developmental potential of intermediate neural progenitors in Drosophila. *Dev. Cell* **18,** 126–135 (2010).
229. Homem, C. C. F. & Knoblich, J. A. Drosophila neuroblasts: a model for stem cell biology. *Development* **139,** 4297–4310 (2012).
230. Wirtz-Peitz, F., Nishimura, T. & Knoblich, J. A. Linking cell cycle to asymmetric division: Aurora-A phosphorylates the Par complex to regulate Numb localization. *Cell* **135,** 161–173 (2008).
231. Prehoda, K. E. Polarization of Drosophila neuroblasts during asymmetric division. *Cold Spring Harb Perspect Biol* **1,** a001388–a001388 (2009).
232. Petronczki, M. & Knoblich, J. A. DmPAR-6 directs epithelial polarity and asymmetric cell division of neuroblasts in Drosophila. *Nat. Cell Biol.* **3,** 43–49 (2001).
233. Atwood, S. X., Chabu, C., Penkert, R. R., Doe, C. Q. & Prehoda, K. E. Cdc42 acts downstream of Bazooka to regulate neuroblast polarity through Par-6 aPKC. *J. Cell. Sci.* **120,** 3200–3206 (2007).
234. Chabu, C. & Doe, C. Q. Dap160/intersectin binds and activates aPKC to regulate cell polarity and cell cycle progression. *Development* **135,** 2739–2746 (2008).
235. Chabu, C. & Doe, C. Q. Twins/PP2A regulates aPKC to control neuroblast cell polarity and self-renewal. *Dev. Biol.* **330,** 399–405 (2009).
236. Schaefer, M., Shevchenko, A. & Knoblich, J. A. A protein complex containing Inscuteable

and the Galpha-binding protein Pins orients asymmetric cell divisions in Drosophila. *Curr. Biol.* **10,** 353–362 (2000).
237. Schober, M., Schaefer, M. & Knoblich, J. A. Bazooka recruits Inscuteable to orient asymmetric cell divisions in Drosophila neuroblasts. *Nature* **402,** 548–551 (1999).
238. Wodarz, A., Ramrath, A., Kuchinke, U. & Knust, E. Bazooka provides an apical cue for Inscuteable localization in Drosophila neuroblasts. *Nature* **402,** 544–547 (1999).
239. Yu, F., Morin, X., Cai, Y., Yang, X. & Chia, W. Analysis of partner of inscuteable, a novel player of Drosophila asymmetric divisions, reveals two distinct steps in inscuteable apical localization. *Cell* **100,** 399–409 (2000).
240. Siller, K. H., Cabernard, C. & Doe, C. Q. The NuMA-related Mud protein binds Pins and regulates spindle orientation in Drosophila neuroblasts. *Nat. Cell Biol.* **8,** 594–600 (2006).
241. Bowman, S. K., Neumüller, R. A., Novatchkova, M., Du, Q. & Knoblich, J. A. The Drosophila NuMA Homolog Mud regulates spindle orientation in asymmetric cell division. *Dev. Cell* **10,** 731–742 (2006).
242. Izumi, Y., Ohta, N., Hisata, K., Raabe, T. & Matsuzaki, F. Drosophila Pins-binding protein Mud regulates spindle-polarity coupling and centrosome organization. *Nat. Cell Biol.* **8,** 586–593 (2006).
243. Siegrist, S. E. & Doe, C. Q. Microtubule-induced Pins/Galphai cortical polarity in Drosophila neuroblasts. *Cell* **123,** 1323–1335 (2005).
244. Shen, C. P., Jan, L. Y. & Jan, Y. N. Miranda is required for the asymmetric localization of Prospero during mitosis in Drosophila. *Cell* **90,** 449–458 (1997).
245. Chu-LaGraff, Q., Wright, D. M., McNeil, L. K. & Doe, C. Q. The prospero gene encodes a divergent homeodomain protein that controls neuronal identity in Drosophila. *Dev. Suppl.* **Suppl 2,** 79–85 (1991).
246. Matsuzaki, F., Koizumi, K., Hama, C., Yoshioka, T. & Nabeshima, Y. Cloning of the Drosophila prospero gene and its expression in ganglion mother cells. *Biochem. Biophys. Res. Commun.* **182,** 1326–1332 (1992).
247. Bello, B., Reichert, H. & Hirth, F. The brain tumor gene negatively regulates neural progenitor cell proliferation in the larval central brain of Drosophila. *Development* **133,** 2639–2648 (2006).
248. Rhyu, M. S., Jan, L. Y. & Jan, Y. N. Asymmetric distribution of numb protein during division of the sensory organ precursor cell confers distinct fates to daughter cells. *Cell* **76,** 477–491 (1994).
249. Knoblich, J. A., Jan, L. Y. & Jan, Y. N. Asymmetric segregation of Numb and Prospero during cell division. *Nature* **377,** 624–627 (1995).
250. Ikeshima-Kataoka, H., Skeath, J. B., Nabeshima, Y., Doe, C. Q. & Matsuzaki, F. Miranda directs Prospero to a daughter cell during Drosophila asymmetric divisions. *Nature* **390,** 625–629 (1997).
251. Schuldt, A. J. *et al.* Miranda mediates asymmetric protein and RNA localization in the developing nervous system. *Genes Dev.* **12,** 1847–1857 (1998).
252. Lee, C.-Y., Wilkinson, B. D., Siegrist, S. E., Wharton, R. P. & Doe, C. Q. Brat is a Miranda cargo protein that promotes neuronal differentiation and inhibits neuroblast self-renewal. *Dev. Cell* **10,** 441–449 (2006).
253. Shen, C. P. *et al.* Miranda as a multidomain adapter linking apically localized Inscuteable and basally localized Staufen and Prospero during asymmetric cell division in Drosophila. *Genes Dev.* **12,** 1837–1846 (1998).
254. Fuerstenberg, S., Peng, C. Y., Alvarez-Ortiz, P., Hor, T. & Doe, C. Q. Identification of

Miranda protein domains regulating asymmetric cortical localization, cargo binding, and cortical release. *Mol. Cell. Neurosci.* **12,** 325–339 (1998).
255. Choksi, S. P. *et al.* Prospero acts as a binary switch between self-renewal and differentiation in Drosophila neural stem cells. *Dev. Cell* **11,** 775–789 (2006).
256. Sousa-Nunes, R., Chia, W. & Somers, W. G. Protein phosphatase 4 mediates localization of the Miranda complex during Drosophila neuroblast asymmetric divisions. *Genes Dev.* **23,** 359–372 (2009).
257. Atwood, S. X. & Prehoda, K. E. aPKC phosphorylates Miranda to polarize fate determinants during neuroblast asymmetric cell division. *Curr. Biol.* **19,** 723–729 (2009).
258. Zhang, F. *et al.* Phosphotyrosyl phosphatase activator facilitates localization of Miranda through dephosphorylation in dividing neuroblasts. *Development* **143,** 35–44 (2016).
259. Lu, B., Rothenberg, M., Jan, L. Y. & Jan, Y. N. Partner of Numb colocalizes with Numb during mitosis and directs Numb asymmetric localization in Drosophila neural and muscle progenitors. *Cell* **95,** 225–235 (1998).
260. Wang, H., Ouyang, Y., Somers, W. G., Chia, W. & Lu, B. Polo inhibits progenitor self-renewal and regulates Numb asymmetry by phosphorylating Pon. *Nature* **449,** 96–100 (2007).
261. Smith, C. A. *et al.* aPKC-mediated phosphorylation regulates asymmetric membrane localization of the cell fate determinant Numb. *EMBO J.* **26,** 468–480 (2007).
262. Betschinger, J., Mechtler, K. & Knoblich, J. A. Asymmetric segregation of the tumor suppressor brat regulates self-renewal in Drosophila neural stem cells. *Cell* **124,** 1241–1253 (2006).
263. Bello, B., Holbro, N. & Reichert, H. Polycomb group genes are required for neural stem cell survival in postembryonic neurogenesis of Drosophila. *Development* **134,** 1091–1099 (2007).
264. Caussinus, E. & Gonzalez, C. Induction of tumor growth by altered stem-cell asymmetric division in Drosophila melanogaster. *Nat. Genet.* **37,** 1125–1129 (2005).
265. Cabernard, C. & Doe, C. Q. Apical/basal spindle orientation is required for neuroblast homeostasis and neuronal differentiation in Drosophila. *Dev. Cell* **17,** 134–141 (2009).
266. Kaltschmidt, J. A., Davidson, C. M., Brown, N. H. & Brand, A. H. Rotation and asymmetry of the mitotic spindle direct asymmetric cell division in the developing central nervous system. *Nat. Cell Biol.* **2,** 7–12 (2000).
267. Fuse, N., Hisata, K., Katzen, A. L. & Matsuzaki, F. Heterotrimeric G proteins regulate daughter cell size asymmetry in Drosophila neuroblast divisions. *Curr. Biol.* **13,** 947–954 (2003).
268. Yu, F., Cai, Y., Kaushik, R., Yang, X. & Chia, W. Distinct roles of Galphai and Gbeta13F subunits of the heterotrimeric G protein complex in the mediation of Drosophila neuroblast asymmetric divisions. *J. Cell Biol.* **162,** 623–633 (2003).
269. Albertson, R. & Doe, C. Q. Dlg, Scrib and Lgl regulate neuroblast cell size and mitotic spindle asymmetry. *Nat. Cell Biol.* **5,** 166–170 (2003).
270. Izumi, Y., Ohta, N., Itoh-Furuya, A., Fuse, N. & Matsuzaki, F. Differential functions of G protein and Baz-aPKC signaling pathways in Drosophila neuroblast asymmetric division. *J. Cell Biol.* **164,** 729–738 (2004).
271. Cai, Y., Chia, W. & Yang, X. A family of snail-related zinc finger proteins regulates two distinct and parallel mechanisms that mediate Drosophila neuroblast asymmetric divisions. *EMBO J.* **20,** 1704–1714 (2001).
272. Giansanti, M. G., Gatti, M. & Bonaccorsi, S. The role of centrosomes and astral microtubules during asymmetric division of Drosophila neuroblasts. *Development* **128,**

1137–1145 (2001).
273. Basto, R. *et al.* Flies without centrioles. *Cell* **125,** 1375–1386 (2006).
274. Varmark, H. *et al.* Asterless is a centriolar protein required for centrosome function and embryo development in Drosophila. *Curr. Biol.* **17,** 1735–1745 (2007).
275. Cabernard, C., Prehoda, K. E. & Doe, C. Q. A spindle-independent cleavage furrow positioning pathway. *Nature* **467,** 91–94 (2010).
276. Roth, M., Roubinet, C., Iffländer, N., Ferrand, A. & Cabernard, C. Asymmetrically dividing Drosophila neuroblasts utilize two spatially and temporally independent cytokinesis pathways. *Nat Commun* **6,** 6551 (2015).
277. Connell, M., Cabernard, C., Ricketson, D., Doe, C. Q. & Prehoda, K. E. Asymmetric cortical extension shifts cleavage furrow position in Drosophila neuroblasts. *Mol. Biol. Cell* **22,** 4220–4226 (2011).
278. Ou, G., Stuurman, N., D'Ambrosio, M. & Vale, R. D. Polarized myosin produces unequal-size daughters during asymmetric cell division. *Science* **330,** 677–680 (2010).
279. Cinalli, R. M. & Lehmann, R. A spindle-independent cleavage pathway controls germ cell formation in Drosophila. *Nat. Cell Biol.* **15,** 839–845 (2013).
280. Lee, C.-Y., Robinson, K. J. & Doe, C. Q. Lgl, Pins and aPKC regulate neuroblast self-renewal versus differentiation. *Nature* **439,** 594–598 (2006).
281. Dempsey, W. P. *et al.* In vivo single-cell labeling by confined primed conversion. *Nat. Methods* **12,** 645–648 (2015).
282. Masuda, T. *et al.* Molecular cloning and characterization of yeast rho GDP dissociation inhibitor. *J. Biol. Chem.* **269,** 19713–19718 (1994).
283. De Simone, A., Nédélec, F. & Gönczy, P. Dynein Transmits Polarized Actomyosin Cortical Flows to Promote Centrosome Separation. *Cell Rep* **14,** 2250–2262 (2016).
284. Cowan, C. R. & Hyman, A. A. Acto-myosin reorganization and PAR polarity in C. elegans. *Development* **134,** 1035–1043 (2007).
285. Walck-Shannon, E. & Hardin, J. Cell intercalation from top to bottom. *Nat. Rev. Mol. Cell Biol.* **15,** 34–48 (2014).
286. Devenport, D. The cell biology of planar cell polarity. *J. Cell Biol.* **207,** 171–179 (2014).